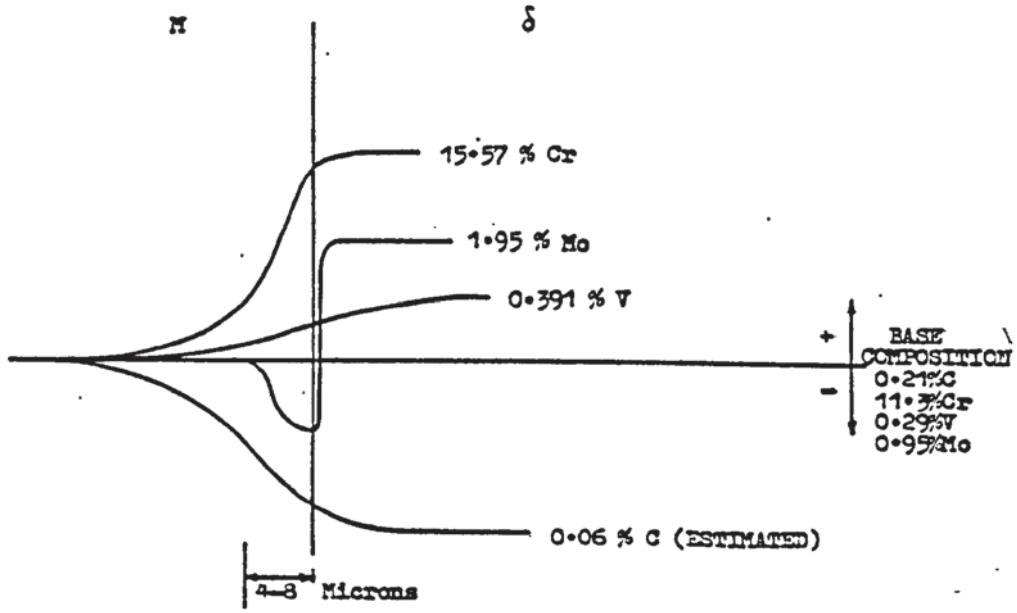


FIGURE 87 Schematic representation of observed alloying element profiles across a δ/martensite interface

heating rate, but no variation in Ms or Mf due to different cooling rates was observed. The CCT diagram for Class 1 steel, produced from this work, is shown in figure 10 and shows a cooling rate dependant variation occurring. This was investigated by prolonged holding of a sample just below the inflexion temperature and was found to be "carbide start" (Cs) point. Heavily carbided martensite was found on optical examination (figure 11) of a held specimen. The location of these regions compares well with published CCT diagrams [1] (c.f.figure 4).

In Class 2 steels the same transformations were noted as in Class 1 material, except that no Cs occurred, transformation temperatures observed being:- $Ac_1$ 861°C, $Ac_3$ 892°C, Ms 275°C and Mf 60°C. Throughout all cooling rates used, no variation in Ms or Mf were noted, whilst on heating slight variations in $Ac_1$ and $Ac_3$ occurred. The CCT diagram produced for this steel is illustrated in figure 12, once again agreeing with published results [1].

During metallurgical examination of Class 2 dilatometer specimens, measurements of prior austenite grain size were performed and then compared with oil quenched untempered samples. Dilatometer samples were found to have average grain sizes of 0.25 to 0.3 mm diameter, whilst oil quenched samples averaged 0.3 mm diameter. On this basis the effect of dilatometry treatments were shown to have no significant effect on grain growth.

# "The microstructure of the weld heat affected zone in the Super 12% chromium-molybdenum steels"

A Thesis Submitted To

THE UNIVERSITY OF ASTON IN BIRMINGHAM

For The Award Of Doctor Of Philosophy

By Robert Fenn MSc

DECEMBER 1977

TO MY WIFE

AND TO THE FULFILMENT OF A LIFETIMES AMBITION

# SUMMARY

## SUMMARY

The Microstructure of the weld heat-affected zone in the Super 12% chromium-molybdenum steels

Robert Fenn PhD December 1977

A systematic investigation has been performed into the phase transformations occurring in the weld heat-affected zone of a commercial Super 12% chromium-molybdenum steel by studying real and simulated welds. Conventional heat-treatments were used to investigate the likely phase transformations produced by welding. Three probable regions were located namely δ ferrite + martensite, homogenous martensite and secondary hardened zones. Welds were produced using arc welding processes covering a wide heat-input range and metallographic examination confirmed the existance of three regions. Small diameter tubes welded at room temperature and 300°C pre-heat showed that the heat-affected zone did not crack nor show loss of ductility in either case.

Weld thermal simulation was performed for selected heat-affected zone regions using computed weld thermal cycles and the phase tranformations were monitored by high speed dilatometry. Attention was concentrated on δ ferrite formation which was shown to commence at 1320-1360°C, depending on the heating rate. It was found that the δ ferrite content rose as heat-input and time above 1320°C increased and it was fully retained to room temperature at weld cooling rates. The presence of δ ferrite did not affect austenite transformations during continuous cooling although isothermal tranformations were retarded. Full details of the significant transformation data are assembled in a representative welding continuous cooling transformation diagram.

Tests, using specimens containing a range of δ ferrite contents, showed that it adversely affects physical properties of these steels. Both ductility and corrosion resistance are reduced by increased δ ferrite quantities. Furthermore, re-solution heat-treatments were required to remove δ ferrite from the material to restore wrought material properties.

Electron microscopy investigations gave an insight into the mechanism of δ ferrite formation. Evidence is produced to show that this occurrence crack-sensitises this steel.



Key words: Steel
Microstructure
Weld Heat-affected zone

# DECLARATION

## DECLARATION

No part of the work described in this thesis was performed in collaboration with anyone else, except where specifically stated. Although advice and help was sought and received from a number of people, all the work described herein is my own.

Acknowledgements have been given to the people whose advice and aid was sought.

This work has not been submitted before for any other award to this, or any other, University.

Robert Fenn

ROBERT FENN
DEPARTMENT OF PRODUCTION ENGINEERING

1977

CONTENTS

# CHAPTER ONE

## INTRODUCTION

# CHAPTER ONE INTRODUCTION

The Super 12% chromium-molybdenum martensitic stainless steels are used widely throughout industry in applications ranging from turbines to forging dies and from airframes to heat exchangers [1,2,3]. Currently, their widest range of application appears to be in steam generating equipment, which may be heated by either conventional or nuclear fuels. These applications are a very severe test of the steels because steam generating plant constantly operates at high pressures and temperatures (540°C to 560°C). Furthermore, in these applications, they must retain sufficient corrosion resistance to resist water chemistry variations in low temperature regions and maintain an economically long operating life of 100,000 to 150,000 hours.

Stringent as these specifications are, they are satisfied by wrought Super 12% Cr Mo steels. It is practice, however, to fabricate all power plant by fusion welding, thus welds and welded regions are likely to occur in critical areas in each application. This, in itself would present no problems if welding produced microstructural and stress distributions similar to the parent material but this is not the case. The weld HAZ is a region of severe microstructural and stress disturbances in these steels and hence, cannot be judged on the same basis as unaffected, wrought material. Therefore, in order to estimate service behaviour of this material, sufficient information concerning the effect of welding on HAZ microstructure, properties and behaviour must be available. It is the aim of this work to provide information on these

topics and thus allow more realistic appraisal of the service behaviour of Super 12% Cr Mo steels.

All Super 12% Cr Mo steels are readily weldable and may be welded by all arc welding processes, under similar welding conditions to mild steel of a similar thickness. There are, however, weldability problems in these steels; namely susceptibility to two types of cracking, one is weld bead cracking, whilst the other is HAZ cracking. Weld bead cracks have been shown to be influenced by weld bead profile, high weldment restraint and the mixed microstructure of the weld bead [101]. Control of these cracks demands concave weld bead profiles [101], although attempts have been made to produce totally martensitic weld bead microstructures [1,6,7,8,9,10]. Hydrogen induced HAZ cracks have been eliminated by careful weldment temperature control [1,4,5,12,13,14,35,36,37,42,44]. This form of cracking is a direct result of the extreme hardenability of these steels ie. their propensity to form martensite on cooling from high temperatures, a fact predicted for the weld HAZ in existing CCT diagrams [1,4,36,42]. Cracks of this type have been eliminated by careful weldment pre-heat. Faber has shown that the best levels are around the Ms temperature of each steel [14]. Interpass temperature control is also important in order to prevent crack formation during multi-run welding. These treatments are performed at temperatures similar to pre-heating [1,14,36,37,43]. On completion of welding, weldments are not allowed to cool to room temperature but are held at elevated temperatures until stress-relieved. Once stress-relieved, weldments are slowly cooled

to room temperature in order to allow full transformation to martensite to take place and are then immediately tempered [1,4,12,13,14,36,44]. These precautions are adequate to prevent cracks in homogenous martensite HAZ's but they do not deal with the δ ferrite which has been reported as occurring within the HAZ close to the weld fusion line [3-13, 21,36,37,44].

Some investigators have reported that δ influences HAZ properties in a number of ways. Creep ductility is increased because Laves phases are preferentially produced in δ during service and the precipitates thus formed control creep [1]. Within the operating temperature range of 740°C - 760°C δ is detrimental to creep resistance as sigma phase forms at the δ/martensite interface in short time periods and causes tertiary creep to occur [1,11]. Many reports state that δ increases HAZ cracking by providing an easy fracture path through the HAZ whilst other investigators state only that δ influences HAZ cracking path [6,7,9,12]. There is no quantified work to explain either case. It is quite feasible that weld stress distribution is affected by the occurrence of δ within the HAZ. Tensile strength of the steel is affected by the presence of δ, although disagreement exists on the effect [1,23]. The production of δ ferrite from austenite is accompanied by an expansion because the δ b.c.c. crystal is less closely packed than the austenite f.c.c. lattice, thus where δ forms some compression occurs [100]. In this manner weld stress distribution variations may occur in ferritised regions.

A lack of information exists concerning the formation and effect of δ in the HAZ's of these steels. Welding CCT diagrams predict only martensite formation, δ production is not mentioned. There is no existing information concerning the location, distribution or subsequent effects of δ on HAZ properties. As δ is retained to room temperature in weld HAZ's some effect on subsequent transformations may occur, but this has not been previously investigated.

The content of this thesis consists, initially, of a review of literature relevant to the understanding of the metallurgy and weldability of the Super 12% Cr Mo steels. At the end of this section, methods are detailed which have been used to assess the weldability of other materials. The second part gives a detailed report of the experimental methods employed throughout the investigation, together with the results obtained from them. Conventional heat-treatments, using varying peak temperatures, were used to produce differing microstructures which were then identified. This knowledge was applied to the study of real weld HAZ's, thus enabling location and identification of the component regions of the weld HAZ. Once each zone had been identified, CCT and isothermal transformation work concerned with the formation of δ was undertaken. This enabled later weld thermal simulations to be performed concurrent with high speed dilatometry to determine phase transformations. As a natural consequence of this work, detailed knowledge of phase transformations occurring within the HAZ was produced. This information takes the form of both CCT and TTT diagrams which are concerned with the formation, decomposition and transformatic

# CHAPTER TWO

# LITERATURE SURVEY

# CHAPTER TWO LITERATURE SURVEY

## 2.1 Introduction

The microstructure, and consequently the properties, of the weld Heat Affected Zone (HAZ) of Super 12% Cr Mo steels are principally determined by their response to various heat-treatments. The first section of this literature survey concentrates on a detailed review of the metallurgy of these steels under both equilibrium and non-equilibrium conditions and also considers the structural effects of various alloying elements.

Weldability of these steels is reviewed in the second section, particular reference being given to the HAZ. In the third part of this survey the techniques available for determining welding Continuous Cooling Transformation (CCT) diagrams are reviewed, as these are an essential feature of the investigation which was undertaken.

Finally, a summary outlines present knowledge of weld HAZs in these steels and indicates areas requiring further investigation.

## 2.2 Metallurgy of Super 12% Cr Mo steels

### 2.2.1 Classification and microstructure of these materials

Historically, and logically, Super 12% Cr Mo steels can be divided into three groups which can be based on either chemical composition or maximum operating temperature.

It is more usual to classify them by composition rather than operating temperatures, but both systems closely agree (see Table 1).

These steels tend to be completely martensitic but individual types may contain areas of either free ferrite or retained austenite depending on chemical composition. It is usual, however, for all steels of this type to be fully "through hardening", the level of chromium additions promoting martensite formation even in heavy sections [1,2]. The Schaeffler diagram (figure 1) predicts homogenous martensite matrices for these steels, although when the alloy balance is incorrect ferrite or austenite may exist in small quantities [1,2]. A completely martensitic matrix is desired after super critical heat treatments followed by quenching[1,2]. In this condition material hardness should be maximised, minimal auto-tempering occurs due to rapid cooling [1].

Tempering the resultant martensitic matrix is performed between 300°C and 700°C, excluding the 425°C to 500°C range, tempering temperature is dependant on service usage [1,2]. Low tempering temperatures are applied when hard, high strength components are required but the most usual range is 600°C to 700°C, which causes softening to occur [2]. In this temperature range $M_{23}C_6$ carbides form, reducing carbon supersaturation in the matrix thus softening the component. Carbides of this type are frequently referred to as the characteristic carbides of these steels [1,2].

### 2.2.2 Constitution of iron-carbon-chromium alloys under equilibrium conditions

Interest in the Fe-C-Cr ternary system is limited to two isopleths, having compositions of Fe, 0.1%C, 11 - 13%Cr and Fe, 0.1 - 0.3%C, 12%Cr (which are illustrated in figures 2 and 3). Both figures show that in the 11 - 13% Cr and 0.1 - 0.3% C ranges, austenite ($\gamma$) can exist alone. Outside these ranges rapid closure of the gamma ($\gamma$) loop occurs when chromium contents of 15% or carbon levels above 0.4% are used.

Above and below the $\gamma$ region austenite co-exists with one or other form of ferrite (ie $\alpha$ or $\delta$ ) [1,2]. At room-temperature the structure of these compositions is $\alpha$ ferrite with mixed iron-chromium carbides of $M_3C$ and $M_7C_3$ types. Continuous slow heating causes austenite nucleation once $Ac_1$ temperature is exceeded, between $Ac_1$ and $Ac_3$ austenite grows at the expense of $\alpha$. Above $Ac_3$ the material is homogenous austenite, further temperature increments only coarsen austenite grain size. Gamma phase is stable until $Ac_4$ temperature is exceeded (about 1220°C for 0.1% C and 1300°C for 0.2% C steel from figure 3 ). At this temperature $\delta$ ferrite is produced from homogenous austenite [2]. Further temperature increases form increasing $\delta$ quantities up to liquation point.

Equilibrium cooling from liquation point reverses all the changes occurring on heating. Cooling a $\delta$ rich matrix from high temperature produces austenite until, on cooling below

$Ar_4$ a totally austenitic matrix once more exists. Continued cooling produces α ferrite at $Ar_3$, ferrite content increasing as temperature declines until at $Ar_1$ the material is wholly α ferrite. Cooling further to room-temperature causes carbide precipitation in response to decreasing carbon saturation in α ferrite. At room-temperature the final microstructure is α ferrite with the mixed iron-chromium carbides $M_3C$ and $M_7C_3$.

### 2.2.3 Constitution of Fe-C-Cr alloys under non-equilibrium heating and cooling conditions

Non-equilibrium conditions are more widely experienced in metallurgical operations than near-equilibrium rates, so during metallurgical working some divergences from the equilibrium diagram predictions can be expected.

Non-equilibrium (rapid) heating can cause austenite formation to occur at temperatures higher than predicted by equilibrium diagrams [1,2]. Continued heating of an austenitic matrix causes δ formation (although the kinetics of this transformation are not known), further heating increases δ contents up to liquation temperature [1].

Cooling of mixed δ-γ microstructures show little or no transformation of δ to γ , δ even being found untransformed at room-temperature [1,3-13]. Austenite remaining in the matrix does not transform to α between $Ar_3$ and $Ar_1$ but remains in a metastable form to low (400°C to 200°C) temperatures [1,3-13]. Austenite transformation occurs by

an athermal shear process to form martensite, over a limited temperature range [1,2,14,15,16]. This temperature range is closely related to compositional factors, e.g. C depresses Ms by 474°C per 1% C [1,2,17].

When rapidly cooled from above $Ac_4$ to room temperature, the structure consists of martensite with areas of δ ferrite within the matrix. If the material was only heated into the homogenous austenite region before cooling, only martensite forms. This is the basic microstructure of Super 12% Cr Mo steels [1,2,15].

### 2.2.4 Effects of alloying elements of Fe-C-12%Cr ternary alloys

Simple ternary Fe-Cr-C alloys are not used industrially, further alloying (using at least Mo) being employed to produce requisite physical properties (see Table 1). Once more highly alloyed, these materials are called "Super 12% Cr Mo steels"[1]. Some alloying elements used in these steels affect primary and secondary phase stability in these steels and are divided into two groups, depending upon their effect on primary phases. These groups are "ferritisers" and "austenitisers". Ferritisers cause closure of the gamma (austenite) loop by promoting ferrite stability, whilst austenitisers increase γ stability and extend the austenite loop [1,2,15,18]. The Schaeffler diagram (figure 1) is one attempt to illustrate the inter-relation between both groups on a graphical base [18]. This figure uses a standard ferritiser and austenitiser

(Cr and Ni respectively) with other elements being expressed as fractions of these standards. On this basis the phase changes resulting from variations in chromium- or nickel-equivalents become reasonably expressed.

2.2.4.1 Effect of austenite stabilising elements on primary phases

These elements are expressed as nickel-equivalents, appearing on the Y axis of figure 1 and are C, Co, Cu, Mn, N and Ni. They extend the $\gamma$ field preventing closure by 12 - 13% Cr, excessive quantities of these can cause retained austenite in the microstructure [1,2,18]. All elements in this group depress $Ac_1$, Ms and Mf transformation temperatures by differing amounts, the most powerful being C, Ni and Mn [2]. The $M_7C_3$ carbides and $M_2X$ carbonitrides minor phases are accelerated in their formation by elements in this group as is reduced matrix C solution [2].

2.2.4.2 Effect of ferrite stabilising elements on primary phases

Such elements are measured as chromium-equivalents and are Al, Cr, Mo, Nb, Si, Ti V and W and are found on the X axis of figure 1 [1,2,18]. Elements in this group close the $\gamma$ loop thus enhancing $\alpha$ and $\delta$ ferrite and producing an increase in $Ac_1$ temperature. All elements behave similarly, having different magnitudes of action whilst all form stable carbides increasing temper-resistance and extending secondary hardening [2]. Excessive quantities

of these elements produce ferritised material which no solution treatment can remove [1,2,18].

2.2.5 Effects of alloying elements on minor phases

Highly alloyed Super 12% Cr Mo steels can have up to ten minor phases within the matrix. Four minor phases are more usual, being common throughout the whole range of steels, and these are carbides, Laves, sigma and $M_2X$ carbonitrides phases [1,2,8,10,11,15,16,19-34].

Many of the properties of these steels depend upon the carbide form present and its dispersion. However, in creep-resisting situations carbides are of secondary importance to Laves phases [1,2,15,16,19,21-25,29]. During creep sigma formation signals the onset of tertiary (rapid) creep [1,30]. The mixed carbo-carbonitride phases ($M_2X$) only become noticeable because of the secondary hardening they cause [1,2,15,20,21,31,32,].

Carbides are produced by tempering quenched material, the carbide form being determined by tempering temperature [1,2,15,21,30,34]. At and below 300°C $M_3C$ carbides form whilst between 300 and 500°C $M_7C_3$ carbides are stable, above 500°C $M_{23}C_6$ types form. Once formed, $M_{23}C_6$ carbides are stable over a wide temperature range and are the characteristic carbides in these steels [1,2,15].

Laves-phase formation is dependant on composition and forms only in response to certain atomic ratios (e.g. W:C and W:Cr) [1]. In commercial alloys the most common Laves

precipitates compositions are $Fe_2Mo$, $Fe_2V$, $Fe_2W$, $Fe_2Ti$ or $Fe_2Co$ depending upon material composition [1,24].

Sigma phase formation occurs in δ containing material in very short time (within 1 hour at 740°C), In δ free material, sigma does not form after 100,000 hours at 650°C [1,11]. Once sigma forms no further useful creep resisting life remains in the steel [1]. Identification of sigma phase in these steels has found it to be an $M_6C$ carbide type [30].

The $M_2X$ phases are physically the smallest precipitates to affect these steels and are sub-(optical) microscopic. These phases have never been positively identified but are thought to be a mixture of chromium rich carbides, nitrides and carbonitrides which form and affect the steel over a wide temperature range from 500°C upwards [1,2,15,20,21,31,32]. When $M_2X$ forms it produces lattice distortions which impede metal deformation and is seen as secondary hardening in these steels [1,2,15].

### 2.2.6 Use of CCT diagrams to predict as-cooled microstructures

In these steels it is possible to produce a variety of microstructures when differing cooling rates are used. These structures are predicted by the CCT diagram appropriate to each material class (see figures 4 and 5). The diagrams for both materials assume controlled cooling from within the γ region i.e. 1000 - 1100°C depending upon composition [1].

In class 1 steels, cooling rates faster than $4^{o}C$ $second^{-1}$ produce martensite at an invariant temperature, whilst cooling rates between $4^{o}C$ and $0.6^{o}C$ per second cause carbide formation within the austenite but have no effect on Ms temperature (see figure 4). Cooling rates slower than $0.6^{o}C$ $second^{-1}$ cause $\alpha$ ferrite and carbides to form between $675^{o}C$ and $800^{o}C$; subsequent cooling causes martensite to form at elevated Ms temperatures. Very slow cooling, below $0.01^{o}C$ $second^{-1}$, forms a completely ferritic structure between $750^{o}C$ and $800^{o}C$ with no subsequent martensite formation at lower temperatures. This structure is equivalent to that predicted by the equilibrium diagram (figures 2 and 3).

The effects of various cooling rates on class 2 steels are more complicated than with the simpler class 1 materials (see figure 5). Cooling rates faster than $0.75^{o}C$ per second produce only martensite from austenite at an invarient Ms temperature. Slow cooling, at rates between $0.75^{o}C$ and $0.38^{o}C$ $second^{-1}$, cause some bainite formation which immediately precedes the martensite transformation, which occurs at a depressed Ms temperature. Even slower cooling rates (0.38 to $0.2^{o}C$ $second^{-1}$) produce ferrite in the $675^{o}C$ to $750^{o}C$ range which precedes bainite formation. When this occurs no martensite formation occurs, the resultant matrix thus becomes a mixed ferrite/bainite microstructure. Formation of pearlite occurs immediately after ferrite when cooling rates are between 0.2 and $0.012^{o}C$ per second, remaining austenite subsequently transforms to bainite at a constant Bs temperature. When cooling rates below $0.012^{o}C$ $second^{-1}$

are used, all the austenite is consumed in forming first ferrite and then pearlite in the 825°C to 725°C range. The final microstructure remains a hetrogenous ferrite/pearlite mixture with no bainite.

Interrupted cooling in the homogenous austenite region of a class 2 steel can cause bainite formation, similar treatment of a class 1 steel would only result in martensite formation. When such heat-treatments are applied to class 2 material and untransformed austenite is kept between Ms and 400°C, bainite formation is expected within one hour. Similar treatment of class 1 steel increases carbide formation in austenite until, when the austenite carbon level is sufficiently depleted, martensite formation begins. Consequently in cases where martensite formation is not immediately required in class 2 materials, temperatures must be maintained above 400°C, which is within the austenite stability field, thus preventing bainite formation (1,2).

2.2.7 Effects of isothermal heat-treatments on these steels

Isothermal heat-treatments, generally called Time-Temperature-Transformations (TTT), are sometimes used to produce non-martensitic matrices to enhance machinability. TTT heat-treatments are performed in the austenitic state, usually within the 600°C to 800°C temperature range (1,2,34).
A typical TTT diagram is shown in figure 6 and, although for class 2 steel, can be taken as representative of all groups, as all types decompose under very similar time-temperature

conditions [1,2,33,34]. Maximum transformation rates occur between 700°C and 750°C, irrespective of class or level of alloying and begin within 10 minutes, reaching completion within a few hours. From this it is clear that compositional factors are not as significant in isothermal. decomposition of austenite as they are in CCT reactions, although why this is has never been explained [2].

Isothermal heat-treatment procedures are alike for all alloys, cooling from solution temperature (1000°C to 1100°C) to transformation temperature is controlled at 14 to 16°C $hour^{-1}$. Components are held at transformation temperature for a few hours then control cooled to 550°C at 28°C $hour^{-1}$, Below 550°C final cooling to room-temperature can be fast [1].

## 2.3 Welding and weldability of Super 12% Cr Mo steels

### 2.3.1 Recommended welding procedures for Super 12% Cr Mo steels

#### 2.3.1.1. Selection of welding parameters and filler wires

These steels are amenable to all welding processes, although it is more common for arc welding to be used. Manual metal arc (MMA) is the most common process in use, whilst metal inert gas (MIG) and tungsten inert gas (TIG) processes are used for thin or sheet material. Thick and very thick sections have been welded by both submerged-arc (sub-arc) and electro-slag techniques [5,7,10,11,12,13,35,36,37,38]. High quality welds in critical applications usually have root passes made by manual or automatic TIG with separate

cold filler wire fed into the weld pool [37, 38,39,40]. Further passes can be put in by TIG, MIG or MMA, depending on the service use of components [37 - 40].

Filler materials used to weld these steels are not critical, being defined more by weldment usage than the parent steel [4,36,38, 40 41]. Where weldments are for critical service use, both major standards (AISI and DIN) require matching filler materials, although for general usage many differing fillers have been used. Such materials are ½%Cr ½%Mo, 2¼%Cr 1%Mo, 9%Cr 1%Mo and 18%Cr 8-10%Ni, the latter being used where hydrogen cracking may be found [38,40].

Argon is the generally recommended shielding gas for inert gas welding processes (TIG and MIG) although argon/$CO_2$ and argon/oxygen mixtures have been successfully used with MIG welding of all filler materials [40]. In all welding processes, forecasting welding parameters is easy as welding conditions for mild steel can be directly applied to these steels [38,40,41]. Recommended welding procedures at all levels for these steels emphasise the need for pre-heating, interpass temperature control & subsequent post weld heat-treatment.

2.3.1.2 Welding procedures used for Super 12% Cr Mo steels

Pre-heating is always applied to weld materials of over 2 mm thickness. Many different pre-heat temperatures are recommended, these vary between 150°C to 425°C [4,12,14,35,36, 40,42,43,44], although the best temperature range has been shown to lie around Ms temperature [14]. Pre-heating is

employed to prevent cold-crack formation and is thought to succeed in a number of ways. The three most important reasons are i) above Ms matrix is austenitic and can plastically deform thus leading to rapid stress relief [14,44], ii) weldment kept above the hydrogen cracking temperature [44] and iii) some high temperature austenite decomposition to form bainite may occur and thus prevent cracking [44].

In multi-run welds, weldment temperature is controlled between each successive deposition. This is termed "Interpass temperature" control and is universally applied [14,36,37,43,44]. Close agreement exists on temperature level, for classes 1 and 3 steels interpass temperatures around Ms are used [14,36,37,43] whilst class 2 materials are usually kept at 425°C to 450°C, ie above Ms, to prevent bainite formation [12,13]. The problem of bainite formation in the weld HAZ occurs only in class 2 materials and results from the bainite "hump" found in the Ms line in CCT diagrams (see figure 5). Maximum bainite formation temperature is about 400°C hence interpass temperature control aims to keep weldments above this temperature and within the austenite stability region. Temperatures in the 425°C to 450°C region achieve this [12,13].

On completion of welding weldments are rarely allowed to cool immediately to room temperature [44]. Controlled cooling to 100°C to 250°C is performed during which time partial transformation to martensite occurs. Weldments are then stress relieved at 650°C to 750°C and allowed to cool to room temperature [3,4,6,12,13,14,].

This heat treatment is used to relieve welding stresses [3,4,6,12,13] and diffuse hydrogen out of austenite [14] but causes some pearlite formation in regions of untransformed austenite [44]. Stress-relieving in this fashion is used to further prevent crack formation in addition to pre-heating [3,4,6,12,13,14].

After stress relieving, weldments are tempered at 590°C to 780°C for 30 minutes per centimetre of wall thickness [4,10 12,13,14,36,42,44]. Tempering temperature is determined by service application of the welds. Where highly ductile welds are required extended tempering times may be employed [4,12, 13,36]. This treatment tempers martensite which forms on cooling from stress relief and thus increases weldment ductility and reduces martensitic hardness [4,12,13,36].

### 2.3.2 Microstructure of untempered weld bead and HAZ

Weld beads in the as-deposited state have a duplex structure consisting of martensite and δ (ferrite); the amount of δ within the structure being unpredictable [1,4,5,6,7,8,9,11, 12,13,36,37,41,43,44]. The quantities of δ within the weld bead are primarily controlled by filler composition although welding parameters have been shown to be significant [1,3,6,7,8,9,13,41,43]. Where control of δ has been attempted, it has been found that welding current has a great influence and thus, for rigorous δ control, must be kept within close tolerances [6,7,10]. Specific weld metal compositions have been developed to produce either small quantities or no δ when correctly deposited [6-10].

Untempered weld HAZ's in Super 12% Cr Mo parent steels consists of three affected zones. Immediately beside the fusion line and extending a short distance is the mixed δ-martensite region abutting this is the homogenous martensite zone with the secondary hardened and tempered area running from martensite and fading out into unaffected material [3-13,16,,21,36,37].

The duplex martensite-ferrite area forms close to the fusion line because only in this region is the peak temperature sufficient to decompose some austenite and form some δ. Austenite decomposition of this type is not confined only to 12% Cr type steels, small quantities (4 - 8%) form in the HAZ's of austenitic stainless steels where it is customary to control welding conditions to maintain 5 - 10% δ in the HAZ to prevent cracking [44,45,46]. In martensitic stainless steels (e.g. Super 12% Cr Mo, AISI 410, 416 types) both quantitative and qualitative information on δ formation and its effect are lacking and no attempts are made to control its formation in the HAZ.

The second heat affected region, homogenous martensite, forms from material heated above $Ac_3$ but not $Ac_4$. This material has the equivalent of a re-solution treatment and is the region predicted by welding CCT diagrams [1,5]. In this region some austenite grain growth and coarsening may be noticed[5].

Abutting the homogenous martensite field is the secondary hardened and tempered zone. This region is connected to

the martensite area by a semi-transformed field consisting of fresh martensite and heavily tempered old martensite which represents material having experienced peak temperatures between $Ac_3$ and $Ac_1$. (This area is so small that it is not separately identified and is included in the tempered region [5]). The secondary hardened and tempered zone is marked by increased carbide size, carbide agglomeration falling with peak temperature experienced until unaffected material is reached [16]. Within this region secondary hardening occurs, although no visible indications can be found, and is due to increased $M_2X$ phase precipitation [2,3,4,6,11,15,16,31]. Micro-hardness surveys easily find and measure the extent of secondary hardening in these steels but little published work exists indicating the extent of this occurrence in weld HAZs.

### 2.3.3 Microstructure of tempered weld bead and HAZ

Tempering of weld bead and HAZs occurs when either subsequent passes are laid on earlier ones (when the earlier regions temper) or where weld regions are externally heated to deliberately temper freshly formed martensite. In both parts (bead and HAZ) carbides precipitate from fresh martensite whilst carbide agglomeration proceeds in the HAZ secondary hardened region [5,10,13].

In δ precipitates have been found after tempering regardless of its location in HAZ or weld bead [1,16,19,20,21,24,25,26]. Investigators have identified them as carbides [26] and Laves phases [20] and they have been blamed for the unexpectedly low impact results of tempered HAZs [20,26].

Post-weld tempering of bead and HAZ is generally used to improve toughness, ductility and shock resistance and is universally applied in industry for these reasons [1,3, 4,10,26,36,37,38,40,41,42].

### 2.3.4 Susceptibility of weld HAZs to metallurgical welding defects

These materials are readily weldable although subject to three forms of cracking. Two forms, liquation and re-heat have been found only in extensively modified steels (class 3) whilst the third, HAZ cold cracking has been found in all classes of these steels.

Liquation cracks form solely in the weld bead, starting from craters and are known to be strongly influenced by compositional factors [1,12]. Re-heat cracking is found in both weld bead and HAZ when weldments are tempered before full transformation of austenite (to martensite) has occurred. Tempering at this stage forms sigma carbide ($M_6C$) around $\delta$ ferrite, consequently reducing overall ductility subsequently leading to crack formation during tempering. Both liquation and re-heat cracks form only in extensively alloyed class 3 materials.

All classes of these steels are susceptible to HAZ cold (hydrogen induced) cracks. These cracks form and propagate at, or around, room temperature, the problem being exacerbated by the presence of diffusible hydrogen within a transformed microstructure [47-52]. All transformed microstructures, whether martensite or bainite, are

susceptible to these cracks [48,49] so two regions within the HAZ of these steels are possible crack sites. The extreme sensitivity of these two regions (martensite - δ and homogenous martensite) of untempered HAZs to very low hydrogen concentrations has been demonstrated [51,52].

Cold crack formation temperature is debatable, as is the stage of microstructural transformations when they form, so accurate knowledge of stresses involved is difficult. Both long range (contractional) and short range (transformation) stresses have been blamed [47-52] but recent work has shown these steels to possess excellent ductility in the austenitic range and good ductility whilst transforming (below Ms) so crack forming stresses are probably overall contractional ones [53].

When cold cracks form in the HAZ their propagation can be delayed [4,6,7,9,10,13,14,35,36,41,42] and may be associated with the presence of δ ferrite [6,7,9,12]. Cold crack formation is therefore equally likely in both martensite regions when hydrogen and stress are present. Crack prevention is usually by post-weld heat treatments, using controlled cooling and holding above $M_f$, to retain austenite. This absorbs stresses, diffuses away hydrogen, and tempers martensite (to increase structural ductility) [3,4,6,12,13,14]. Where hydrogen problems may be encountered it is common industrial practice to use austenitic steel filler materials, which act as hydrogen "sinks" absorbing hydrogen from the transforming HAZ, to alleviate these cracks [40,41].

### 2.3.5 Prediction of weld HAZ microstructure

Weld HAZs in these steels have a definite three zone structure, acknowledged by many workers [3,4,6,11,16,21,22] (see figure 8). Only one zone, that of homogenous martensite, is consistently predicted (usually by CCT diagrams) whilst the other zones are often found although not predicted [1,4-14,36,37,42].

Existing CCT diagrams predict only the formation of martensite and not the duplex high temperature region which surrounds the weld bead. Conventional CCT diagrams have frequently been used to predict weld HAZ microstructure [1,26,42] (see figure 5). Such diagrams cover typical weld cooling rates but have not been produced from a sufficiently high temperature to either show or predict δ. It is necessary to be able to predict δ quantities, as this phase may be detrimental to the weldment. It is reported that δ is involved in cold cracking [6,7,9,12], reduction of impact properties [26], reduced hardness [1,7,42], effects on tensile properties [1, 5,6,7,8,9,10,12] whilst thought to cause re-heat cracking [1] by providing an easy fracture path [9]. Cold cracking propensity has been thought to increase because δ reduces matrix ductility [7,9] thus making the matrix less able to withstand contractional strains. This matrix embrittlement probably accounts for the effect δ has on impact [26] and tensile properties [1,5-10,12]. Re-heat cracking in steel occurs because σ phase forms very rapidly at the δ/martensite interface during heating and thus prevents any deformation occurring [1]. Increasing quantities of δ have been shown to promote brittle failure, fractures having preferentially passed through the δ region [9]. Trans-δ fracture paths may explain the embrittling effects on tensile and impact

properties.

No other HAZ region appears so potentially detrimental to weld service properties. The homogenous martensite zone is involved only in cold cracking [51,52,53], whilst the secondary hardened zone appears to have no effect on weldment properties.

Duplex regions could be predicted by CCT diagrams produced from material treated at high temperatures (ie above $Ac_4$). Construction of such a diagram suitable for welding requires extremely accurate knowledge of weld thermal cycles, a technique to simulate weld HAZ heating and cooling rates and high speed dilation measuring apparatus. This approach is not new, having been adopted on many occasions and found suitable for a wide range of metals [3,54-63].

## 2.4 Methods available for construction of weld HAZ CCT diagrams

Four areas of information are required if accurate weld HAZ CCT diagrams are to be produced. These are i) Weld thermal cycles and the conditions producing them; ii) HAZ microstructure produced by a given thermal cycle; iii) a simulation technique to reproduce weld HAZ heating and cooling rates; iv) a high speed dilatometer to record phase transformations during thermal cycling [54,55,57,59,60,61,62,63].

Weld thermal cycles have been produced both experimentally [58,60,61] and numerically [57,59,62,63,64,65]. Each system

has its own advantages and disadvantages but the current trend is towards computer modelling using complex numerical solutions [64,65]. Mathematical modelling of dynamic processes using computers is an increasing trend having reached a high degree of sophistication and accuracy which supersede more established hand-computed equation techniques [64,65].

### 2.4.1 Numerical solutions of weld HAZ cooling rates

Heat transfer through solid metallic bodies and the factors affecting it have been understood for many years. Adaptation of this steady state model to welding has required modifications to account for edge effects, mobile heat source and other factors. These were made and equations for both two- and three-dimensional heat flow conditions were calculated by Rosenthal [65] and Rykalin [66]. These given here are by Rosenthal:-

$$\text{Two dimensional} \quad (2D), T = \frac{q^1}{2\pi K} e^{\frac{Vx}{2\alpha}} Ko\left(\frac{Vr}{2\alpha}\right)$$

$$\text{Three dimensional} \quad (3D), T = \frac{q}{2\pi Kr} e^{\frac{-V(r+x)}{2\alpha}}$$

where T = peak temperature required

q = rate of heat emission from point source

$q^1$ = rate of heat emission per unit length from a line source

V = relative velocity of heat source to solid body

x = distance from source along line of arc travel

$\alpha$ = thermal diffusivity

Ko = Zero order Bessel function second kind

K = Thermal conductivity

$r = (x^2 + y^2 + z^2)^{\frac{1}{2}}$

(From 65)

Both equations are widely used although limited to certain cases, modifications were made to deal with cases between 2- and 3D and utilise information more appropriate to welding (eg. melting point and weld bead widths)[67-71]. Although these equations are widely used their accuracy is suspect and their use tends to result in cooling rates considerably faster than experimental observations [64]. The inaccuracies in these results are produced by the equations insensitivity to specific heat and thermal conductivity variation with temperature. Such problems are, however, easily overcome when more complex techniques are computer solved [64,65].

### 2.4.2 Finite element solution of weld thermal cycle

The most powerful computing technique dealing with dynamic or transient situations is that of finite element array (ie. matrix algebra). In this technique the object is modelled as a three dimensional vector array, the solution being found for each cubic region within the overall limits. A widely used weld thermal history program is "Variab", a finite element analysis developed by Westby, which provides solutions for heat flow from 2- to 3-D inbead-on-plate or close butt joints [64]. This program has been modified by other workers to determine heat-flow in welding preparations

and was shown by them to be very accurate [65].

This program uses temperature dependant material properties and latent heats of transformation and fusion to model the welding situation, which contributes to an accurate solution. This modelling process has been shown to be accurate by both measured temperatures and metallurgical phase transformation data [64,65]. A complete thermal history of the whole weld is produced, with heating information, by this program, a task not equalled by other numerical solutions [64 - 70]. From this thermal history the thermal cycle of any peak temperature may be easily determined.

### 2.4.3 Weld thermal simulators

Weld thermal simulators which use electrical resistance for heating have been in use since about 1954 [3] although other simulators have been used before and since this date [55,59,60]. Resistance heating simulators use the sample as the fuse in a high current short circuit. This means that very rapid heating rates can be achieved [3,55,59]. Other types of simulators use either induction heating or thermal radiation to heat the sample and these techniques give much slower heating rates [56,58,60].

Water cooling the copper sample jaws enables fast cooling rates to be achieved in resistance heating machines [3, 55,57,59,61,62,63,74-78], however faster cooling rates can be achieved by gas quenching in other types of simulator [55,56,58,60]. D'Anderea and Adams have shown that for

accurate weld HAZ thermal simulation an ability to reproduce the full thermal cycle, on both heating and cooling, is desired and that it is insufficient to reproduce only peak temperature and cooling rate through a given temperature range [78]. Resistance heating simulators are capable of fulfilling these requirements whilst induction heated types are not [55,57,59,61,62,63,74-78].

During simulation, temperature control must be accurate within $\pm 5^{o}C$ throughout the whole sample cross-section [59,72,73]. The cross-sectional temperature plateau must be ascertained before any worthwhile work can be performed [73]. Previous work has shown that resistance heating simulators can fulfil this requirement with many sample sizes [55,57,59,61,62,63,74-78].

### 2.4.4 High speed phase transformation measurement

Two techniques are widely used for phase transformation studies. These are dilatometry and thermal analysis. In resistance heating weld thermal simulators, thermal analysis can only be used during natural cooling ie. cooling from a given temperature at the samples' maximum rate. During either heating, or controlled cooling, heating current flows through the sample in short bursts and is sufficient to cause problems with thermal analysis, so this technique is rarely used in these simulators.

It is common to find high speed dilatometry used on these welding simulators to determine phase transformations [3,54,55,57,59,61,62,74-78]. When using dilatometry on a simulated

sample to produce welding CCT diagrams, three criteria must be considered. There are i) only a short sample length is at temperature, therefore both positioning and measurement must be very accurate; ii) no scale must form on the sample thus dilation must be performed in either vacuum or inert gas and iii) account must be taken of the transverse temperature gradient [59]. The first is satisfied by locating the measuring device at the control thermocouple circumferential line and using accurate transducers to measure the dilation produced [3,57,59,61,62,63,74-78]. To fulfil the second criterion requires that either a controlled atmosphere box or a vacuum chamber is used to contain the specimen [59,74-78]. The problem of transverse temperature gradients can be overcome by either selecting appropriately sized samples which have little or no gradient or by accurate calibration work to establish centre and surface temperature relationships [59, 72,73].

Having satisfied these criteria, accurate welding CCT diagrams have been produced for many materials using resistance heating simulators and high speed dilatometry since the first used in 1954 [3,54,55,57,59,61,62,74-78].

## 2.5 Final summary

From this literature survey it can be seen that the HAZ microstructure in Super 12% Cr Mo steels comprises of three regions, which are a martensite/δ ferrite duplex, an homogenous martensite area then a secondary hardened region. The extent of each zone depends upon the alloying elements in the steel

and the welding variables employed during welding. Little quantitative information is available about the proportions and extent of each region, neither is there information on the effect of welding variables on each area.

Since the HAZ results from the interaction of composition and thermal history, it is evident that there is an outstanding need for accurate prediction of weld HAZ microstructure and hence, for representative welding CCT diagrams. Whilst most data is suitable for predicting low peak temperature HAZ regions, nothing is available for high peak temperatures which involve $\delta$ ferrite formation. There is evidence that $\delta$ ferrite formation may be significant in determining weld HAZ performance and properties. Thus, it is apparent that a requirement exists for a systematic investigation involving the determination of representative welding CCT diagrams which correspond to the peak temperature ranges found within each area of the weld HAZ. This involves accurate determination of weld HAZ thermal cycles applicable to each region and high speed dilatometry during weld simulations, techniques which have been shown by the literature review to be suitable for this purpose.

# CHAPTER THREE

# EXPERIMENTAL TECHNIQUES AND RESULTS

# CHAPTER THREE EXPERIMENTAL TECHNIQUES AND RESULTS

## 3.1 Introduction

The first stage of this work involves assessment of the "as-received" microstructures of these alloys and their response to heat-treatment; one material was then studied to determine the effects present in weld HAZ's. This work is followed by a detailed description of the techniques used and results obtained from isothermal, continuous heating and continuous cooling studies of the principal phase transformations which occur. On the basis of this information and theoretical calculations of weld thermal cycles a representative weld CCT diagram is determined. Comparisons are made between real and simulated weld HAZ's, particular attention being given to δ ferrite formation in weld HAZ's since it is evident that its presence in regions close to the weld fusion line is unavoidable.

## 3.2 Microstructure of Super 12% Cr Mo steels and their responses to heat-treatments.

### 3.2.1 Identification of basic microstructures after solution treatment and subsequent tempering.

The chemical compositions of both steels are given in Table 2 together with manufacturers recommended heat-treatment. These recommendations were followed and samples from each material were taken immediately after oil quenching for metallurgical examination. Tempering followed, again

as recommended, and further samples were taken for examination. The Schaeffler diagram (fig 1) predicts that both materials ought to be completely martensitic after quenching; this was shown to be correct. After polishing, various etchants were tried in order to identify constituent parts of the microstructure. Two martensite etchants were used, 25% nital and Adlers reagent (see Table 3), both of which attacked only martensite. No unetched areas were found, but samples were re-polished and electrolytically etched in oxalic acid to etch untransformed austenite, but none was located. This process was then repeated after sub-zero treatment, again with a negative result. Electrolytic etching in NaOH was used to identify free ferrite, but again proved unsuccessful, thus the microstructure after quenching was lath martensite, in both Class 1 and 2 steels. In each of these materials some free carbides were noted, these being more noticeable in Class 1 steel and were thought to be due to auto-tempering [1]. A carbon extraction replica of the "as-quenched" Class 2 steel was prepared and examined by high resolution T.E.M. and the typical features of lath martensite were observed. A few very small carbide particles were noted on lath boundaries (figure 9).

Tempered specimens were examined in the same way and found to have coarse carbide particles within martensite laths. Carbide identification in Class 2 material was performed by X-Ray diffractometry analysis on solid specimens which identified two $M_{23}C_6$ carbides in the matrix. The strongest

response, and hence the predominant type, was from $Cr_{23}C_6$, $(Fe,Cr)_{23}C_6$ responded weakly, but was still discernable. No traces of $M_7C_3$ carbides or Laves phases were detected during this survey.

Bulk quantities of both materials were in the tempered state ("standard state") and were used throughout the work in this form. All succeeding experiments used these materials all of which had been heat-treated at the same time as the base material. The unaffected microstructures were thus known to be tempered lath martensite containing predominantly $Cr_{23}C_6$, but with no $M_7C_3$ carbides or Laves phase present in detectable quantities.

### 3.2.2. Phase transformations occuring during solution treatments.

This work was performed on a conventional metallurgical dilatometer. Small samples, each 20 mm long x 5 mm diameter, of both steels were made and were subjected to appropriate re-solution heat-treatments (1000°C for 1 hour for Class 1 and 1050°C for 1 hour for Class 2). Heating rates were slow, taking 2 hours to reach maximum temperature, whilst cooling rates were varied from 1500°C $min^{-1}$ (25°C $sec^{-1}$) to 100°C $min^{-1}$ (1.6°C $sec^{-1}$).

On heating, both $Ac_1$ and $Ac_3$ were found, whilst on cooling only Ms and Mf appeared. In the case of Class 1 steel, these temperatures were found to be thus:- $Ac_1$ 830°C, $Ac_3$ 897°C, Ms 323°C and Mf 140°C. Minor variations in $Ac_1$ and $Ac_3$ were also noted, due to slight variations in

### 3.2.3 The effect of short time, subcritical heat-treatments on Class 2 steel

Highly alloyed Super 12% Cr Mo steels secondary harden after tempering, due to $M_2X$ forming as a fine, dispersed precipitate which impedes dislocation movement (dispersion hardening)[1,2,21,22,31,32]. As Class 2 steel was the most highly alloyed type available, short duration, sub-critical heat treatments were used to assess its secondary hardening capability.

Thin samples (3 mm thick) were produced from standard state material and were surface ground to size. Vickers micro-hardness measurements were performed on each sample and averaged to give a pre-treatment hardness for each sample. They were then placed in an air circulating furnace at pre-determined temperatures, for either 5 minutes or 1 hour, after which they were removed and cooled on a large steel block. When cold, each sample was surface ground to 2.5 mm thickness and then re-tested for hardness, at least five times. The results of these tests show that this steel secondary hardens very rapidly (figure 13 and Table 4.) Long holding times produce lower hardening, due to $M_2X$ agglomeration or even matrix softening caused by carbide coarsening, whilst short treatments can elevate hardness towards untempered martensite levels (520 min.Hv).

### 3.2.4 High temperature furnace heat-treatments.

A series of high temperature heat-treatments were undertaken to obtain approximate location of $Ac_4$ (when $\delta$ production starts from austenite) over the range 1100°C to 1450°C

using Class 1 material. Small test coupons, 10 mm square x 3 mm thick, were produced. Platinum - platinum/13% rhodium (hereinafter abbreviated to Pt/Rh) thermocouples were welded onto sample edges and checked for calibration by immersing in boiling water and measuring the e.m.f.generated. Thermocouples were removed and replaced if the measured milli-voltage was greater than $\pm$ 0.0148 mV different from 0.644 mV (which represents 100°C $\pm$ 2°C).

A muffle furnace was used, the hearth of which was filled with fire bricks so that sample insertion did not cause rapid temperature loss in the furnace. Once the furnace was at the pre-determined temperature, the test coupon with attached thermocouple was rapidly inserted through the door and the temperature rise of the samples were monitored by thermocouple output. Once at temperature, samples were left to transform, for either 5 or 10 minutes, before being withdrawn and quenched in oil. All samples were metallurgically examined after severe eletrolytic etching in NaOH, which blackened martensite but left ferrite unattacked. In both materials, the onset of ferritisation was regarded as the temperature when an unetched constituent could be found when examined at 400x magnification. The transformation temperatures were located by noting the highest temperature sample which did not contain visible quantities of $\delta$ ferrite. Sufficient samples were used to enable transformation temperatures to be determined with reasonable accuracy and the values obtained were 1250°C for Class 1 steel and 1320°C for Class 2 materials.

During examination it was noticed that δ always appeared in similar places in both steels, and this was observed as being on prior austenite grain boundaries and triple points. The morphology of this phase was consistent between materials and it was always found along prior austenite grain boundaries (see figures 14 and 15). An anomaly noted during this survey was that once δ formation began, austenite grain growth ceased, therefore austenite grain size remained constant from 1250°C to 1450°C in Class 1 materials. This fact was attributed to δ formation pinning austenite grain boundaries and thus preventing further grain growth.

## 3.3 Microstructure, defects and properties of weld HAZ's in Class 2 steel.

### 3.3.1 Microstructure and defects found in commercially welded joints

The preceding study of the heat-treatment response of this steel indicates that three zones were likely to exist within a weld HAZ. These are i) a region of martensite/δferrite duplex microstructure, ii) an area of homogenous martensite and iii) a secondary hardened zone (as schematically illustrated in figure 8). Each region represents an area where some minimum temperature value has been exceeded. The duplex region, which consists of martensite and δ ferrite forms where austenite has been heated above the $Ac_4$ temperature (ie approximately 1320°C), hence quantities of austenite transform to δ (c.f. 3.2.4). The region of homogenous martensite is found where temperatures have exceeded $Ac_3$ but not $Ac_4$ (ie 900°C to 1320°C). Throughout this temperature range only austenite exists and this

subsequently transforms to martensite on cooling. Below $Ac_3$ (ie below 900°C) the temperature is unsufficient to transform the parent microstructure, but it is sufficient to precipitate $M_2X$ particles in the otherwise tempered matrix. This precipitation process is sufficient to reverse the softening trend and, in fact, increase matrix hardness [2] (c.f. 3.2.3).

Welds were obtained from industrial sources and were examined metallographically, the three zone HAZ structure being verified at once. Commercial welding of these steels is not performed extensively in the UK at present. This is not a reflection on the weldability of these steels but more an acknowledgement of the specialised usage of these weldments. Two major companies * having fabrication experience with these steels were visited and both supplied test welds and information. Only one defect consistantly re-appeared at both companies, and this was small HAZ cracks which occurred at room temperature and were found in about 1 - 1½% of fillet welds, butt welds being completely free of this fault [40].

To eliminate these cracks, which both companies believe to be hydrogen induced, very careful control of welding parameters is exercised. Specified pre-heat and interpass temperatures were similar and close to recommended values [1,4,7,12,13,14,35,36,37,40,42,43,44] (as in figure 7), whilst practices on post weld tempering diverged. One

* These were Clarke-Chapman, Gateshead and International Combustion, Derby.

company stress relieved before temperature fell below 100°C, whilst the other allowed full cooling to occur and stress relieved within 24 hours. Neither practice seemed to affect crack susceptibility for both suffered similar cracking level. In numerous attempts to eradicate cracks, various changes have been tried, including extreme precautions to prevent hydrogen production by high standards of cleanliness. The most successful palliative in both companies has been found to be filler material composition. One company will only butt weld with matching filler wire but prefers austenitic electrodes which preferentially absorb hydrogen when fillet welding. The other uses lower chromium fillers (2.0% or 9%Cr) believing that reduced transformation temperatures of these alloys allow greater stress accommodation within the weld bead and prevents cracks by thus reducing stresses. Lower chromium fillers are also less hydrogen sensitive (being less hardenable) and are capable of accepting hydrogen from the HAZ without detriment [40]. Some work has been performed on untempered weldments which indicates pre-existing crack growth occurs very rapidly under low stress levels in the presence of hydrogen [52,53].

It is the experience of both fabricators that cracks nucleate from stress raisers. These could be caused by undercut, bad weld bead profile, lack of fusion, incomplete fusion or bad fit-up. Where no stress concentrators occur, no cracks form even in fillet welds [40]. All cracks examined during the course of this work began in the duplex martensite/ferrite region, close to the weld bead, and not in the more likely homogenous martensite area. Crack paths appear to

have some relation to δ shape, closely following the shape of the ferrite network (figures 16 - 18). Cracks may enter ferrite but never follow completely ferritic paths.

Two theories have been advanced for this behaviour. The first is that δ reduces Ms temperature into the range of increasing hydrogen activity (≈0 - 200$^0$C) and thus renders weldments more susceptible to cracking [14]. The second is that δ "weakens" the martensite and having both lower yield point and ultimate tensile strength, fails during either transformation or cooling, when stresses of some magnitude are generated [7,9,12].

In commercial situations, all cracks occur as small HAZ cracks generated from stress raisers(see figures 19 and 20). Weld defects become operational when long-range (contractional) stresses accumulate at temperatures just above $M_S$ [80, 94, 95]. At such temperatures these materials are very ductile being basically austenite[54] and when transformation starts, stress levels are reduced as is ductility [94,95]. Further cooling increases general stress level [94,95], which, around stress concentrations, exceed matrix ductility causing crack nucleation to occur. The presence of hydrogen in the HAZ will tend to exacerbate this situation by reducing martensite ductility still further, especially in stress concentration localities [49,50].

### 3.3.2 Production and examination of thin and thick plate weldments

Butt welding small diameter tubes is a widely used fabrication process for these steels, as they are mainly used for cooling plant, heat exchangers or steam generators. Circumferential butt welds between tubes or in tube-to-tube sheet positions are made using TIG, MIG or MMA processes [40]. In this situation industrial practice is to pre-heat to 250 - 300°C weld continuously to completion, cool to low temperature and then stress relieve [40].

A series of experiments were formulated in which tubes were TIG welded with and without pre-heat, using 1 to 4 runs, some welds being subsequently tempered whilst the rest were not [40]. An industrial tube weld preparation was used (figure 21) and 1 - 4 runs, each representing different stages of completion, were deposited to attempt to determine which part of the process produced problems [40]. Cold wire automatic TIG welding was used for all runs. This was achieved by rotating the tube under a static welding head, tube rotation being accomplished by an industrial manipulator, the apparatus is illustrated in figures 22 and 23. Tubes (38 mm O.D. 24 mm I.D.) were accurately aligned on a mandrel, carried by the manipulator, which rotated them between two three-point steadies that controlled overall axial alignment (see figure 23). When pre-heating was used, commercial resistance heating pads were employed, temperature control was automatic using a 3 mm chromel-alumel thermocouple to monitor tube temperature. Visual weldment temperature measurement was accomplished using a digital thermometer, no recording

of pre-heat temperatures being made.

Each tube was machined to form the welding preparation and a distance of 5cm from each preparation was cleaned to base metal before degreasing. After mounting on the mandrel, rotation speed was set and the welding torch positioned $5^{o}$ advanced (ie on the "uphill" side) and wire feed set to pre-determined levels (Tube and wire composition given in Table 5).

Un-pre-heated welds were performed with the tubes at room temperature. This proved to be no difficulty for single and multi-pass welds, as both were deposited in single run increments, the weldment being allowed to cool fully before further deposition. The welding conditions used throughout this work are given in Table 6.

Tubes for pre-heated welds were assembled as before and heating pads were then wrapped around and clamped in position. The thermocouple was placed in hole located 5 mm from the weld preparation (as in figure 21) and the heaters turned on. Heating to pre-heat temperature was accomplished in about 20 minutes and maintained at $300^{o}C \pm 5^{o}C$ (as in industrial practice [40]). When at temperature, heating power was turned off, thermocouple removed and welding performed immediately. Where multipass welds were deposited, the weldment was allowed to cool to $300^{o}C$ before subsequent runs were deposited. After the final pass, weldments were allowed to cool to room temperature before removal from the manipulator.

When cold the welded zone was removed from each assembly and sectioned to produce both microstructural and bend test samples. During sectioning, the start and finish region of each was discarded as non-representative, whilst the remainder was sawn into pieces approximately 4 mm thick. Samples with the best weld profiles were retained for bend testing, whilst others were used for metallographic examination.

Optical examination of these weld HAZ revealed all the same zones as those which are found in commercial welds, although of a somewhat smaller size. Only one major visible difference was noted between pre-heated and un-pre-heated welds and this was the fact that the pre-heated HAZ's were larger and the untransformed areas of the HAZ were more tempered. Further specific studies of single pass HAZ's, however, were difficult because of their small physical size (at best 2.5 mm wide).

During metallographic examination the major portion of the time was spent searching for HAZ cold cracks, which necessitated multiple polishing and re-etching to prevent metal flow hiding any cracks. Despite this, no HAZ cracks were located in any weld by this investigation.

After the crack search, microhardness surveys were performed on all metallurgical samples. This showed that pre-heated welds were generally slightly softer than unheated ones. This is due to increased auto-tempering of freshly formed martensite and increased tempering of untransformed material. Figure 24 illustrates this fact by comparing the hardness values of single run welds produced from both pre-heated

and cold tubes.

Once hardness testing was complete bend tests were performed on selected samples. The best four pieces of each weld were marked and surface ground to 3 mm thickness. During grinding all samples were arranged so that square section test pieces were produced, the inner and outer curves of these being so small as to be effectively flat. After grinding, a random selection of two pieces of each weld was made. These were then tempered for 1½ hours at 610°C in an air circulating furnace. This was performed to discolour and oxidise pre-existing HAZ cracks so that during testing, accurate location of pre-existing cracks would be simplified.

Once cold, all samples were bent in the equipment illustrated in figure 25. Bending point on each sample was individually set at the weld bead/HAZ interface on the inner face. Slow, continuous bending to failure was used, care being taken not to apply sudden loads to any sample. Bending was stopped when samples broke or reached a 90° angle, samples were then measured to determine bend angle, and location of failing crack determined.

The results of this work were inconclusive (see Table 7) as no HAZ cold cracks were found in any sample. Most failures occurred through the weld bead and were pre-existing cracks formed on weld bead cooling but no brittle HAZ cracks were found. The effect of tempering increasing weld ductility was clearly visible, whilst the value of pre-heating weldments to prevent HAZ cracks was not demonstrated. Weld

restraint was high, illustrated by the fact that after mandrel removal weldment distortion was frequently sufficient to prevent replacement. Even with contractional stresses of that magnitude no HAZ cold cracks were produced in unpre-heated steel. This finding is contrary to current thought.[1,5,8,9,14,18,28,32,61]

Microhardness surveys were performed across the untempered metallographic specimens with a view to correlating hardness and HAZ microstructure. Testing commenced at the fusion line and moved into the HAZ in 0.1 mm increments. During the survey, hardness path was kept parallel to a section edge. Each hardness was recorded as was the microstructure of the region tested. Testing finished in the parent material when four similar results were successively recorded.

Each weld was tested in this manner, typical results being illustrated in figures 26 and 27. Correlation of microstructure and hardness was straightforward in unpre-heated welds, where martensite zones finished at about 520Hv, whilst secondary hardened material was between 520 to 320Hv, the parent material exhibiting a hardness of $320 \pm 10$Hv. Some hardness variations were noted in the martensite regions close to the weld fusion line and were due to $\delta$. The small size of $\delta$ did not allow for direct hardness measurements although it lowered hardness in the duplex region.

Attempts were made to calculate the peak temperature distribution in the weld HAZ from a theoretical equation

based on two dimensional steady state heat flow [68]. The results did not correlate well with the observed microstructure except in the one run, unpre-heated weld. In this case, the theoretical heat flow results agree quite closely with the observed microstructure (see figure 28). Large plate, three dimensional (3D), welds were thought necessary for further work, therefore thick walled material was welded. These welds were produced to provide large size HAZ's for examination and also sufficient information to calculate thermal cycles for later weld HAZ simulation studies. Four welding processes were used to deposit the welds and all weld parameters were recorded for later use. All welds were deposited as bead-on-plate on 17 mm thick tube using two current ranges of all four processes (TIG, MIG, MMA and submerged arc). Material composition is given as Class 2 steel in Table 2.

Semi-infinite welding conditions were desired so an estimate of plate size required to achieve these conditions was made from published literature [81]. In this method, plate length and width are described as increments of weld bead width (w.b.w.), hence an estimate of w.b.w. for each process was required. Weld bead widths are related to electrode diameter and welding speed and have been previously identified [48], thus by using published charts w.b.w. of 10 mm were expected from the TIG, MIG and MMA processes whilst 20 mm wide weld beads were predicted for sub-arc welds. Material dimensions for semi-infinite 3D situations are given as 20 w.b.w. wide and 30 w.b.w. long (ie 200 mm x 300 mm for MIG, TIG, MMA and 400 mm x 600 mm for sub-arc).

Plate thickness invariate at 17 mm (1.7 or 0.85 w.b.w.) producing 3D heat flow down to 250°C isotherm (from the expression $\frac{\text{Temperature isotherm}}{\text{Melting temperature}}$ x w.b.w.). Tubes from which the test plates were cut were 175 mm outside diameter, so the actual width of TIG, MIG and MMA test pieces were 275 mm (ie ½ tube circumference) and 550 mm for sub-arc (full diameter tube slit down 1 wall).

After cutting, all pieces were given the standard heat-treatment, then wire brush descaled along the welding line. Before welding any test piece conditions were established on pieces of 19 mm thick mild steel plate. During set up of each tube piece care was taken to ensure that the welding torch always passed along the top of the curved section, so that no arc length changes would result. After set up, test plates were welded without pre-heat and welding conditions automatically recorded (these parameters are given in Table 8). Two single pass welds were made by each process one being high power, the other low. After welding, all plates were allowed to cool to room temperature before being moved. Once cold, all samples were cut at the weld bead mid-point to remove steady-state microstructural specimens.

On examination, after etching, all HAZ's showed the same three regions as before but on a larger scale, as schematically shown earlier in figure 8. Areas of δ were located in each weld in close proximity to the fusion line (within about 0.5 mm), typical illustrations are given in figures 29 and 30. Ferrite quantities were measured in each weld by point counting at a constant depth of 1.4 mm below the

upper surface, and recorded. This depth was chosen as it coincided with an element in the computed heat flow solution (see 3.5.1). During this work S2 was found to have a large HAZ crack, nucleated from bad weld bead profile, passing through the δ/martensite duplex region (figure 31).

After microstructural investigations, hardness surveys were performed across HAZ's on one weld from each process and again at 1.4 mm depth, running from fusion line to parent material in 0.2 mm increments. The results of this work are given in figures 32 to 35 and show similar hardness profiles to unpre-heated tube welds (c.f. figure 26), which is to be expected. The only physical difference found between both series of HAZ's was the increased size of the thick plate weld HAZ's.

### 3.3.3. Quantitative study of δ contents in real weld HAZ's

Microstructural investigations performed on the thick plate weld HAZ's showed a general trend of increased δ contents with increasing heat-input. The variables, δ content and heat input $mm^{-1}$, were statistically examined by using multiple linear regression analysis, the weld parameters are shown in Table 9.

Analysis showed that a relationship did, in fact, exist between δ content and heat input, the resulting equation was: $\%\delta = 2.9620 + 0.001885 \times$ heat input and had a correlation

co-efficient (r) of 0.8752. This result is shown graphically in figure 36 and illustrates the strong relationship between the two variables. From this result it can be seen that weld HAZ δ content in close proximity to the fusion line is directly dependant on the heat input per unit length of weld. Other investigators have reported similar trends in a variety of materials (3,5,6,7,8,10,12,13,44 - 47).

## 3.4 Production of isothermal, continuous heating and continuous cooling transformation diagrams predicting δ formation and decomposition behaviour

### 3.4.1 Introduction

The foregoing section has shown that δ ferrite is found within weld HAZ's even at room temperatures. The conditions under which δ forms in these steels have not been studied. Neither are the circumstances for the retention or decomposition of δ known. To undertake this work a high speed dilatometer was required, operated in conjunction with a welding simulator. Only the simulator was immediately available, the remainder of the desired equipment had to be constructed specifically for this task. The first part of this section deals with the design, construction and calibration of the relevant components. Later sections detail investigations undertaken to study the formation and effects of δ on subsequent transformations. These studies were performed under a variety of thermal conditions.

### 3.4.2 Design and construction of equipment for weld simulator

To produce phase transformation diagrams under representative weld heating and cooling conditions, it was necessary to design and construct specialised pieces of equipment. Two different pieces of equipment were needed, the first involved sample jaws to hold test pieces, the second was a high speed dilatometer.

#### 3.4.2.1 Sample jaws

The pieces of equipment were designed to serve three purposes,

a) to hold the test pieces

b) to carry heating current to the specimen, and

c) to provide fast cooling of the samples.

The jaws were made from oxygen free high conductivity copper and they were continuously water cooled throughout the test. The design of this equipment was restricted by four further factors, these being i) the jaws must fit the existing vacuum box, ii) they must give increased sample cooling rates over existing equipment, iii) they must carry high currents with minimal resistance to maximise sample heating rate and iv) they must be usable as hot tensile/ductility jaws. These restrictions are now discussed in greater detail and their solutions are included.

i) Vacuum box

This box was designed around jaws of 57.1 mm diameter (2¼") and 203.2 mm in length (8"). New jaws were designed to these sizes so that no modifications to vacuum seals were

required. New jaws also used the same length and diametric tolerances as the old equipment to ensure no loss of vacuum performance.

ii) Increased cooling rates

In the new jaws, cooling water was circulated through an annulus surrounding the sample to reduce heat flow path. This entailed a major re-design in the sample mounting area but this was overcome at the expense of some manipulation ease.

iii) Minimal electrical resistance

This is conventionally achieved by using oxygen free high conductivity copper (O.F.H.C) and was used for the new equipment. OFHC copper is also an excellent thermal conductor.

iv) Hot tensile/ductility capability

The use of hot tensile or ductility tests was proposed and therefore the jaws had to withstand reasonable loads without permanent deformation. Water channels, carrying cooling water to the low annulus, reduced cross sectional area to no less than 6.5 sq cms, giving each jaw a maximum load capability (before plastic deformation) of 8.5 tonnes.

3.4.2.2 <u>High speed dilatometer</u>

Dilatometric measurements in weld simulators are made across the sample diameter in the hot zone of the test piece. This

fact effectively determines the high speed dilatometer arrangement. Two transducers, set in water cooling jackets, were used and were located in the vacuum box walls through vacuum seals at sample mid point and diametrically opposite each other. Each transducer was calibrated to an accuracy of $\pm$ 0.000254 mm (.0001 inches) by the manufacturer and the pair were matched to remove inequalities, so the final resolution of the dilatometer should be about $1.27.10^{-4}$mm.

Both transducers carried a 2 mm diameter fused silica probe which contacted the test piece and transmitted sample size changes. The dilatometric arrangement is shown in figure 38. Coarse transducer adjustment (to cater for various sample diameters) was by means of screw collars on the inside and lock bolts on the outside. The arrangement also prevented transducer movement during evacuation.

### 3.4.3 Description and operation of weld thermal simulator and high speed dilatometer

#### 3.4.3.1 Description of weld thermal simulator

Weld thermal simulators are machines which rapidly resistance heat the metal specimens, and cool them quickly whilst closely controlling sample load. These requirements often mean that simulators are based on mechanical testing machines, which carry large copper jaws to hold test pieces through which high currents are passed to resistance heat them. These features can be seen in figure 37.

Sensitive operation requires certain refinements of the mechanical testing frame such as load control capability, thermal cycle control, high current availability and good

cooling of sample jaws. These features are visible in figure 37.and will be more closely identified. The mechanical control console (a in figure 37) comprises two parts, position control (1) and load control (2). The former causes large displacements of the lower (mobile) jaw and is used for mounting and dismounting specimens, the second channel accurately loads the test pieces before and during thermal cycling.

The thermal control equipment (b) consists of 2 pieces, the first (3) a programmable drum onto which heating and cooling rates are drawn, then beneath this (4) is the temperature controller onto which desired peak temperatures are pre-set before cycling commences.

High electrical heating current is produced in the transformer (c), being conducted to the jaws (d) by heavy copper cables. Current control occurs by monitoring sample thermocouple output (control thermocouple) and comparing this to required values (generated by temperature controller (4)). Effective control of both heating and cooling rates are achieved in this manner.

Water cooled copper jaws (d) provide both electrical contact to, and cooling for, the specimen under test. Sample temperature control is the balance of current heating and constant cooling by the water flow through the jaws.

Also visible in figure 37 is the vacuum box carrying the dilatometer and the associated amplifiers and recorders. A detailed description of this apparatus will be given later (section 3.4.3.3).

### 3.4.3.2 Operation of simulator

Before operating the simulator, thermocouples must be welded onto the specimen, one of which is at mid-point of gauge length and is the control thermocouple. Thermal programs must be checked at this stage to ensure consistency and accuracy.

When these points have been checked, a sample is mounted in the upper (fixed) jaw and the thermocouples connected. The mobile jaw is moved so that the specimen can be inserted and then a slight tensile load applied to give good fit up of all connecting surfaces. Control is transferred into load control to allow accurate load adjustment and control throughout the subsequent cycle. (At this stage the dilatometer chamber may be evacuated if required).

Heating current, to specimen is turned on manually with the switch situated on left-hand side of temperature controller (4), and henceforward controlled by the programmed thermal apparatus (3). The rotation of this drum causes the programmed thermal cycle to be reproduced in the specimen, temperature control being by the attached Pt/Rh thermocouple.

At the end of the program, power is manually turned off, drum rotation stopped and position channel brought into

operation. Sample removal can be undertaken and the simulator is ready for further work.

### 3.4.3.3 Description and operation of the high speed dilatometer

This equipment is shown in detail in figure 38. The two water cooled transducers (A) carry fine fused silica probes (B) which are held in light spring contact with the sample at its mid-point i.e. on the same circumferential line as the control thermocouple. These transducers are mounted on the sample vertical centre line and opposite to each other so that diametrical size changes are always recorded.

Both transducers enter the dilatometer box through vacuum seals, thus enabling adjustment of transducers to accommodate varying sample diameters without loss of vacuum performance. The transducers are water cooled to prevent thermal drift and the silica rods are ball ended to produce minimal contact area and hence reduce heat pick-up. These two precautions are used to retain calibration even during long periods at high temperature.

Before operation commences, transducer output is brought to zero on the transducer monitor (M in figure 37). Output of this amplifier is relayed to the X axis of an XY graph plotter (N in figure 37) then to one channel of a two-pen Yt recorder (O in figure 37). Control thermocouple output is registered on the Y axis of the graph plotter and a "slave" thermocouple (on sample gauge length mid-point) is used for the second channel of the two-pen recorder.

Once the thermal cycle commences, sample dilation is recorded automatically against time and temperature (actually thermocouple output), throughout the whole cycle. When cold, both transducer probes are removed to facilitate sample removal and are re-attached to the transducers after the next sample is mounted.

This dilatometer is termed "high speed" because it constantly monitors and records all transformations occurring even over very short time periods, its detection ability is enhanced by using very accurate transducers, the total measurement accuracy of which is guaranted to be better than $2.54.10^{-4}$mm.

### 3.4.4 Selection and calibration of simulator samples

Previous experience indicated that acceptable cooling rates and dilation changes could be achieved using a 10 mm diameter sample [3,57,59,61,62,72]. Hence, a sample diameter of 10 mm was chosen but this did not prevent reduced size samples being employed. The gauge length was not finalised. An essential further stage involved calibration of the control thermo-couple and a systematic investigation of the temperature distribution existing in the sample during thermal cycling. This was done to ensure that an adequate proportion of the specimen accurately, and consistently, followed the prescribed thermal program.

3.4.4.1 Temperature gradient along sample gauge length

Three sample gauge lengths were used for this work (15, 25 and 35 mm) all were 10 mm diameter. Pt-Rh control thermocouples were resistance welded on gauge length mid-point, whilst similar measuring thermocouples were attached at various distances from the centre point. These measuring thermocouples were spaced 10, 5, 2 and 1 mm from control couple and 1100°C holding temperature was used. A slow heating rate was used (15 seconds) and peak temperature held for 5 seconds to allow sufficient recording for scrutiny. One measuring thermocouple per sample was used and each sample was discarded after one test. This work was repeated using 1200 and 1300°C peak temperatures, the results being given in figures 39, 40 and 41.

It was found that samples "necked" during 1300°C cycles with subsequent thermocouple displacement, unless very low loads were used. This was because 1300°C is within the "Nil Strength Range"(NSR) of the Class 1 steel which was used for this investigation, higher temperatures were subsequently excluded because of possibility of brittle failure in the "Nil Ductility Zone" (NDZ). Studies had to be made in this temperature range later so this problem had to be surmounted. Two small screw jacks were used in the jaw cavity to drive home the contact wedges so that good electrical and thermal contact was established and maintained under very small tensile loads. These screw jacks are visible in figure 38.

3.4.4.2 Sample natural cooling rate

Four sample gauge lengths were used for this work, 15, 25, 35 and 65 mm, the first three at 6.3 and 10 mm diameter, the latter at only 10 mm and were tested with peak temperatures of 1100, 1200 and 1300°C. The reduced diameter samples were produced to a previously employed design and is shown in figure 42 (61). Each sample was heated to temperature in 10 seconds, held for 20 seconds and cooled by turning off the heating current. Samples thus cooled at their maximum possible rate (natural cooling rate) and the fall in sample temperature was recorded by a Yt pen recorder. Adjustment of recording paper speed travel in the pen recorder allowed very accurate cooling times to be recorded for each sample. Typical results are given in figure 43.

Sample size selection was possible at this point, the 25mm gauge length specimens were selected because their natural cooling rate was faster than the expected rates of the test thermal cycles and therefore quite acceptable for programmed cooling rates in the simulator. The strong influence of sample diameter on cooling rate is obvious in figure 43 but 10 mm was selected because of the larger area available for later examination. If more rapid cooling rates were required, reduced diameter samples (25 mm gauge length x 6.3 mm diameter) could be employed with subsequent diminution of examinable surface area (3).

### 3.4.4.3 Thermal gradient across sample diameter

Measurement of diametric thermal gradients is usually performed using a radially inserted sheathed thermocouple [72, 73]. This method was utilised for this work using a 0.5 mm diameter chromel-alumel sheathed thermocouple inserted into a 0.52 mm diameter hole, which extended completely through the sample. The sheathed thermocouple was inserted to a depth of 10 mm, i.e. completely through the sample until its tip reached the opposite face, and the sample cycled to 1200°C, being held at this temperature for 5 seconds before being cooled. The thermocouple was withdrawn in 1 mm increments, being taken to 1200°C for 5 seconds after every withdrawal. This was performed until insertion was 1 mm.

All results were recorded on a calibrated Yt recorder, one pen monitoring control thermocouple output, whilst the other pen recorded the inserted thermocouple output. From these results it was possible to compare surface and centre profile temperatures, the results are given in figure 44. Temperature fall off, on small thermocouple insertions, is due to the heat-sink effect [72,73]. The results of this work show that a gradient of less than 10°C exists at 1200°C between centre and surface of the specimen, thus these samples are suitable for dilatometry [59].

### 3.4.4.4 Calibration of centre against surface temperature

Calibration of centre temperature against surface temperature over a wide temperature range is necessary for

accurate recording of phase transformation temperatures. If reproducable correlation does not exist between surface and centre temperatures, all transformation work requires inserted thermocouples to measure temperature directly.

Two techniques were used for this work, the first being a stepped program with three steady temperatures, whilst the second was cyclic, peak temperature being increased by 100°C increments up to 1300°C. In the first work a radially inserted thermocouple was located 5 mm deep, the sample then being held at 1100, 1200 and 1300°C each for 20 seconds. This work was replicated twice more to produce statistically valid results and comparison of surface against centre temperatures are given in Table 10.

The second technique for surface-centre calibration again used a 5 mm deep radially inserted thermocouple but the sample was cycled between 100 to 1300°C in 100°C increments and was held for 5 seconds at peak temperature. Heating rate was slow (30 seconds) to avoid overshoot, this rate being used for all samples.

One specimen was used which was subjected to all peak temperatures before removal from the simulator. Once completed, a replicate was tested under identical conditions. These results were correlated by using multiple linear regression analysis, and were shown to have a correlation co-efficient (r) of 1. The resulting equation was $y = 1.0049x - 5.051377$ (where x is centre temperature and y is surface temperature). This is plotted as a graph in figure 45. From this graph

it can be seen that effectively surface and centre temperatures are equal.[59] Calculations taking a surface temperature of 1350°C shows centre temperature to be 1351.5°C - an insignificant difference.

### 3.4.4.5 Effect of dilatometer probe contact on local sample temperature

During dilatometry two fused silica probes are held in light contact with a hot specimen. Although point contact exists between sample and probe, an obvious temperature gradient is present. This may cause heating of the probe by localised cooling of the sample. This effect was measured by using a measuring thermocouple located at the point of probe contact (as illustrated in figure 46).

The sample was heated to 1000°C in 6 seconds and held for 120 seconds, then cooled. The same sample was re-exposed to 1300°C for the same time and cooled. Overshoot occurred in both cases, followed by temperature stabilisation, and produced two areas at each temperature for comparison, which were peak and steady temperatures. In neither case, at both temperatures, was any difference noted between control or measuring thermocouple output. This indicates that no local cooling of the sample occurs in either dynamic or static situations due to probe contact. The correlation between measured temperature and actual surface temperature beneath the transducer probe was shown to be satisfactory.

### 3.4.5 Phase transformation measurement using fast heating and cooling rates and short austenitising times at low temperatures

Microstructure and phase transformations occurring, at low peak temperatures, had already been determined by a conventional metallurgical dilatometer. However, the influence of more rapid heating and cooling, coupled with shorter austenitising times produced by the weld simulator, was unknown. Samples of both Classes 1 and 2 steel were produced in gauge lengths of 25 mm at 6.3 and 10 mm diameter.

Two Pt-Rh thermocouples were welded on each sample, diametrically opposite each other, at gauge length mid-point. One was the control thermocouple, the other was connected to the Y axis of the XY graph-plotter. (It was found at an early stage that the control couple output, <15 mV, was insufficient to power two recorders and provide accurate temperature measurement; so an independant measuring thermocouple was used for the XY plotter). Once mounted in the machine the thermocouples were attached and the dilatometer prepared (as detailed in 3.4.3.3).

Heating rates were between 3 and 30 seconds to austenitising temperature (1000°C for Class 1, 1050°C for Class 2) with holding times between 1 and 100 seconds, then cooling followed at each sample's natural cooling rate. Constant dilatometer recording was used on heating and cooling, so that all phase transformations could be studied.

It was found in both materials that $Ac_1$ and $Ac_3$ temperatures varied with heating rate, both tending to occur at elevated

temperatures with more rapid heating. On cooling, transformation temperatures in both steels (ie Ms and Mf) were found to be invarient with cooling rate, agreeing with earlier work (Ms323°C, Mf140°C - Class 1, Ms275°C, Mf60°C - Class 2). These temperatures are the same as determined by earlier dilatometry, showing that the high speed dilatometer attached to the weld simulator was performing satisfactorily.

Metallographic work performed on these specimens showed the existence of lath martensite in both materials, with some carbides visible in Class 1 material. These findings duplicate results found by conventional dilatometer work. Prior austenite grain size measurements were made on Class 2 samples and showed slight coarsening due to increased austenitising temperature. Generally little change was noted from earlier measurements (average sizes were still 0.25 to 0.3 mm) and no effect of austenite grain size was noticed on Ms or Mf.

### 3.4.6 Variations of $Ac_1$ and $Ac_3$ occurring with differing heating rates and isothermal treatments

Equilibrium phase transformations have little value in the welding situation as non-equilibrium situations dominate the whole process. Process variations can occur which may seriously alter the heating rate experienced in the HAZ and rate dependant processes will be subsequently affected. Previous work showed that austenite formation appears to be heating rate sensitive and therefore a series of

samples of Class 1 steel were heated to 1000°C using times from 6 to 120 seconds. Variations in dilatometrically detected $Ac_1$ and $Ac_3$ transformation temperatures were noted. These results are tabulated in Table 11, which shows that both $Ac_1$ and $Ac_3$ are somewhat elevated, with increasingly rapid heating rates in Class 1 steel.

A similar investigation was performed on Class 2 steel and show the same trend, which prompted a systematic isothermal investigation into austenite formation in order to enable reasonable estimates of thermal behaviour to be made.

All samples were heated in the simulator to 780°C and held for 10 minutes, to produce a constant homogenous starting structure, before being heated to transformation temperature, in 1 second. Transformation behaviour was noted on the Yt recorder and was shown as a contraction commencing ($Ac_1$) and progressing until no further contraction occurred ($Ac_3$). Further monitoring continued in all cases for a minimum of 10 minutes to ensure transformation was complete. After this, samples were cooled and metallographically examined. The results of this investigation are given in figure 47 which shows that between 812 and 836°C a ferrite-austenite miscibility gap exists and the transformation does not go to completion. Microstructural samples taken from this region show co-existence of austenite and tempered martensite (figure 48).

These findings indicate that during rapid heating, enlargement of the austenite-ferrite miscibility gap occurs

with subsequent elevation of $Ac_1$ and $Ac_3$ temperatures. Only when heating rates are very slow will this miscibiltiy gap be minimised with constant $Ac_1$ and $Ac_3$ values. These results also cast some light on the transformation mechanism of austenite formation. The temperature dependence of both $Ac_1$ and $Ac_3$ are clearly shown which indicates a diffusion mechanism producing this transformation [79].

### 3.4.7 δ phase formation during continuous heating and isothermal heat-treatments

Kinetics of δ formation were studied by two means in both steels. Class 1 steel was first examined using continuous heating techniques with 1320°C peak temperature, heating taking between 6 and 120 seconds and was linear. During heating, after austenite formation, sudden rapid expansions occurred, This was δ formation (see Appendix I ). Replicate results were obtained for each heating rate and the δ formation temperature ($Ac_4$) obtained. All results were compared, found to agree and recorded, graphic presentation being simplified because linear heating rates had been employed (therefore temperature was directly related to time, thus time required to cause transformation was easily determined). All samples were retained and subsequently metallographically examined to verify the existence of δ ferrite. It was soon noted that the dilatometer and optical observations agreed very closely. Optical investigations at high magnifications (1000 x +) showed the presence of very small quantities of δ in samples that had shown the barest dilatometric evidence

of δ ferrite growth. Estimates of δ ferrite quantities in these cases were statistically poor (eg 0.2% $\pm$ 0.5%) hence dilatometric evidence was accepted as indicating the observable metallographic start of transformations.

It was decided to investigate the isothermal transformation behaviour of Class 1 steel in order to be able to compare it to continuous heating formation of δ. A constant linear heating rate was employed, this being 0 - 1320°C in 4.5 seconds and was the maximum possible heating rate consistent with accurate peak temperature control. All samples were heated at this rate to their pre-selected transformation temperature (within the range of 1250°C to 1320°C). Once at temperature all samples were left until δ formation commenced (noted from time V's dilation recordings), the samples were then cooled and later metallurgically examined. Replicate tests were performed at each temperature and were found to be in good agreement.

The results for both continuous heating and isothermal production of δ in Class 1 steel are given in figure 49. From this graph reasonably good agreement on δ formation kinetics can be seen between both techniques. It was also noted that isothermal short time transformations (ie 1 - 40 seconds) seemed to be almost on a straight logarithmic line so a regression analysis was performed on these points. The resulting equation had a high correlation co-efficient (0.934) and was $y = 41.9 - 0.0319x$ (where y was log time to transformation, and x was transformation temperature °C). A sample was transformed at 1270°C to check this equation,

predicted time being 28.99 seconds, experiment result was 28.25 seconds, a difference of 3.08%. On this basis, the logarithmic short time linear relationship was validated.

The same experimental methods were used to study δ formation in Class 2 steel. It was soon found that 1320°C was too low to cause δ formation, especially on very short heating times, so 1360°C was nominally chosen for subsequent work. Heating to this temperature took between 4.5 and 180 seconds and all heating rates caused subsequent δ production. $Ac_4$ temperature was located, as in Class 1 steel case, from the XY graph plotter results. A typical dilation curve for this steel is shown in figure 50 along with the tangent method used to locate change points. Once more replicate tests were performed to enhance accuracy.

An attempt was made in the isothermal treatments to produce δ from a uniform austenite matrix and see if this fact affected transformation kinetics. Samples were heated to 1150°C in 30 seconds, held at this temperature for a further 50 seconds and then heated at 80°C $sec^{-1}$ to pre-decided transformation temperatures between 1315 and 1480°C, where they were held until transformation was underway. Whilst δ formation was proceeding samples were cooled and preserved for metallographic study. These results are given in figure 51, from which it is noticeable that zero transformation times are some 30°C different. This can only be explained by increased austenite stability

removing, or reducing, austenite compositional gradients. As δ production is essentially diffusion controlled, the effect of local inhomogenities is important and could enhance transformation [79]. The representative transformation behaviour for δ formation during welding is therefore the continuous heating case which registers the effect of inhomogenities.

### 3.4.8 Isothermal decomposition of δ ferrite to austenite

Although the formation of δ from austenite occurs rapidly at high temperatures, re-transformation of this δ back to austenite on cooling is delayed. This much is obvious since quantities of δ remain untransformed in weld HAZ's. Little is known of δ decomposition kinetics, some authors believing that re-transformation begins during cooling, even after welding [13].

Decomposition kinetics were examined by dilatometry during isothermal heat treatments. Two ferritisation levels were investigated in Class 2 steel which were approximately 48 and 65% δ, produced by 50 and 320 seconds respectively at 1360°C, this latter value representing equilibrium content at 1360°C. A constant heating rate of 9 seconds to 1360°C was used and samples held for the requisite time (50 or 320 seconds) and then cooled at half natural cooling rate to transformation temperature. Time was measured from the point when samples reached temperature until a constant contraction occurred, signifying the commencement of δ decomposition to γ. This time was located for ferritisation

groups

between 1050 and 1250°C, these results being expressed in figure 52.

Metallographic examination of each specimen was performed to determine transformation mechanisms and quantities involved. All samples showed some δ regions where the sharp δ grain boundary became "gauzy" and indistinct and martensite laths projected into the ferrite (see figures 53 and 54). In these areas austenite has formed from δ, often on distinctly different orientation to existing austenite, so that when transformation to martensite occurs lath orientation between "old" and "new" austenite is clearly visible.

One random sample was shown to have transformed about 8% of the δ to austenite - this sample having been left transforming for some time before being cooled.

These results show that long periods of time are required to decompose δ even under isothermal conditions, with time extending as δ content increases. It is unlikely that even in very high heat input welding situations (when cooling rates are at their lowest) decomposition of δ will occur. To remove, or reduce, δ in a HAZ a treatment equal to a supercritical heat-treatment is required. Even when transformed immediately after formation, extended times are required.

### 3.4.9 Effect of δ on low temperature isothermal decomposition of austenite

Under slow cooling or isothermal conditions austenite can decompose to a mixed microstructure of α ferrite and carbides [1]. This reaction is composition dependant, although the accepted values for this transformation in Class 2 materials are widely known [1]. Determination of homogenous austenite decomposition kinetics for Class 2 steel was performed by heating samples to 1050°C for 20 seconds before cooling at half natural cooling rate to the transformation temperature and leaving to transform. On completion of transformation (as seen by completion of expansion on the dilatometer) samples were cooled and metallographically examined. Beginning and completion of the reaction was timed from Yt recordings and these are given in figure 55. The graph is of the usual shape with the "knee" at 795°C and 13 minutes (typical values for this transformation in Class 2 material [1], and is thus in good agreement with accepted values for this transformation.

Metallographic work was performed on all samples to confirm dilatometric evidence, all structures showing similar details. Fully transformed samples showed heavy carbide precipitation on prior austenite grain boundaries extending deep into the grain structure, of which the centre is ferrite (see figure 56). Examination of the ferrite and carbide interface under high magnification show them to lie in a pearlite-type relationship (see figure 57).

These results indicate the slowest cooling rates that achieve a martensitic matrix. They are also valid for the exclusively martensite zone in weld HAZ's which will decompose to ferrite and carbides if cooled too slowly or tempered before full transformation.

In the high temperature region of weld HAZ's some δ exists and the effect of δ on austenite decomposition is not known. Consequently samples were heated to 1360°C in nine seconds and held for 320 seconds before being cooled as before, to similar transformation temperatures (580 - 760°C) and left to transform. Transformation monitoring and recording was as before, the results are illustrated in figure 58 and a compound table to compare transformation behaviour between austenite and austenite/δ duplex microstructure is given in Table 12. Figure 59 shows the results of this table graphically and illustrates transformation retardation behaviour of δ ferrite. Within the 600 to 700°C temperature range transformation rate differences are not very marked, but above 700°C duplex material becomes increasingly stabilised.

Metallographic work was performed on all transformed structures (see figures 60 and 61) and is remarkably similar to the transformed austenite structures (figures 56 and 57) except that more grain size inhomogenity exists. In both transformations, high magnification examination of grain boundary regions show the lamellar pearlite type structure of ferrite and carbide (figures 57 and 61).

### 3.4.10 Effect of δ on the martensite transformation

Formation of δ from austenite in these steels is by a diffusion mechanism involving, at least, carbon and chromium (this is predictable from figures 2 and 3). Chromium diffusion into δ must occur whilst carbon rejection from δ (0.02%C) into austenite also happens. This increases the carbon content in austenite, which should be evenly distributed throughout remaining austenite because of high carbon diffusivity. On cooling, martensite ought then to form at reduced temperatures depending on δ content, because carbon depresses Ms by 474°C per 1% [1,2]. This gives a basis for calculation in order to find Ms depression by δ content, the results of these calculations are given in figures 62 and 63.

This hypothesis was tested by austenitising samples of both steels at their respective solution temperatures (1000°C for Class 1, 1050°C for Class 2) then cooling and thus determining Ms and re-heating to produce various amounts of δ, followed by cooling and re-measurement of Ms. Class 1 materials were held at 1320°C for 5 - 60 seconds (producing 5 - 35%δ) whilst Class 2 steels were treated at 1360°C for up to 60 seconds (≈50%δ). On cooling, no Ms depression was noted in any sample of either steel. All samples transformed at their pre-determined Ms temperatures although Ms reductions as large as 60°C had been expected. These results were unexpected but replicated each time. They do, however, disprove a previous theory that Ms depression occurs, which then results in martensite formation within

the hydrogen activation temperature range [14].

An explanation of this phenomenon was attempted on the basis of limited carbon diffusion. This theory states that carbon diffusion is insufficient to cause homogenity in the austenite but just locally enriches austenite near ferrite. On cooling, bulk Ms temperature is noted because this reflects bulk austenite carbon levels and the enriched austenite transformation is "hidden" in mass reaction. This idea fits experimental data but is undermined by new views on the diffusivity of carbon. It is thought that carbon diffusivity is high enough to remove free carbon inhomogenities (as opposed to combined carbon) at temperature levels of 900 to 1000°K; thus carbon levels should equalise throughout bulk austenite (figure 64).

Another suggestion has been that carbon combines with some metallic alloying elements to form carbides, hence surplus carbon is removed. This mechanism, although theoretically sound, was not substantiated at this stage. High magnification optical microscope examinations located no visible carbide particles at, or near, the δ/martensite interface. Further attention to this aspect is documented in a later section.

### 3.4.11 Results of δ phase transformation survey

From this work it is clear that δ formation and retention is to be expected in an area of weld HAZ's in both steels studied. This δ forms on heating to temperatures below

the solidus value and will not decompose unless very slow cooling occurs. Further decomposition of austenite to α ferrite and carbides is retarded by the presence of δ. Therefore even slow cooling rates should result in the retention of a δ/martensite duplex zone remaining within the weld HAZ. Occurrence of δ within an HAZ does not affect the martensite transformation at all, this reaction occurs at the same invariant temperature whether ferrite is present or not.

The application of such results to welding situations is obvious, although no considerations of possible variations in weld heating and cooling rates, due to welding parameters, or processes, have been considered. Results obtained from isothermal, continuous heating and continuous cooling studies may not be directly applicable to critical weld HAZ simulation studies, although they may clarify subsequent findings.

## 3.5 Production of welding CCT diagrams

### 3.5.1 Introduction

It has been shown that δ ferrite always forms on heating Class 2 material above 1360°C although slow heating rates may cause its production at temperatures as low as 1320°C. This δ ferrite is then retained to room temperature, at the cooling rates encountered in weld HAZ's and may influence subsequent transformations. Effective application of this information to weld HAZ's requires the determination of representative CCT diagrams produced

with thermal cycles typical of the range of welding processes envisaged. A necessary first step is the determination of weld thermal cycles, These were performed theoretically using numerical techniques. This made the simulation of the high temperature regions of the thick plate weld HAZ's possible and hence enabled the determination of a representative welding CCT diagram.

### 3.5.2 Theoretical predictions of weld cooling rates

As only limited quantities of suitable material was available for welding work, experimental measurement of weld thermal cycles was not possible, a finite element computer program was used instead to predict weld cooling rates from welding parameters. This program (Variab) is the most sophisticated computational technique available to predict weld cooling rates [64] and was modified to suit 12% Cr Mo steel. The program has been widely proved by its originator [64], and others [65], and has been shown to be very accurate for peak temperature determination and produces cooling rates identical to experimentally measured values (using implanted thermocouples [64, 65]). It achieves this accuracy by using temperature-dependant properties and also making allowance for latent heats of transformation and solidification, rather than by using thermal properties suitable only for one temperature range [64,65,66,67]. Accurate thermal properties of steel when used in Variab produce true reflections of transformation behaviour[65].

Inputs required for Variab are: arc time (seconds) plate thickness (cms), welding current (A), welding voltage (v), arc travel speed (cms sec $^{-1}$) and arc efficiency. From this information, and pre-programmed data within the program, a full thermal history of the weld area is calculated. A fuller description of Variab is given in Appendix 2.

Variab output is in terms of temperature at finite, three dimensionally defined positions within the weldment. Rapid inspection of such an output approximately locates the extent of HAZ regions and size. Determination of specific peak temperature thermal cycles is more complex requiring, eventually, integration of a three dimensional matrix. The whole technique is described in detail in Appendix 2.

All information supplied to Variab is real, ie accurately known or measured from real welds, except the arc efficiency factory which is a value based on published data [64, 82]. The arc efficiency effect was determined for sample S1 (see table 8) by calculating thermal cycles using arc efficiency factors representative of low, medium and high levels of the published values. The resulting thermal cycles were compared and it would found that for two given peak temperatures (1360°C and 750°C) theoretical isotherm placement variations were less than 0.3 and 0.75 mm respectively at a constant depth (0.14 cms). On this basis an average of the published arc efficiency values was taken to calculate thermal cycles for all welds (e.g.

0.95 was used for sub-arc welds, published values being 0.9 to 0.99).

Variab uses arcing time to calculate the thermal cycle for that time, so in all cases arcing time to metallurgical sample position was determined (and termed sample equivalent time, S.E.T.). This term (S.E.T.) was not important when quasi-steady state conditions existed but was used to determine the sampling range of weld available. Computer runs for weld TI were performed with arcing times of 25 and 100 seconds (SET = 50 seconds). These results show that at SET and beyond, quasi-steady conditions existed, whilst at ½SET unsteady heat flow conditions occurred, thus defining approximate sampling limits.

3.5.2.1 Selection of peak temperatures for thermal simulation and production of respective thermal cycles.

Two peak temperatures were selected for simulation, these were 750°C and 1360°C. The former is in the secondary hardening field whilst the latter is in the δ formation field and also represents practical machine limitations. These thermal cycles were determined for each weld using the methods detailed in Appendix 2. Once each thermal cycle was determined it was converted to a time basis, as distinct from distance and plotted on to program charts for the thermal controller.

### 3.5.3 Production of representative weld HAZ CCT diagrams

#### 3.5.3.1 Phase transformations occurring throughout the range of weld HAZ thermal cycles

The thermal cycles used for this work were produced, as described, from the computed weld thermal history of each individual weld. Comparing thermal cycles with the natural cooling rates of simulator samples, it was noticed that samples T1, T2 and M1 were required to cool faster than 25 mm gauge length x 10 mm diameter samples. Reduced diameter samples, of 25 mm gauge length, 6.3 mm diameter were therefore used for these simulations. These smaller samples cooled faster, allowing closer simulation of thermal cycles without risk of under cooling.

Simulations were performed as before, dilation being simultaneously recorded. Each cycle was replicated until four accurate simulations were obtained, samples in which overshoot of 10°C or more occurred on peak temperature were ignored. Transformation information recorded for each sample was the average value of all four accepted simulations, few differences in any information was found throughout the whole work. Formation of δ ferrite was noted in all 1360°C peak temperature runs as was expected and no phase transformation occurred in the 750°C simulation used to study secondary hardening.

The results from this work are given in figure 65 and show clearly that no unpredictable phase transformations occur throughout the range of welding processes surveyed. This finding agrees with earlier results and confirms that

once δ is formed in the HAZ during welding, it is retained, untransformed, to room temperature.

### 3.5.3.2 Continuous cooling transformation of two hypothetical welds

All weld cooling rates previously considered fall within the γ+δ continuous cooling field and hence to the left of any line depicting δ retransformation. Data from two high heat input welding situations were obtained [80,83] and their cooling rates predicted by Variab for welds in Super 12% Cr Mo steel. These welds were i) a deep penetration submerged arc weld and ii) a very thick plate electro-slag weld, both of which could be used in fabricating these steels. The welding parametersfor both welds are given in Table 13, These are the values used in Variab, whilst figures 66 and 67 illustrate the sub-arc and electro-slag weld HAZ thermal cycles. As expected both welds cooled more slowly than the other welds and simulation showed both to lie to the left of any critical cooling rate. Metallurgical examination of both simulated microstructures showed no evidence of δ retransformation.

In an attempt to determine approximate cooling rates to cause subsequent transformations some isothermal work was performed.

### 3.5.3.3 Isothermal decomposition of δ to austenite in representatively ferritised steel

The material utilised in this work was ferritised by isothermally transforming samples at 1360°C for either

0.5 or 2 seconds producing 9.5 and 16.6% δ respectively. These two time periods were selected to represent near-fusion regions of the lowest power weld to the highest power weld (ie T1 and S2), based upon the earlier computer predicted weld thermal cycles. This technique was used to scan the whole range of ferrite contents existing within weld HAZ and hence rapidly determine overall transformation time ranges.

After the ferritising treatment, samples were cooled at half natural cooling rate to transformation temperature, which was between 1000 to 1200°C. Once at temperature, samples were left until no further size change occurred (as defined in 3.4.8). Transformation time was accurately measured from the Yt dilating recording, the sample cooled and subjected to metallographic analysis This experimental technique was applied to both ferritisation levels.

The results from this work are very similar (Table 15) and are given in figure 68, This shows that there is a very small decomposition range of δ for all welds considered. The inference of this finding is that continuous cooling rates to cause δ retransformation will be very similar for all welds.

3.5.3.4 Isothermal decomposition of mixed δ/austenite matrices to α ferrite and carbides

The two ferritisation levels used in section 3.5.3.3 were also utilised for this investigation (the ferritising

treatments being isothermal holding at 1360°C for 0.5 or 2 seconds), similar heating and cooling rates were also employed. Transformation temperatures used were in the range of 675°C to 875°C and samples were held until transformation finished (as defined in 3.4.9) when the samples were cooled and metallographically examined. Transformation time was taken from the Yt dilation recording (as before) and these results are given in Table 15 and figure 69.

Once again the similarity of results is obvious, thus similar cooling rates will cause transformation to α ferrite and carbides throughout the whole welding range. Metallographic studies were undertaken on all samples and showed great similarity to previous structures (figures 56 and 60) and are illustrated in figure 70.

### 3.5.3.5 Continuous cooling transformations in ferritised steel at very slow cooling rates

The two previous ferritisating treatments consisting of 0.5 or 2 seconds at 1360°C were used in this work and after isothermal transformation, cooling commenced at pre-selected linear rates. Five rates were used and were 2, 1.36, 1.13, 0.8 and 0.68°C $sec^{-1}$; replicates of each test at both ferrite levels were performed. Transformation temperatures of all reactions were taken as the average of both specimens (ie first and replicate), but little difference existed between the two results. After testing, each sample was sectioned and metallographically investigated to substantiate dilatometric findings.

These results are illustrated in figure 71 and listed in Table 16, once more the striking similarity between both levels of ferritisation is noticeable. Figure 71 also includes the isothermal transformation information for δ to γ and δ + γ to α + carbides, and it can be noted that the isothermal reaction kinetics fall within the corresponding CCT envelopes. This is especially true for the δ to γ transformation, whilst the decomposition of remaining δ and austenite to α ferrite and carbides is accelerated, which could probably be due to reduced austenite stability in the continuous cooling situation. Formation of small quantities of α ferrite and carbide elevate Ms temperature whilst depressing Mf. This is probably due to compositional gradients generated by formation of α ferrite. This phenomenon also occurs if homogenous austenite matrices decompose to form some α during continuous cooling [1]. It is probable that carbide formation on a massive scale causes austenite to be locally denuded of some carbon thus causing Ms elevation [34], Mf reduction results from carbon rejection during α formation, regionally enriching austenite and hence reducing transformation temperature. Ms therefore reflects transformation temperature of a reduced carbon austenite whilst Mf is the end of higher carbon martensite transformation range (c.f. 3.4.10).

3.5.3.6 Effect of cooling rate on δ finish temperature

Rapid cooling rates from 1360°C causes δ growth to cease abruptly at various temperatures, ie. samples T1 to I1 show

this behaviour. Slow cooling rates allow δ growth to occur at a lower, invariant temperature, probably equilibrium temperature, and is 1320°C (±3°), whilst faster cooling causes this reaction to stop between 1347 and 1323°C. These results are given in Table 17 and figure 72. On low arc power welds (e.g. T1, T2 and M1) δ production ceases abruptly, whilst slower cooling enhances δ growth. This effect of elevated δ finish point is of little consequence in the real welding situation, for it means δ is produced for about 0.2 seconds more in S2 than M1 and any δ increase due to this elevation will be swamped by the effect of heating and cooling rate differences.

## 3.6 Comparison of real and simulated weld HAZ's

### 3.6.1 Microstructures

The thermal cycle simulated in larger test-pieces is only valid for a particular point in the real weld HAZ, and because of the thermal gradient across the HAZ the simulated sample is representative of 0.5 mm (at best) on either side of the mean point in the real HAZ. Rapid location of this very small region was required for reference and comparison purposes, therefore careful measurement was used to locate the mean point and a 1 mm square was outlined around this point by micro-hardness indentations. This task was performed twice on each real weld HAZ to locate both 1360 and 750°C peak temperature regions. This facilitated comparison of real and simulated microstructures. One simulated sample for each peak

temperature (each one being taken at random from each group of simulations) was mounted and polished and then examined metallographically. Photographs were taken of significant features, especially ferrite shape and quantity in the 1360°C sample.

Real weld HAZ's were likewise inspected and photographed, figures 73 to 76 show comparisons between real and simulated 1360°C zones, from which it can be seen that a close similarity exists between the two types of microstructure. The major feature such as δ shape, quantity, distribution, and prior austenite grain size were all comparable. Quantities of δ were measured by point counting in both microstructures. and found to agree very closely despite the fact that more points were counted in the simulated HAZ's than in real HAZ's because of the small nature of the representative area of the real HAZ. In all microstructures, both real and simulated, δ was always found on prior austenite grain boundaries, especially on triple points.

In the low peak temperature zones both areas (real and simulated) looked alike, etched darkly, and were composed of tempered lath martensite containing large carbide agglomerations. X-ray diffractometry analysis, as performed in section 3.2.1, was used to identify basic microstructural components and both zones were shown, once again, to contain only $M_{23}C_6$ carbides (almost exclusively $Cr_{23}C_6$). No visible differences could be noted between either real or simulated secondary hardened zones.

Hardness of real and simulated microstructures was tested and compared in both high and low peak temperature areas. Small differences were found between real and simulated microstructure of an insignificant nature. In this respect both real and simulated HAZ's are comparable (see Table 20).

### 3.6.2 Properties of simulated weld HAZ's

Physical property determination in real weld HAZ's is fraught with difficulties because of the small volume of representative material available and metallurgical in-homogenity of HAZ's. Simulated samples, however, are larger and more homogenous and for this work they have been shown to be essentially larger HAZ regions. Physical properties of simulated zones should therefore represent real HAZ properties very closely.

#### 3.6.2.1 Tensile properties

Simulated samples were machined into Houndsfield number 11 test pieces having gauge lengths of 11.33 mm, the sample gauge length centre corresponding to middle of the tensile specimen gauge length. Tensile test-pieces were made from T1 - S2 1360 and 750°C zone simulations, fully hardened samples (100% martensite) and standard state material (Class 2). They were tested on a 20kN (2 tons) maximum load machine, producing a maximum stress of 2464 N $mm^{-2}$ (160 tons $in^{-2}$) on all samples. Each sample was tested at a constant strain rate of 2% $min^{-1}$. Results were only counted from specimens failing within the 11.33 mm gauge

length. After fracture each sample was checked to determine elongation and area reduction at fracture, maximum load and yield point being determined from each load-extension graph. Results of this work are tabulated in Table 18 cross indexed with % δ content.

In these results, a weak relationship between yield point (YP) and δ content emerges, with resulting yield point decrease as δ increases. Ultimate tensile strength appears to be affected weakly by δ quantity, increasing as δ increases. Ductility, however, is definitely reduced by δ, both elongation and area reduction falling with increased δ amounts. Samples T1, T2 and M1 were produced from reduced diameter specimens and appear to be highly ductile. This is, however, incorrect. Tensile failure occurred at gauge length extremities which were not regions of the correct microstructure (due to extreme thermal gradients) and which deformed preferentially to material within the gauge length. Ignoring these three results, it may be seen that ductility (expressed by elongation and reduction in area) falls drastically as δ content increases. (see figure 77).

### 3.6.2.2 Corrosion Resistance

These materials are used in applications where their corrosion resistance is of great value [1,39]. Welding produces stable microstructural changes, the resulting phase inhomogenity may be sufficient to seriously affect the corrosion resistance of the steel.

The effect of a strong corrosive agent on differing HAZ areas was investigated using simulated specimens. Samples of all 1360°C peak temperature simulations were used as were homogenous martensite, secondary hardened and standard state specimens. All samples were cut through at gauge length midpoint and this face polished. An identification number was stamped on, the polished face lacquered and the sample heavily copper plated. Each sample was weighed after plating and then introduced into the corroding medium which was 5 wt % NaCl, 0.1 wt % $FeCl_3$ and 0.01 wt % H Cl in de-ionized water. The test was performed at 25°C for 100 hours in non-aerated conditions to simulate crevice corrosion (which may result from poor penetration welds). After 100 hours exposure the samples were removed, washed in distilled water, dried in warm air and re-weighed. Weight losses were calculated in grammes $cm^{-2}$ of exposed face and the results are given in Table 19 and figure 78.

From these results, it appears that corrosion rate increases as $\delta$ content increases but not linearly, corrosion accelerating rapidly above approximately 8%. Highest corrosion level was in secondary hardened material, with standard state material being very similar. High corrosion rates in this material reflect chromium depletion in some regions. This is obvious in secondary hardened and tempered material as carbides are almost exclusively chromium carbides with $M_2X$ precipitation (which is also Cr rich) in secondary hardened material. (This mechanism is parallel to the cause of weld decay in unstabilised 18/8 austenitic

stainless steels [48]. Increasing δ contents also deplete matrix chromium levels (chromium content of δ is about 16% - from figure 2). Therefore as δ increases, martensite chromium levels fall thus corrosion rate increases.

### 3.6.2.3 Hardness Surveys

Hardness surveys on several areas of each simulated weld HAZ (both 1360 and 750°C simulations) and their respective areas in each real weld HAZ were performed. More hardness measurements were possible on the simulated specimen than the real HAZ, and were used to compare microstructural hardness.

Only microhardness comparisons could be made between real and simulated structures because real zones were of very small extent. Microhardness results are given in Table 20 and show close correlation between the real and simulated microstructures.

Macrohardness measurements taken on simulated specimens should represent macrohardness values in real HAZ's. Therefore a macrohardness survey was performed across the simulated samples. Some differences were noted between micro and macrohardnesses but were thought only to reflect the larger area tested by macrohardness thus showing less sensitivity.

### 3.6.2.4 Correlation of predicted weld thermal cycle to microhardness and microstructure in thick plate welds

Examination of tube welds (Section 3.3.2) showed that

microhardness and microstructure were related. Subsequent work has shown that the weld thermal cycle and weld microstructure correlate closely together (see 3.6.1). This prompted an investigation into the interrelationship of all three variables (weld thermal cycle, microstructure and microhardness).

Real weld HAZ microstructures display the effects of a variety of peak temperatures, in a direction normal to the welding bead. Unfortunately, the thermal cycle information already to hand represented the position of only one random temperature (1360°C). Further information was necessary and was thus produced from the Variab outputs by using the differential solution to the Fourier series orthogonal equation, which is described in detail in Appendix 3. When using this technique to determine specific isotherm location, the mathematical matrix is revolved through 90° and, hence, may be imagined as looking at the plate end on. This method is accurate, but it is arduous and time consuming requiring a complete differential solution for each temperature. Thermal gradients were thus only produced for one weld out of each group. These were welds T1, M1, R1 and S1. The resulting gradients were drawn and then the results of the microhardness and microstructural surveys were superimposed.

The results show that in all welds, secondary hardening is produced by peak temperatures of about 500°C to 900°C (approximate $Ac_3$ temperature), whilst homogenous martensite

is found where temperatures have been between 900°C and 1320°C. Above 1320°C δ formation is located both optically and by reduced matrix hardness. The findings show a good degree of correlation, both between themselves and prior dilatometric findings ($Ac_3$ ≈ 880 - 910°C, $Ac_4$ 1320 - 1360°C) and are illustrated in figures 79 to 82.

## 3.7 δ formation in Class 2 steel weld HAZ's

### 3.7.1 Objectives

The preceding work has shown that quantities of δ form in a weld HAZ and are retained, untransformed, down to room temperature. The extent of δ formation in weld HAZ's, the mechanism of formation and the effect of δ on other transformations are, as yet, unknown. An earlier part of this work has shown that the amount of δ in a weld HAZ is related to the heat-input per unit length, used to make the weld. This and other relationships are investigated in the first portion of this section and an attempt is made to indicate how weld HAZ δ content can be predicted.

The second part of this section will explain δ formation mechanism and thus, why formation of this phase affects other phase transformations. Some later observations on the behaviour of δ under conditions likely to be experienced in multi-pass welding are also included.

### 3.7.2 Prediction of δ contents in weld HAZ's

#### 3.7.2.1 Isothermal transformation behaviour of δ formation

Earlier work shows that δ formation is both time and temperature dependant, in both classes of steel studied. Isothermal and continuous heating studies found that there was no incubation period, thus there are ample nucleation sites and hence the transformation is controlled by diffusion rates [79]. During isothermal transformation, a period should exist when a linear relationship exists between δ ferrite formation and time [79]. This assumption was tested by performing isothermal transformations on Class 2 steel involving quantitative determination of δ ferrite formation.

Three peak temperatures were used, 1340, 1360 and 1380°C, with transformation times between 0 and 250 seconds. To achieve accurate temperature control a steady approach to peak temperature was made. The programmed heating cycle involved heating to 1000°C in four seconds, then 11 seconds to transformation temperature, the last 60°C taking 5 seconds. This technique was found to produce very accurate peak temperatures, i.e. to within ± ,1°C.

Transformation times were programmed and thus were machine controlled. This ensured reproducibility of the time variable at all peak temperatures. On expiration of transformation time power was automatically turned off and the sample cooled at natural cooling rate to room temperature. All samples were monitored by the dilatometer throughout the whole transformation period, although no ultimate use

was made of these records.

After isothermal transformation all samples were metallurgically examined, four random areas of each being used for ferrite determination by point counting. These values were averaged and recorded as percentage transformation in each specimen. These results are given in Table 21 and expressed fully in figure 83. It can be seen in figure 83 that primary region (that of time dependant nucleation) is missing. This is due to slow heating, close to transformation temperature, causing premature $\delta$ formation. The secondary part, that of linear transformation behaviour is clear in figure 83 and exists for all three peak temperatures considered, Figure 84 reproduces this linear behaviour region; the straight lines used are regression analysis values. Also on figure 85 are 95% confidence limits (Table 22 gives values used in regression analysis), all of which overlap considerably. The regression analyses on the data in Table 18 produced these equations:

1340°C temperature. $y(\text{time}) = 0.214x(\%\delta) - 0.625$, $r = 0.998$

1360°C temperature. $y(\text{time}) = 0.200x(\%\delta) - 1.354$, $r = 0.999$

1380°C temperature, $y(\text{time}) = 0.110x(\%\delta) - 2.147$, $r = 0.995$

When these lines are all drawn on a common graph with their 95% confidence limits, extensive overlapping occurs which indicates that over these small temperature differences transforming time is more important than temperature. This means that it is probable that over small time periods transformation temperature is not important.

### 3.7.2.2 Prediction of weld HAZ δ contents at the 1360° C isotherm from isothermal transformation behaviour

There is sufficient information readily available from simulated HAZ microstructure and weld thermal cycles, to attempt a correlation of transformation to time above the transformation temperature. A number of assumptions were made in order to produce information for correlation, the two most important being that heating rate to, and cooling rate from, peak temperature were linear above transformation temperature and that δ formation began and finished at 1320°C in both directions. The time information thus derived was correlated with δ contents of simulated weld HAZ's by multiple linear regression analysis and produced the following equation:-

$$y \text{ (time above } 1320^{\circ}C) = 0.2116x(\%\delta) - 0.603224 \quad (r = 0.990)$$

(The information used to compute this equation is given in Table 23). When plotted on an isothermal transformation graph the dynamic line falls between the 1340 and 1360 isothermal line (figure 85), demonstrating a close measure of agreement. This substantiates the experimental findings. Although δ formation is a diffusion controlled reaction (see figure 86) and hence both time and temperature dependant, over the linear transformation region (figure 85) only time is important. This empirical relationship reflects some experimental error, whilst the wide confidence limits on all lines are the direct result of statistically analysing a limited number of experimental observations.

The foregoing work has also demonstrated that weld HAZ δ content can be accurately estimated from knowledge of the weld thermal cycle. This equation has been validated by isothermal transformation work and is usable over the linear region of the isothermal transformation. Time periods involved in this linear part exceed four seconds, which, in weld heating/cooling terms, covers a wide range of possible welding processes.

3.7.2.3 Elemental distribution occurring during δ formation and its consequences

During δ formation, at least two elements must diffuse either into or away from δ, these elements are chromium and carbon, the extent to which they diffuse is estimable from figures 2 and 3. To investigate elemental redistribution, ferritised samples were examined by electron probe microanalysis techniques.

Large samples (12.5 mm x 12.5 mm x 3 mm) were ferritised by furnace heat-treatments for 5 minutes at 1360°C, then oil quenched and sub-zero treated to transform any retained austenite. Samples were surface ground to 1 mm thickness by removing equal depths of material from both faces, This was to remove any effects of decarburisation. Polishing, followed by etching, then microstructural examination was used to locate δ areas suitable for further examination. Two large δ regions were located and outlined by micro-hardness indentations and then photographed before being gently re-polished to remove the etched surface, but not the identifying hardness indentations. After de-greasing and ultrasonic cleaning, both areas were examined in the

electron probe micro-analyser (E.P.M.A.). Scan analyses were performed concentrating in the centre of the martensite region, close to martensite - δ interface, and also on the interface proper and the centre of the δ area. Only heavy elements (i.e. heavier than Na) are readily detected by this technique, so carbon distribution was not accurately determinable. Concentration profiles for chromium, molybdenum and vanadium were produced and are given in Table 24 and figure 87. From this it can be seen that Cr, V and Mo increase in δ, whilst C falls even on the outside δ. This decrease in C is matched by a slight Mo reduction in the austenite close to δ.

Carbon detection is not accurate by E.P.M.A. techniques, for the X-rays emitted from C atoms during testing are very low energyand easily absorbed (even by the detector window). The inherent inaccuracy of this technique for C determination was thought to be responsible for the anomalously low result for carbon in martensite close to the δ boundary (ie within 20 microns). To verify this finding, microhardness traverses were performed across both analysed areas, from deep within the martensite to δ centre, the results being given in figure 88. These results indicate that a carbon gradient does indeed exist within martensite adjacent to δ, and is in the order of 200 Hv softer than the hardness of bulk martensite. This produces a layered effect, with a low carbon martensite film surrounding δ and extending for some 25 - 30 microns deep into bulk martensite.

These results are not readily resolvable with other experimental facts because no carbon increase in bulk martensite has been located, nor is the reduced carbon martensite "halo" easily explained. These regions which initially exist as diminished carbon austenite therefore transform to martensite above bulk $M_s$ temperatures (because of the carbon reduction, although increased metal concentrations will diminish this effect), but this has not been noted [1,2]. It could be that small amounts of this low carbon austenite do transform but are not noted by the dilatometer. Whatever the effect of the lower carbon austenite film on transformation behaviour, the mechanism causing carbon reduction demanded further investigation.

Formation of δ establishes concentration profiles of various elements normal to the austenite - δ interface. These gradients form because of diffusion rate differences in austenite and ferrite (Cr diffuses 100 x faster in δ than γ [90]) and the resistance to diffusion presented by grain boundaries. On cooling, these gradients are "frozen" in, and have been measured, However optical microscopy cannot detect any significant effect of these composition inhomogenities. High resolution transmission electron microscopy (TEM) was used to overcome this difficulty.

Carbon extraction replicas were taken from a number of δ containing samples and were examined in the TEM. The replicas were both isothermally transformed and simulated microstructures. In all δ region studies, precipitates

lying parallel to the δ interface were found. These precipitates were much finer in simulated specimens (smaller δ regions and shorter transforming times) than in isothermally transformed specimens (see figures 89 to 93). It was suspected that these precipitates were carbides, since they appeared to be located as an interphase precipitate, for it is known that final carbide formation in this mechanism can locally denude austenite of some carbon [86, 87, 88]. Consequently, electron diffraction studies were performed on selected fine carbides and many diffraction patterns were found to be mixed ie. two different phases were present (see figure 94 for an example). Eventually two clear individual patterns were found, both were F.C.C. but of differing lattice parameters. One was shown to be probably $(Cr_3Nb_3)C$ (see figures 95 - 97) whilst the other is almost certainly $Mo_6C$ (see figures 98 - 100)[84,85]. It is probable that only small quantities of the former carbide ($Cr_3Nb_3C$) are present because only 0.1% Nb is present in this steel whilst the latter one is possibly the overwhelming carbide present.

Carbide formation occurs in response to the element concentration gradients at the $\delta \rightarrow \gamma$ interface and controls the forward movement of the ferrite boundary. At some stage a sharp partition of carbon occurs across the interface which results in carbide formation in the ferrite. This carbide production occurs all along the interface and depletes the adjacent austenite of carbon and by doing so enhances forward interface movement. As a result carbon concentration in austenite re-establishes, interfacial movement slows and

carbon partitioning occurs once again. This is schematically illustrated in figure 101 (after reference 86). This growth mechanism accounts for the carbide rows found within ferrite and for the carbon depletion zone found around δ regions.

It should also be stated that this precipitation process increases mechanical strength and hardness of ferrite (by dispersion hardening) but at the cost of much ductility [87,88]. Where vanadium is present, ferrite becomes enriched in this element and is subsequently solid solution hardened. This process alone can elevate ferrite yield point from 250 to 500 N $mm^{-2}$ [87]. Areas of δ ferrite in Class 2 steel, therefore, are both dispersion and solid solution hardened. This accounts for the high ferrite hardnesses, of about 260Hv, found earlier. The increased strength of ferrite is sufficient to affect tensile strength and significantly reduce ductility.

### 3.7.2.4 Effect of prolonged holding around $M_S$ temperature on a ferritised matrix

Many authors report that bainite formation in weld HAZ's in these steels is caused by prolonged holding at interpass temperatures [1,4,10,23,42,44,51,63,83]. Bainite forms when untransformed weld regions (i.e. undercooled austenite) are held at temperatures close to $M_S$ for some time (ten minutes to 1 hour depending on steel composition)[1,4,42], which makes hydrogen diffusing heat-treatments difficult to operate. An investigation was launched to determine the time for bainite formation in a mixed δ/austenite matrix, because it was thought that δ would retard bainite formation

as it does in other reactions.

Weld cycle TI was used with pre-programmed holding temperatures between 430°C and $M_s$ (275°C). Samples were held at the programmed temperature for no less than eight hours (to represent 1 working day) and were constantly monitored by dilatometry [40]. After this time samples were cooled and metallurgically examined.

No bainite formation was located by dilatometry nor by optical microscopy. It is unlikely, therefore, that interpass holding will cause bainite formation in the duplex region of an untransformed HAZ. During such a treatment bainite formation within the homogenous austenite zone is likely, especially if held at temperatures close to $M_s$ [1,10,23, 42,44,51,63,83]. Industrially, the problem of-interpass and hydrogen diffusion temperatures is solved by using temperatures of 425°C, which does not form bainite in reasonable time periods in the austenitic region [1,51].

### 3.7.2.5 Effect of subsequent weld thermal cycles on a ferritised matrix

Most welds made are multipass welds, during which underlaying weld beads and HAZ's are subjected to a series of heating and cooling cycles with a declining peak temperature. Only the first one or two succeeding runs re-austenitise part of the ferritised HAZ. Subsequent deposition tempers both weld bead and HAZ. Re-austenitisation, caused by succeeding passes, means that δ and austenite once more co-exist for some time and the effect of this co-existence

on either phase is not known.

Two samples were heated to 1360°C in 9 seconds and held for 2 seconds then cooled at natural cooling rate to room temperature. Once cold, it was re-austenitised at 1100°C for four seconds, then cooled and metallurgically examined. Throughout the work both samples were monitored by dilatometry and no sign of change (besides $Ac_1$ and $Ac_3$) was found.

Metallurgical examination showed that no δ transformation had occurred, but it was soon noticed that δ ferrite was no longer exclusively on grain boundaries but located within prior austenite grains. This means that δ does not pin prior austenite grain boundaries on re-austenitising but allows them to wander, the normal behaviour is for precipitates to prevent grain boundary motion (79).

It is unlikely that δ transforms to high chromium austenite during austenitising, reforming ferrite on cooling through $Ar_3$ and $Ar_1$ because no dilatometric evidence was noted. It is more reasonable to assume, that due to chromium segregation between austenite and δ, the duplex zone behaves (for short periods) as a higher chromium alloy where austenite and δ co-exist at elevated temperatures (c.f. figure 2). Examples of δ re-location are given in figures 102 to 104.

# CHAPTER FOUR

# DISCUSSION

# CHAPTER FOUR DISCUSSION

It is evident that the most significant feature of the heat-affected zones found after welding the Super 12% Cr Mo steels is the formation of δ ferrite. An extended consideration is therefore given to δ ferrite formation in weld HAZ's and its effects on both subsequent transformations during the weld thermal cycle and the physical properties of the HAZ. This is followed by a discussion of the microstructure of the whole weld HAZ. Finally attention is given to the practical implications of the investigation.

## 4.1 δ ferrite formation in weld HAZ's of Super 12% Cr Mo steel

Dilatometric data, supported by metallographic results, shows conclusively that δ ferrite formation occurs when these steels are thermally cycled into the austenite + δ phase field, i.e. above the $Ac_4$ temperature. The threshold value of this temperature, and hence for δ formation, depends upon the heating rate employed. Heating rates below $8^{\circ}C\ sec^{-1}$ caused δ formation at $1320^{\circ}C$, whilst heating rates above $300^{\circ}C\ sec^{-1}$ showed δ to be formed at $1360^{\circ}C$. Intermediate heating rates caused δ formation between the two limits. This is illustrated in figure 51. A similar occurrence has been identified in Class 1 steel, $Ac_4$ varying between $1250^{\circ}C$ and $1320^{\circ}C$. This is shown in figure 49. Such transformation hysteresis is typical of diffusion controlled reactions, as the Johnson-Mehl graph shows the γ to δ transformation to be (fig.86). The heating rates employed to study δ formation on continuous heating, cover the range of heating rates encountered in welding processes.

They therefore indicate that δ ferrite formation is unavoidable in some region of the weld HAZ during welding. This fact is confirmed by metallographic studies of real weld HAZ's as the metallographs in figures 29, 30, 73 - 76 show, which cover a wide range of welding processes.

Isothermal heat-treatments, performed over the temperature ranges of 1280°C - 1320°C (class 1) and 1320°C - 1360°C (class 2) will also produce δ ferrite. Values for the TTT results are illustrated in figures 51 (class 2 steel) and 49 (class 1 steel).

δ ferrite is retained on cooling even over a wide range of cooling rates. This is obviously the case in weld HAZ's where δ is retained (see figures 29, 30, 73 - 76) and can be seen to occur by studying the dilatometry recording (see figure 50). Cooling rates which cause decomposition of δ are in the order of $2^{\circ}C\ sec^{-1}$ (see Table 16 and figure 71), cooling rates slower than those found even in electro-slag welding (see figures 66, 67 and 71). Thus, all δ ferrite formed in the HAZ during welding, will be retained to room-temperature. Hence, the quantities of δ ferrite formed in the duplex region and the width of this region will be related to the peak temperature distribution. Hence it should be a function of welding variables and, in fact, an empirical relationship has been found and has also been explored using a statistical analysis technique. The results from real weld HAZ's were compared with each heat input using linear regression analysis, the information given in Table 9 was analysed and a valid relationship was found.

Figure 36 shows this result and the resulting equation shows that heat input (in kilo-joules per m.m.) multiplied by 0.001885 is directly proportional to the δ content (the equation is given in section 3.3.3). Low heat input welds, of say 1000 J $mm^{-1}$, would be expected to have 4.85% δ whilst a high heat input weld of 3000 J $mm^{-1}$ should have 10.5%δ. A further technique, which can be used to predict weld HAZ δ contents, is the empirical experimental relationship which relates time above 1320°C to weld HAZ δ contents. This relationship has been demonstrated practically in section 3.7.2.2. using theoretically predicted weld thermal cycles and, graphically represented, agrees very closely with isothermal transformation data (figure 85). A wide overlap of confidence limits exists between the isothermal and dynamic (weld thermal cycles) data, hence the actual value of the dynamic equation is somewhat uncertain. The relationship expressed in the equation is valid and is useful over a sufficiently wide time scale to cover most welding conditions and processes from TIG to high current submerged arc (see tables 8.9.13.17 and 23).

When δ ferrite forms from austenite heated above the $Ac_4$ temperature, its location and morphology is constant. Early high temperature work showed that δ forms on, and around, prior austenite grain boundaries, this point being made by figures 14 and 15. In weld HAZ's, δ is located in the same places (i.e. on prior austenite grain boundaries and triple points) and this location of δ is found in thermally cycled simulated specimens (see figures 29, 30, 73 - 76).

δ morphology remains constant but is affected by the amount of δ being produced. Its form is always as stringers along prior austenite grain boundaries, all of which radiate from triple points (this morphology is clearly shown by figures 14 and 15). Where small quantities of δ form, its morphology is less stringer like, being found at triple points and having only shallow penetration down austenite grain boundaries, as shown in figures 29 and 30. As the quantity of δ increases so does austenite grain boundary penetration length, the effect being clearly illustrated in real weld HAZ's by comparing figures 74(B) and 75(A). In these two figures δ content rises from 5.6% to 7.9% whilst the shape of δ becomes more elongated. Thus δ is always identifiable by its characteristic shape and position, whether in real weld HAZ's or wrought material subjected to high temperature heat-treatments.

Once δ forms in a weld HAZ it is retained, requiring long time, re-solution heat-treatments to remove, or reduce, its quantity. The parameters for these heat-treatments can be gauged from the information supplied in figures 69 and 71 and Tables 14 and 16. To remove δ completely, heat-treatments similar to full re-solution heat-treatments are necessary (see figure 69). The short time periods for which the matrix is re-austenitised during multi-pass welding thus have no effect on the δ ferrite. During re-austenitisation, austenite grain boundaries are not pinned by δ and some grain boundary movement occurs. No δ retransformation occurs although subsequently some δ regions may be located within prior austenite grains, as shown in figures 102 - 104. Post weld heat-treatments,

often performed to soften commercial welds, are carried out at temperatures below the δ retransformation range and hence, serve only to temper the freshly formed martensite [1,13,26].

When austenite is heated beyond the $Ac_4$ temperature a free-energy driving force exists to cause some austenite decomposition to δ ferrite. The actual production of δ ferrite occurs by elemental diffusion and this process may be recognised in numerous ways. A transformation hysteresis has been identified for both Class 1 and 2 steels, figures 49 and 51 respectively illustrate this occurrence. Isothermal transformation rate of γ to δ has been shown to be a typical "S" type diffusion controlled reaction (see figures 83 and 84) whilst the Johnson-Mehl graph (figure 86) is a linear form with a slope of 3.6. This is the expected shape and approximate slope for diffusion controlled reactions [79]. Direct evidence of the diffusion of some metallic elements into δ ferrite has been obtained. Concentration profiles for chromium, molybdenum and vanadium have shown large increases of these elements in δ ferrite. This information is given in Table 24 and illustrated schematically in figure 87. A carbon denudation zone was also located around δ ferrite regions by microhardness testing and E.P.M.A. analysis, the results of which are also included in table 24 and figure 87.

High resolution electron microscopy was used to examine carbon extraction replicas of both isothermally transformed samples and simulated specimens. Both groups showed similarities

in that small carbide particles were located within the δ ferrite and were positioned in regular arrays parallel to the δ/martensite interface (figures 90 - 93). This mechanism for second phase production is well known and is termed "Interphase precipitation" [86,87,88] and is also known to cause a carbon denudation zone around ferrite [88]. The carbides produced by this process, act as a "sink" for carbon, and absorbs all carbon released from the ferritising area and also some from the surrounding austenite [86]; this mechanism of carbide production and interfacial advance is shown schematically in figure 101 [86].

This δ ferrite formation mechanism operates very rapidly and has been identified in weld simulation specimens and isothermally transformed samples. Figure 90 is taken from a simulated specimen which used 1360°C as peak temperature, whilst figures 91 and 93 were produced from isothermally transformed material. The only differences between the two types is in their physical size i.e. the simulated samples show finer ferrite layers. Both show the layered carbide structure within ferrite and, once more, the simulated sample has a finer structure. It is thus reasonable to assume that this transformation mechanism operates within the weld HAZ where δ is produced, even though times spent at peak temperature may be very short.

One carbide type has been located within δ ferrite and has been shown to exist in two forms. The carbide type is $M_6C$ and has been noted as both $(Cr_3Nb_3)C$ and $Mo_6C$ (see figures 95 - 100), whilst some mixed phase precipitates have been found

(figure 94) which may be mixtures of both carbide forms.

## 4.2 The effect of δ ferrite on solid state transformations in the weld HAZ

Cooling these steels from the homogenous austenite region can result in any one of three solid state transformations occurring depending upon the cooling rate [1,2]. These transformations are i) γ to α + carbides; ii) γ to martensite; and iii) γ to bainite. When a δ/austenite duplex structure is cooled, the only fact that is known is that a bi-phase martensite/δ mixture results (as confirmed by weld HAZ metallography), although the three following further transformations could be possible:- i) δ to γ; ii) δ + γ to α + carbides; and iii) δ + γ to bainite. Consequently experiments were undertaken in which a range of δ contents from 9.7% to 67% were produced in samples and their transformation behaviour monitored by dilatometry. The range of δ contents used, covered all contents likely to be encountered during welding and thus, the CCT and TTT diagrams resulting from this work are applicable to welding situations.

### 4.2.1. TTT studies

Three transformations were investigated in this way and these were a) δ to γ; b) δ + γ to α + carbides; and c) δ + γ to bainite. The γ + δ to martensite reaction was not investigated because martensite production is athermal [79].

The transformation of δ ferrite to austenite was performed isothermally over the temperature range of 1000°C to 1200°C

and reaction times were found to be very similar over a range of 9.7% to 16.6% δ (see figure 68 and Table 15). As δ contents increased above 16.6%, transformation became increasingly delayed (see figure 52). However, such levels (up to 67% δ) are very unlikely to be found in weld HAZ's, thus the two lower levels of δ content (9.7% and 16.6%) can be taken as being representative of welding conditions since welding produces similar δ ferrite levels (see Tables 9 and 14).

Solid phase transformation may occur over a lower temperature range when the mixed structure of δ and γ decomposes to form α ferrite and carbides. The conditions under which homogenous class 2 austenite decomposes to α and carbides are widely known and well documented (see figure 6) [1,2,36,44] and have been determined for this particular material (figure 55). After decomposition, the resulting microstructure consists of α ferrite grains with carbides randomly dispersed throughout the α, and dense carbide films at α grain boundaries (see figures 56 and 57). When a mixed δ + γ microstructure is isothermally transformed, the transformation times again increase as δ content increases. This is shown by Table 12 and figures 58 and 59. Table 15 shows that when two austenitic matrices containing 9.7% and 16.6% δ are isothermally transformed to α ferrite, a retardation occurs once more, but it is only a small amount (see also figure 69). This behaviour, where transformation incubation periods increase with increasing δ ferrite contents, is similar to that of the δ to γ transformation. (A possible mechanism for this retardation will be mentioned later in this section). After transformation, the microstructure of the mixed δ - γ samples is strikingly similar to that of homogenous

austenite samples (compare figures 56 and 57 to 60 and 61). Thus, although the presence of δ markedly affects the transformation kinetics of low temperature austenite decomposition, it hardly affects the resulting microstructure.

Isothermal holding of a mixed δ/austenite structure is likely to happen during the course of multipass welding when a newly deposited weld bead and its HAZ is held at the interpass temperature. This treatment has been thought to cause bainite formation within short time periods at these temperatures (1,4,10,23,42,44,51,63,83) (see figure 5). This was investigated using thermal simulated samples which were not immediately cooled to ambient temperature but were held for eight hours at Ms to Ms + 150°C. The weld simulation sample contained 5.0% δ (thermal cycle for weld T1 was employed) and prolonged holding produced no detectable bainite formation. Thus, the presence of small quantities of δ ferrite retards bainite formation in a simulated weld HAZ. This behaviour is, once more, analogous to that found in the other isothermal decompositions studied.

### 4.2.2. CCT studies

Continuous cooling transformation studies are more applicable to welding situations because welding is a dynamic, non-equilibrium process involving rapid cooling rates. When low peak temperatures were employed (ie between 900°C and 1320°C) an homogenous austenite matrix formed, which on cooling over a wide range of cooling rates, transformed to lath martensite (see figure 12). These results agreed with published data (1), consequently slower cooling rates were not investigated as

published CCT diagrams adequately describe such transformation. When high peak temperatures were employed (ie above 1320°C) quantities of δ were produced, the formation of which is not noted by published CCT diagrams; thus, the existing CCT diagrams become inadequate to describe solid phase transformations on cooling of such matrices.

During cooling, three possible phase transformations may occur. These are i) δ to γ reversion; ii) δ + γ to α + carbides; and iii) δ + γ to martensite + δ . Only one transformation is known to occur in the weld HAZ. This is the formation of the martensite/δ duplex structure (see figures 14 - 18, 29 - 30). The effect of δ on this transformation was examined by producing varying δ quantities in samples (from 2 - 67% δ) and cooling the samples over a range of rates applicable to welding. Increasing δ quantities should have depressed the martensite start (Ms) temperature by predictable amounts (see figures 62 and 63) but no such depression was observed. Later work using δ contents of 4.2% and 16.6% re-emphasised the veracity of these findings (see figures 65 and 71). The solution to this unexpected behaviour was determined later, and is a direct result of the mechanism of δ formation and the consequent carbide production (see figure 101 and section 4.1). Thus, increasing quantities of δ ferrite have no effect on Ms temperature which remains completely invariant.

Two other transformations remained to be observed and no traces of either had been detected over the cooling rates employed for weld simulation (see figures 65-67 and 71).

An estimate of cooling rates likely to cause some transformation of δ to austenite was obtained by super-imposing previously determined TTT results on to a CCT diagram. When this hypothesis was checked it was found to be correct, the results for CCT and TTT being very close (see figure 71). Slower cooling rates also detected the lower temperature decomposition of austenite to α ferrite and carbides and the subsequent Ms elevation (compare figures 5 and 71). This transformation was found to occur under very similar time-temperature conditions whether δ was present or not (compare figures 5 and 71). Thus δ has little or no effect on continuous cooling transformations in these steels when some δ decomposition occurs.

### 4.2.3 Explanation of the possible mechanism of the effects of δ ferrite on TTT and CCT reactions

When δ ferrite forms, it does so on prior austenite grain boundaries and thus reduces the available austenite to austenite grain boundary area on which second phase nucleation can occur. Increasing quantities of δ are accommodated by first broadening the δ stringer and then by extending the stringer length (see figures 29 and 30 and 74B) and 75A)). Hence, increasing quantities of δ reduce the active γ to γ grain boundary area, from which the second phases ( γ or α or carbides) nucleate [79]. No second phase nucleation occurs from the δ/γ interface as a) if it were then reactions would be accelerated and b) the transformation morphologies would commence from the δ/γ interface and not from the γ/γ interface as observed (see figures 56, 57 and 60, 61). During the δ to γ isothermal transformation, decomposition of δ can only commence at the δ/γ interface,

where it does so along specific crystallographic directions (see figures 53,54). Thus, during TTT reactions, the available austenite to austenite interfacial area dominates transformation incubation periods. This is still true during CCT reactions as the transformation of δ to γ shows by occurring over a very similar time and temperature range to TTT reactions (see figure 71). Continued cooling at rates which cause some δ transformation to γ eventually produces α ferrite. This phase formation is not significantly retarded by the presence of δ during continuous cooling, because prior decomposition of some δ to γ effectively increases the available γ/γ interfacial area (c.f. figures 5 and 71). Thus, during slow cooling of a simulated weld HAZ at cooling rates where δ retransformation occurs, subsequent decomposition of γ can be expected under conditions which are predicted by existing CCT diagrams (c.f. figures 5 and 71).

This mechanism has been proposed as a solution to the different transformation behaviour between TTT and CCT conditions. It has not been directly investigated as part of the research programme and has been formulated after a study of resultant transformation microstructures and diagrams.

### 4.2.4 The effects of δ ferrite on phase transformations and their relevance to weld HAZ's

Isothermal transformations are delayed by increasing quantities of δ ferrite, whilst continuous cooling transformations are not, if some δ retransformation occurs. When cooling has been sufficiently rapid to retain all δ (e.g. during welding)

then subsequent diffusion transformations are retarded (e.g. the γ to bainite reaction). Diffusionless transformations i.e. martensite formation, occurs at an invariant temperature unless prior transformation to α ferrite occurs, i.e. during very slow cooling (see figure 71).

After welding, the heat-affected zone cools quickly, the actual cooling rate depends upon the process, plate thickness and welding parameters employed, but always appears to be sufficiently fast to retain all the δ formed (see figures 65,66,67 and 71). Thus, the duplex δ/austenite HAZ region shows only one phase transformation (austenite to martensite) and this occurs at a single, invariant temperature. Interpass holding will not cause bainite formation to occur in the duplex region within 8 hours, nor will stress relieving (see figure 7). The homogenous austenite area, formed at temperatures between $Ac_4$ and $Ac_3$, should undergo transformation to bainite if held at an interpass temperature below 430°C for some time, any remaining austenite may also transform to α ferrite and carbides during stress-relief [1,4,10,23,42,44,51,63,83].

## 4.3 The effect of δ ferrite on physical properties and behaviour

The investigations performed to assess the effect of δ ferrite on mechanical properties were not exhaustive and were limited to tensile, hardness and corrosion tests. The materials used represented the 1360°C isotherm of each simulated weld from T1 to S2 and martensite, secondary hardened (ie the 750°C isotherm simulations) and standard state materials. No efforts

were made to extend the findings beyond the δ ferrite levels tested (4.2 to 8.4 % δ) nor were real HAZ's tested, except for hardness comparisons.

### 4.3.1 The results of tensile tests

Three interesting series of results are quickly discernible from tensile tests, these are i) ductility; ii) yield point and iii) ultimate tensile strength, the results of which are illustrated in Table 18. Ductility can be measured by reduction in area and elongation during tensile testing, highly ductile materials show large values of both properties. Thus, when samples containing over 5% δ were tested, ductility was seen to fall, until at about 8% δ samples failed in an almost totally brittle manner (less than 5% elongation and reduction in area) (see figure 77). Extrapolation of the line for % elongation in figure 77 indicates that 12% δ would produce total embrittlement. This phenomena has been previously noted but these results were confined to only impact testing and showed that where δ is present transition temperature elevates, hence, the material becomes embrittled [1,26].

Throughout the range of δ contents investigated, a progressive increase in UTS values appeared as δ contents rose. Homogenous martensite (0%δ) had a UTS of 1.7205 KN whilst sample S2 (8.4%δ) had a UTS of 2.048 KN (see Table 18). At high δ contents (8%+) the increase in UTS is of the order of 20%. Yield point is similarly affected but not to such a high degree

and shows little effect due to the levels of δ ferrite (see Table 18). Elevation of tensile strength has been previously noted in real weld HAZ's [1,37] but has not been explained. That the effect is repeated in simulated HAZ's, where thermal gradients and microstructural differences are not as severe as in real HAZ's, infers that the increase in strength is due to the production of finely dispersed δ regions. A possible explanation for this behaviour is the mechanism of dispersion strengthening, a well documented process[47,79,87, 100, 102].

Many uses of these materials require a degree of corrosion resistance from the steel in the welded form. Corrosion tests were performed on 1360°C isotherm weld simulation samples for welds T1 to S2, homogenous martensite, secondary hardened and standard state materials. The results showed that corrosion rate was minimal in the homogenous martensite material, but the rate increased steadily with increasing δ content from 4.2% to about 8% δ (see figure 78 and Table 19). Above 8%δ, corrosion rates increase dramatically and approach the levels of tempered and secondary hardened materials. The upper and lower corrosion limits are theoretically quite sound. When chromium and molybdenum are completely in solution (Homogenous martensite) corrosion rate is minimal, but when quantities of these elements exist as carbides, corrosion rates increase [47]. Where free δ ferrite exists, however, corrosion rates may be expected to fall, due to chromium and molybdenum activity in ferrite [90], but this does not happen. A possible explanation is that regions of δ ferrite are areas of high chromium concentration (greater than 15% Cr) in a

matrix of below 12% Cr, thus, the matrix becomes anodic with respect to δ and preferentially corrodes. Therefore, real HAZ's will show increased corrosion resistance in the homogenous martensite region and increased attack in the secondary hardened and duplex zones.

Weld HAZ hardnesses are reduced where δ is present, the effect being more clearly indicated by macro-hardness testing than by microhardness tests. Table 20 shows that little difference exists between real and simulated HAZ microhardness values, but as δ increases, simulated sample macro-hardnesses fall. This effect occurs because the macrohardness indenter is much larger and thus tests larger areas of sample and is more affected by the lower hardness of δ ferrite. Hardness surveys performed across real weld HAZ's, also show hardness values in the duplex region below that of the homogenous martensite zone. This feature is visible in figures 26, 27, 28, 32, 33, 34, and 35. Initially there may appear to be some conflict between the hardness results and results from tensile testing as δ reduces hardness but increases yield point and UTS. A possible explanation to this anomaly is that because δ is finely dispersed throughout the martensitic matrix, its present dispersion strengthens the steel on tensile testing. Hardness tests, however, examine small regions and thus the softening effect of δ is determined.

δ ferrite has been noted to have an effect on HAZ crack path [7,9,12,14] and these studies indicated that the failure route was allied to δ ferrite shape (see figures 16-18).

All cracks examined, whether from commercial or experimental sources, were found to remain in duplex microstructural regions (see figures 19,20,31). The region through which all cracks passed, seems to be the low carbon-molybdenum martensite halo which surrounds δ and is formed as a function of δ ferrite production (see sections 3.7.3.2 and 4.1). Behaviour of this type is typical of a stress concentrating mechanism [102], thus HAZ fractures do not appear to require hydrogen in order to occur. This finding, although not conclusive, opposes previous investigators who believe that HAZ cracks in these steels are exclusively hydrogen induced [1,4,7,13,36,40,42,44,48,51,52,53]. The proposed mechanism may be affected by hydrogen, and may even be a subtle modification of hydrogen induced HAZ cracks, but its effect is to crack sensitise the steel to a greater degree than hydrogen. As δ is unavoidable in weld HAZ's the only way to avoid cracking is to reduce, or remove, stress concentrations which initiate failures [40] (see section 3.3.1 and figures 19,21 & 31). This approach has been shown to be valuable in reducing weld bead cracking in filler metals of these compositions, where δ has once more been shown to be involved in the failure route [101].

## 4.4 The microstructure of the weld heat affected zones in Super 12% Cr Mo steels

During the course of this project the vast majority of work has been concerned with the microstructure of weld heat-affected zones, both real and thermally simulated. The production of thermally simulated HAZ's has allowed high

speed dilatometry to be performed and thus has aided in the production of representative welding CCT diagrams. Comparisons have been performed between real and simulated HAZ microstructures. Hence, the inter-relation between real HAZ's, simulated HAZ areas and the CCT diagrams presented has been determined.

### 4.4.1 Real weld HAZ microstructures

The production of a HAZ region containing δ ferrite has been shown to be unavoidable during fusion welding, representative zones are shown in figures 16-18,29,30 and 73-76. This produces a three region HAZ, schematically shown in figure 8, in which the duplex δ/martensite area lies close to the weld fusion line, the homogenous martensite region occurs outside the duplex area with a secondary hardened zone finally being formed. A typical HAZ is shown in figure 31, the darkly etched region being the secondary hardened area.

The formation of each HAZ region is controlled by the temperature experienced in that region. Duplex microstructures form when temperatures exceed $Ac_4$, whilst the homogenous martensite region remains between $Ac_4$ and approximately 900°C (see figures 12,50,51). These dilatometric findings were verified when heat flow equations were fitted to single run weld HAZ microstructures and hardness surveys (figures 28,79,80,81,82). When the heat flow approach was utilised, it was found that regions containing δ were formed between 1320°C and fusion point (1420°C), homogenous martensite existed in the 1320°C to 900°C region whilst secondary hardened areas formed between

900°C and 500°C, below 500°C no microstructural or hardness changes were noted (see figures 79-82). Thus, for a single pass unpre-heated weld HAZ, the phase boundaries readily define peak temperature isotherms.

Pre-heating does not affect the microstructural composition of a single pass weld HAZ, although it does increase the extent of all three regions besides further softening the parent material (see figures 24 and 27). Therefore, for any given heat input, pre-heated weld HAZ's are wider than unpre-heated ones, although consisting of the same microstructural regions (see figures 27 and 28). Post weld heat-treatment, when performed at 600°C for 2 hours [1,4,13,16,36,37,38,40,41,42,44,51], increases HAZ ductility by tempering the freshly formed martensite in the duplex and homogenous martensite regions (see Table 7). These heat-treatments perform the same function for both unpre-heated and pre-heated weldments (see Table 7).

Multi-run welds were subjected to only an exploratory investigation (see section 3.3.2) but it emerged from this that multi-pass HAZ's were complicated structures. Much of the complication results from the position of upper weld beads, which changes the thermal conditions experienced by the lower HAZ's. However, it was possible to say that the first run on a HAZ caused tempering of some fresh martensite in close proximity to the secondary hardened layer, whilst re-austenitising all the rest of the HAZ. During re-austenitisation, austenite grain boundaries move and surround $\delta$ although no $\delta$ decomposition occurs (as illustrated in figures 102-104).

The second weld bead caused all the martensite re-formed in the initial bead to be tempered, whilst causing the previously described changes in the first run HAZ. This process continues until welding is finished. The underlaying HAZ's become increasingly tempered and the final run shows the usual three zone structure of an untempered weld HAZ.

The secondary hardened zone is formed as a result of low peak temperatures, insufficiently high to cause phase transformations, which are experienced for only a short time (see sections 3.2.3, 3.5.3.1, Table 4). Hardening occurs because of $M_2X$ phase production in the already tempered material. This phase, although not visible by optical microscopy, has been previously identified [1,2].

The absence of bainite in any microstructures examined is contrary to the expectations of previous authors [1,44,51]. Its formation was never noted even on long, low temperature isothermal holding (section 3.7.3.3) and was probably retarded by the presence of δ ferrite (section 4.2.1)

### 4.4.2 Continuous cooling transformation diagrams

Two of the three heat-affected regions in the weld HAZ undergo phase transformation, whilst the third (secondary hardened) does not. The two regions undergoing phase changes both transform to austenite on heating but one (the duplex region) endures a further transformation. Two CCT diagrams are, therefore, required to describe weld HAZ microstructures

completely. The region which forms homogenous martensite must be described by a CCT diagram produced from steel heated to temperatures between 900°C and 1320°C (see section 4.4.1). Many diagrams exist which have been produced from steel austenitised within this temperature regime, and a previously published example is given in figure 5. A CCT diagram was produced for the experimental Class 2 material, during the course of this project (figure 12) and agrees with the previously published diagram.

The duplex region consisting of δ ferrite and martensite has never been previously described by a CCT diagram. Therefore, the diagrams produced by this work are the only ones suitable for describing the effects of high temperature heat-treatments on these steels (figures 65 and 71). The first diagram (figure 65) is exclusively for welding. Figure 71, however, includes this information and also illustrates subsequent phase transformations which occur during slow cooling. Thus the information provided by this diagram is unique in its description of phase transformations undergone by mixed γ/δ matrices during continuous cooling. CCT diagrams currently accepted, and in use, describe only the homogenous martensite region and do not mention the duplex δ/martensite region which has been shown to influence weld HAZ properties.

Weld HAZ microstructure in the high temperature region can be predicted by either of the two CCT diagrams produced in this work (figure 65 or 71), although the former is exclusively for welding. This diagram predicts that a region containing δ

ferrite will exist in fusion welds produced by any process although it does not predict the extent of ferritisation or the width of the duplex zone. Allied techniques in the production of welding CCT diagrams can be used to determine HAZ region widths and quantities of ferrite formed. The theoretical numerical process used to determine weld thermal cycles has been shown to be accurate in describing weld HAZ widths (see figures 79-82 and Appendix 2 ). The theoretical results are presented as a 3-dimensional temperature-dimension matrix, which, when analysed as in Appendix 2 , determines peak temperature loci for the whole HAZ region. Thus, HAZ width and the spatial position of each constituent region can be found to a reasonable degree of accuracy (see figures 79-82).

The quantities of $\delta$ ferrite which form during welding may be determined directly from the predicted theoretical weld thermal cycle. An empirical relationship has been formulated, and validated, in which the time spent above a temperature of 1320°C is related to the quantity of $\delta$ ferrite found at the 1360°C isotherm (see figure 85 and section 3.7.2.2). This technique appears to be applicable for a wide range of "super 1320°C" transformation times and therefore, for a wide range of welding heat inputs. The relationship between heat input, time at temperature and quantity of second phase formed has been investigated [illegible] and has been theoretically validated.

### 4.4.3 Correlation of real HAZ's, simulated HAZ's and the prediction of CCT diagrams

Real HAZ's and simulated HAZ's are best correlated by metallographic and hardness correlations [58,59,60,61]. This has

been performed with the emphasis on the 1360°C isotherms of both real and simulated samples and has demonstrated that a close correlation exists between the two types (see figures 73 to 76 and Table 20).

The CCT diagrams (figures 65 and 71) were produced from dilatometric studies performed during thermal simulation of the 1360°C isotherms of real weld HAZ's. Thus, the predictions of these diagrams directly illustrate the phase transformations occurring in the 1360°C peak temperature simulation samples (see figure 65). Microstructural and hardness correlation has been shown between real and simulated samples, therefore, implicit correlation exists between the CCT diagrams and real HAZ microstructures. Real HAZ microstructures can, therefore, be predicted by either CCT diagram produced (figures 65 and 71) when used in conjunction with published CCT diagrams which describe the martensite region (figure 5),. The extent and location of each zone can be determined by theoretical numerical methods (Appendix 2 and figures 73-76 and Table 20).

It has therefore been demonstrated that the HAZ of single pass welds consists of the following three zones, δ/martensite duplex structure, homogenous martensite and a secondary hardened region. The microstructure of the transformed zones has been described and can be predicted by the CCT diagrams produced during this work. HAZ width and individual region size and location is dependant on peak temperature distribution and hence, the heat input per unit length employed during welding (48,66,67). This parameter has been linked in two ways to the amount of δ ferrite produced in the duplex region (figures

36 and 85) and this relationship has been theoretically demonstrated (appendix 1). Thus, the prediction of microstructure and the extent and location of each weld HAZ region of a single pass weld can be carried out.

In multi-run welds, the freshly formed martensite in both duplex and homogenous martensite regions is progressively tempered and secondary hardened. The δ ferrite formed by the initial weld run remains untransformed, although temper carbides may form within it [26], thus, a further region will eventually form which consists of δ ferrite dispersed within a matrix of tempered and secondary hardened martensite.

## 4.5 Practical implications of this study

All the points of greatest significance in the assessment of HAZ microstructure and behaviour are concerned with the role played by δ ferrite. This phase always forms in regions close to the weld fusion line during fusion welding thermal cycles. It remains untransformed in the HAZ despite the usual post-weld heat-treatment cycles. The formation of δ ferrite is unavoidable during fusion welding and it is always present in the HAZ along with all the associated harmful effects. Its prevention is difficult and would probably require welds to be performed by solid phase welding techniques. These processes are, however, not as flexible in their joint design as is fusion welding and therefore will not completely replace fusion welding. Development of totally martensitic Super 12% Cr Mo filler metals has been successful, some types of these now being in use [1,6,7,8,9,10]. Thus, similar compositions could be employed as

parent material to prevent δ ferrite formation in the HAZ. Such an idea is, however, speculative.

It must be accepted that fusion welding will always produce quantities of δ ferrite in steels of this composition. Efforts should, therefore, be made to control the amount of δ ferrite in, and the width of, the HAZ. Techniques have been investigated which enable the amount of δ ferrite in the HAZ to be controlled. One is to use the heat input per mm of weld to govern the quantity of ferrite forming. This relationship is illustrated in figure 36 and from this chart it can be seen that low heat input produce small quantities of δ ferrite and as heat inputs rise so do δ ferrite levels. The second technique for δ ferrite control is to manipulate the time spent above 1320°C during welding (see figure 85). This technique, although more accurate than the previous one, is more difficult to apply and requires some means of forecasting weld cooling rates. It is implicit in this method that control is exercised by varying heating and cooling rates above 1320°C. This is, in fact, control by heat-input, thus both techniques are complementary and related. Their common basis having been illustrated by the work of Appendix 1.

Control of δ ferrite should be aimed at producing about 5% δ in the HAZ; less than this requires such low heat-inputs that welding is difficult, whilst more than this causes substantial degradation of mechanical properties (see figure 77). To do this, heat inputs of a maximum of 1.5KJ $mm^{-1}$ are required (from figure 36). This, therefore, suggests that low power

TIG and MIG welds should be used to join these steels; thus, to join thick sections, multi-run welds would be required. The use of low power TIG or MIG welding would ensure that small quantities of δ ferrite were produced and that the resulting weld HAZ was narrow, thus confining the potentially troublesome material to a small region. Such techniques are disadvantageous from the fabrication time aspect. The value of δ control must, therefore, be weighed against the increased welding time and cost.

Weld HAZ widths have been accurately predicted by using the computer program given in Appendix 3. This program confirms that low heat input welds (e.g. welds T1, T2, M1 and M2) have small HAZ dimensions and high HAZ cooling rates. Rapid cooling rates are advantageous in keeping δ ferrite contents low (see Appendix 1 and figure 85). Traditionally, slow cooling rates are preferred for alloy steels to prevent martensite formation. Thus, when welding hardenable material, high heat input welds and pre-heating are used. This approach is disadvantageous with this steel from two respects. High heat input welds increase δ content and enlarge the HAZ, whilst pre-heating similarly widens the HAZ (see figures 26 and 27) and will increase the amount of δ ferrite produced. In this steel, the slow cooling rates produced by pre-heating (or high heat input welding) are insufficient to prevent martensite formation; thus, they can only increase the quantity of δ ferrite formed in the HAZ. Most experimental welds were produced from unpre-heated steel and were found to be quite sound. Bend testing of both pre-heated and unpre-heated welds, showed that pre-heated welds were a little more ductile

than unpre-heated welds whilst neither type had HAZ cracks (see Table 7).

Where HAZ cracks were found, it was noticed that they all initiated from stress raising defects within the HAZ (see figures 19, 20 and 31). This finding is of some importance, because if stress raising defects are removed then cracks will not be able to initiate within the duplex HAZ region. This fact is valuable in practical welding situations. Such defects are an easy parameter to control and are one's which have a significant effect on weldment quality.

All results have been obtained for one particular Super 12% Cr Mo steel and, as such, are accurate only for that particular steel. However, the similarity between this Class 2 steel and a simpler Class 1 steel has been demonstrated for $\delta$ ferrite formation (see figures 49 and 51) and for the invariability of Ms temperature with increasing $\delta$ ferrite contents. Thus, in many reactions, the two different classes may be expected to behave similarly. The principle results, therefore, determined by this work should be generally applicable to the whole range of Super 12% Cr Mo steels. Transformation temperatures will vary from material to material and certainly from class to class, but the general principles expounded in this work should be applicable to all steels in the Super 12% Cr Mo classification.

# CHAPTER FIVE

# CONCLUSIONS

## CHAPTER FIVE CONCLUSIONS

5.1 Some quantities of δ ferrite always form in Class 2 Super 12% Cr Mo steels in regions of the HAZ where peak temperatures have exceeded the $Ac_4$ temperature. On cooling this ferrite is retained to room temperature, untransformed. The threshold temperature for δ ferrite formation varies from 1320°C, on slow heating rates (about 8 - 10°C $s^{-1}$) to 1360°C during rapid heating ($\geq$ 300°C $s^{-1}$). Therefore δ is always present in weld HAZs.

5.2 δ forms at austenite grain boundaries by a diffusion process involving Cr, Mo, V and C and is retained in this position, to room temperature, over a wide range of cooling rates. It exists unaffected in weld HAZ's despite subsequent post weld heat-treatments.

5.3 The amount of δ ferrite formed increases as both peak temperature and transformation time advance. The quantities of δ ferrite formed during welding may be calculated from the time that the 1360°C peak temperature region spends above 1320°C by using an empirical relationship determined during this work. Hence, δ quantities forming in the weld HAZ can thus be estimated from a knowledge of weld thermal cycles.

5.4 The presence of up to 16.6% δ ferrite in an austenitic matrix does not affect subsequent decomposition

of γ to form α + carbides during continuous cooling. Quantities of up to 67% δ do not affect Ms temperature in either Class 1 or 2 steel. The martensite transformation begins at the invariant temperature of 323°C for Class 1 steel and 275°C for Class 2 materials.

5.5 The presence of δ in an austenite matrix retards isothermal decomposition of austenite to α ferrite and carbides. Bainite formation, at temperatures between 275°C to 400°C, is also retarded by the presence of δ.

5.6 The properties and behaviour of weld HAZ's are affected by the presence of δ. When quantities of δ increase, ultimate tensile strength, yield point and corrosion rate rise, whilst hardness and ductility fall. Presence of δ ferrite reduces the HAZ tolerance to weld defects and thus increases the risk of HAZ cracking.

5.7 A CCT diagram has been produced using standard thermal cycles, which involved heating to 1360°C in 6 seconds, holding at this temperature for either 0.5 or 2 seconds (which produced 9.7% δ and 16.6% δ respectively), followed by cooling at various rates. These boundary conditions have been shown to be adequate to describe phase transformations occurring in a series of HAZ's produced by a wide range of welding processes.

5.8 It has been demonstrated that the microstructure and properties of thermally simulated and real HAZ's are in good agreement. High peak temperature regions (ie 1360$^{o}$C peak temperature isotherms) in both real and thermally simulated HAZ's had similar quantities, shapes and distributions of $\delta$ within a martensitic matrix. Low peak temperature areas (ie 750$^{o}$C peak temperature isotherm) in both types of HAZ's contained identical carbide forms in similar dispersions. Hardness values between real and simulated HAZ's, of both high and low peak temperatures, are comparable.

# CHAPTER SIX

# RECOMMENDATIONS FOR FURTHER WORK

## CHAPTER SIX RECOMMENDATIONS FOR FURTHER WORK

6.1 An overall effect of δ on weld HAZ cracking susceptibility has been indicated by this work, although a quantitative effect of δ has not been demonstrated. An investigation based on fracture mechanics could determine the effects of δ quantity, morphology and distribution on weld HAZ toughness. Results from this work would enable standards of acceptable δ contents to be established for weld HAZ's.

6.2 Weld HAZ cracks initiate from stress concentrations within the HAZ and propagate through the duplex HAZ region. A study of the effects of weld bead profile, weldment fit-up and weld penetration variables on the HAZ cracking propensity of these steels could be of use. The results of this study would be of significance to fabricators and would aid them in increasing weldment quality.

6.3 Super 12% Cr Mo steels are most frequently used in high temperature oxidation resistant applications. However, welding has been shown to produce regions of reduced corrosion resistance, thus, premature failures may occur within the HAZ during service. This possibility could be studied by a combined creep and corrosion test, using weldments containing differing δ quantities and tested at operating temperatures and stress levels in harsh gaseous industrial environments.

6.4 Variab SS, the computer program modified specially for these steels, has been shown to produce accurate weld HAZ thermal predictions. Further modifications are possible and may result in weld HAZ hardness values being predicted. If this were done, the newly modified program would form a useful quality control tool.

6.5 The present applications of Variab and its derivatives are limited to use on un-preheated welds and thus, in this form are unsuitable for many applications. A project to modify the program to deal with pre-heated situations and experimentally verify the computed results would be of wide use. Suitably modified thus, Variab would be available as a more accurate research technique.

# TABLES

TABLE 1

Classification of Super 12% Cr Mo steels by either composition or operating temperature

a) by composition

| CLASS NO | % Alloying elements present | | | | | | |
|---|---|---|---|---|---|---|---|
| | C | Cr | Mo | Ni | V | W | Co |
| 1 | .1-.2 | 12-13 | .25-1.0 | 1.0 | - | - | - |
| 2 | .1-.3 | 11-13 | 0.1-1.2 | 1.0 | .25-1 | 0.5-3 | - |
| 3 | .1-.3 | 10-13 | 0.5-5.0 | .3-2.7 | .2-1 | .4-1 | 2-13 |

b) by maximum operating temperature

| CLASS NO | MAXIMUM CONTINUOUS OPERATING TEMPERATURE ($^{o}C$) | COMMENTS |
|---|---|---|
| 1 | 510 | |
| 2 | 595 - 620$^{+}$ | Highly alloyed$^{+}$ |
| 3 | 625 -650$^{*}$ | Predicted $^{*}$ |

(both tables from reference 1)

TABLE 2

Chemical composition of Classes 1 and 2 steels used throughout the research

| | C | Si | Mn | P | S | Cr | Mo | Ni | V | Nb | HEAT TREATMENT |
|---|---|---|---|---|---|---|---|---|---|---|---|
| CLASS 1 (FIRTH VICKERS MOLYBDENUM STAINLESS STEEL) | 0.09 | 0.30 | 0.46 | 0.017 | 0.016 | 12.39 | 0.61 | 0.55 | - | - | 1 hour at 1000°C, OQ, 2hrs at 640°C |
| CLASS 2 MANNESMANN STAHL F12 | 0.21 | 0.24 | 0.47 | 0.012 | 0.009 | 11.30 | 0.96 | 0.78 | 0.29 | 0.11 | 1 hour at 1050°C, OQ* 2 hrs at 650°C |

* OQ = Oil quench

TABLE 3

Composition of Adlers Reagent

Stock solution, made of:-

| | |
|---|---|
| 150 grammes | Ferric Chloride |
| 30 grammes | Copper ammonium chloride |
| 500 cc's | Conc. hydrochloric acid |

Made to 1 litre with distilled (or de-ionized) water.

Dilute 2 - 4 times immediately before use.

TABLE 4

Secondary hardening treatments and hardness values for Class 2 steel

| H.T. TEMP ($^{o}$C) | TIME (MINS) | INITIAL HARDNESS Hv | FINAL HARDNESS Hv | INCREASE Hv |
|---|---|---|---|---|
| 400 | 5 | 385 | 402 | 17 |
| 451 | 5 | 385 | 410 | 25 |
| 470 | 5 | 396 | 437 | 41 |
| 501 | 5 | 385 | 460 | 75 |
| 544 | 5 | 385 | 483 | 98 |
| 606 | 5 | 396 | 505 | 109 |
| 401 | 60 | 396 | 414 | 15 |
| 446 | 60 | 396 | 429 | 33 |
| 468 | 60 | 385 | 444 | 59 |
| 497 | 60 | 396 | 459 | 63 |
| 554 | 60 | 385 | 411 | 26 |
| 615 | 60 | 385 | 314 | -71 |

TABLE 5

Composition of weld metal filler wire and small diameter tubes used to determine the effects of pre-heating on weld crack susceptibility

| | C | Si | Mn | P | S | Cr | Mo | Ni | V | Nb | W |
|---|---|---|---|---|---|---|---|---|---|---|---|
| 1.6 mm dia. WIRE (Bohler 20 MV.W - IG) | 0.20 | 0.15 | 1.75 | NQ | NQ | 12.0 | 1.0 | NQ | 0.35 | 0 | 0.50 |
| 38mm O.D. TUBE (Sandvik HT9) | 0.21 | 0.37 | 0.48 | 0.023 | 0.007 | 11.2 | 1.0 | 0.52 | 0.30 | 0.01 | 0.02 |

NQ = Not Quoted

TABLE 6

Welding conditions used to produce small tube welds

| | ARC VOLTAGE (volts) | ARC CURRENT (amps) | WELDING SPEED ($m.m.s^{-1}$) | WELDMENT REVOLVING SPEED (r.p.m) | WELDMENT DIAMETER (m.m.) | WIRE FEED SPEED ($m.m.s^{-1}$) |
|---|---|---|---|---|---|---|
| 1 PASS (ROOT RUN) | 11 | 140 | 2.7 | 3 | 25.6 | 20 |
| 2 PASSES (FILLING PASS) | 12 | 147 | 2.2 | 2.5 | 28 | 23 |
| 3 PASSES (FILLING PASS) | 12 | 150 | 3.0 | 1 | 29 | 25 |
| 4 PASSES (CAP PASS) | 12 | 150 | 3.5 | 1 | 32 | 25 |

TABLE 7

Results of bend testing 1-4 run welds, in the as welded and post weld tempered conditions

| WELD NO | AS WELDED | | TEMPERED | |
|---|---|---|---|---|
| | BEND ANGLE TO FAILURE (°) | WELD FAILURE POSITION | BEND ANGLE TO FAILURE (°) | WELD FAILURE POSITION |
| 1 | 10 | w.b. | 60 | Ductile HAZ |
| 1 | 55 | Ductile HAZ | 90 | unbroken |
| 2 | 34 | w.b. | 40 | w.b. |
| 2 | 20 | w.b. | 90 | unbroken |
| 3 | 30 | w.b. | 90 | unbroken |
| 3 | 20 | w.b. | 90 | unbroken |
| 4 | 44 | w.b. | 75 | w.b. |
| 4 | 30 | w.b. | 10 | w.b. |
| 5 | 30 | w.b. | 90 | unbroken |
| 5 | 40 | w.b. | 90 | unbroken |
| 6 | 32 | w.b. | 90 | w.b. |
| 6 | 20 | w.b. | 90 | w.b. |
| 7 | 10 | w.b. | 75 | w.b. |
| 7 | 15 | w.b. | 30 | w.b. |
| 8 | 5 | w.b.(2nd run) | 70 | w.b. |
| 8 | 60 | Ductile HAZ | 15 | w.b.(2nd run) |

KEY:- Welds 1-4, unpreheated 1-4 runs respectively
Welds 5-8, pre-heated 1-4 runs respectively
w.b. = failure through weld bead.

TABLE 8

Welding parameters employed to produce the thick plate welds

| WELDING PROCESS EMPLOYED | WELD IDENTITY | WELD VOLTAGE (V) | WELD CURRENT (A) | WELD SPEED ($m.m.s^{-1}$) | SHIELDING MEDIUM |
|---|---|---|---|---|---|
| T.I.G (A.C.) | T1<br>T2 | 20<br>17.5 | 292<br>370 | 2<br>3 | Argon at 28.5 $ls^{-1}$<br>Argon at 42.8 $ls^{-1}$ |
| M.I.G (D.C. electrode +) | M1<br>M2 | 36<br>37 | 256<br>250 | 4<br>5 | Argon at 30 $ls^{-1}$<br>Argon at 30 $ls^{-1}$ |
| M.M.A.(D.C. electrode +) | R1<br>R2 | 29.5<br>31 | 253.3<br>296.7 | 2.5<br>3.25 | Basic Electrode[38]<br>Dried at 250°C - 2 hrs |
| SUB-ARC (D.C. electrode +) | S1<br>S2 | 37.5<br>44.5 | 326.7<br>353.3 | 5<br>5 | Neutral Flux[41]<br>Dried at 300°C - 6 hrs |

TABLE 9

Heat input for each thick plate weld and amount of δ formed in the HAZ during welding

| WELD No | WELD VOLTAGE | WELD CURRENT | WELD SPEED | ARC EFFICIENCY FACTOR % | HEAT INPUT ( $m.m.^{-1}$ ) | δ CONTENT (%) |
|---|---|---|---|---|---|---|
| T1 | 20 | 292 | 2 | 32 | 934 | 5.0 |
| T2 | 17.5 | 370 | 3 | 32 | 690.67 | 4.6 |
| M1 | 36 | 256 | 4 | 60 | 1555.2 | 4.2 |
| M2 | 37 | 250 | 5 | 60 | 1249.12 | 5.6 |
| R1 | 29.5 | 253.3 | 2.5 | 75 | 2249.6 | 7.9 |
| R2 | 31 | 296.7 | 3.25 | 75 | 2122.3 | 6.4 |
| S1 | 37.5 | 326.7 | 5 | 95 | 2329.5 | 8.2 |
| S2 | 44.5 | 353.3 | 5 | 95 | 2986.84 | 8.4 |

TABLE 10

Replicate tests of centre and surface temperature distribution for 3 steady temperatures, performed for simulation sample calibration

| PROGRAMMED TEMPERATURE (°C) | THERMOCOUPLE POSITION | RECORDED TEMPERATURE (°C) | | |
|---|---|---|---|---|
| | | SAMPLE 1 | SAMPLE 2 | SAMPLE 3 |
| 1100 | SURFACE | 1140 | 1130 | 1130 |
| | CENTRE | 1135 | 1140 | 1120 |
| 1200 | SURFACE | 1225 | 1220 | 1213 |
| | CENTRE | 1215 | 1222 | 1210 |
| 1300 | SURFACE | 1317 | 1317 | 1310 |
| | CENTRE | 1300 | 1320 | 1295 |

TABLE 11

Effect of heating rate on $Ac_1$ and $Ac_3$ phase transformation temperatures in Class 1 steel

| TIME TO HEAT TO 1000°C (Secs) | HEATING RATE ($^{o}Cs^{-1}$) | $Ac_1$ TEMP ($^{o}C$) | $Ac_3$ TEMP ($^{o}C$) |
|---|---|---|---|
| 6 | 166.7 | 908 | 956 |
| 9 | 111.1 | 850 | 897 |
| 15 | 66.7 | 847 | 865 |
| 30 | 33.3 | 843 | 890 |
| 37.5 | 26.7 | 830 | 886 |
| 60 | 16.7 | 830 | 865 |
| 100 | 10.0 | 830 | 869 |
| 120 | 8.3 | 830 | 857 |

TABLE 12

Isothermal transformation times for both γ and γ + δ to form α + carbide

| HOMOGENOUS AUSTENITE | | | | | MIXED AUSTENTIE AND δ FERRITE (67% δ) | | | | |
|---|---|---|---|---|---|---|---|---|---|
| TRANSFORMING TEMPERATURE (°C) | TIME TO START | | TIME TO COMPLETION | | TRANSFORMING TEMPERATURE (°C) | TIME TO START | | TIME TO COMPLETION | |
| | SECONDS | HRS MINS | SECONDS | HRS MINS | | SECONDS | HRS MINS | SECONDS | HRS MINS |
| 676 | 17,560 | 4 . 55 | 49,020* | 13 . 25 | 586 | 87,660 | 24 . 21 | | |
| 702 | 13,920 | 3 . 52 | 41,700 | 11 . 35 | 609 | 22,260 | 6 . 11 | 38,880 | 10 . 48 |
| 720 | 7,740 | 2 . 09 | 12,540 | 3 . 29 | 665 | 21,240 | 5 . 54 | 34,620 | 9 . 27 |
| 752 | 4,080 | 1 . 08 | 7,320 | 2 . 02 | 683 | 12,360 | 3 . 26 | 25,140 | 6 . 59 |
| 770 | 3,350 | 0 . 55.8 | 6,850 | 1 . 54 | 706 | 9,300 | 2 . 35 | 11,280 | 3 . 08 |
| 795 | 780 | 0 . 13 | 4,140 | 1 . 09 | 732 | 6,240 | 1 . 44 | 7,380 | 2 . 08 |
| 825 | 2,450 | 0 . 40.8 | 22,000 | 6 . 06.6 | 753 | 51,660 | 14 . 21 | | |
| 860 | 54,180 | 15 . 3 | 86,400* | 24 . 00 | | | | | |

* TRANSFORMATION INCOMPLETE

TABLE 13

Welding parameters employed for the numerical solution of weld thermal cycles for high heat input submerged arc and electro-slag welding processes.

| WELDING PROCESS | ARC TIME (secs) | PLATE THICKNESS (cms) | WELD VOLTAGE (v) | WELD CURRENT (A) | ARC TRAVEL SPEED ($cms^{-1}$) | ARC EFFICIENCY FACTOR |
|---|---|---|---|---|---|---|
| SUB - ARC | 60 | 2.5 | 30 | 1125 | 0.6 | 0.99 |
| ELECTRO - SLAG | 250 | 9.0 | 60 | 1800 | 0.1 | 0.99 |

TABLE 14

Times for isothermal decomposition of $\delta$ to austenite using two pre-selected levels of $\delta$

| 9.7 % $\delta$ | | | 16.6 % $\delta$ | | |
|---|---|---|---|---|---|
| ISOTHERMAL TEMPERATURE ($^{o}C$) | TRANS-FORMATION START (secs) | TRANS-FORMATION FINISH (secs) | ISOTHERMAL TEMPERATURE ($^{o}C$) | TRANS-FORMATION START (secs) | TRANS-FORMATION FINISH (secs) |
| 1213 | 126 | 1760 | 1206 | 220 | 1474 |
| 1141 | 141 | 970 | 1152 | 126 | 1026 |
| 1104 | 150 | 640 | 1095 | 180 | 792 |
| 1060 | 740 | 1690 | 1066 | 701 | 2990 |
| 1008 | 1050 | 1630 | 1019 | 780 | 3200 |
| 957 | 1345 | 2670 | 1008 | 1148 | 3542 |

TABLE 15

Transformation start time for the $\gamma + \delta$ to $\delta + \alpha$ + carbide isothermal transformation of two austenite - $\delta$ ferrite matrices

| HOLDING TEMP ($^{o}C$) | 9.7% $\delta$ | | 16.6% $\delta$ | |
|---|---|---|---|---|
| | SECONDS | HRS MINS | SECONDS | HRS MINS |
| 660 | 18,600 | 5 . 10 | 19,300 | 5 . 21.6 |
| 720 | 7,950 | 2 . 12.5 | 8,267 | 2 . 17.75 |
| 765 | 3,670 | 1 . 10.1 | 4,990 | 1 . 23.3 |
| 810 | 1,500 | 0 . 25 | 1,774 | 0 . 29.5 |
| 855 | 55,000 | 15 . 16.6 | 58,000 | 16 . 06.6 |

TABLE 16

Continuous cooling phase transformation temperatures obtained by slow cooling sample of 2 δ ferrite levels

| TRANSFORMATION | TRANSFORMATION TEMP. with 9.7% δ | | | | | TRANSFORMATION TEMP. with 16.6% δ | | | | |
|---|---|---|---|---|---|---|---|---|---|---|
| | A | B | C | D | E | A | B | C | D | E |
| δ finish | 1324 | 1320 | 1320 | 1321 | 1318 | 1320 | 1321 | 1320 | 1319 | 1319 |
| δ → γ start | 1120 | 1170 | 1220 | 1243 | 1241 | 1120 | 1220 | 1191 | 1241 | 1212 |
| δ → γ finish | 1075 | 1080 | 1060 | 1083 | 1053 | 1080 | 1069 | 1025 | 1097 | 1060 |
| γ + δ → α + c start | — | 935 | 970 | 946 | 900 | — | 891 | 915 | 938 | 903 |
| γ + δ → α + c finish | — | 751 | 727 | 650 | 710 | — | 689 | 660 | 680 | 720 |
| Ms | 275 | 274 | 281 | 295 | 313 | 275 | 274 | 281 | 300 | 320 |
| Mf | 60 | 60 | 55 | 54 | 54 | 60 | 57 | 55 | 54 | 54 |

KEY:- A, B, C, D, E are linear cooling rates, A was $2^{o}C\ s^{-1}$, B was $1.36^{o}Cs^{-1}$, C was $1.13^{o}Cs^{-1}$, D was $0.8^{o}Cs^{-1}$ and E was $0.68^{o}Cs^{-1}$

TABLE 17

Variation in δ finish temperature with differing initial cooling rates

| SAMPLE IDENTITY | INITIAL COOLING RATE ($^{o}C\ s^{-1}$) | δ FINISH TEMP. ($^{o}C$) |
|---|---|---|
| T1 | 120 | 1336 |
| T2 | 160 | 1332 |
| M1 | 140 | 1347 |
| M2 | 100 | 1328 |
| R1 | 50 | 1323 |
| R2 | 40 | 1327 |
| S1 | 55 | 1330 |
| S2 | 40 | 1328 |
| I1 | 20 | 1324 |
| ESW | 2 | 1321 |
| A | 2 | 1322 |
| B | 1.36 | 1321 |
| C | 1.13 | 1320 |
| D | 0.80 | 1320 |
| E | 0.68 | 1318 |

TABLE 18

Physical properties of various simulated weld HAZ regions

| SAMPLE IDENTITY | HAZ region simulated | δ content % | Yield Point ($N\ mm^{-2}$) | U.T.S ($N\ mm^{-2}$) | Reduction in area ( % ) | Elong. ( % ) |
|---|---|---|---|---|---|---|
| T1 | 1360°C isotherm of same weld as sample identity | 5.0 | 1755.6 | 1940.9 | 40 | 17 |
| T2 | | 4.6 | 1601.6 | 1955.8 | 46 | 20 |
| M1 | | 4.2 | 1771.0 | 2009.7 | 51 | 18 |
| M2 | | 5.6 | 1601.6 | 1663.2 | 0 | 5 |
| R1 | | 7.9 | 1416.8 | 1416.8 | 2 | 2 |
| R2 | | 6.4 | 1694.0 | 2063.6 | 16 | 11 |
| S1 | | 8.2 | 1601.6 | 2017.4 | 5 | 5 |
| S2 | | 8.4 | 1694.0 | 2048.2 | 5 | 5 |
| MART. | 100% martensite | 0 | 1674.0 | 1720.5 | 38 | 14 |
| SS | parent material | 0 | 926.0 | 1174.0 | 63 | 33 |
| 2H | secondary hardened | 0 | 1081.0 | 1453.0 | 62 | 33 |

TABLE 19

The effect of simulated sample HAZ microstructure on corrosion rate in a standard corrosive liquor

| Sample microstructure | % δ | Weight loss after 100 hours exposure (grms $cm^{-2}$) |
|---|---|---|
| T1, All mixed martensite/δ ferrite and correspond to 1360°C zone of appropriate weld. | 5.0 | 0.0693 |
| T2, | 4.6 | 0.0747 |
| M1, | 4.2 | 0.0719 |
| M2, | 5.6 | 0.0830 |
| R1, | 7.9 | 0.0900 |
| R2, | 6.4 | 0.0811 |
| S1, | 8.2 | 0.2012 |
| S2, | 8.4 | 0.2108 |
| Homogenous martensite | 0 | 0.0640 |
| Standard State | 0 | 0.2263 |
| Secondary hardened | 0 | 0.2293 |

TABLE 20

Comparison of micro- and macro-hardness values obtained from real and simulated samples

| Sample Identity | AVERAGE Micro-hardness (Hv) | | AVERAGE Macro-hardness (Hv) | |
|---|---|---|---|---|
| | Real | Simulated | Real | Simulated |
| T1 | 551 | 546 | Appropriate zone too small for macrohardness test | 555 |
| T2 | 555 | 561 | | 578 |
| Mt | 572 | 590 | | 589 |
| M2 | 551 | 549 | | 491 |
| R1 | 530 | 523 | | 501 |
| R2 | 540 | 540 | | 504 |
| S1 | 560 | 556 | | 507 |
| S2 | 538 | 542 | | 504 |

TABLE 21

The isothermal transformation of austenite to δ ferrite using three transformation temperatures at differing times

| TRANSFORM. TIME (SECS) | % transformed at each temperature | | |
|---|---|---|---|
| | 1340°C | 1360°C | 1380°C |
| 0 | 2.5 | 6.5 | 18.8 |
| 0.5 | 5.9 | 9.7 | 25.1 |
| 2 | 12.0 | 16.6 | 37.3 |
| 4 | 21.6 | 26.8 | 43.7 |
| 10 | 34.6 | 37.2 | 54.8 |
| 20 | 37.4 | 41.0 | 61.8 |
| 50 | 41.3 | 44.4 | — |
| 100 | 50.6 | 53.7 | — |
| 200 | 54.0 | 58.3 | — |
| 250 | 56.0 | 61.9 | — |

All transformation results given were measured by point-counting techniques. Accuracy is better than ± 0.5%.
Note - 320 seconds at 1360°C produced 67% δ

TABLE 22

Isothermal transformation information used for linear regression analysis

| TRANSFORMATION TEMPERATURE (°C) | % transformation at each time | | | |
|---|---|---|---|---|
| | 0 secs | 0.5 secs | 2 secs | 4 secs |
| 1340 | 2.5 | 5.9 | 12.0 | 21.6 |
| 1360 | 6.5 | 9.7 | 16.6 | 26.8 |
| 1380 | 18.8 | 25.1 | 37.3 | — |

TABLE 23

Information used in linear regression analysis of the amount of δ formed and time spent above 1320°C

| Sample identity | Calculated time spent over 1320°C | δ content ( % ) |
|---|---|---|
| T1 | 0.5692 secs | 5.1 |
| T2 | 0.47347 " | 4.9 |
| M1 | 0.3698 " | 4.3 |
| M2 | 0.55865 " | 6.0 |
| R1 | 1.0942 " | 7.9 |
| R2 | 0.08769 " | 6.4 |
| S1 | 1.0394 " | 8.2 |
| S2 | 0.7558 " | 8.4 |
| 2SS | 2.9685 " | 16.6 |

TABLE 24

Alloying element concentration variations in close proximity to δ ferrite

| REGION ANALYSED | % of Element | | | |
|---|---|---|---|---|
| | C | Cr | V | Mo |
| Matrix | 0.21 | 11.3 | 0.29 | 0.95 |
| Matrix adjacent to δ | 0.15 | 15.01 | 0.349 | 0.927 |
| δ edge | TRACE | 15.03 | 0.359 | 1.283 |
| δ centre | TRACE | 15.57 | 0.391 | 1.953 |

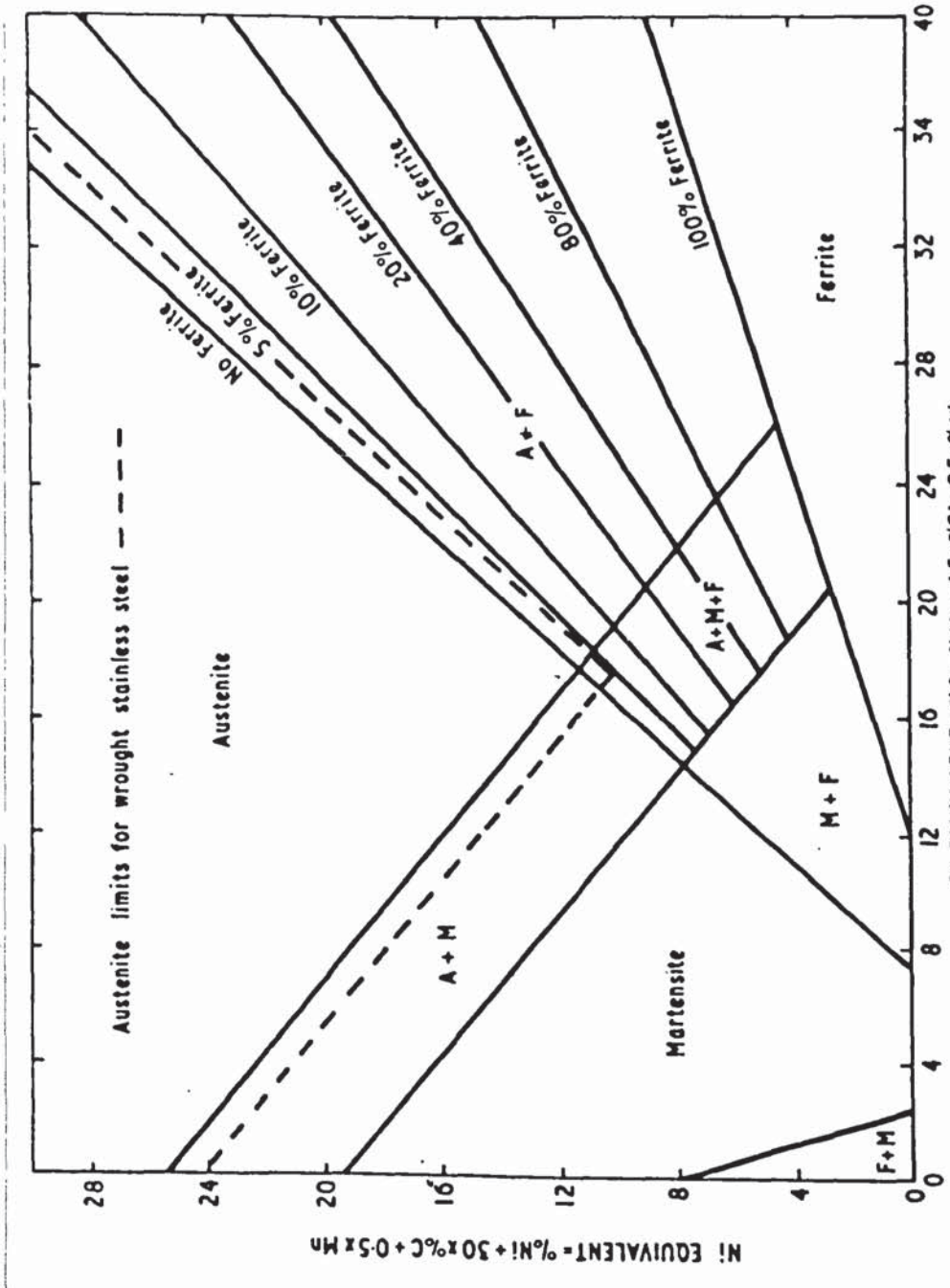


*Constitution or Schaeffler diagram for stainless steel weld metal. (Brit. Welding J., 1960, 7, 27)*

FIGURE 1 The Schaeffler diagram, showing the inter-relation between chromium and nickel equivalent elements and expected weld bead microstructures[18].

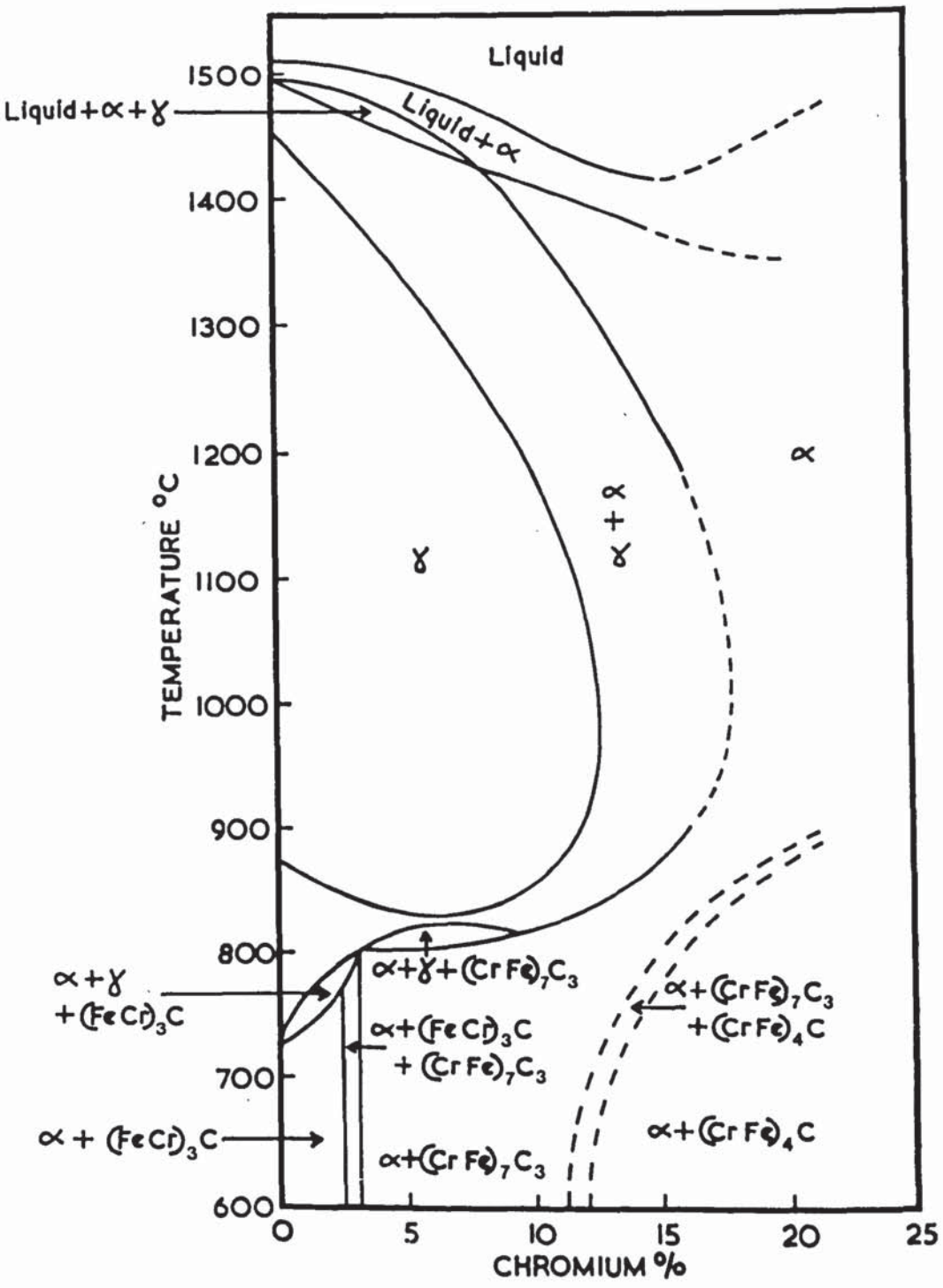


FIGURE 2 Isopleth of the iron-chromium-carbon ternary equilibrium system, taken where carbon is 0.1 wt % concentration[2].

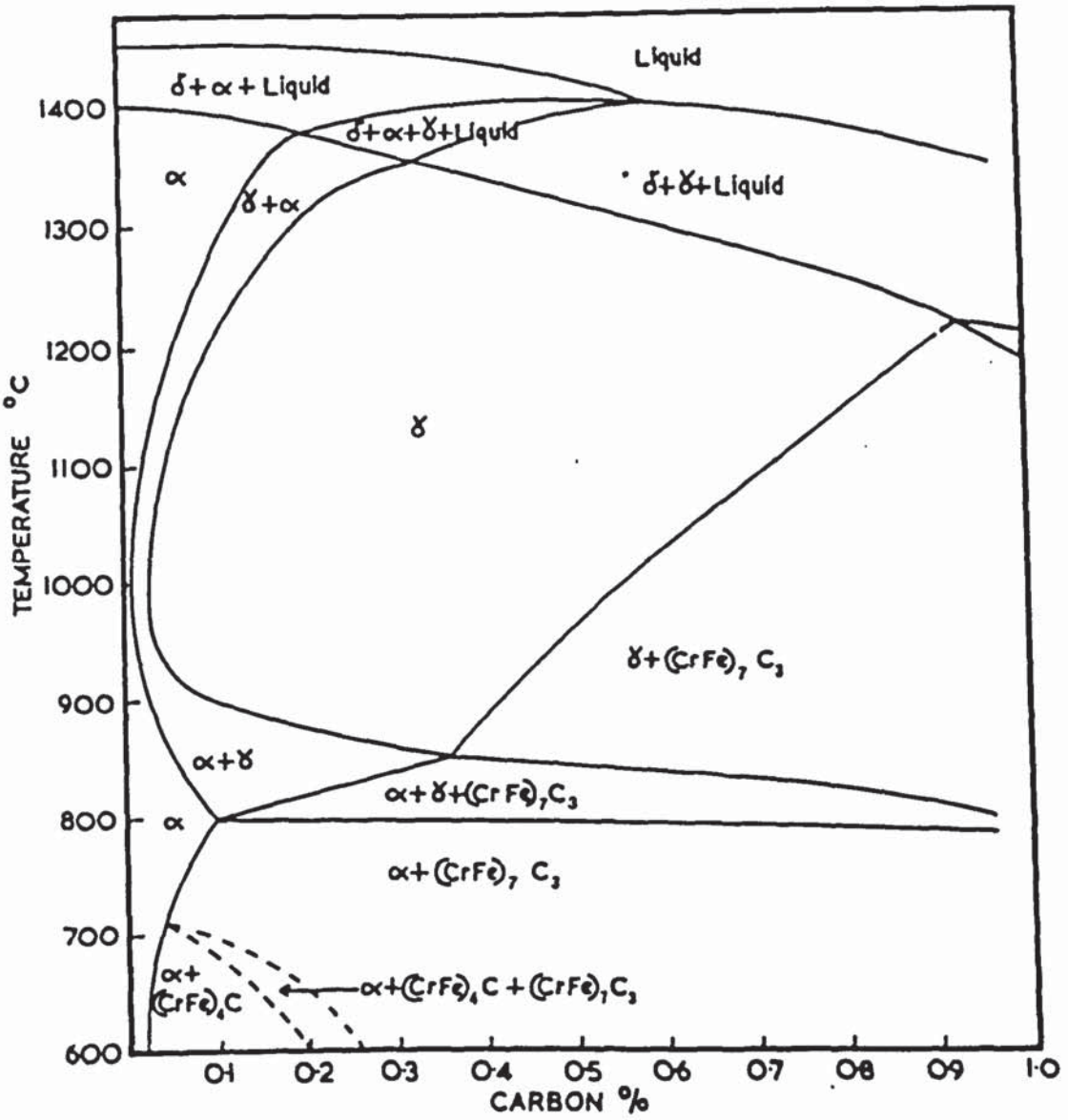


FIGURE 3 Isopleth of the iron-chromium-carbon ternary equilibrium system, taken where chromium is 12 wt % concentration (2).

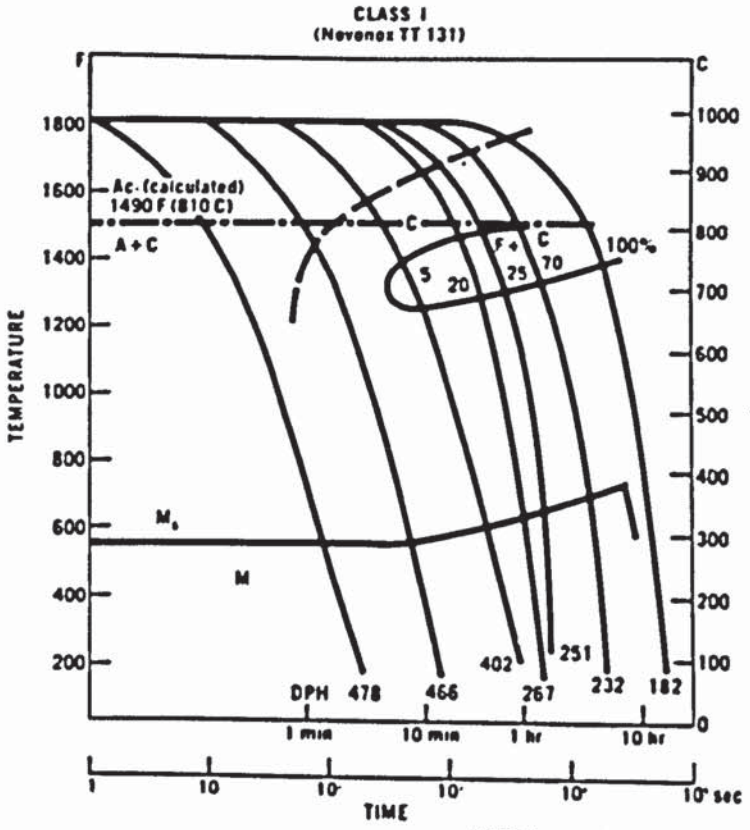


FIGURE 4 Typical CCT diagram for a Class 1 steel of the simple 12% Cr Mo type[1]

FIGURE 5 Typical CCT diagram for a Class 2 steel of 12% Cr Mo V W type [1]

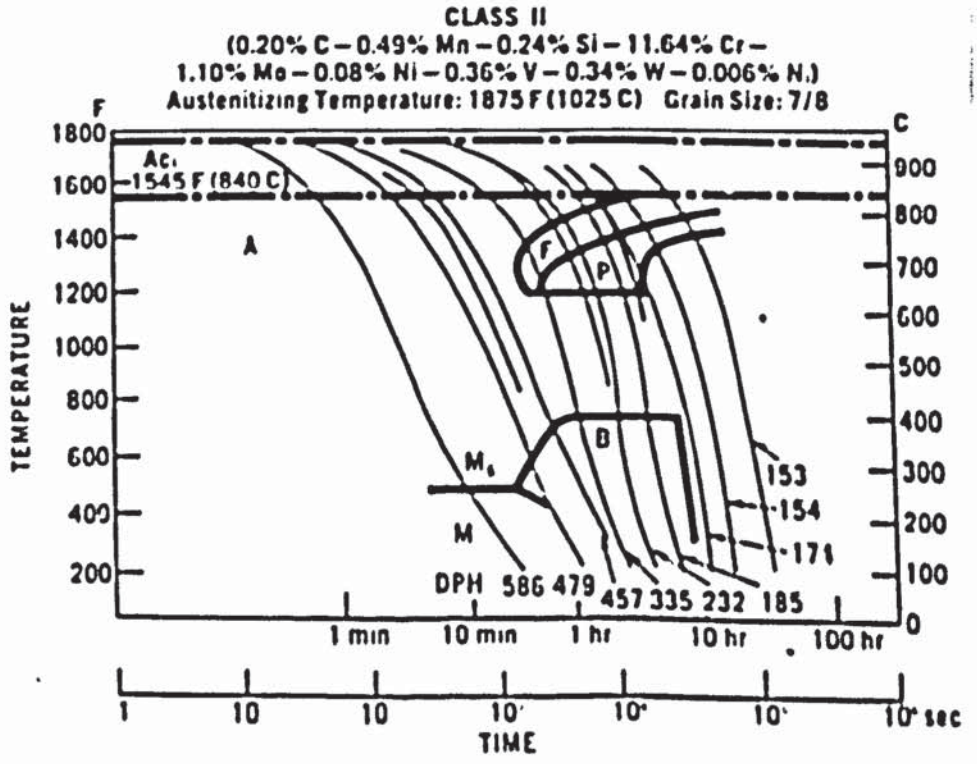

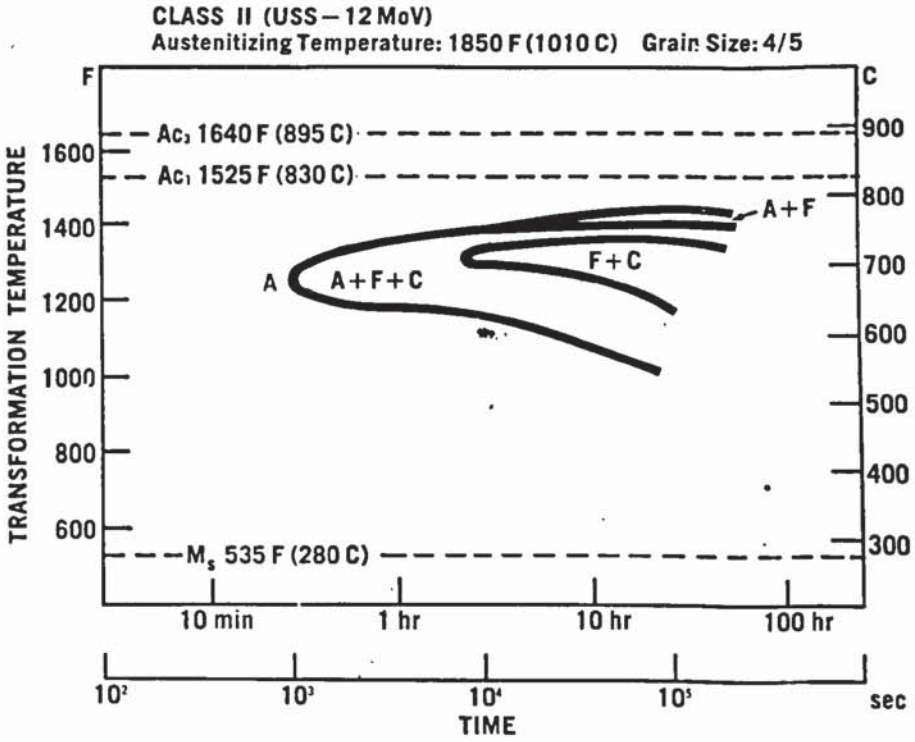


FIGURE 6 Typical TTT diagram for a 12% Cr Mo V type class 2 steel (1)

FIGURE 7 Recommended temperature cycle for multi-pass welds used to prevent HAZ cracking (1)

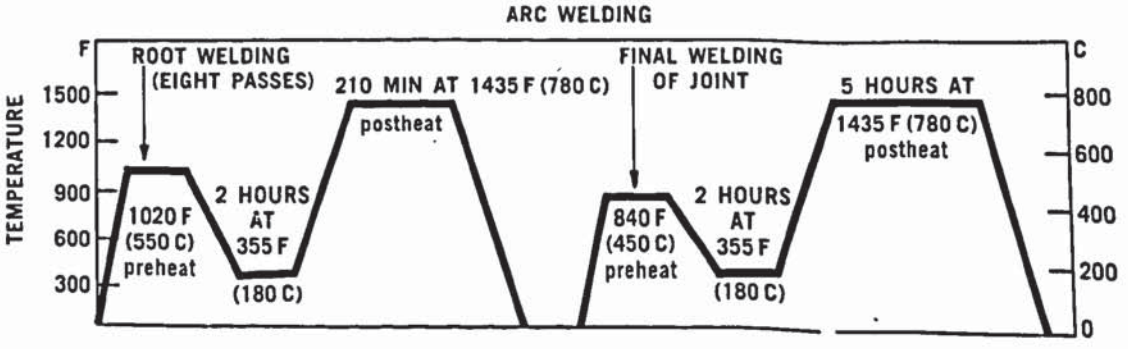

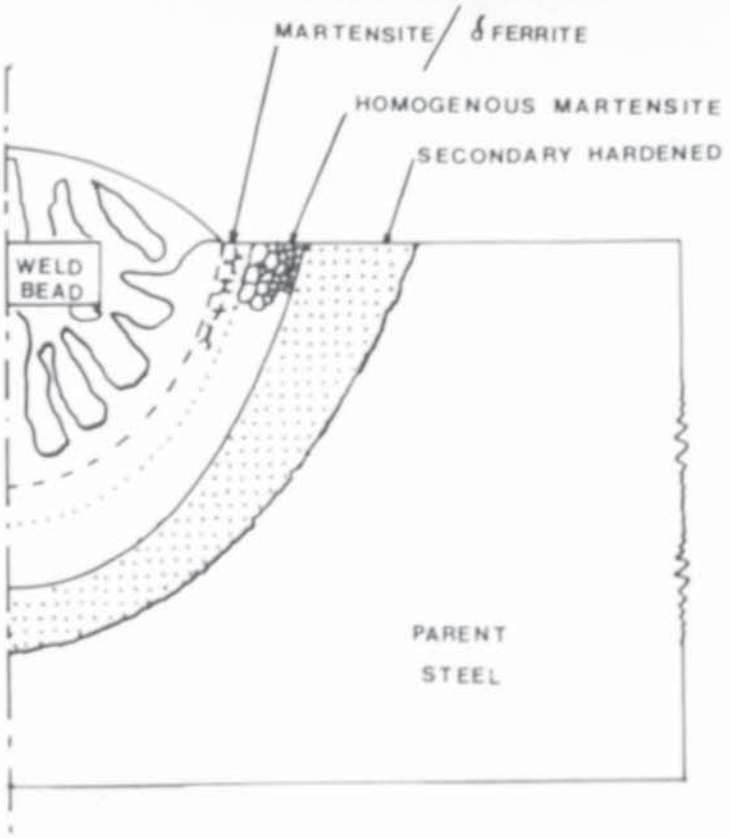


FIGURE 8

Schematic diagram of weld HAZ in Super 12% Cr Mo steels which shows relative location of all three heat affected areas

FIGURE 9 Transmission Electron Micrograph of lath martensite in the Class 2 steel (plate x 30K)

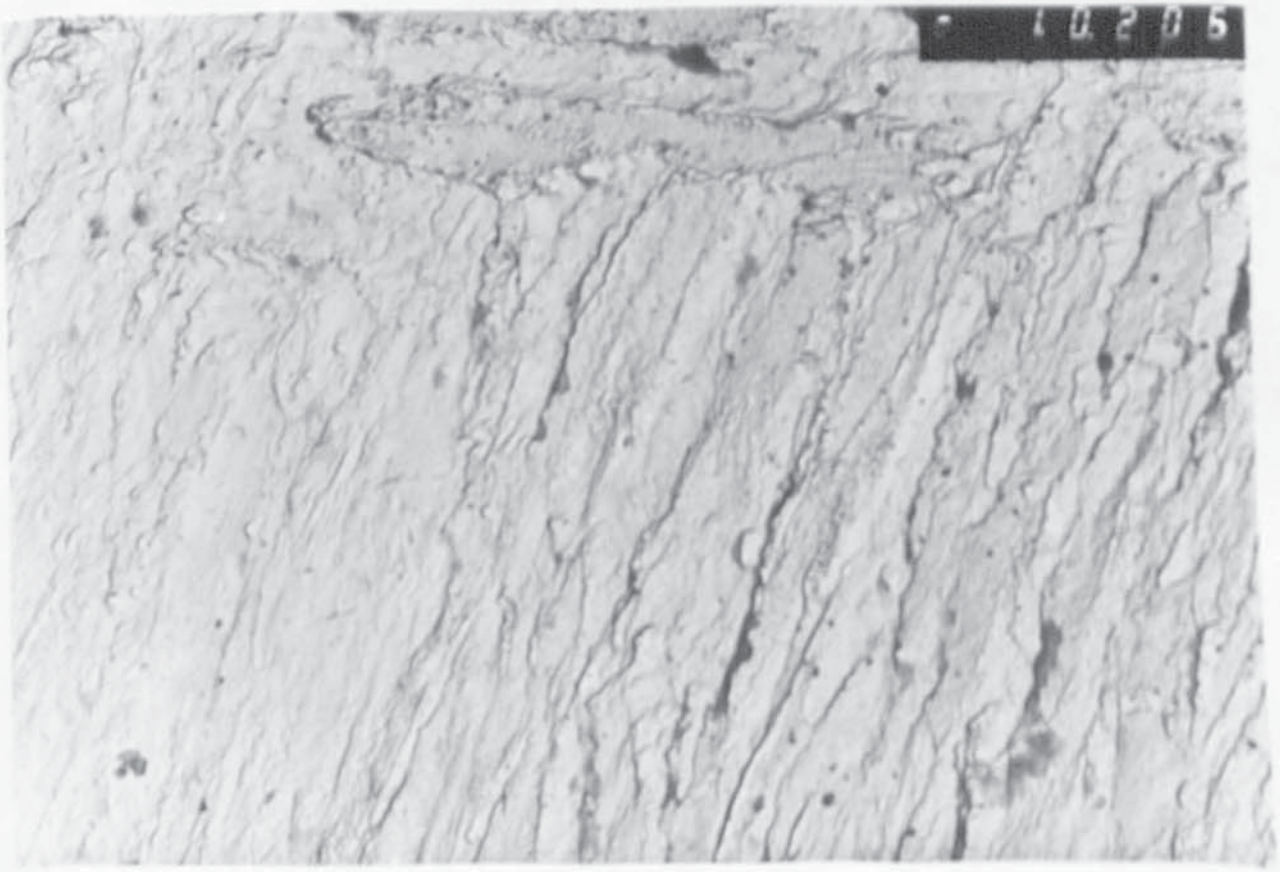

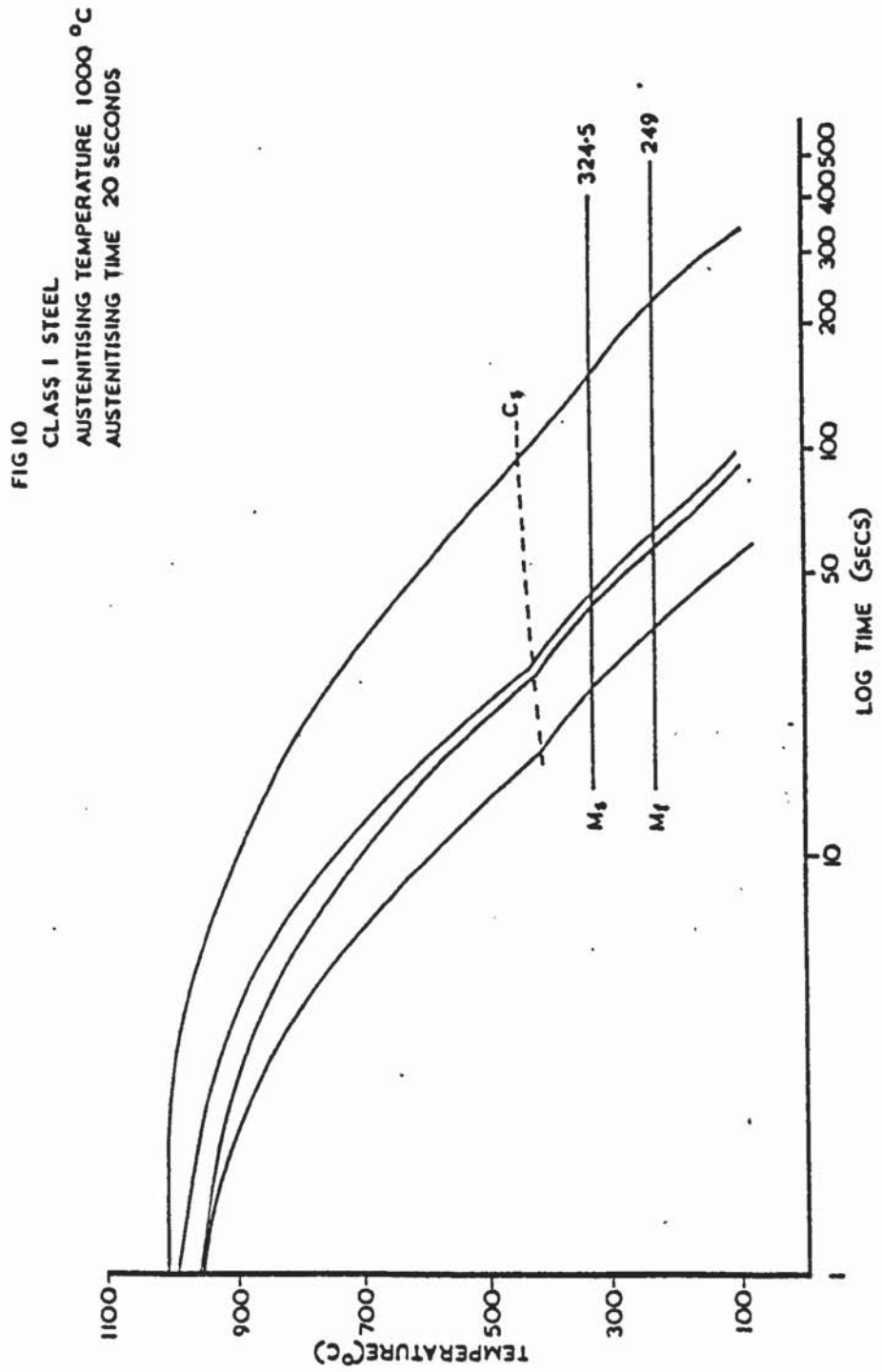


FIGURE 10 CCT diagram for Class 1 steel austenitising temperature 1000°C austenitising time 20 seconds

FIGURE 11

Carbide particles found in the Class 1 steel, after prolonged holding below $C_s$ temperature

Note: Many carbides are on prior austenite grain boundaries and thus outline parts of austenite grains ( x 400, Adlers reagent)

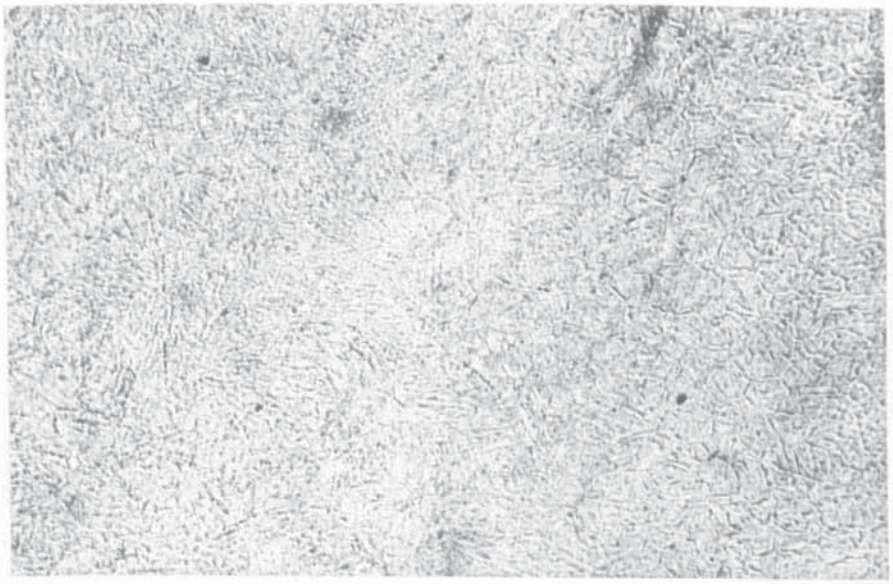

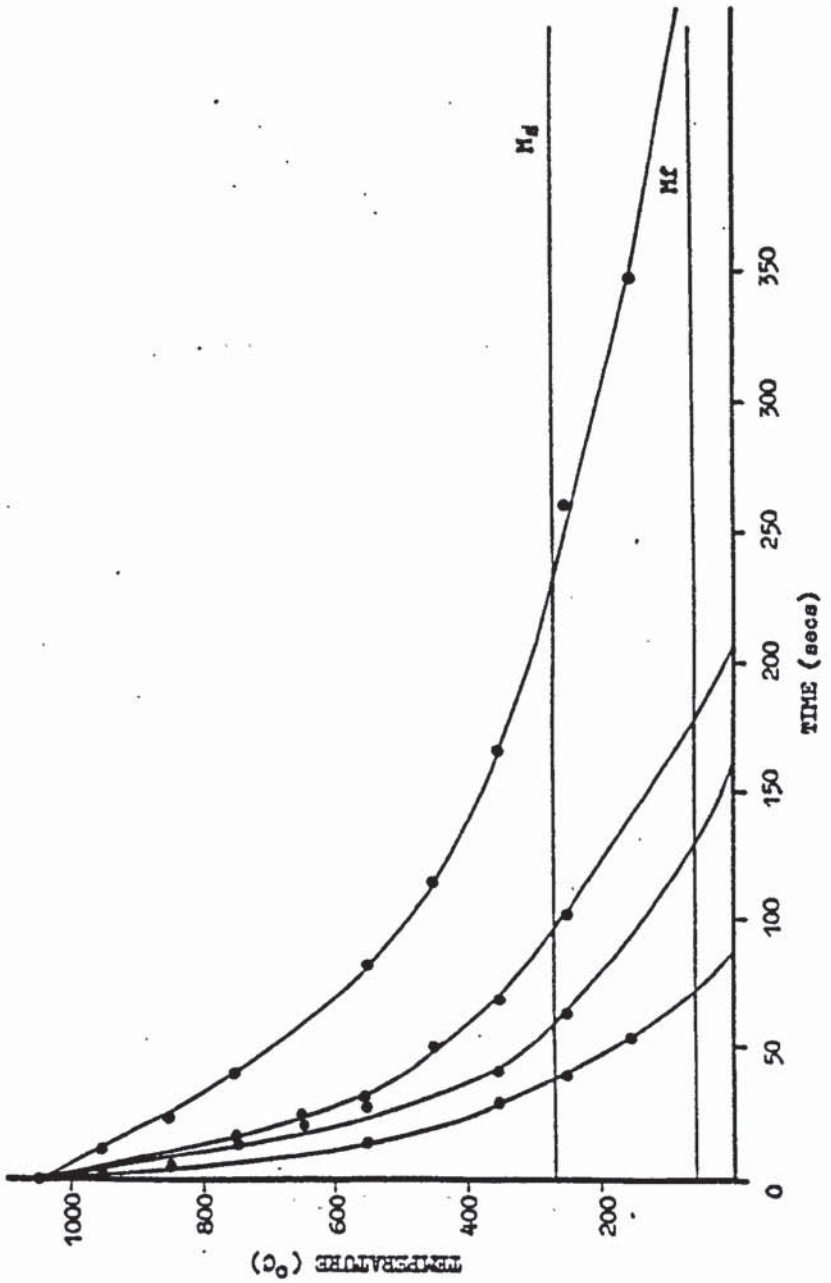


FIGURE 12 CCT diagram for Class 2 steel
(Austenitising temp. 1050°C)

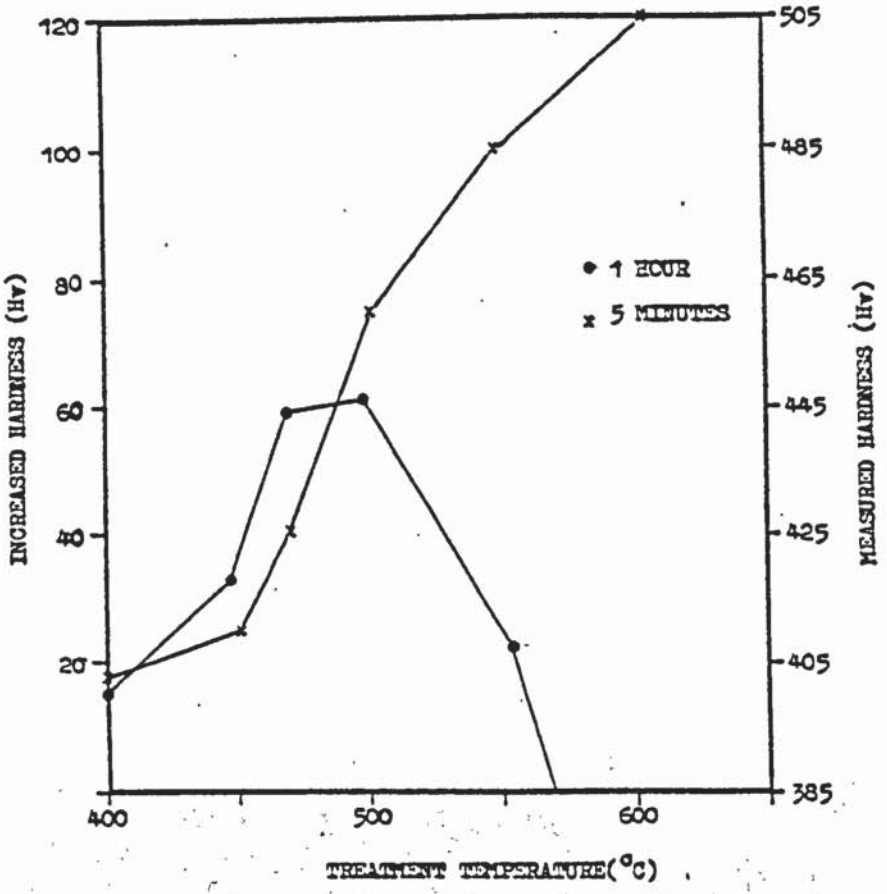


FIGURE 13 The effect of short-time, subcritical heat-treatments on hardness of tempered Class 2 steel

FIGURE 14 δ ferrite formation in prior austenite grain boundaries, class 1 steel, heat-treated for 5 minutes at 1340°C (x1100, electrolytically etched in 0.1M NaOH at 6V·1A)

10u

FIGURE 15 As figure 14, different area
(x 1100, electrolytic NaOH etchant)

FIGURES 16, 17 and 18 <u>The effect of δ on crack path of weld HAZ cracks,</u> note fracture follows along edge of δ. (all x 1000, Adlers etch)

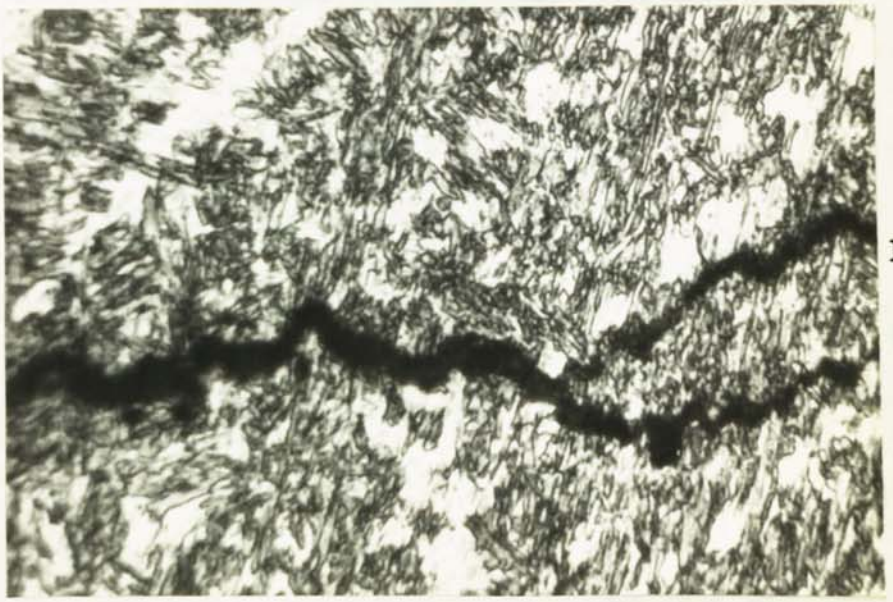

FIGURE 16

FIGURE 17

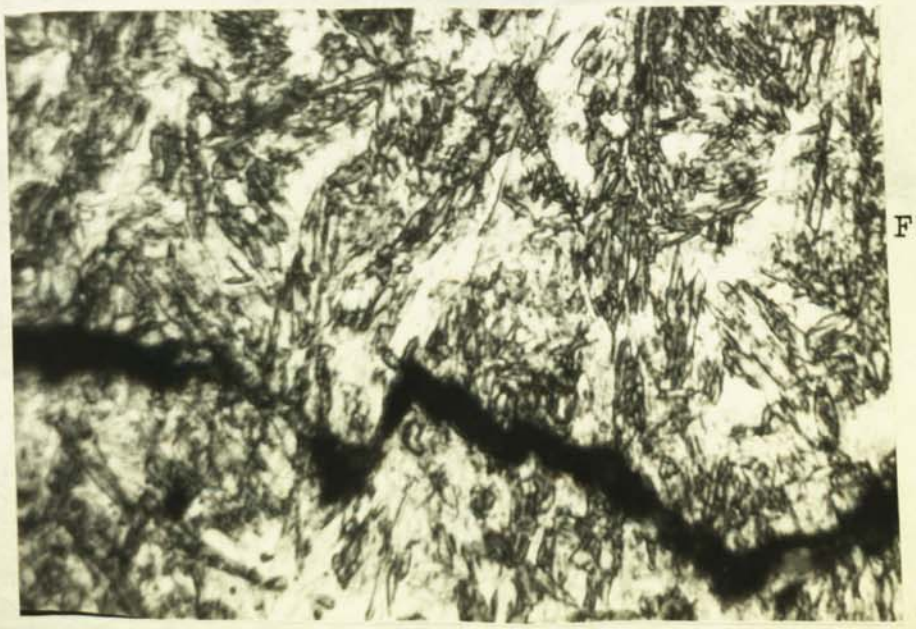

FIGURE 18

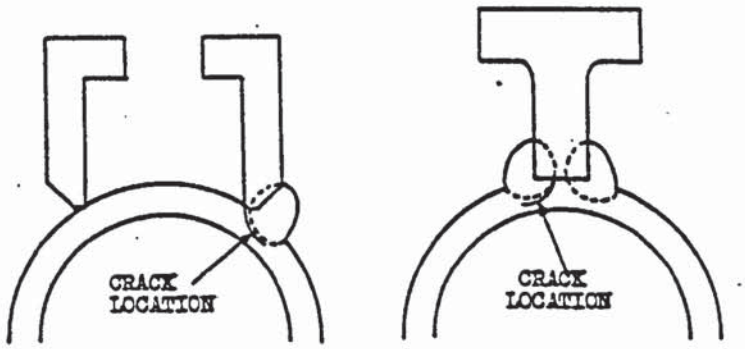


A) C – SPACER ATTACHMENT

B) T – SPACER ATTACHMENT

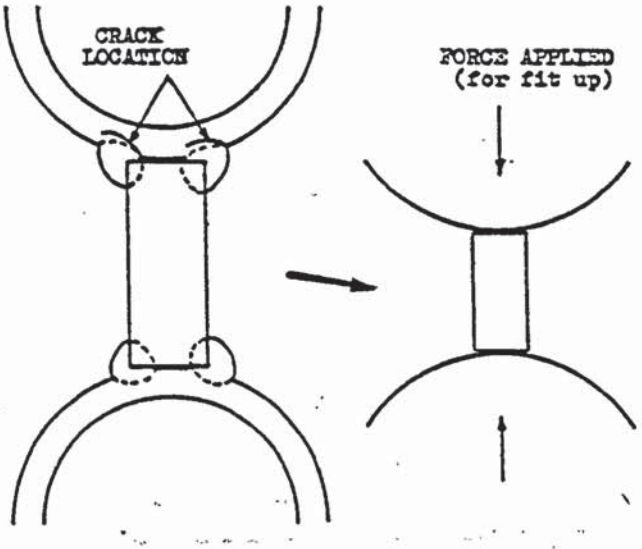


C) TUBE TO TUBE SPACER ATTACHMENT
AND METHOD UTILISED

FIGURE 19 Schematic drawing of cracking situations found in commercially welded joints

FIGURE 20 Macrosection of tube spacer attachment weld (as in Figure 19c) showing HAZ cracks which initiate as a result of bad weldment fit up (Etched in Adlers reagent, x 3)

FIGURE 21 Industrial welding preparation used for all tube to tube welding experiments (40)

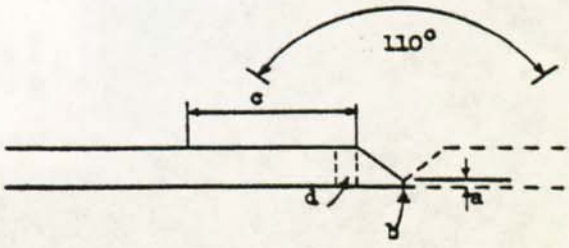


a = 0.8 - 1.0 mm
b = 0 - 0.5 mm
c = 50 mm
d = 3 mm THERMOCOUPLE HOLE (in 1 tube only)

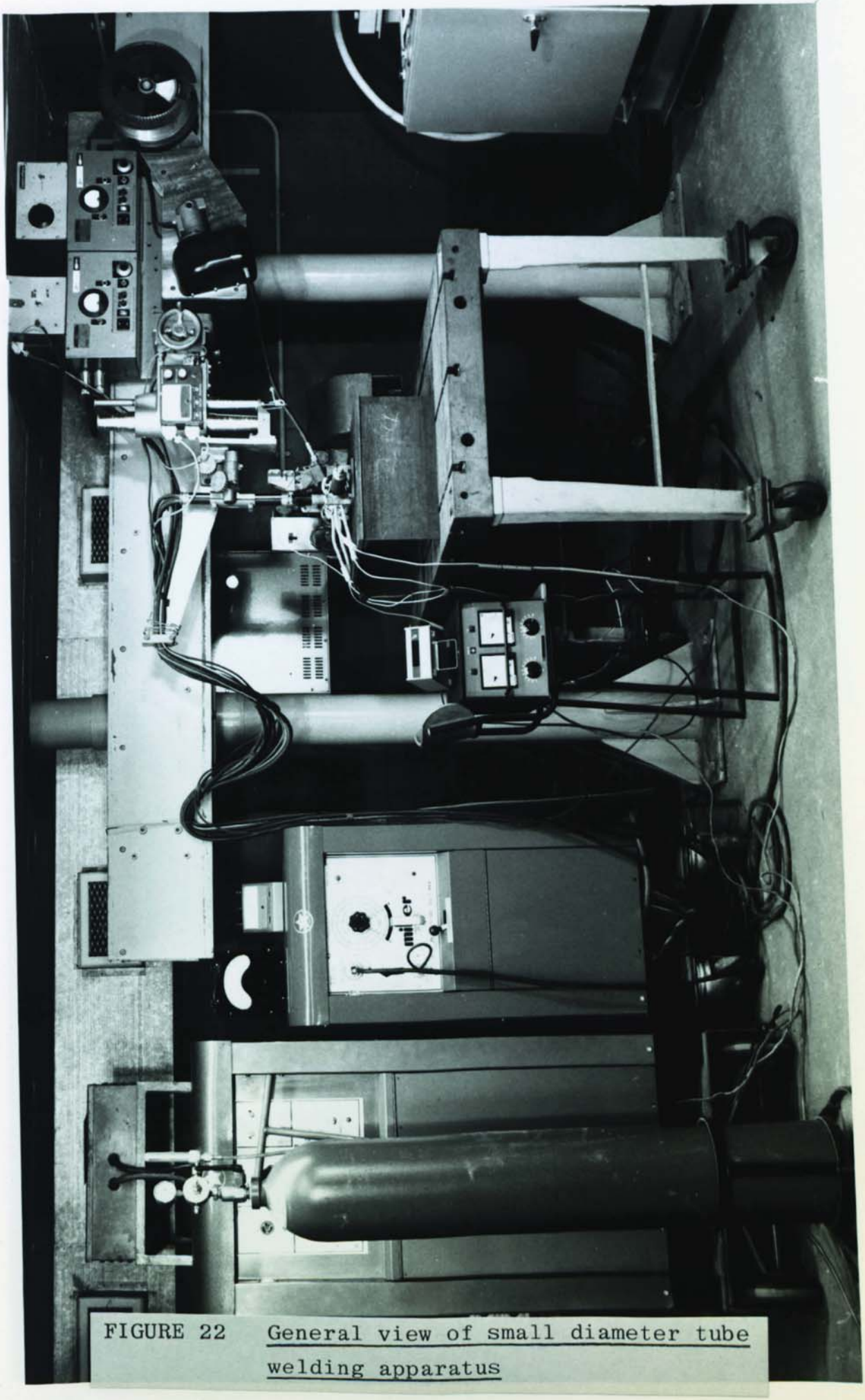

FIGURE 22 General view of small diameter tube welding apparatus

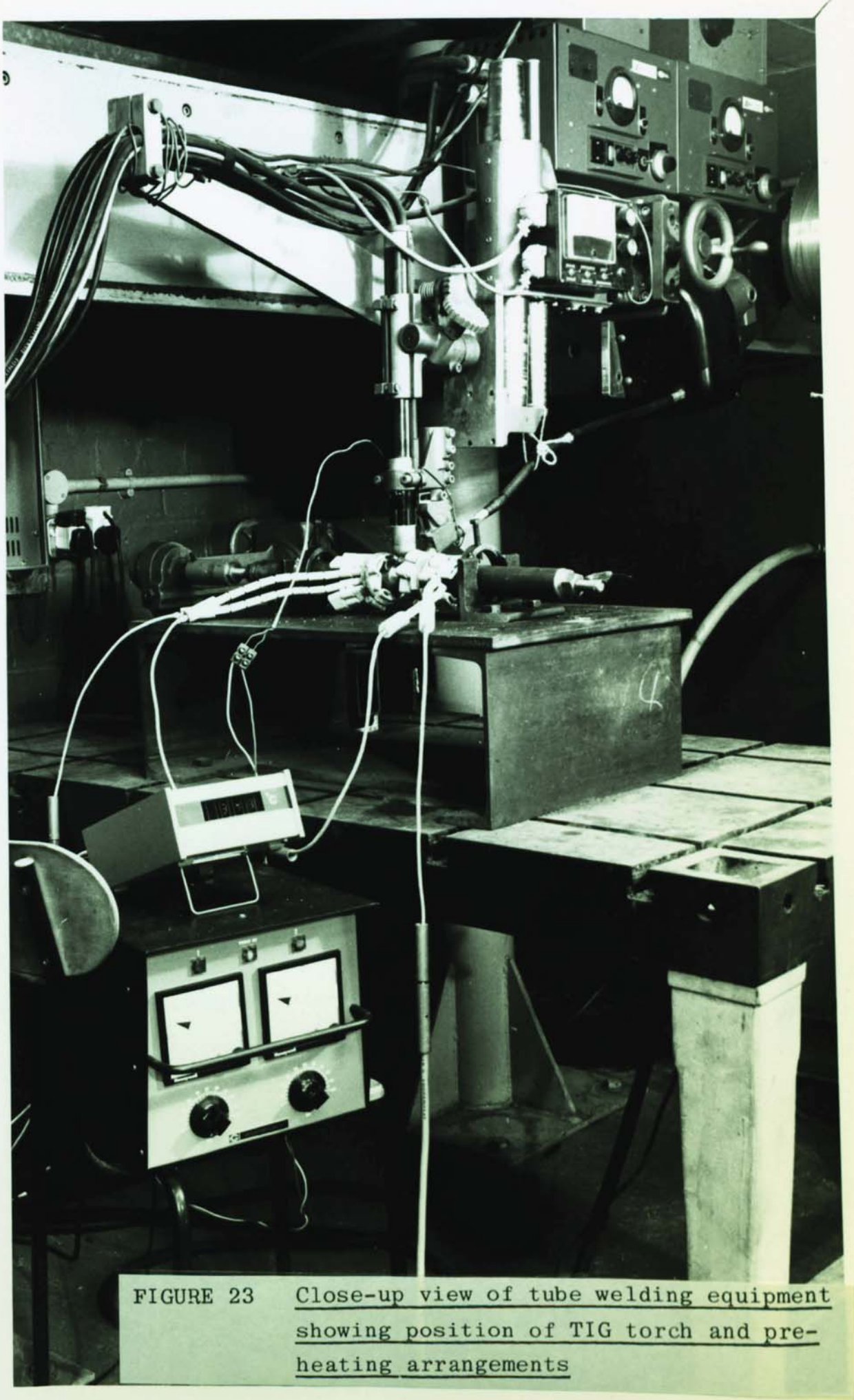

FIGURE 23 Close-up view of tube welding equipment showing position of TIG torch and pre-heating arrangements

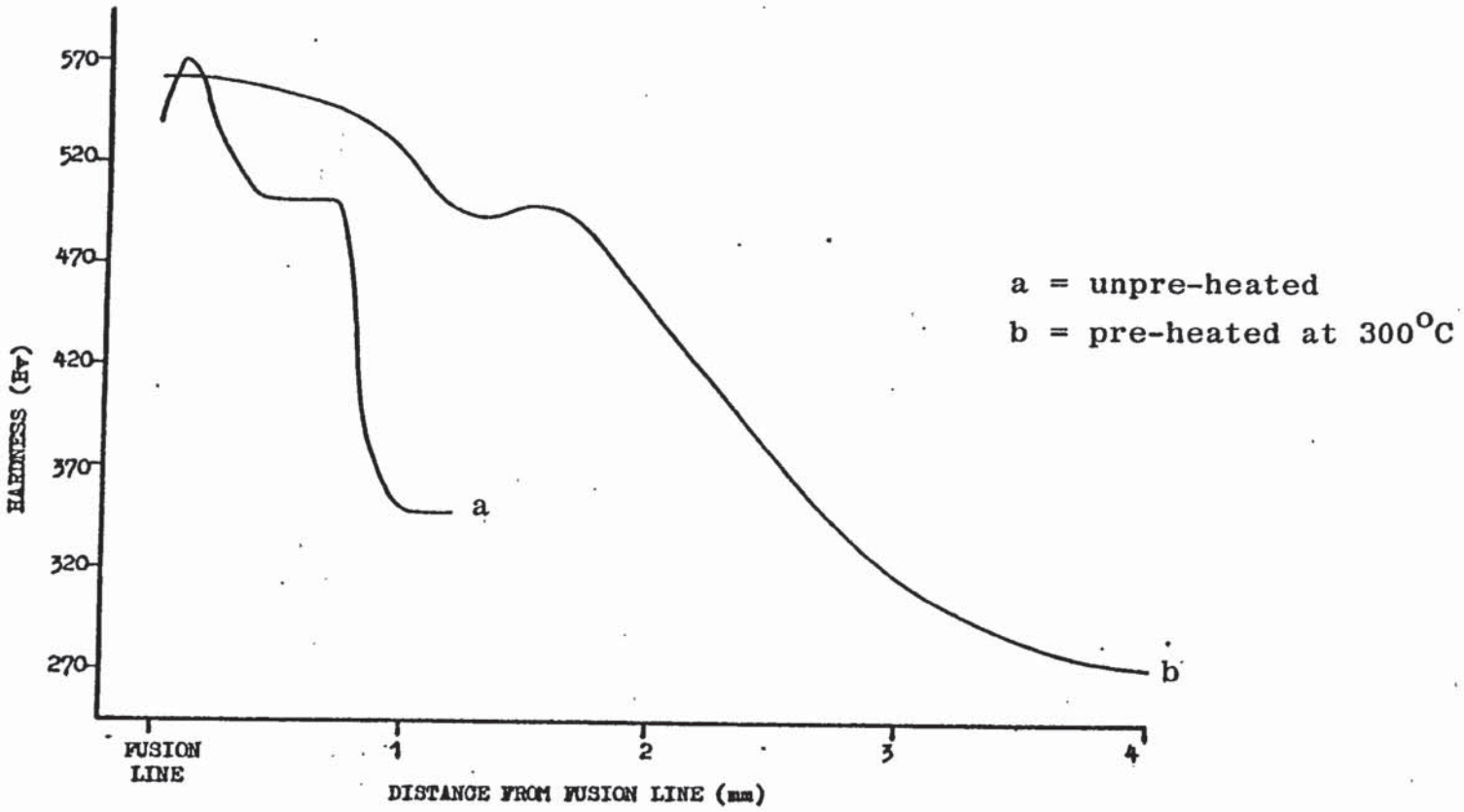


FIGURE 24 The effect of pre-heating on size of weld HAZ in a single pass weld

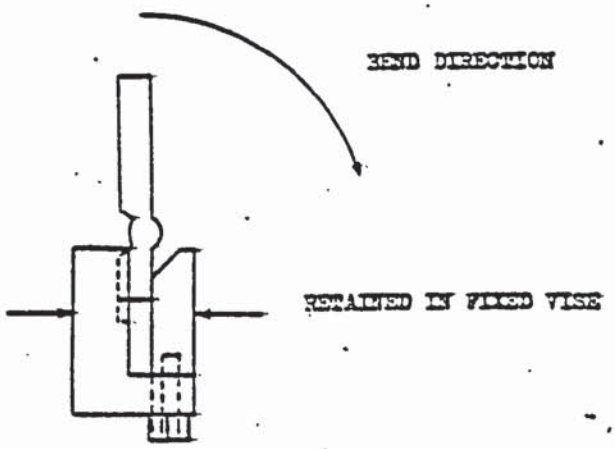


FIGURE 25 Schematic diagram illustrating the arrangement employed for bend testing small diameter tube welds

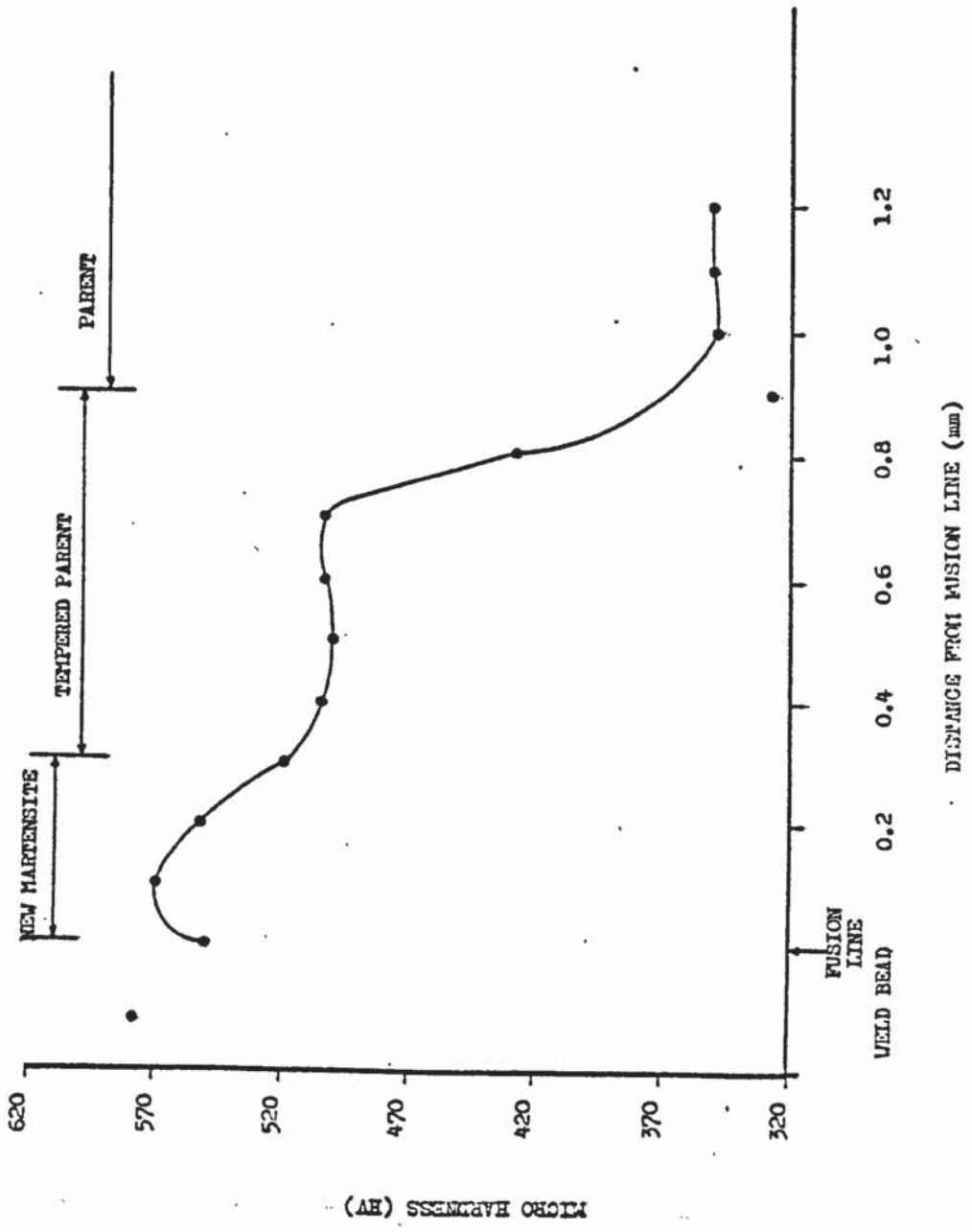


FIGURE 26 Hardness and microstructure of a single pass unpre-heated small diameter tube weld

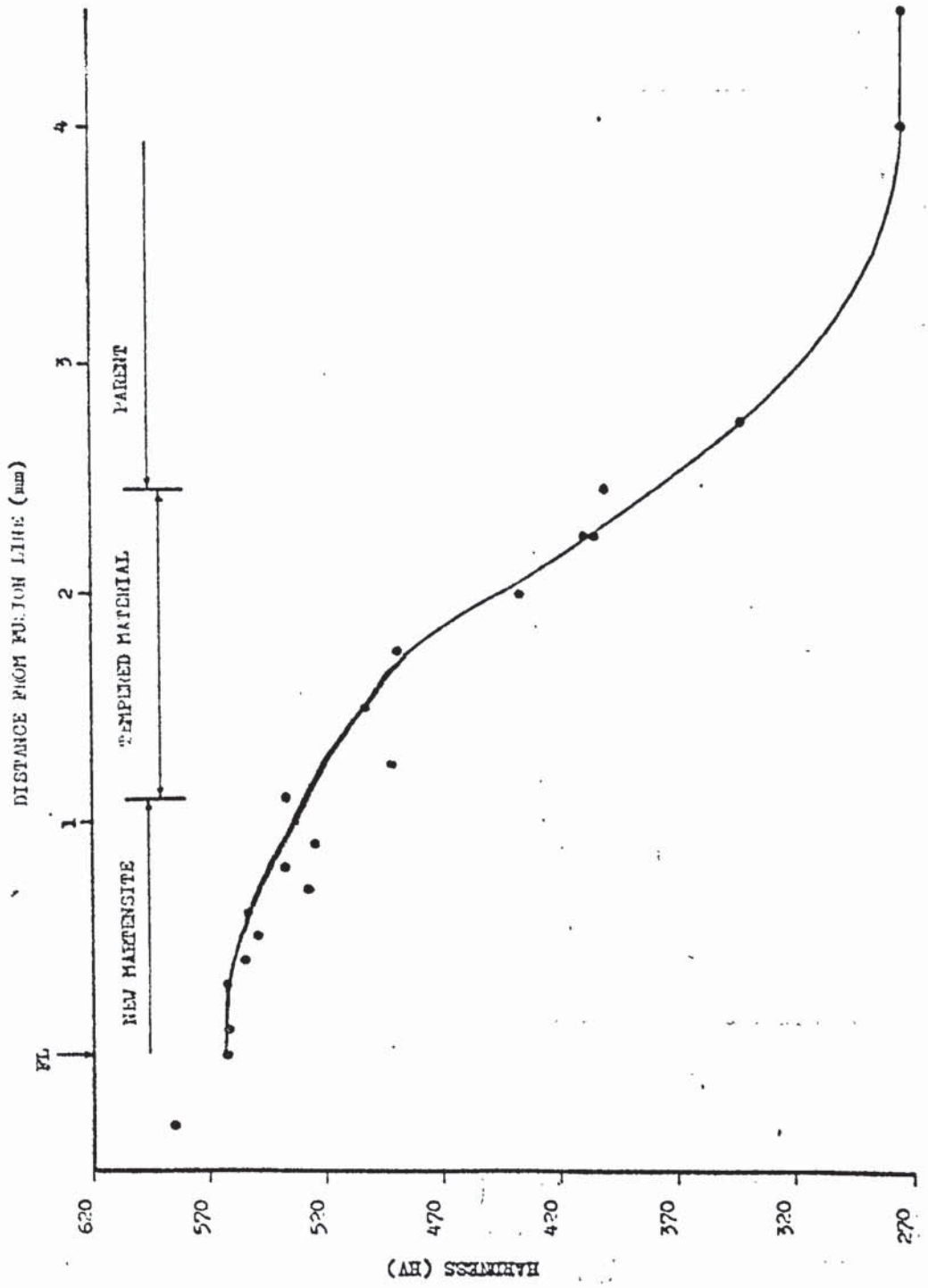


FIGURE 27 Hardness and Microstructure of a single pass 300°C pre-heated small diameter tube weld.

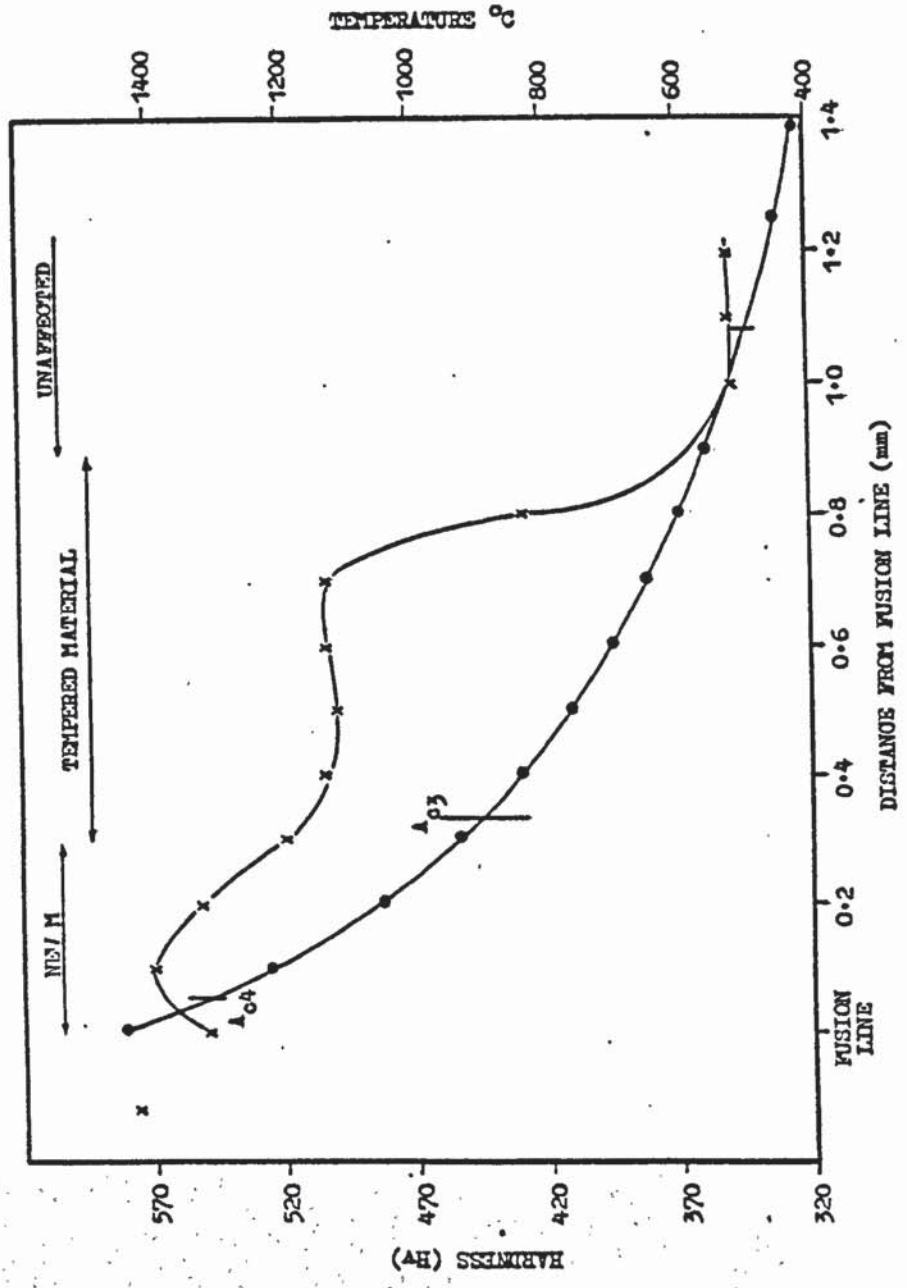


FIGURE 28 Predicted thermal cycle for unpre-heated single pass weld fitted onto hardness and and microstructural survey

N.B. Close agreement between predicted $Ac_3$ and $Ac_4$ temperature points and hardness values.

FIGURES 29 and 30 δ located at prior austenite grain boundaries in thick plate weldments (δ ferrite in unetched phase, matrix is lath martensite). Both x 1100, etched in Adler reagent

FIGURE 29

10μ

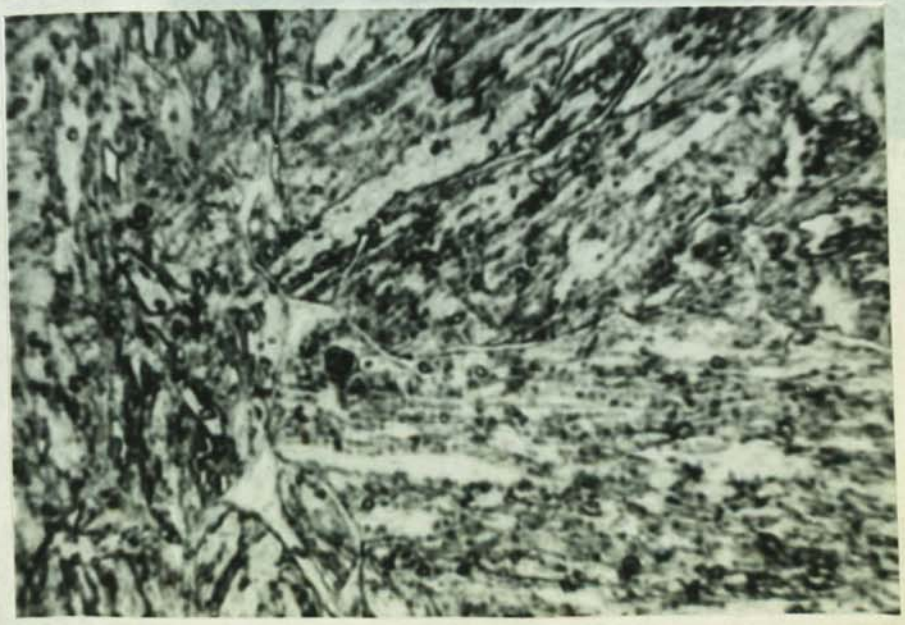

FIGURE 30

FIGURE 31

Macrosection showing crack in test weld S2

Note: failure initiates from sharp angle produced by bad weld bead profile. Failure route remains in duplex region before entering weld bead.

(Adlers reagent x 3.5)

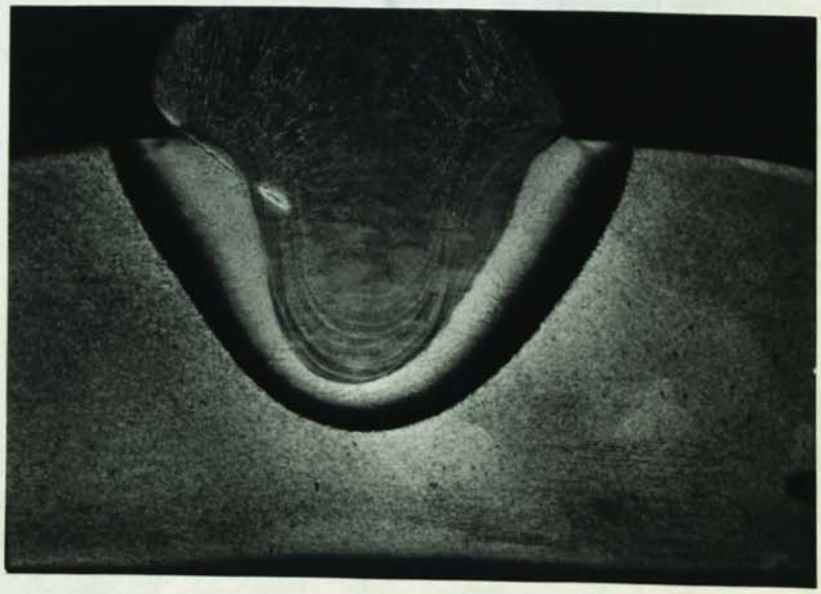

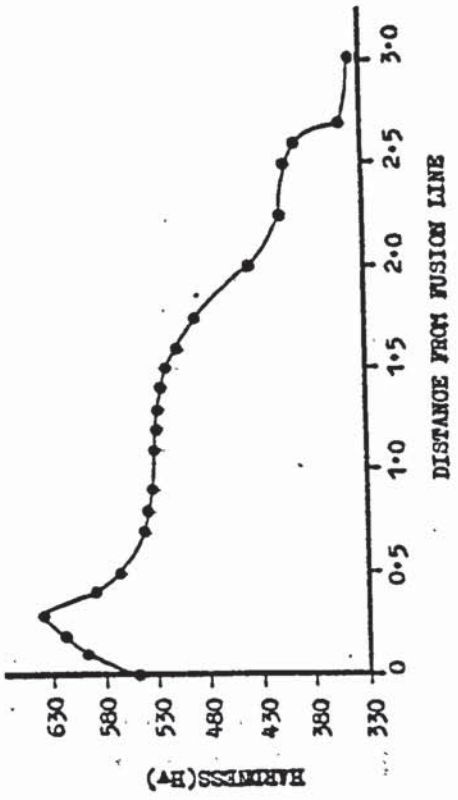


FIGURE 32 Microhardness survey performed on thick plate weld T1

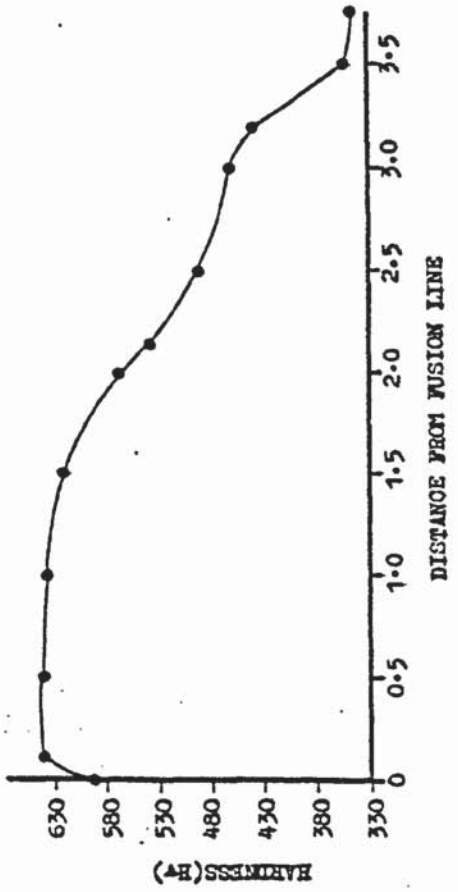


FIGURE 33 Microhardness survey performed on thick plate weld M1

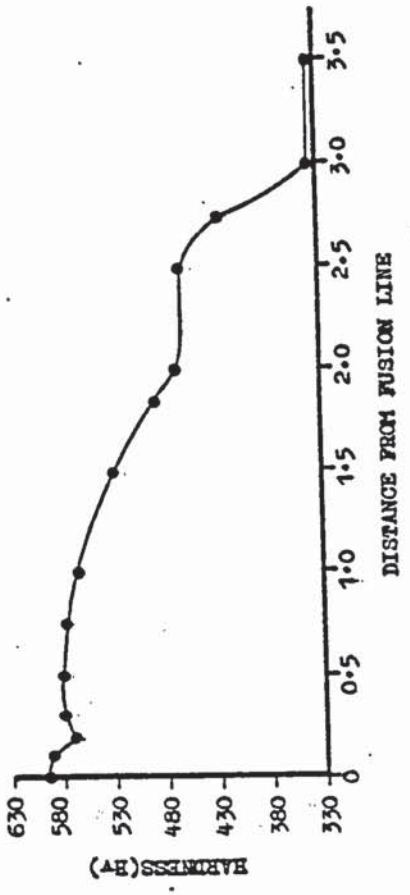


FIGURE 34 Microhardness survey performed on thick plate weld R1

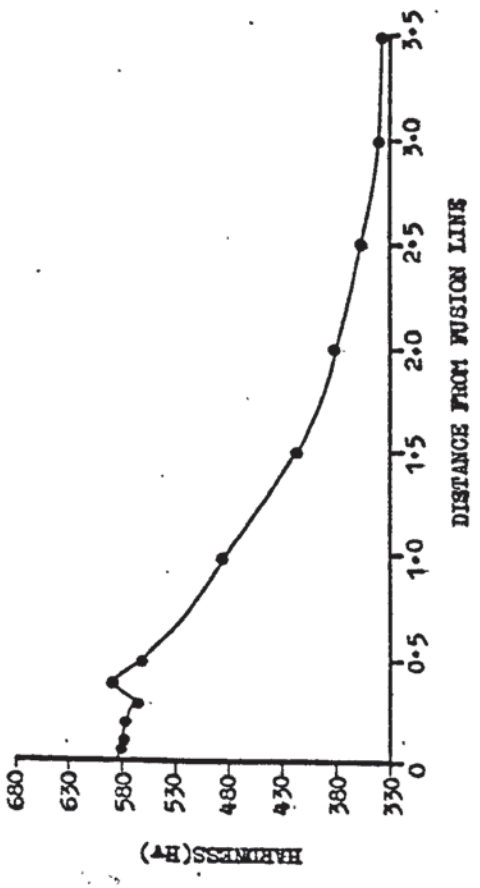


FIGURE 35 Microhardness survey performed on thick plate weld S1

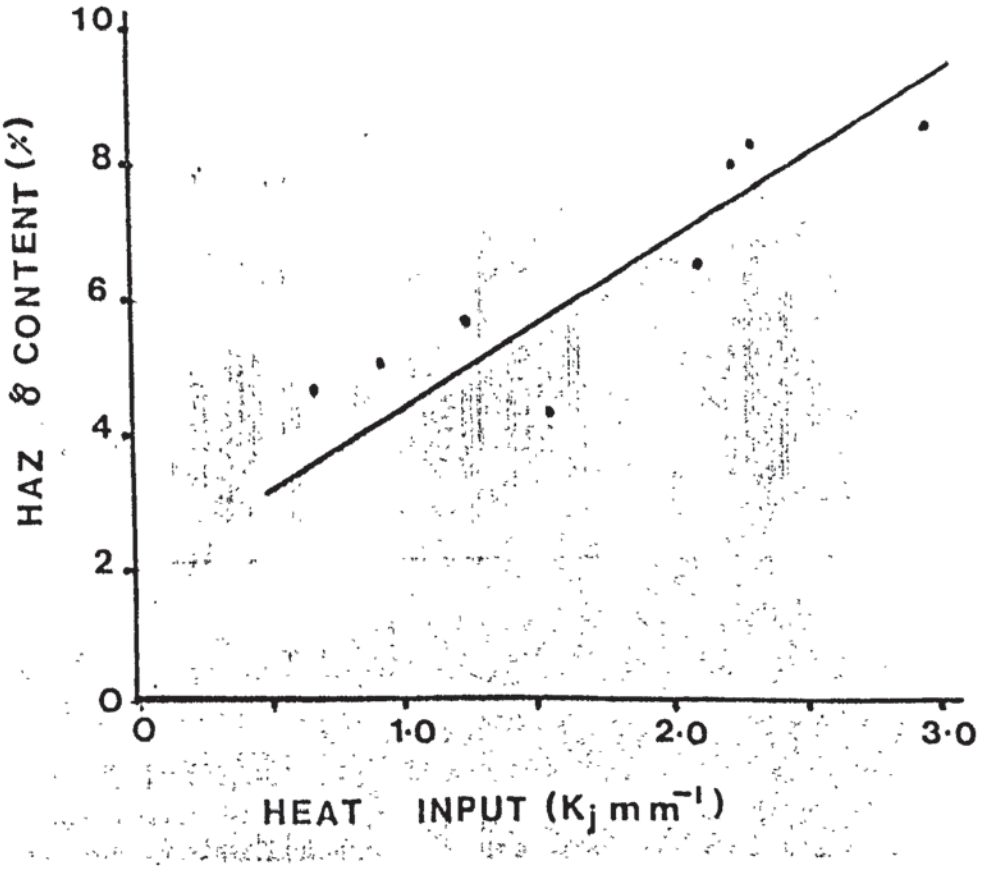


FIGURE 36 Correlation of the δ content in the weld HAZ and the heat-input used to form the weld

NB. This graph is statistically based and cannot be extrapolated beyond the experimental range.

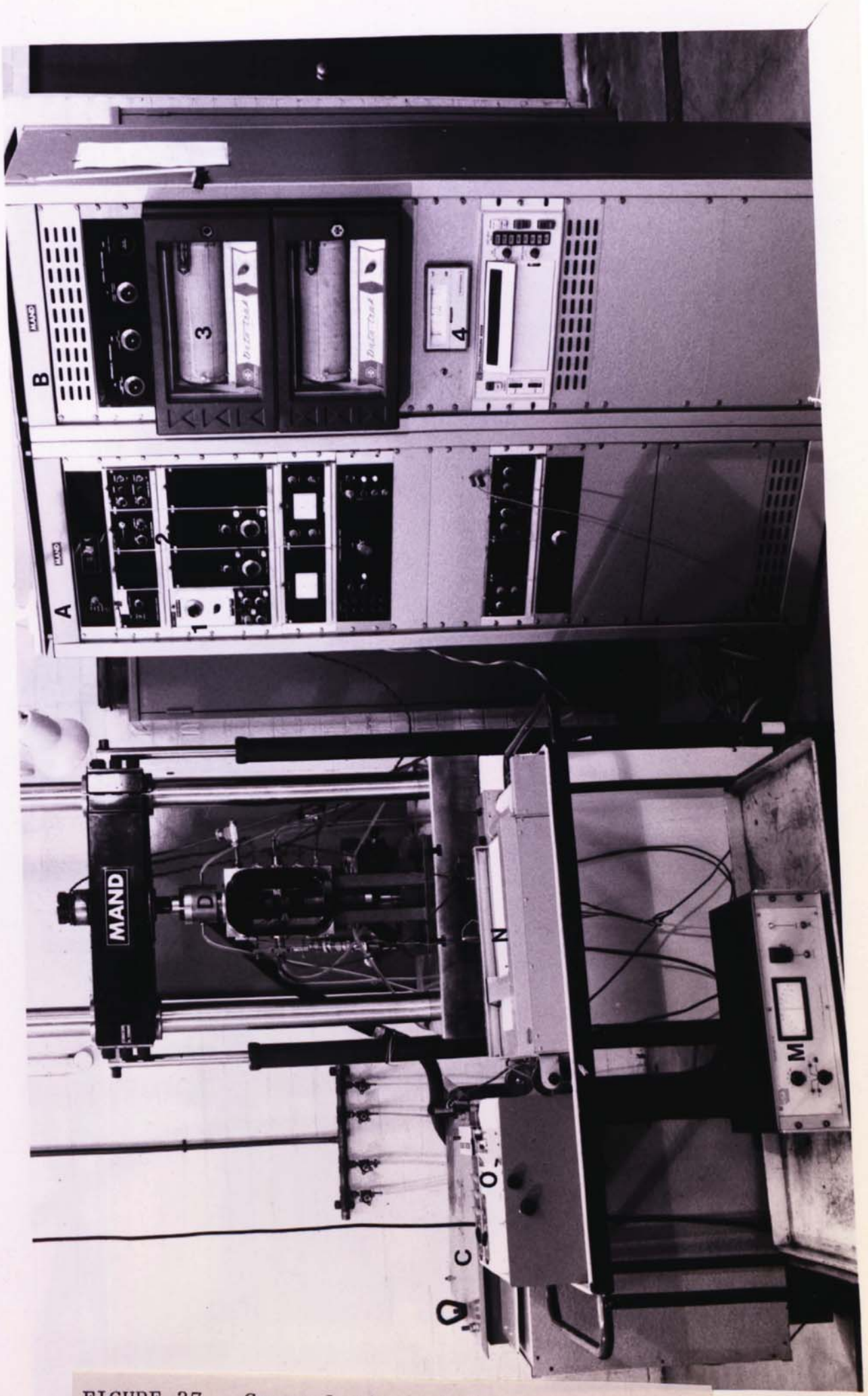


FIGURE 37 General view of thermo-mechanical weld simulator

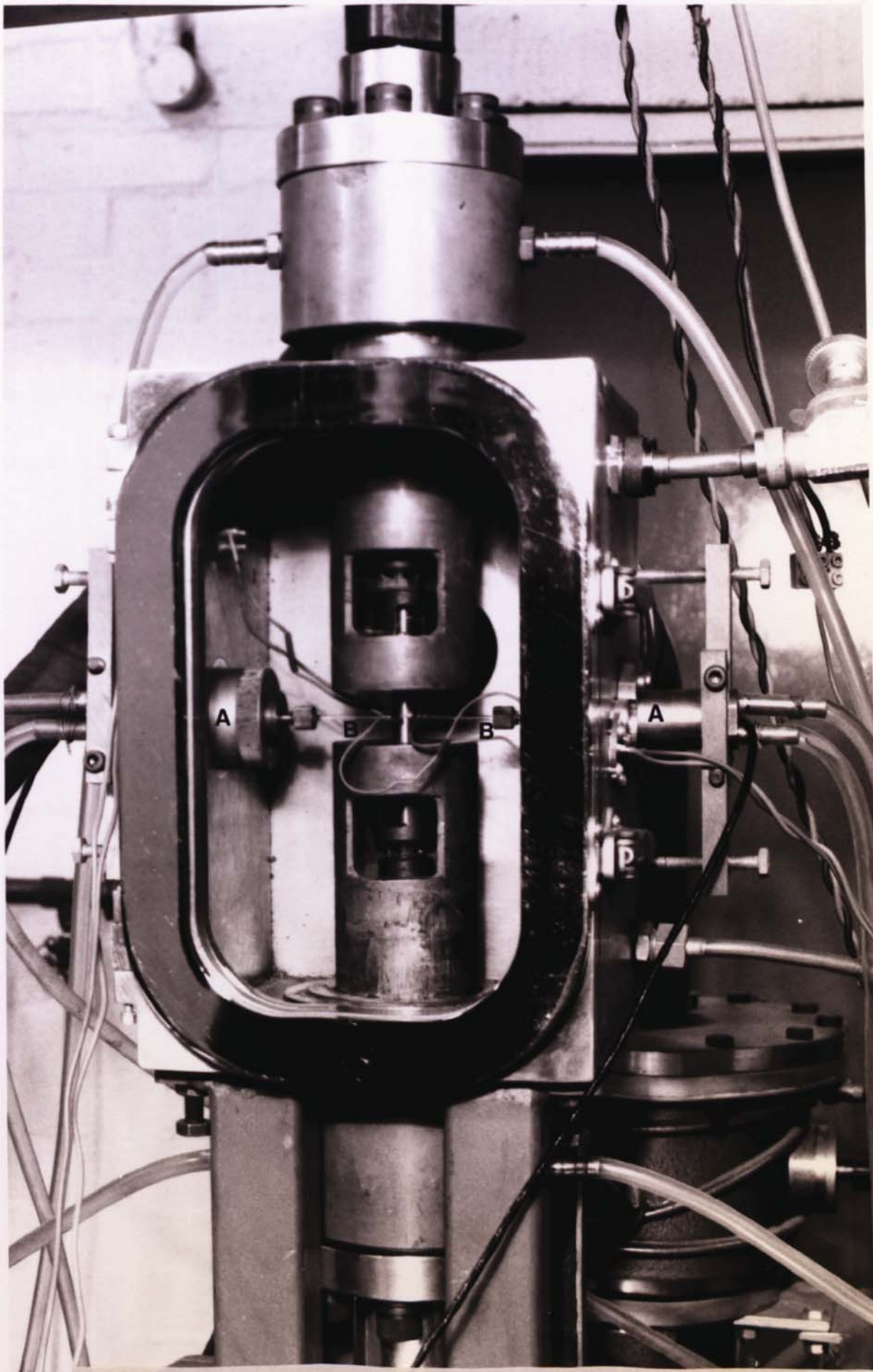


FIGURE 38 Close-up of dilatometer box showing sample prepared for high speed dilatometry

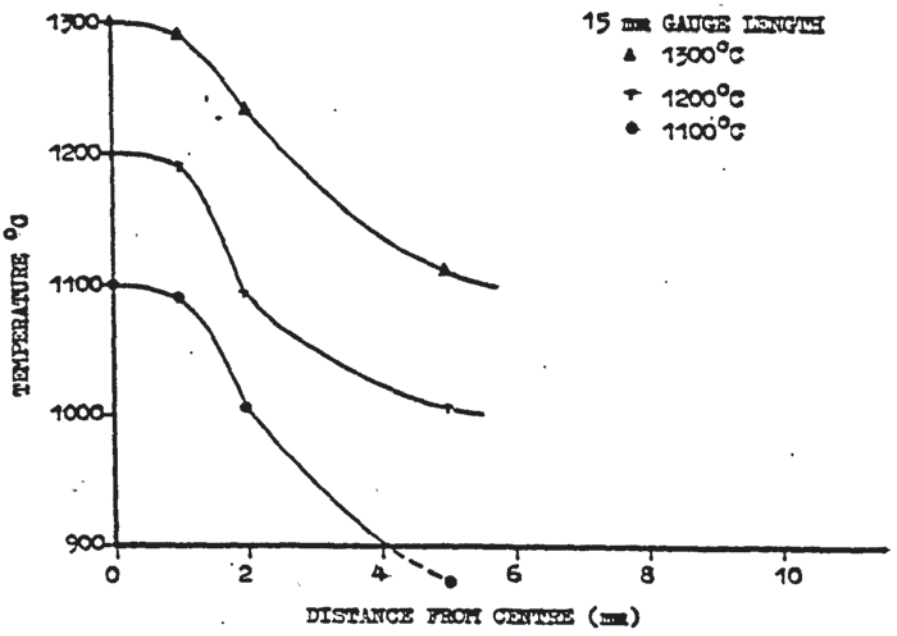


FIGURE 39 Thermal gradients along guage length of a 15 m.m. gauge length x 10 m.m. diameter specimen

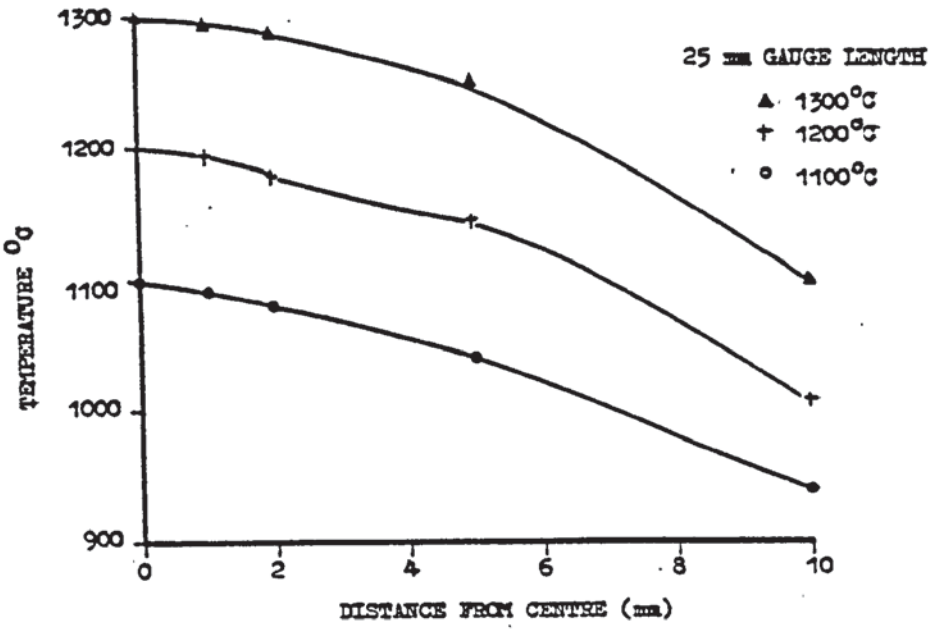


FIGURE 40 Thermal gradients along the gauge length of a 25 m.m. gauge length x 10 m.m. diameter specimen

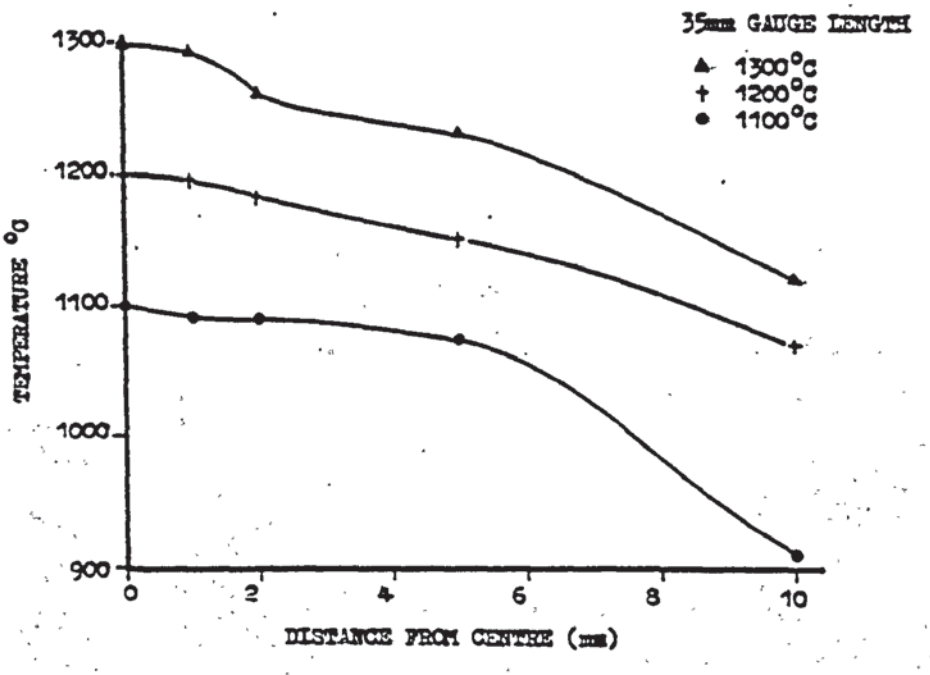


FIGURE 41 Thermal gradients along the gauge length of a 35 mm gauge length x 10 mm diameter specimen

FIGURE 42 Photograph of samples used for dilatometry and thermal simulation (25mm G.L x 6.3 or 10 mm diameter).

FIGURE 43 Natural cooling rates of various size simulator samples from 1350°C peak temperature

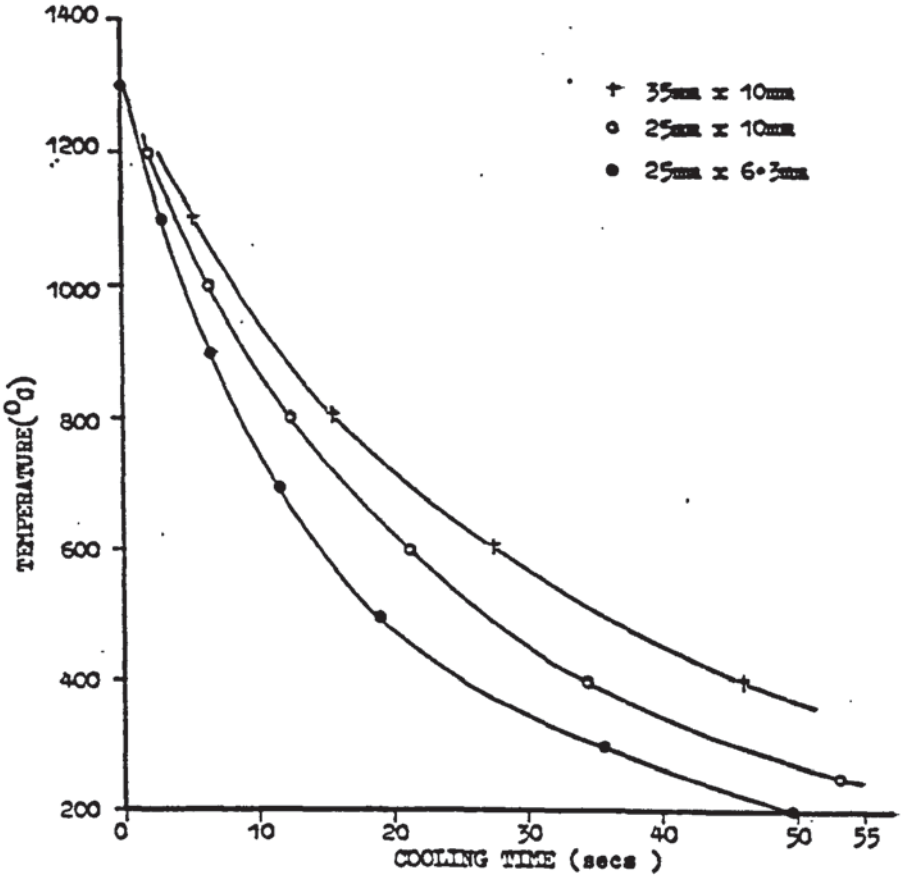


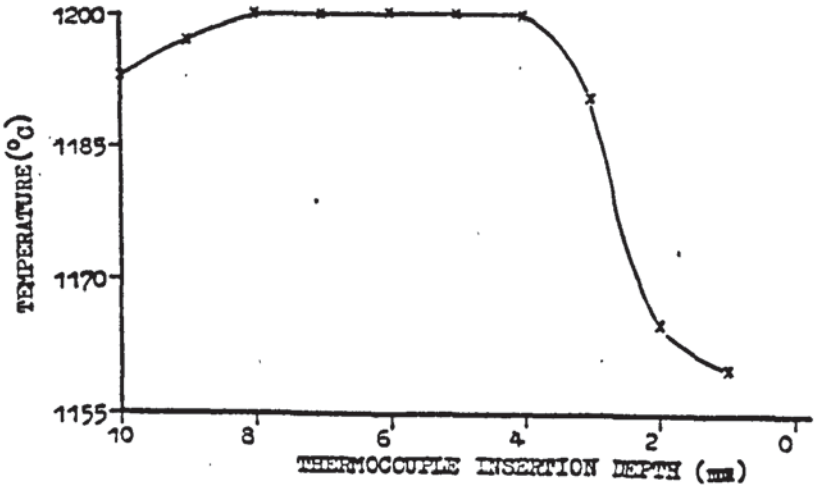


FIGUEE 44 Thermal gradient across a 10 mm diameter sample, measured at gauge length mid-point

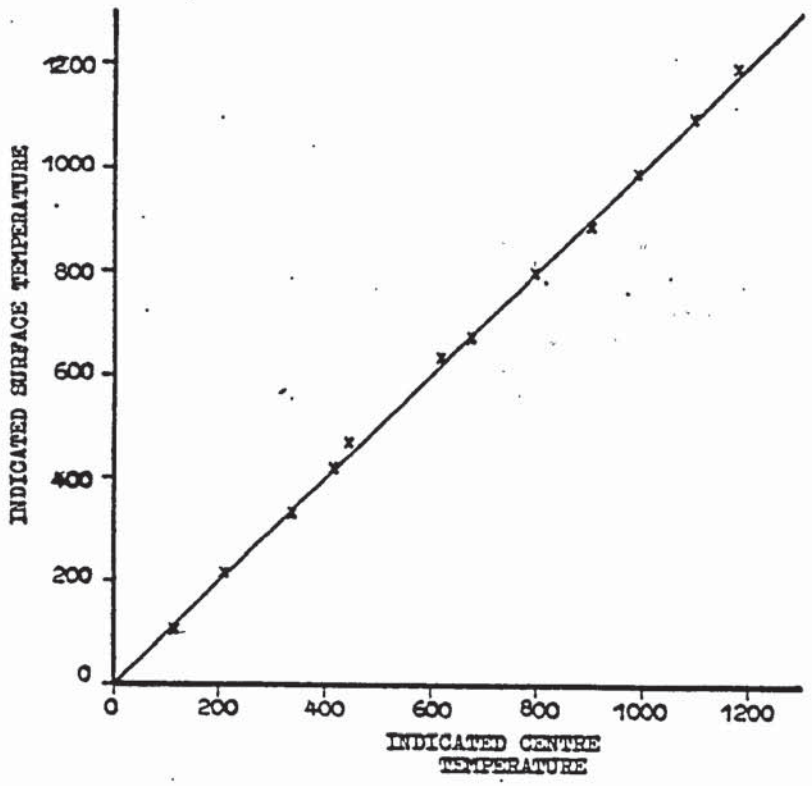


FIGURE 45 Centre v's surface temperature calibrarion chart

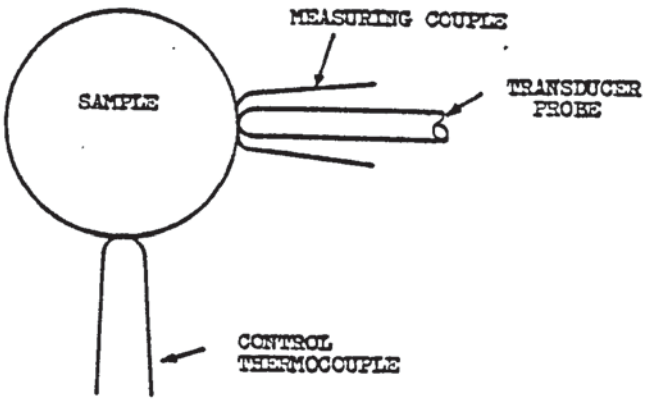


FIGURE 46 Schematic view of thermocouple arrangement employed to measure the effect of transducer probe contact

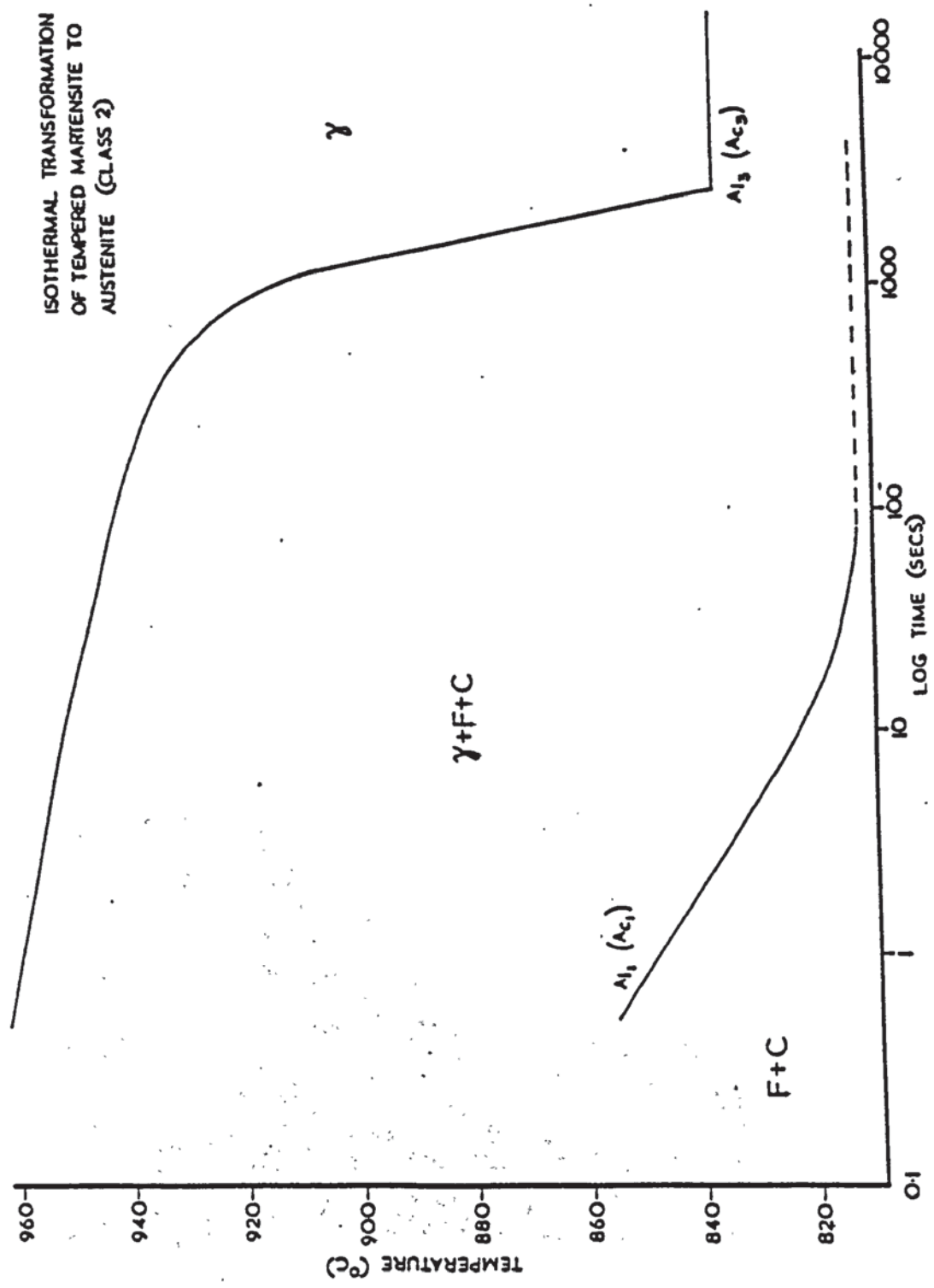


FIGURE 47 The isothermal transformation of tempered martensite to austenite

FIGURE 48

Microstructure of class 2 steel held for over 1000 seconds in $\alpha$-$\gamma$ miscibility region (ie 812 - 836$^{o}$C)

Note: co-existence of tempered martensite and regions of freshly formed martensite (from $\gamma$). Darkly etched material is tempered martensite, lightly etched material is fresh martensite. (x 400, Adlers Reagent)

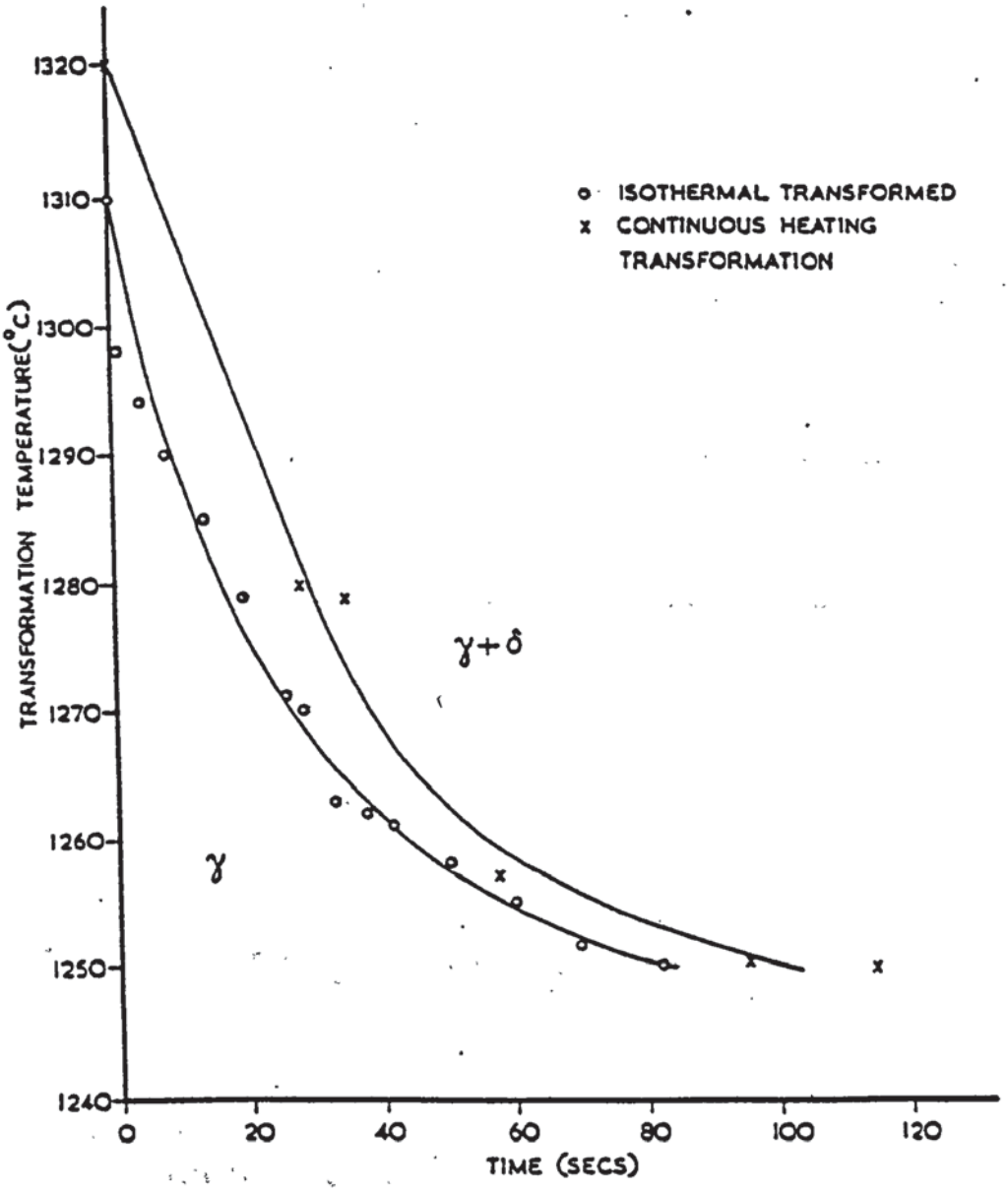


FIGURE 49 Isothermal and continuous heating transformation of austenite to δ ferrite (Class 1)

FIGURE 50 Typical dilatometry test result for Class 2 steel

N.B. Method for identifying change points schematically illustrated

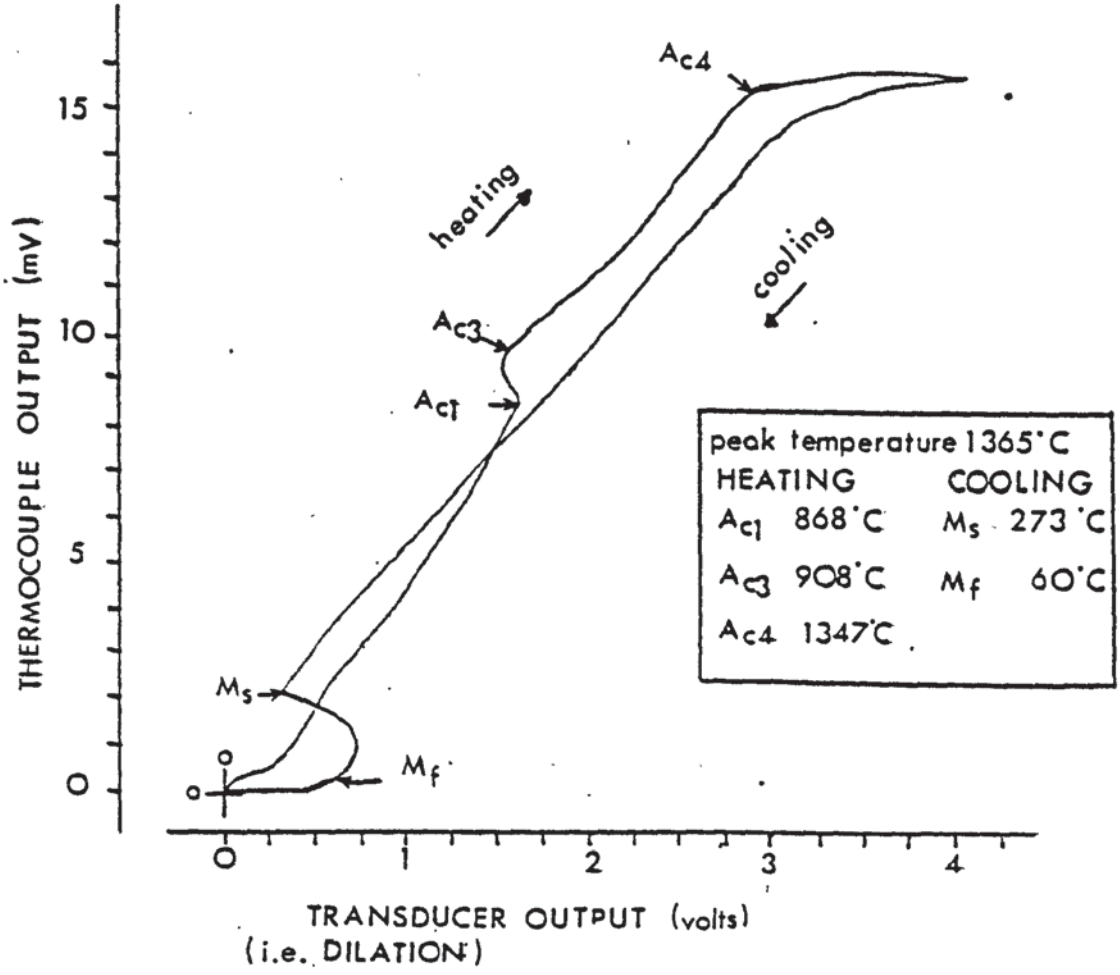


DIAGRAM REDUCED BY 45% FOR REPRODUCTION

## TANGENT METHOD TO IDENTIFY CHANGE POINTS

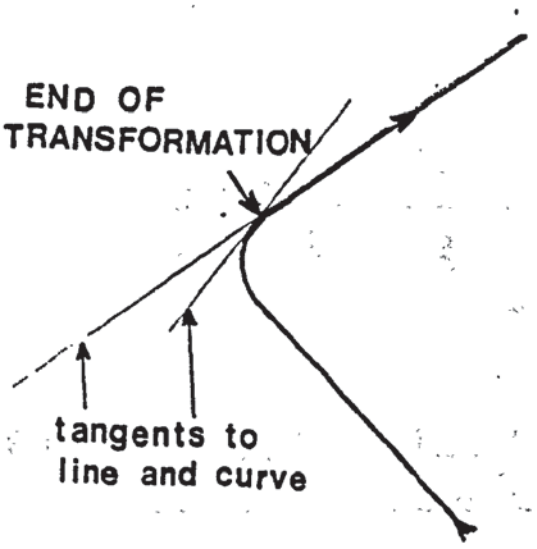

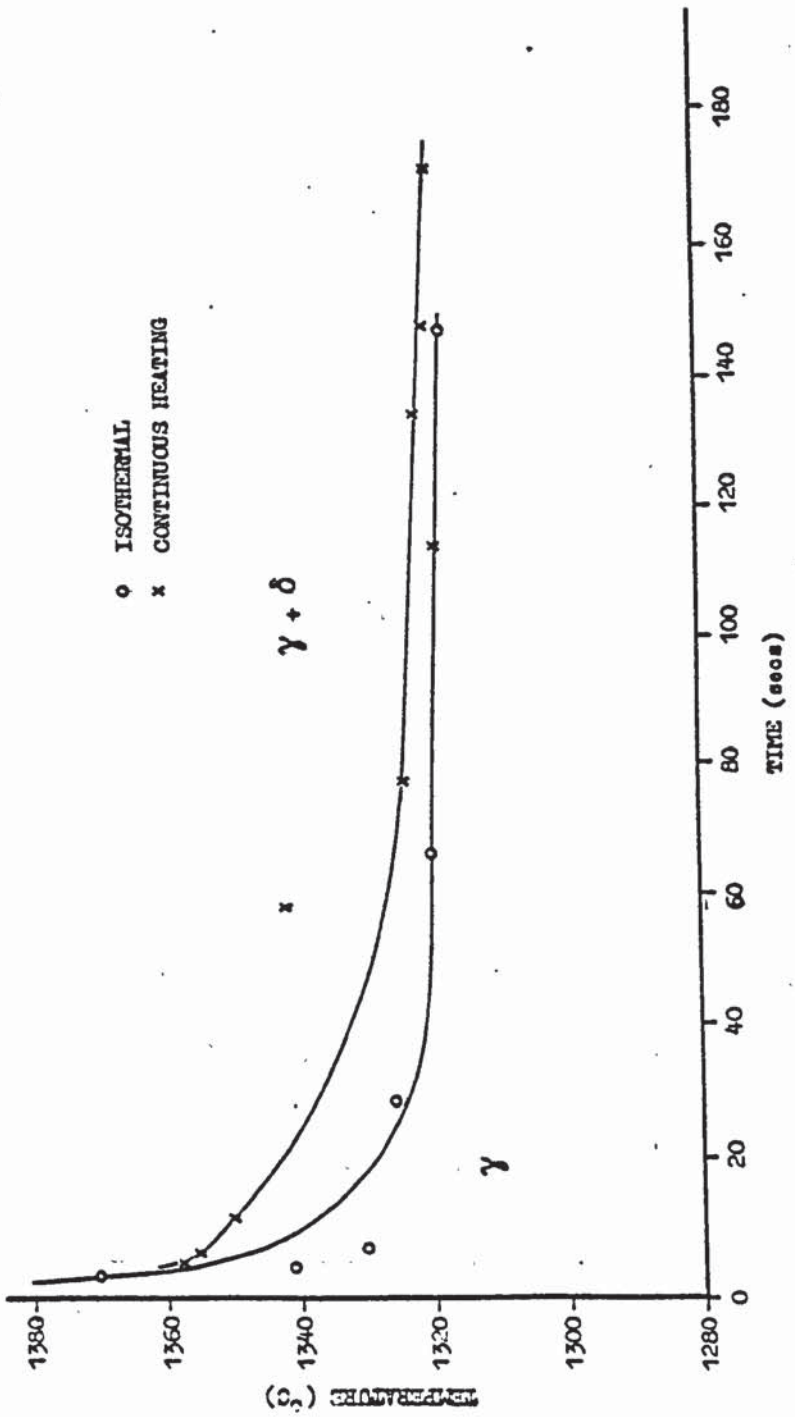


FIGURE 51 Isothermal and continuous heating formation of δ ferrite from austenite in Class 2 steel

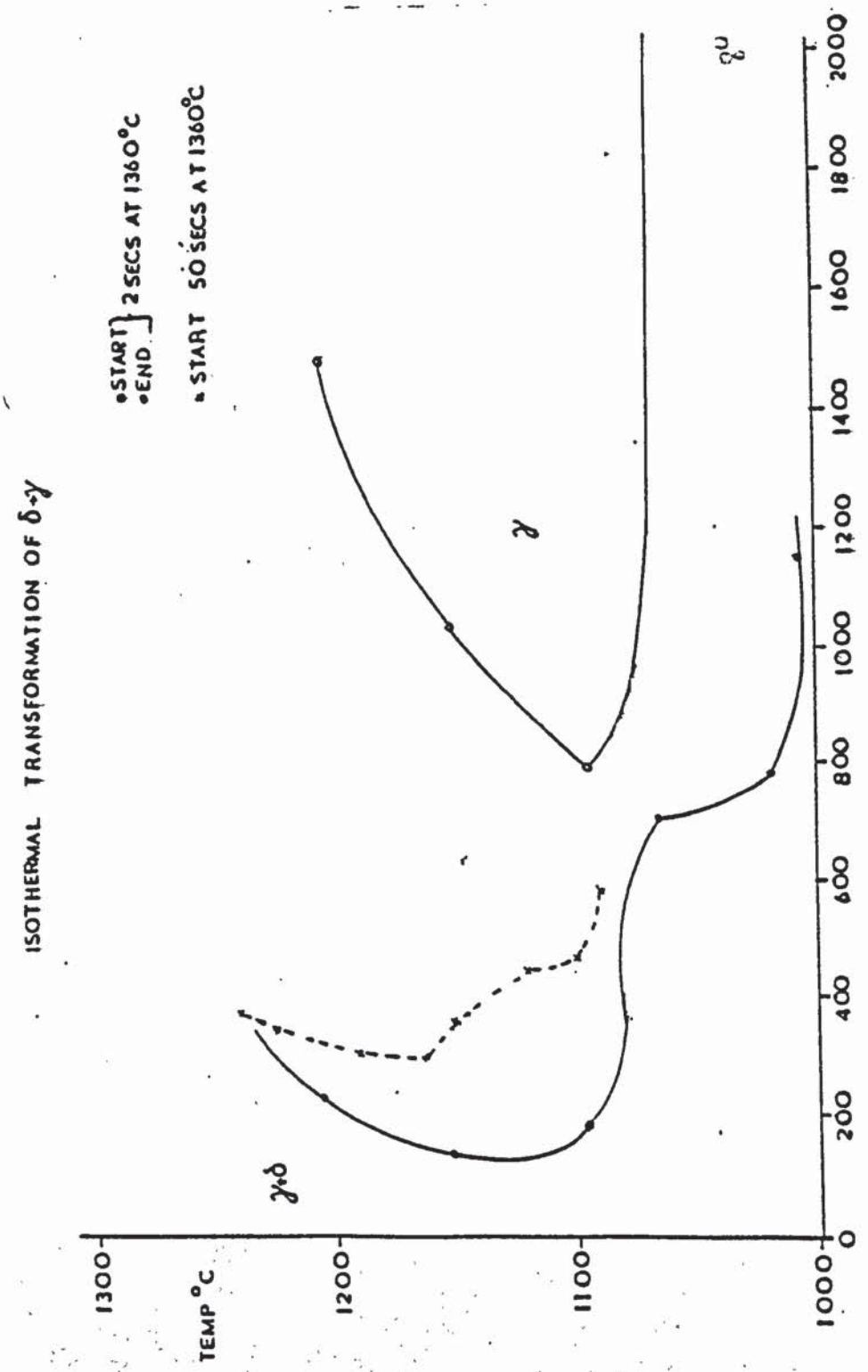


FIGURE 52 Isothermal transformation of δ → γ in Class 2 steel for δ ferrite contents

FIGURE 53 Micrograph showing regions where δ has partly retransformed to γ
(Dark etched region is martensite, light etched areas are δ ferrite)
Note: common directions of γ growth
(x 570, Adlers reagent)

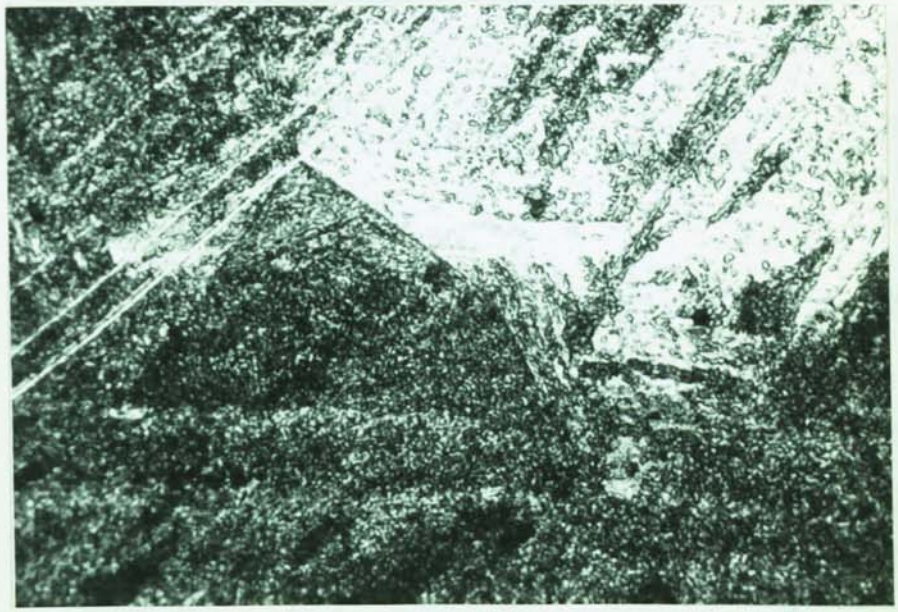

FIGURE 54 Selected area micrograph of figure 53 near well defined δ-martensite grain boundary. Note: gauzy and ill defined grain boundary edge caused by δ transformation to γ
(x 1100 Adlers reagent)

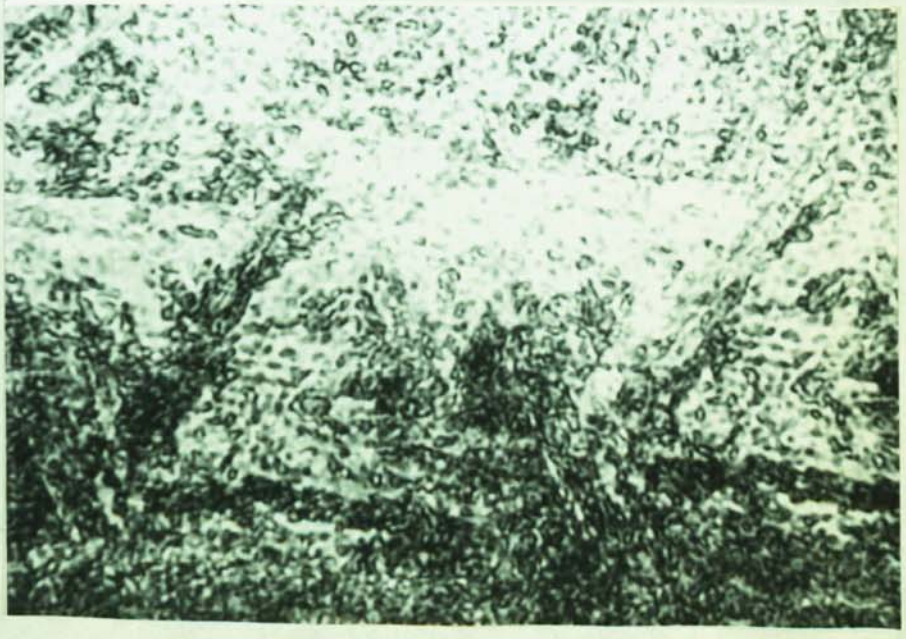

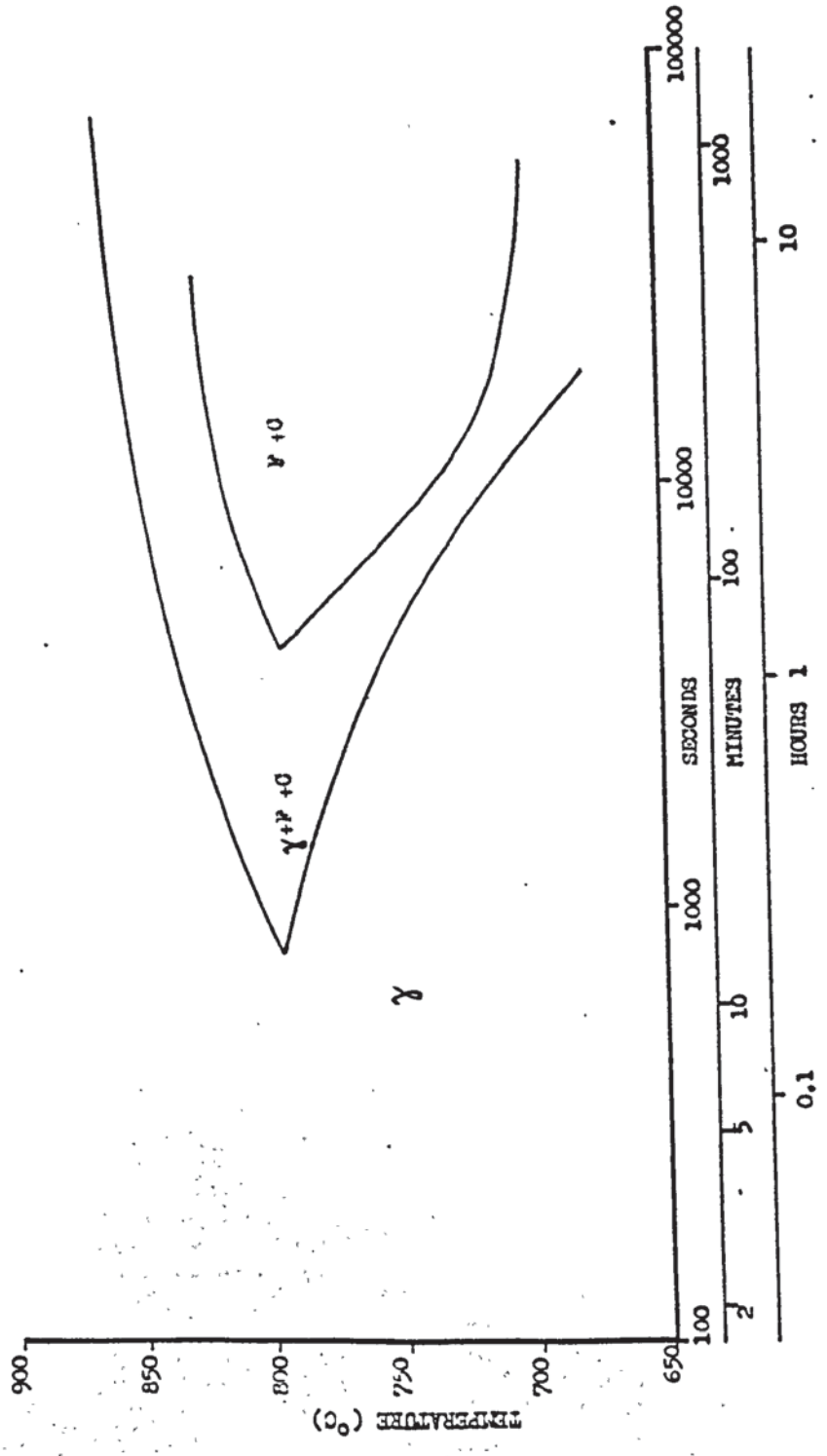


FIGURE 55 Isothermal decomposition of austenite to α ferrite and carbides in Class 2 steel

FIGURE 56 Microstructure of mixed α ferrite and carbides which results from isothermally decomposed γ (class 2 steel)
Note: some α ferrite grain size inhomogenity, α grains being surrounded by carbides.
(x 420, Adlers Etch)

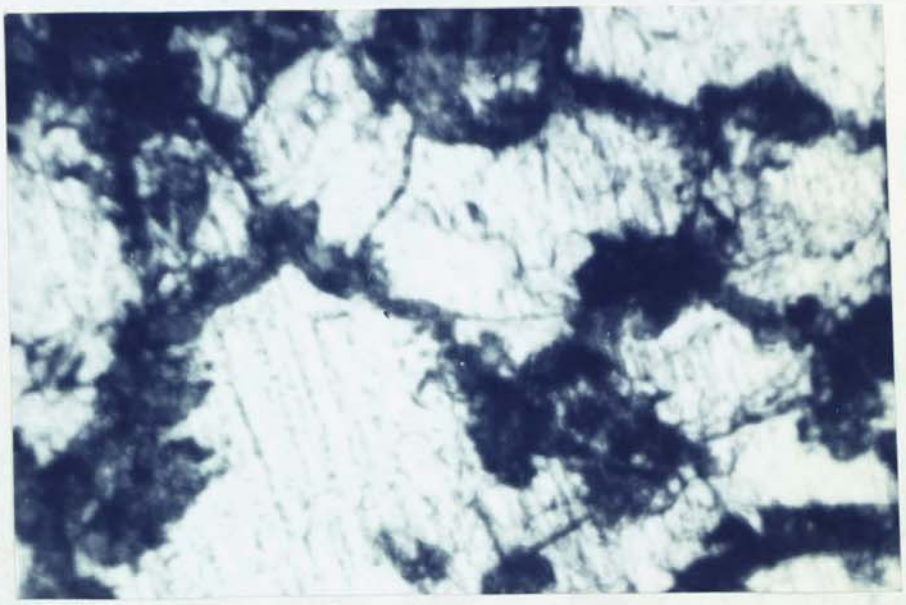

FIGURE 57 Carbides on α ferrite grain boundaries of isothermally decomposed γ. The lamellar carbide orientation is similar to that found in pearlite.
(x 2000 (optical) etched in Adlers reagent)

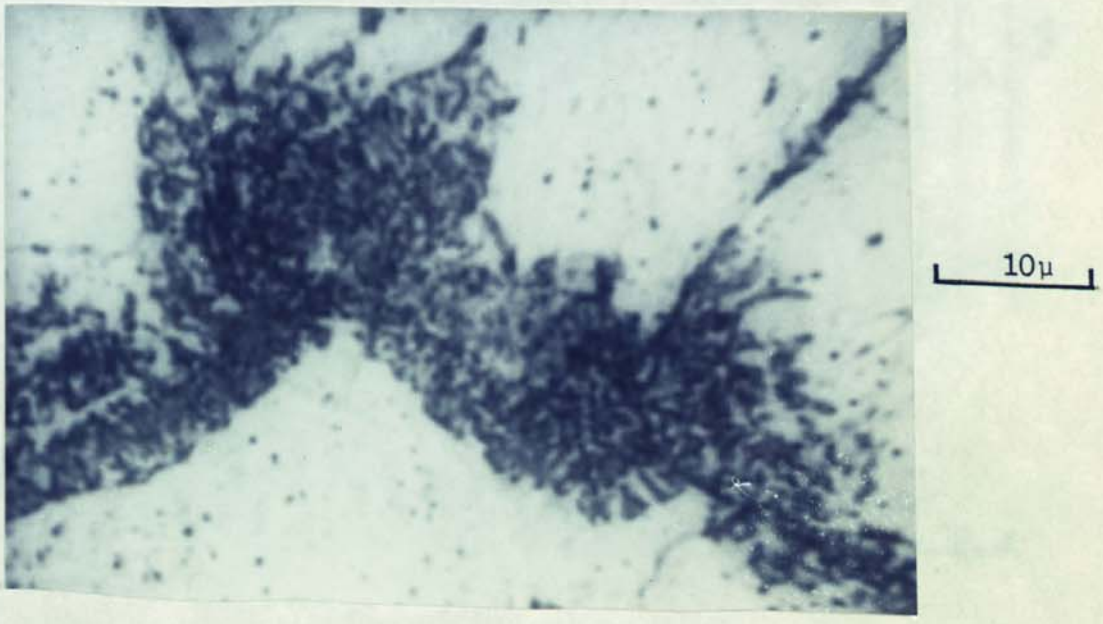

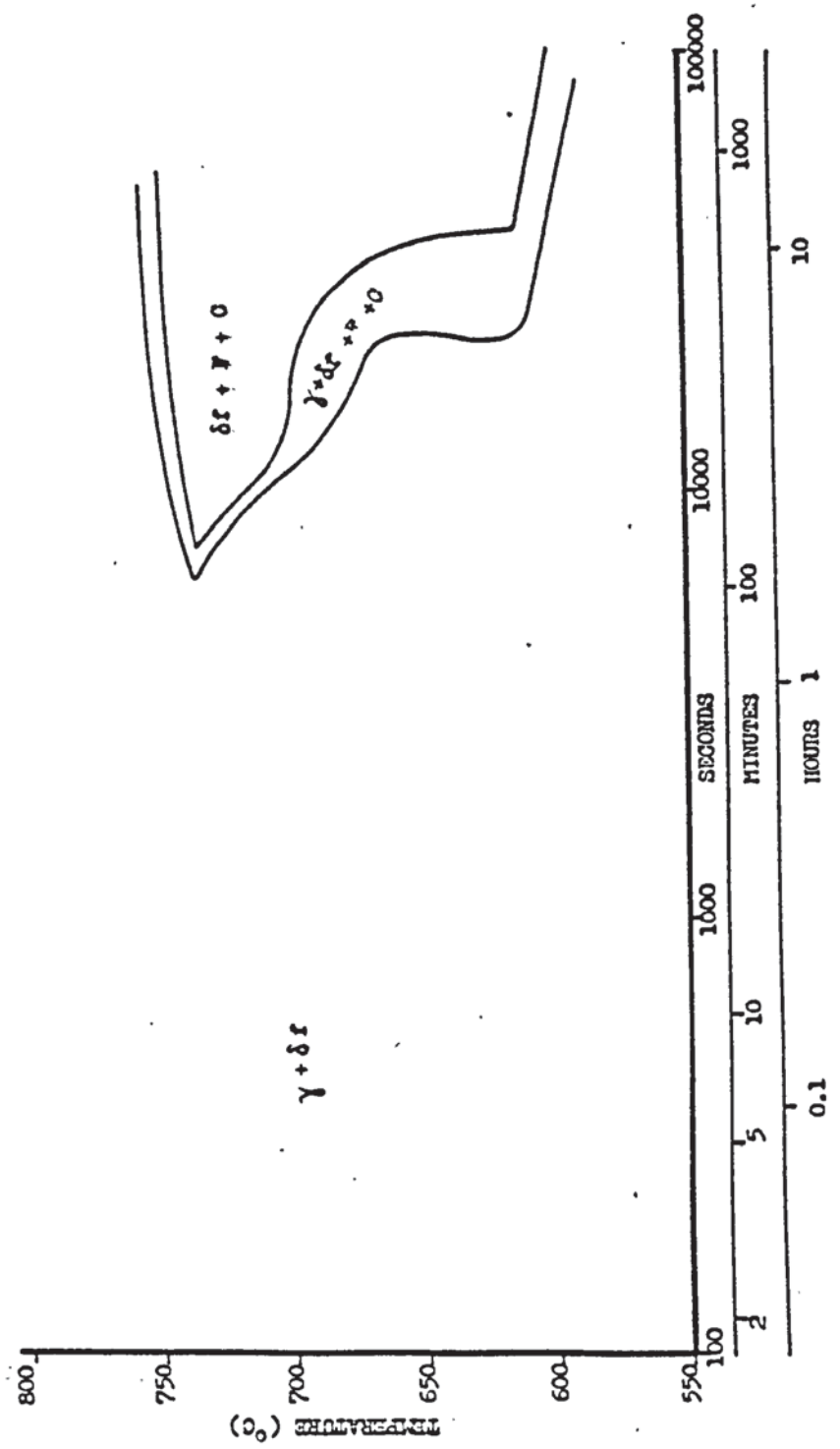


FIGURE 58 Isothermal decomposition of a mixed γ + δ matrix to form δ + α + carbides in a Class 2 steel

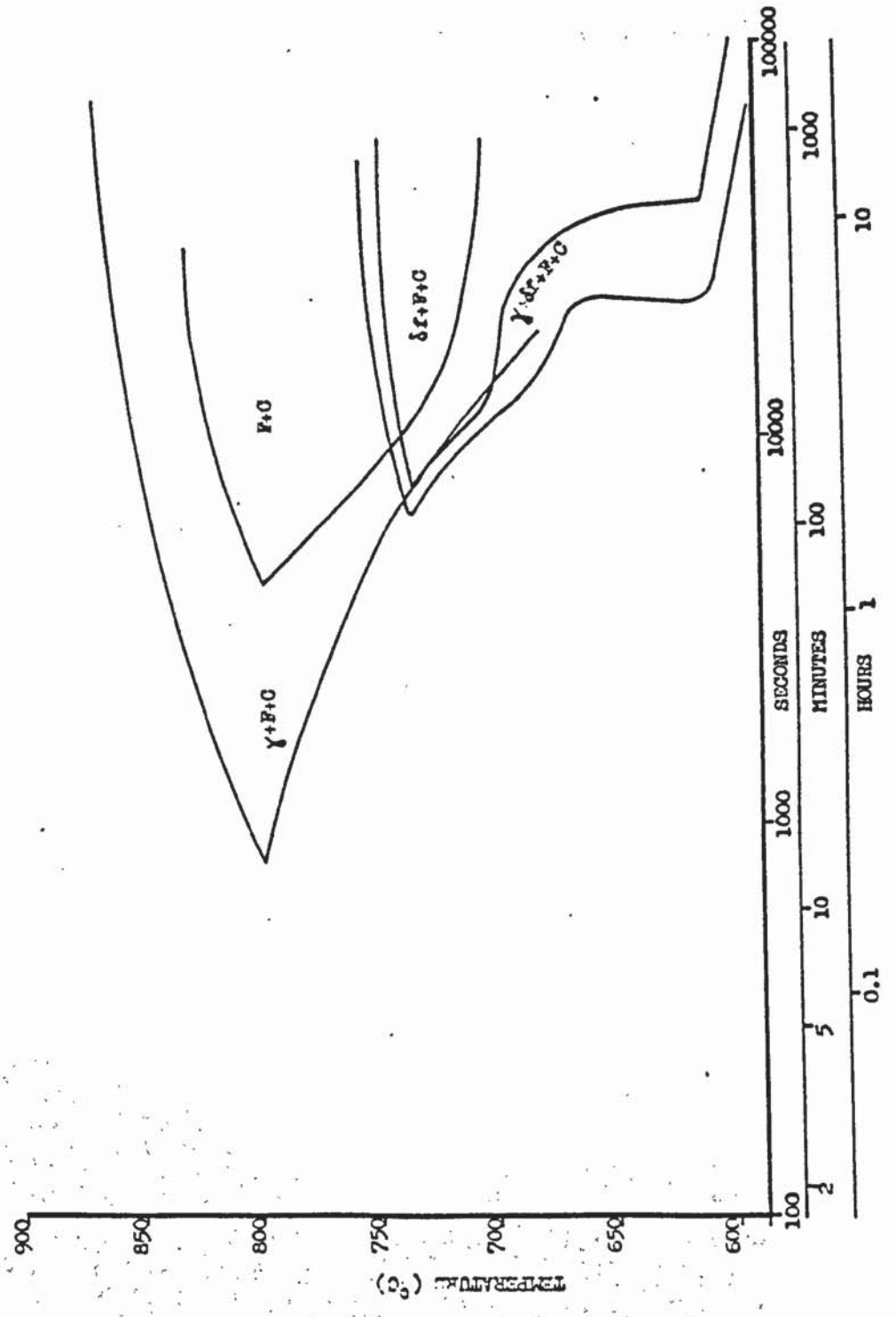


FIGURE 59 Comparison between isothermal decomposition kinetics of homogenous γ and mixed γ + δ matrices

FIGURE 60 Microstructure of isothermally transformed $\gamma+\delta$. Resulting structure is comprised of $\delta+\alpha$ (ferrites) and carbides. Note extreme ferrite grain size inhomogenity (c.f.figure 56) (x 420, Adlers Etchant)

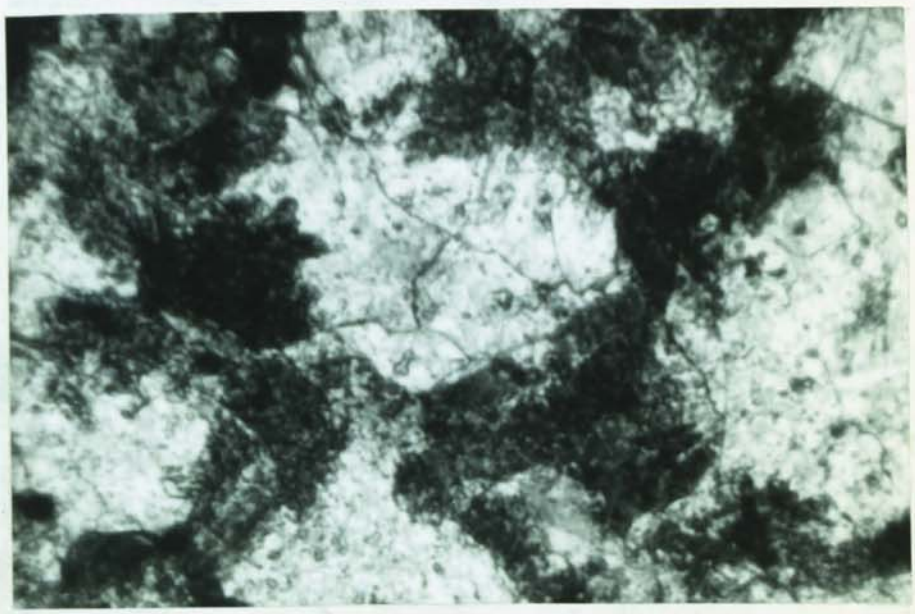

FIGURE 61 Carbides on ferrite grain boundary in isothermally transformed $\gamma+\delta$.
Carbides have the pearlite type lamellar pattern as in figure 57.
(x 2000 (optical), Adlers Reagent)

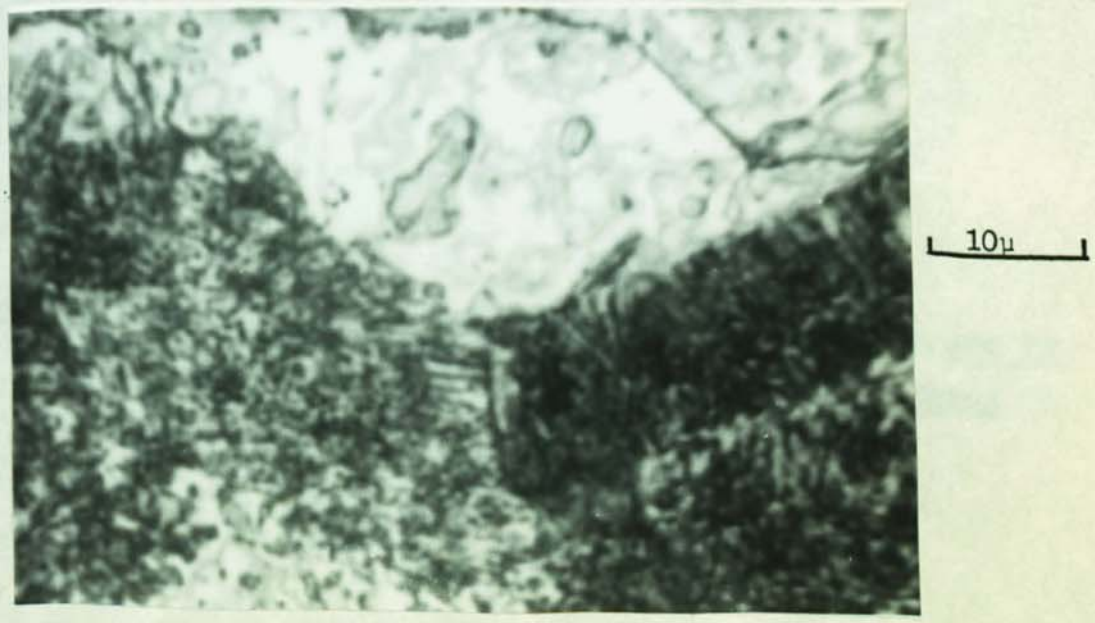

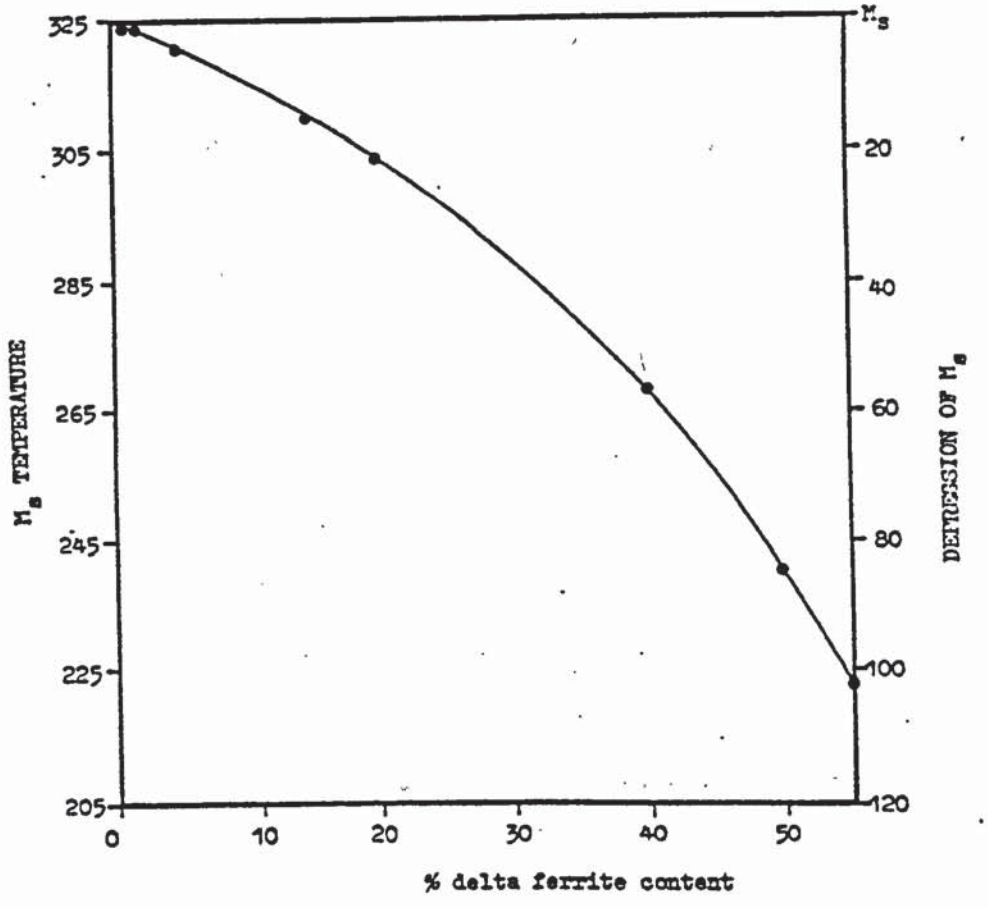


FIGURE 62 Theoretical depression of Ms temperature by quantities of δ ferrite in Class 1 steel

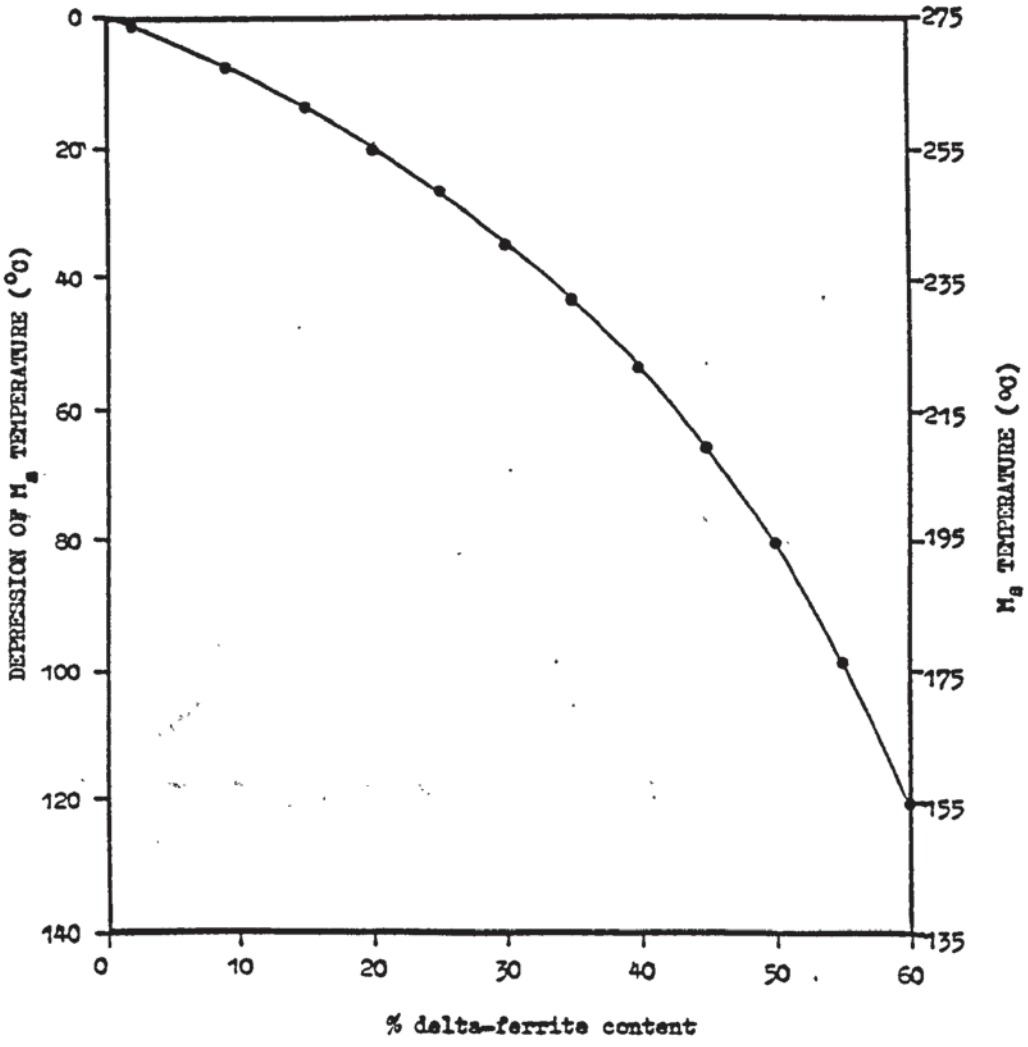


FIGURE 63 Theoretical depression of Ms temperature by quantities of δ ferrite in Class 2 steel

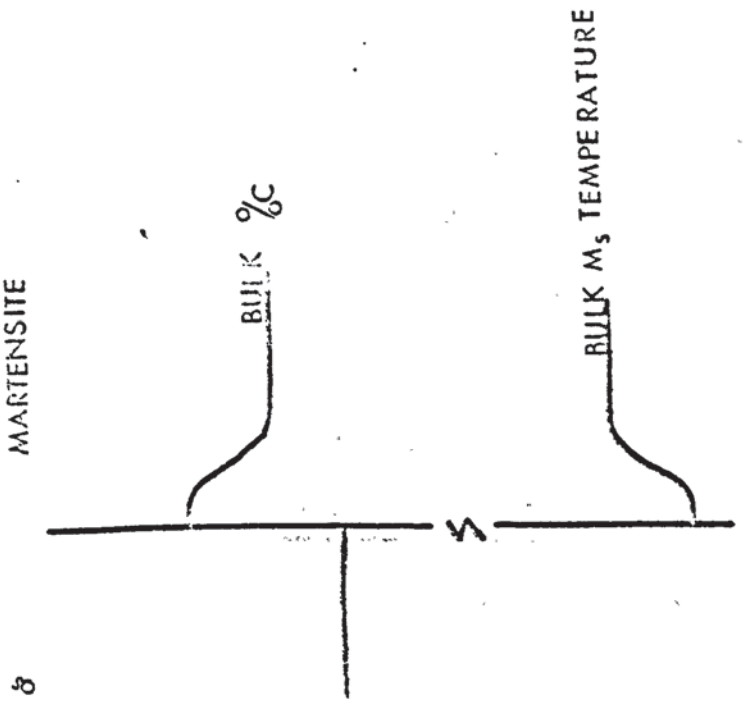


FIGURE 64 Schematic representation of Ms depression around δ regions due to limited carbon diffusion.

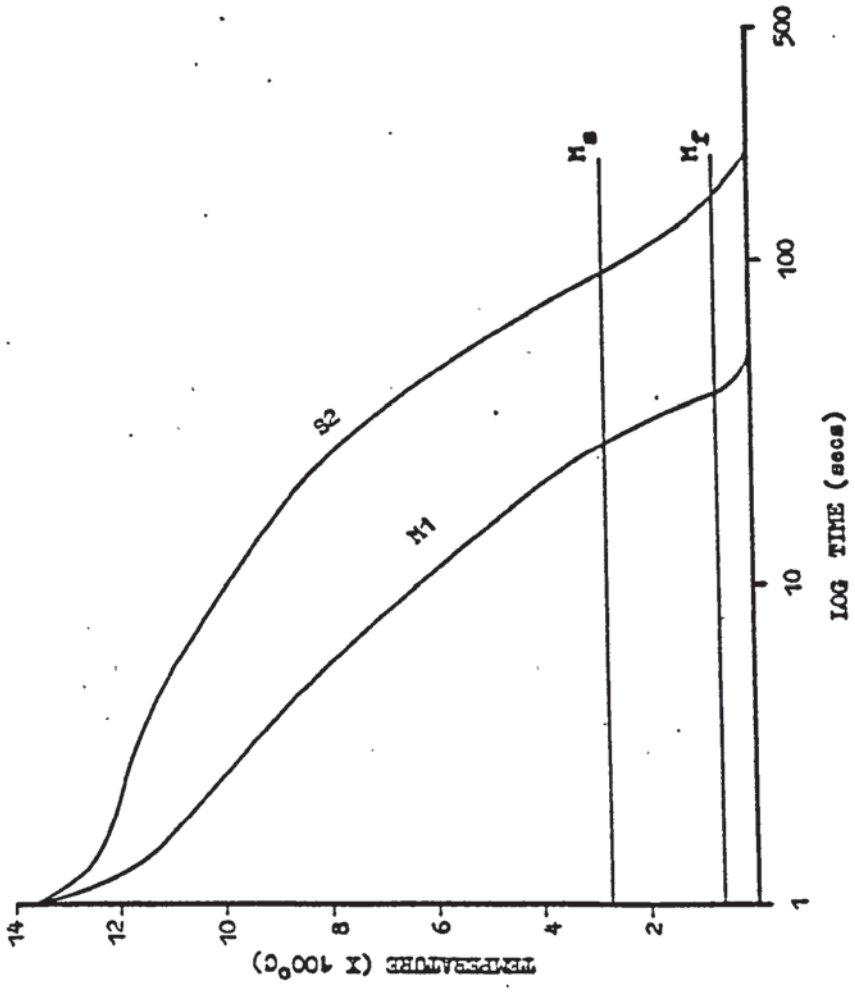


FIGURE 65 CCT diagram produced from computed weld HAZ thermal cycles

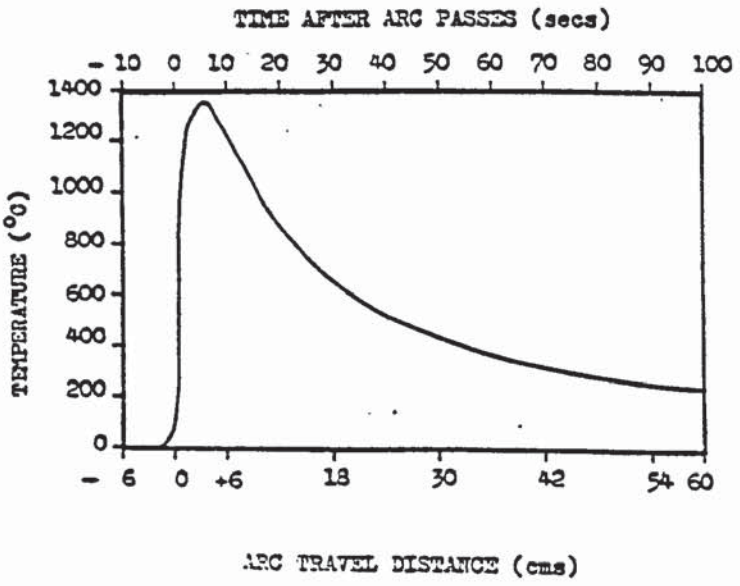


FIGURE 66 Thermal cycle determined for theoretical weld I1 (high heat input submerged arc) with a peak temperature of 1360°C

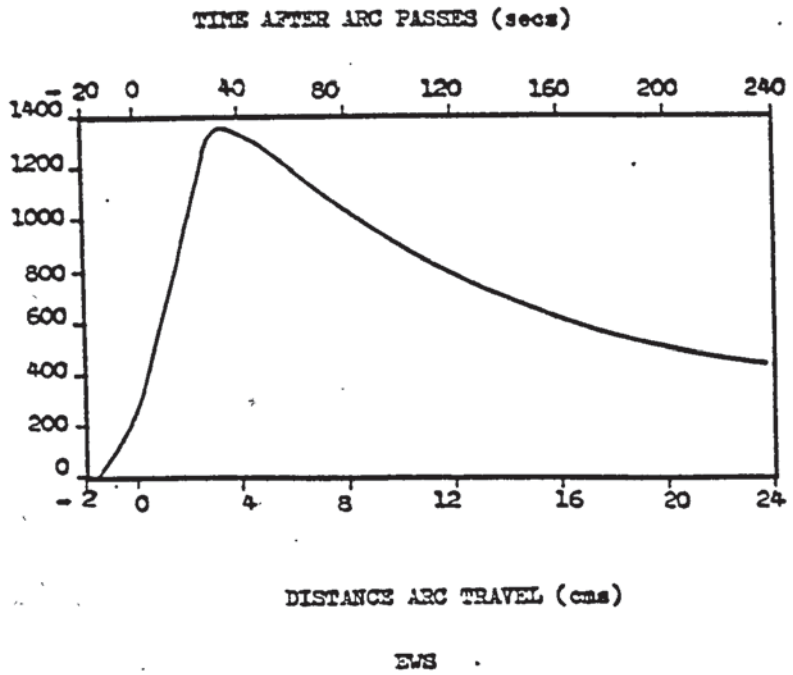


FIGURE 67 Weld HAZ thermal cycle for theoretical weld ESW (electro-slag weld) with a peak temperature of 1360°C

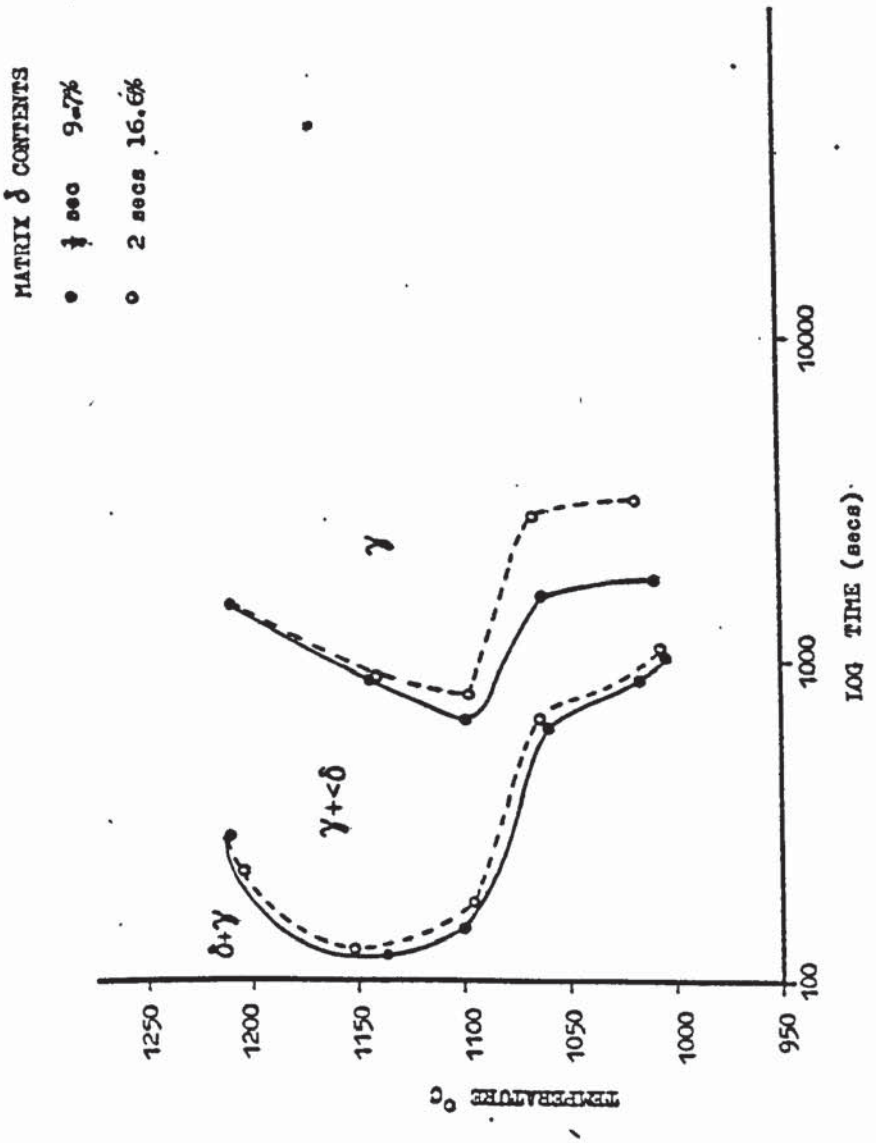


FIGURE 68 Isothermal decomposition of δ to γ in two matrices containing 9.7 and 16.6% δ ferrite

FIGURE 69 Isothermal decomposition of two mixed γ + δ matrices to δ + α + carbides

FIGURE 70 Microstructure of slowly cooled ferritised sample. Cooling rate was sufficiently slow to cause some reversion of $\delta$ to $\gamma$ and then $\gamma$ to $\alpha$ and carbides.
(x 1100, Adlers Reagent)

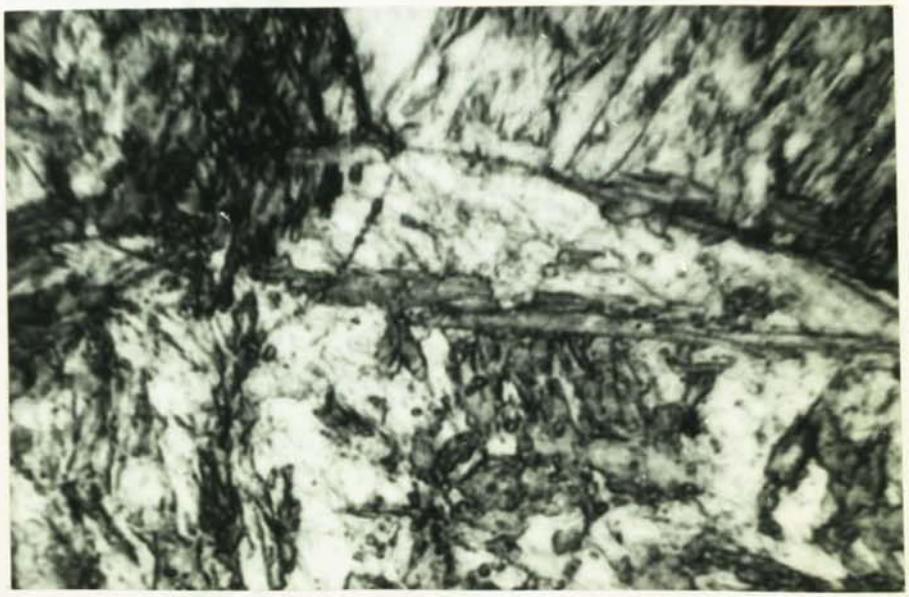

Microstructure consists of untransformed $\delta$, some $\alpha$ ferrite and carbides and lath martensite which formed from untransformed $\gamma$.

10μ

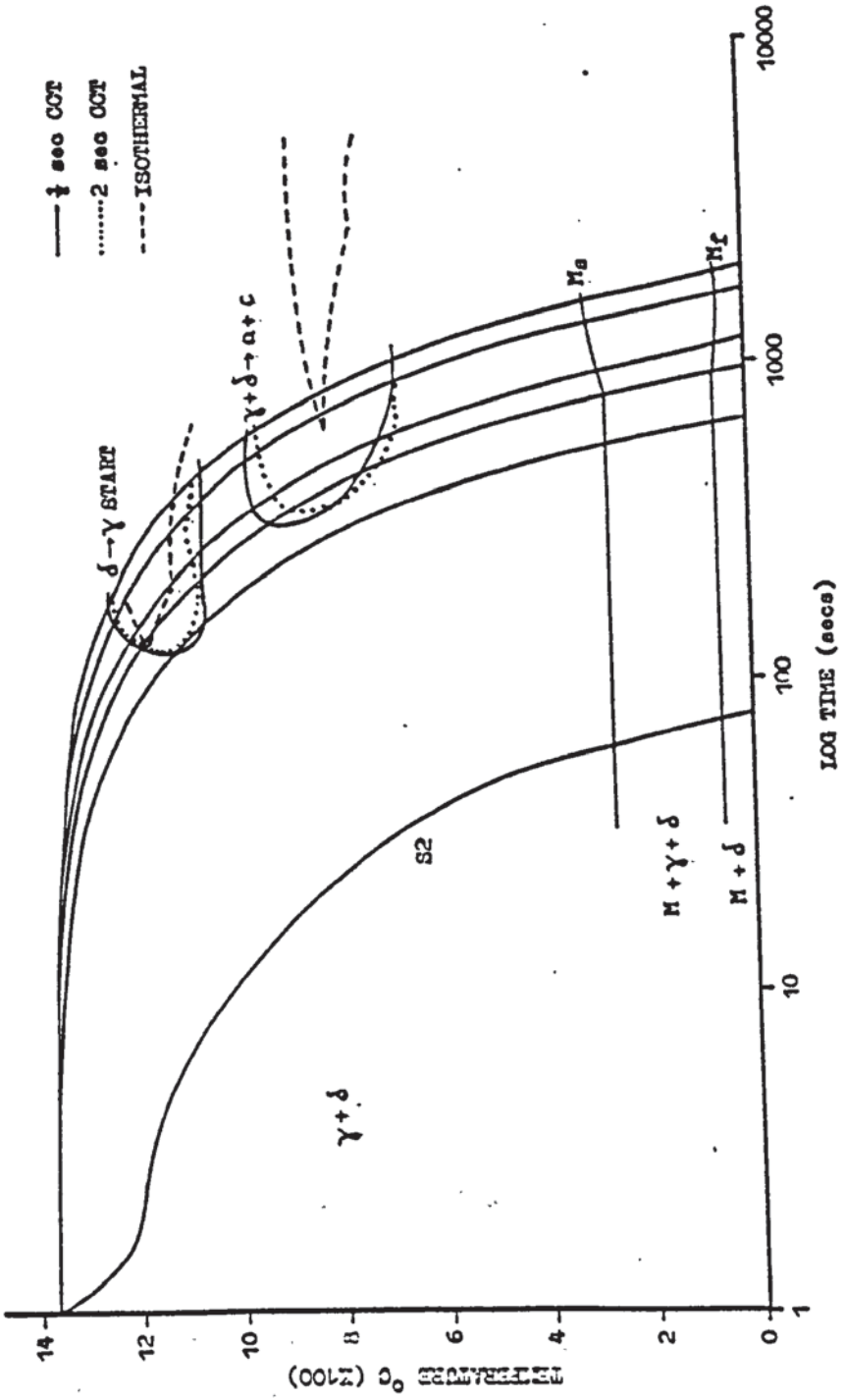


FIGURE 71 CCT diagram showing δ decompositions on cooling for 2 matrices containing 9.7 and 16.6 % δ respectively. Peak temperature 1360°C
(NB δ finish kinetics not shown)

FIGURE 73(A) Micrographs of 1360°C peak temperature isotherm in real and simulated samples of weld T1

Note: similar quantities and shapes of δ in both samples (δ is unetched regions)
(Both x 2000, etched in Adlers reagent)

Real

10μ

Simulated

FIGURE 73 (B) Micrographs of 1360°C peak temperature isotherm in real and simulated samples of weld T2

Note: similar dispersions, shapes and quantities of δ, the unetched material, in both microstructures.

(Both x 1100, Adlers reagent).

Real

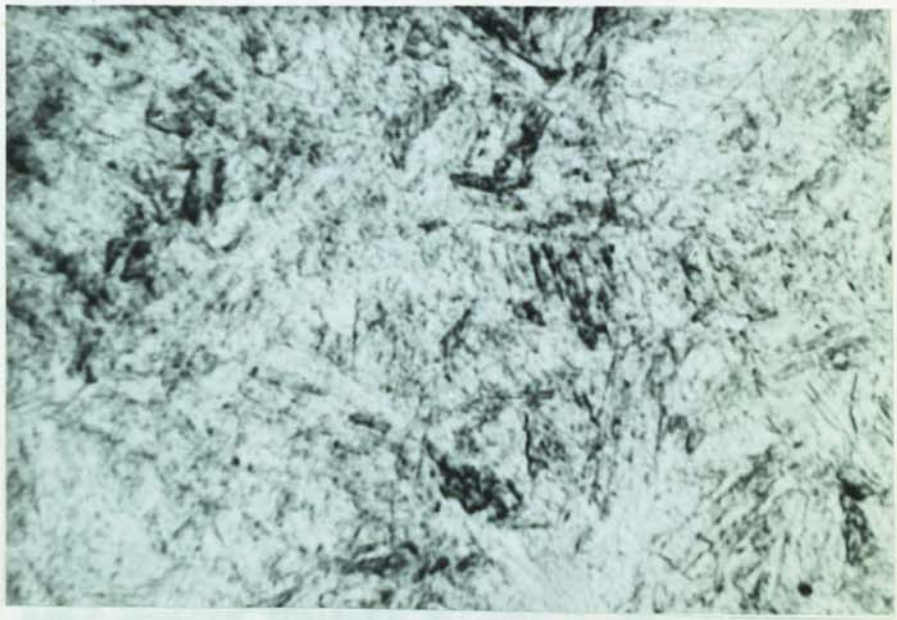

10μ

Simulated

FIGURE 74(B) Microstructure of 1360°C peak temperature isotherm in real and simulated samples of weld M2

Note: similarities in the dispersion of δ throughout the lath martensite.

(Both x 1000, Adlers reagent).

Real

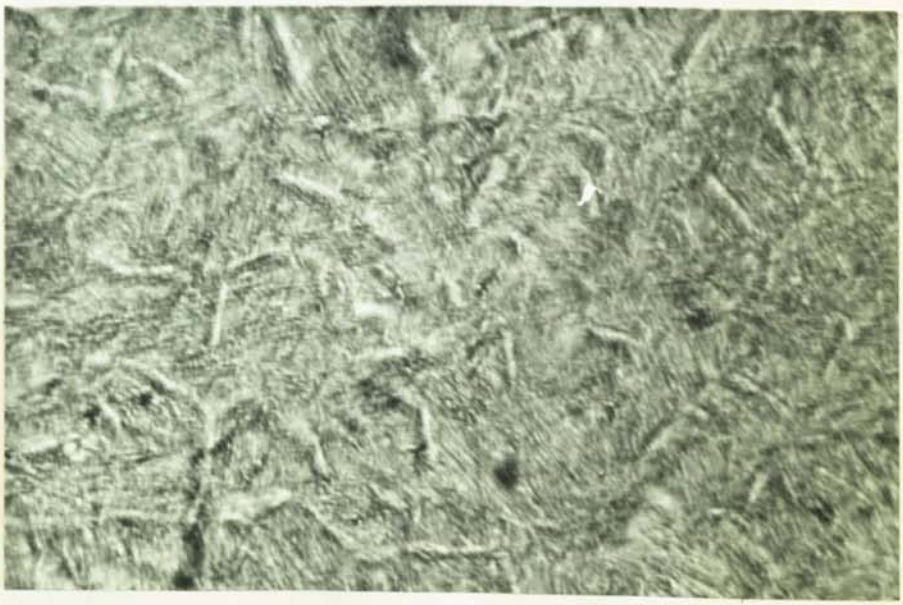

Simulated

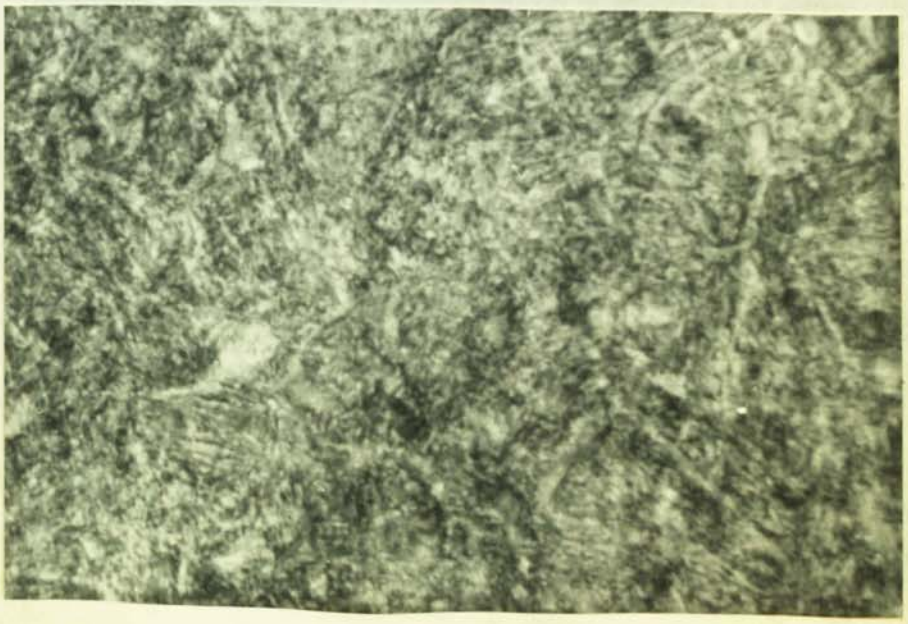

FIGURE 75(A) Microstructure of 1360°C peak temperature isotherm in real and simulated samples of weld R1.
Note: similarity of both microstrctures with equal δ dispersions.
(Both x 1000, Adlers etch)

Real

Simulated

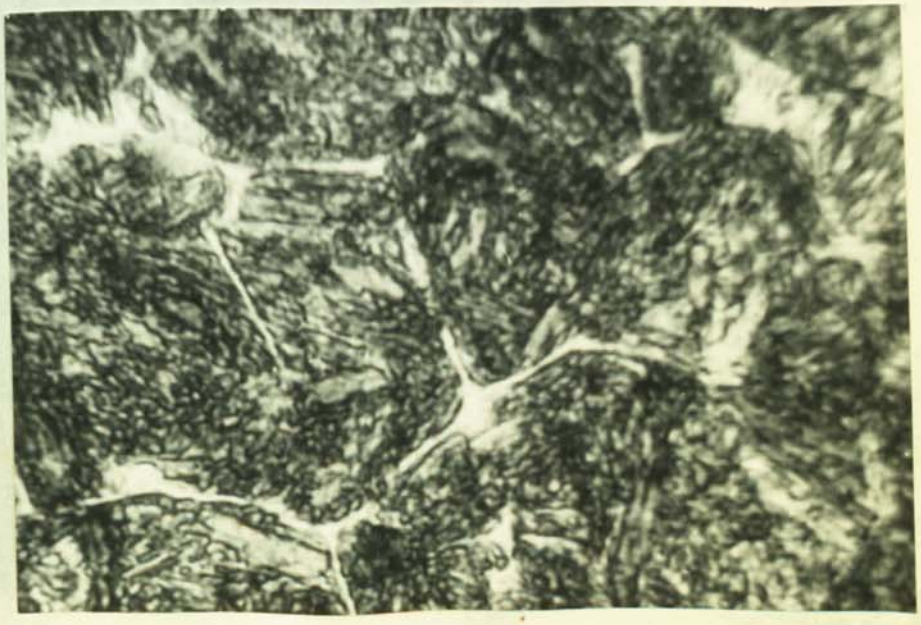

FIGURE 75(B) Microstructure of 1360°C isotherms in real and simulated samples of weld R2.

Note: close similarity between δ dispersion and prior austenite grain size.

(Both x 1000, Adlers etch)

Real

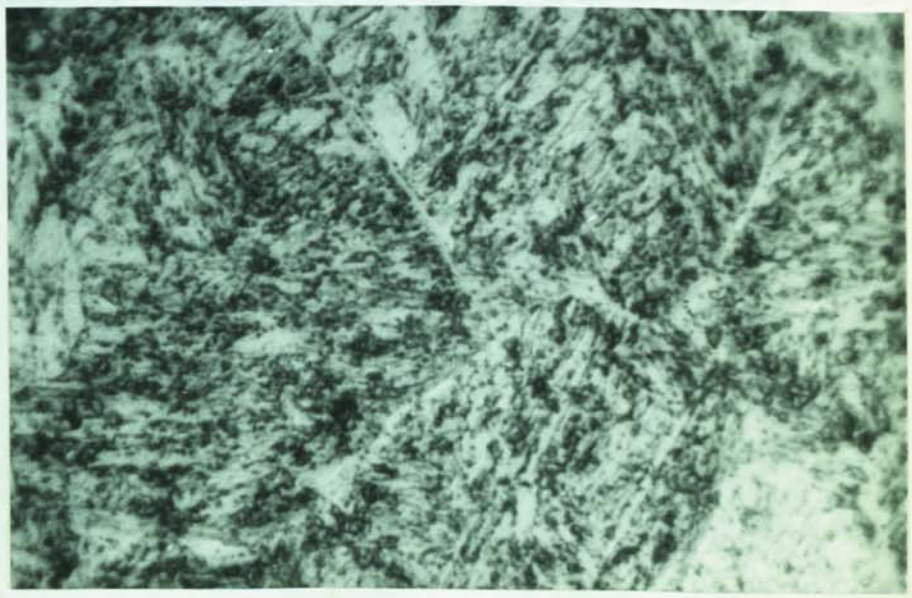

Simulated

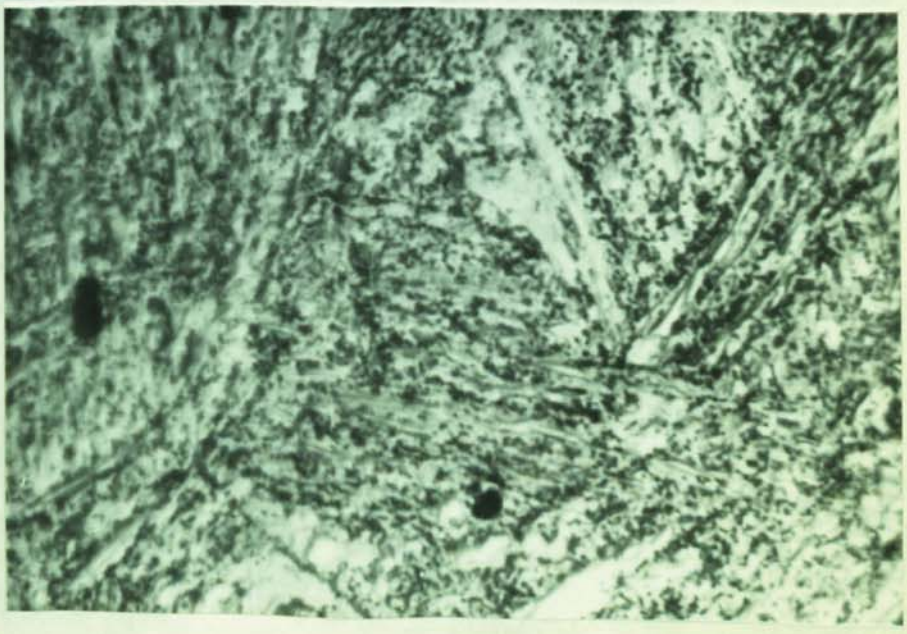

FIGURE 76(A) Microstructure of 1360°C isotherm of real and simulated samples in weld S1.

Note: both structure show very similar shapes and dispersions of δ with equal prior austenite grain size.

(Both x 1000, Adlers etch)

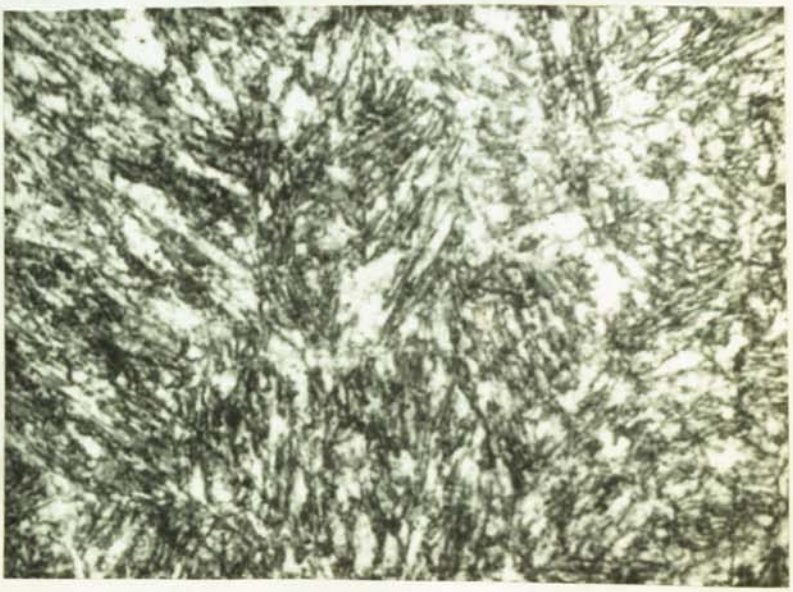

Real

Simulated

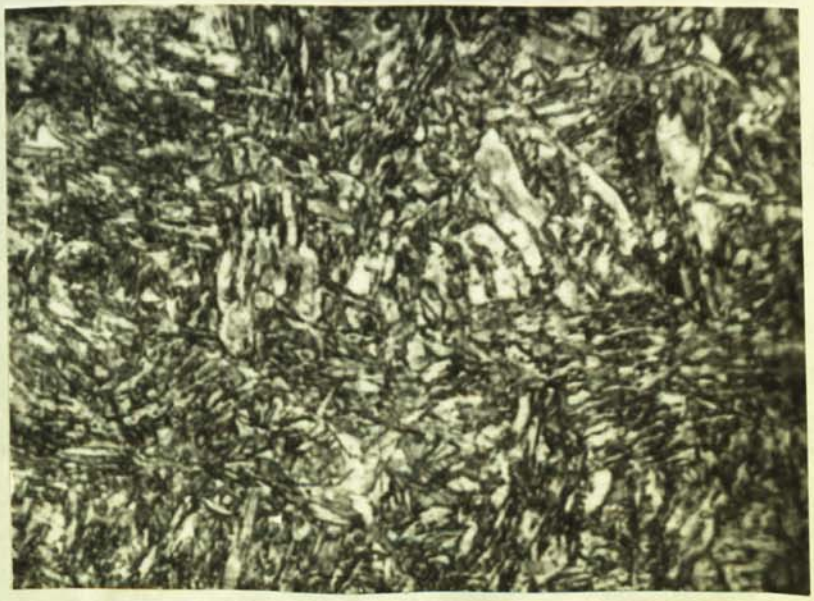

FIGURE 76(B) Microstructure of 1360°C isotherm of real and simulated samples of weld S2.
Note:similar prior austenite grain size and δ quantities in both samples.
(Both x 1000, Adlers etch).

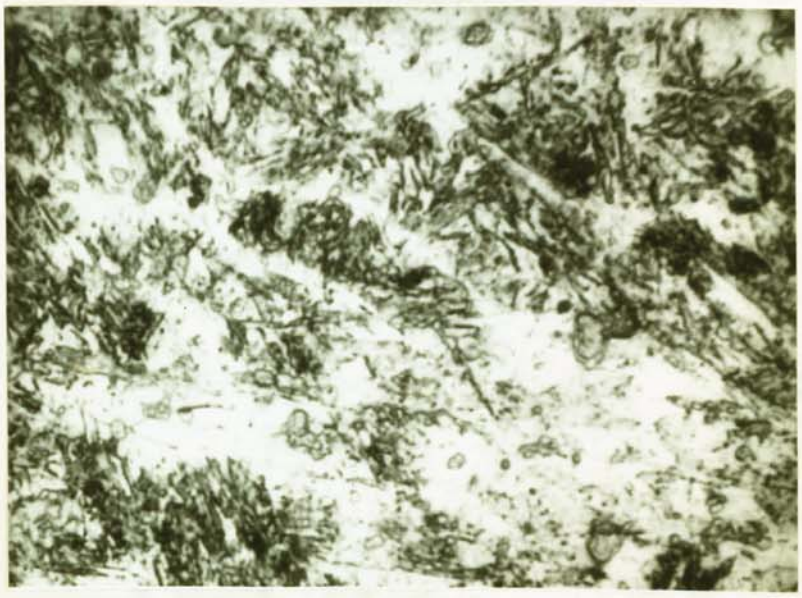

Real

Simulated

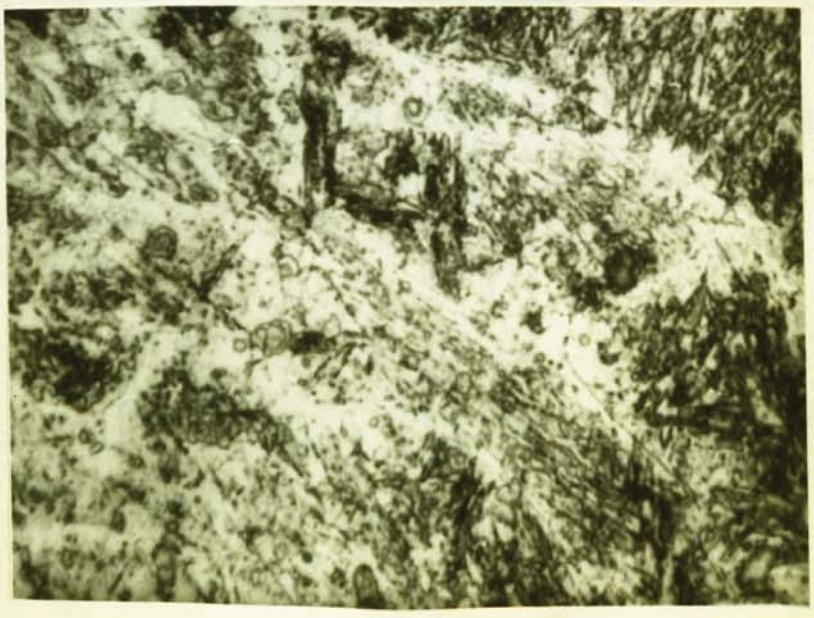

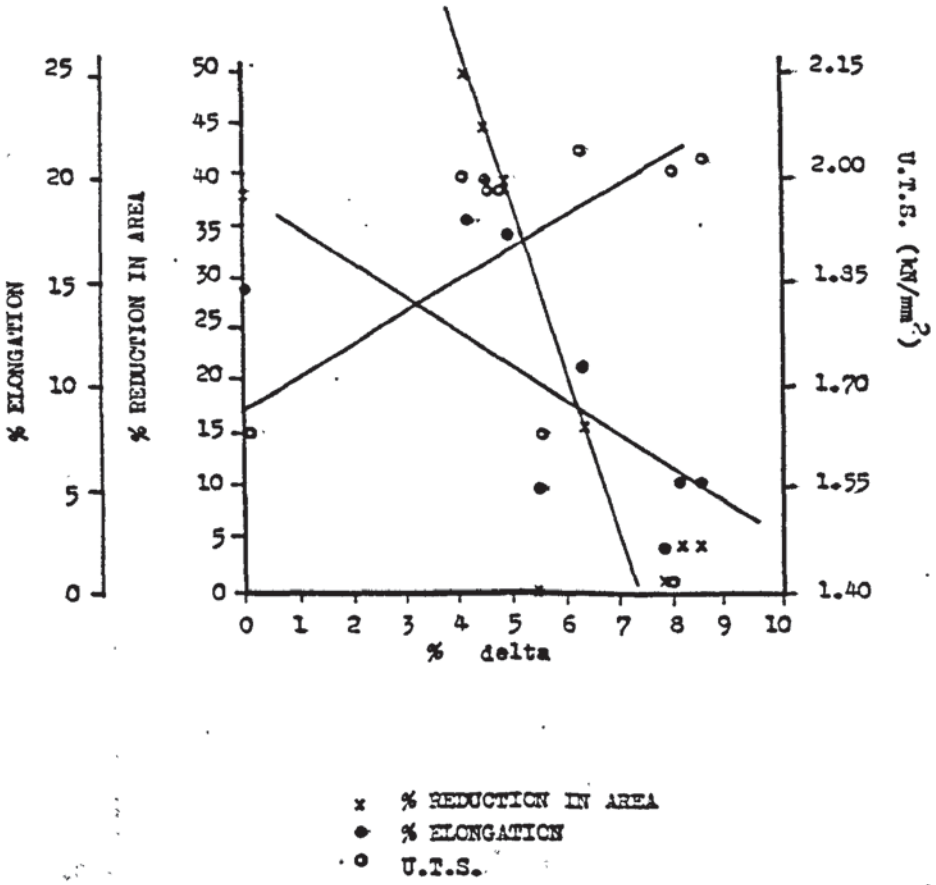


FIGURE 77 The effect of δ ferrite content on tensile strength, % reduction in area and % elongation values of the Class 2 steel

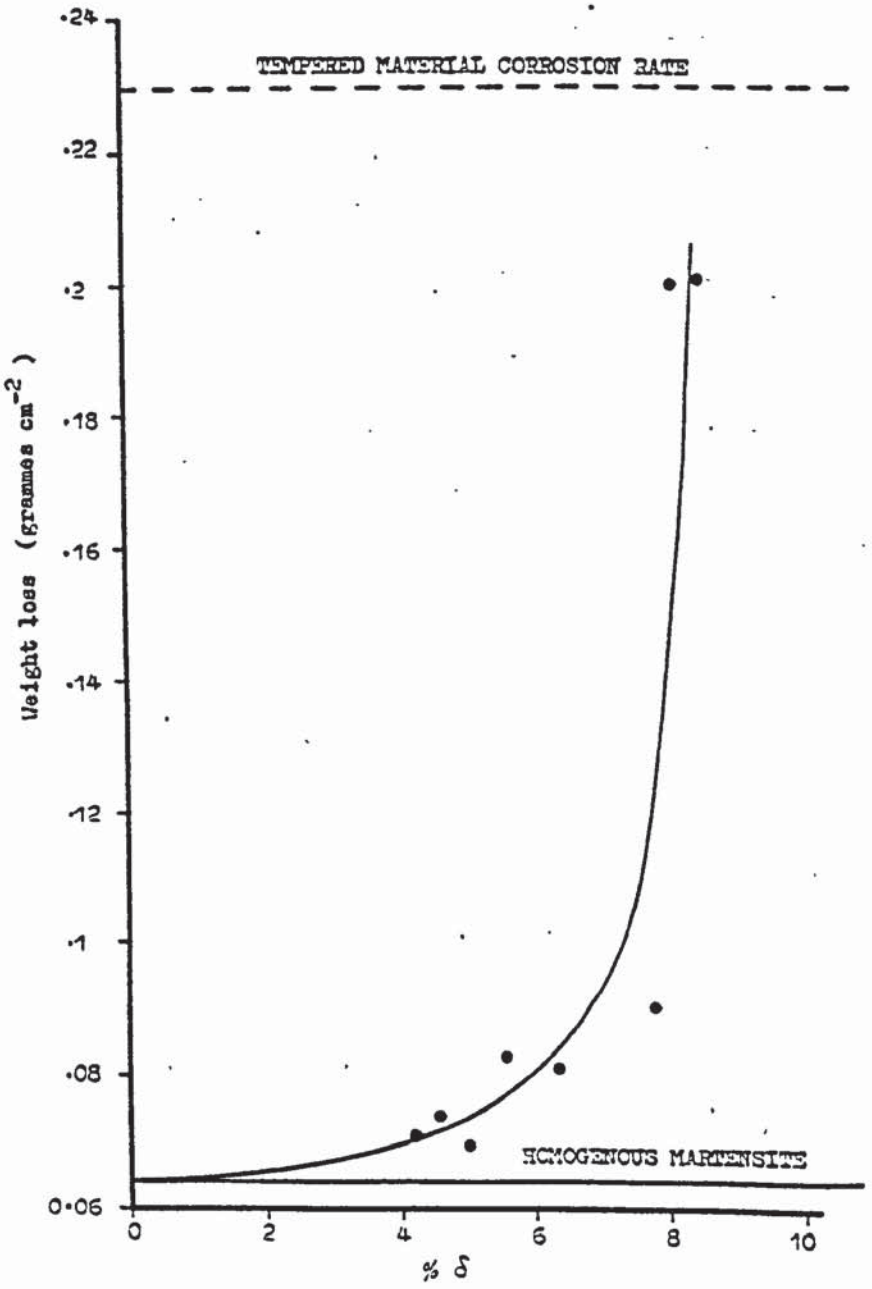


FIGURE 78 The effect of δ ferrite content on the corrosion rate of Class 2 steel

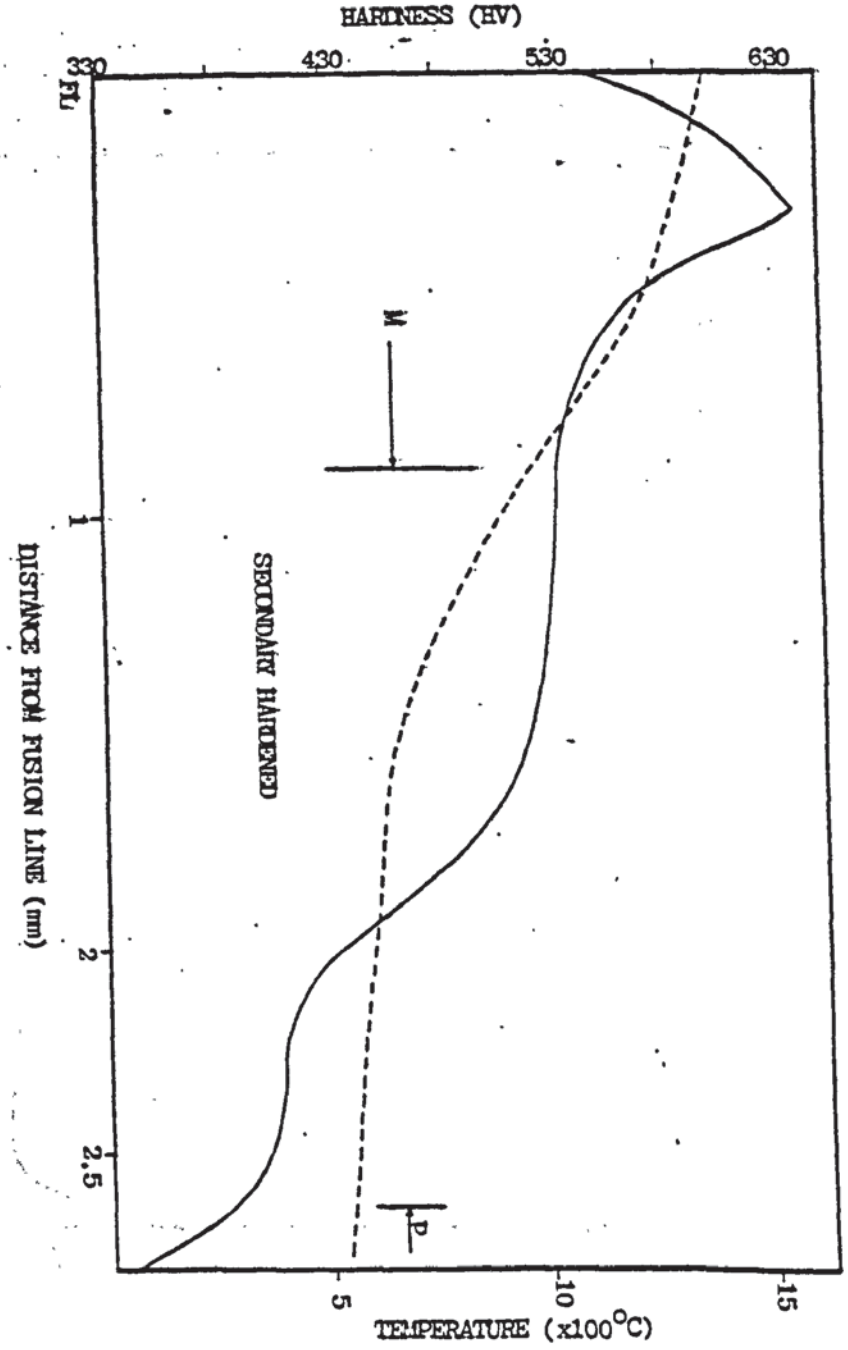


FIGURE 79 PEAK TEMPERATURE DISTRIBUTION FITTED TO HARDNESS AND MICROSTRUCTURAL findings for weld T1

NB The martensite zone (M) begins at approximately 900°C and material softens (ie $\delta$ formed) at about 1320°C

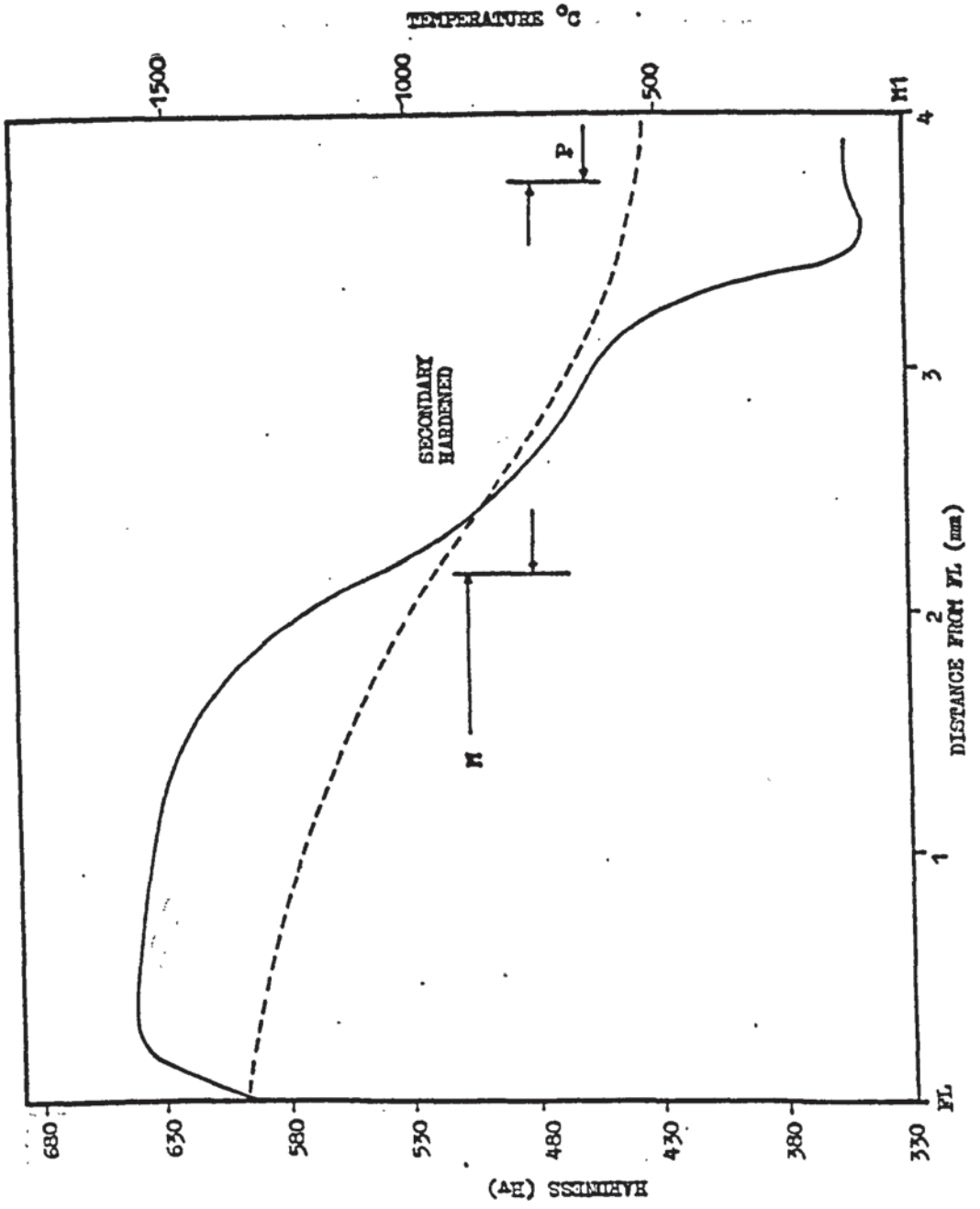


FIGURE 80 PEAK TEMPERATURE DISTRIBUTION FITTED TO HARDNESS AND microstructural findings for weld M1.
NB The martensite zone (M) begins at about 900°C and δ forms at about 1320°C.

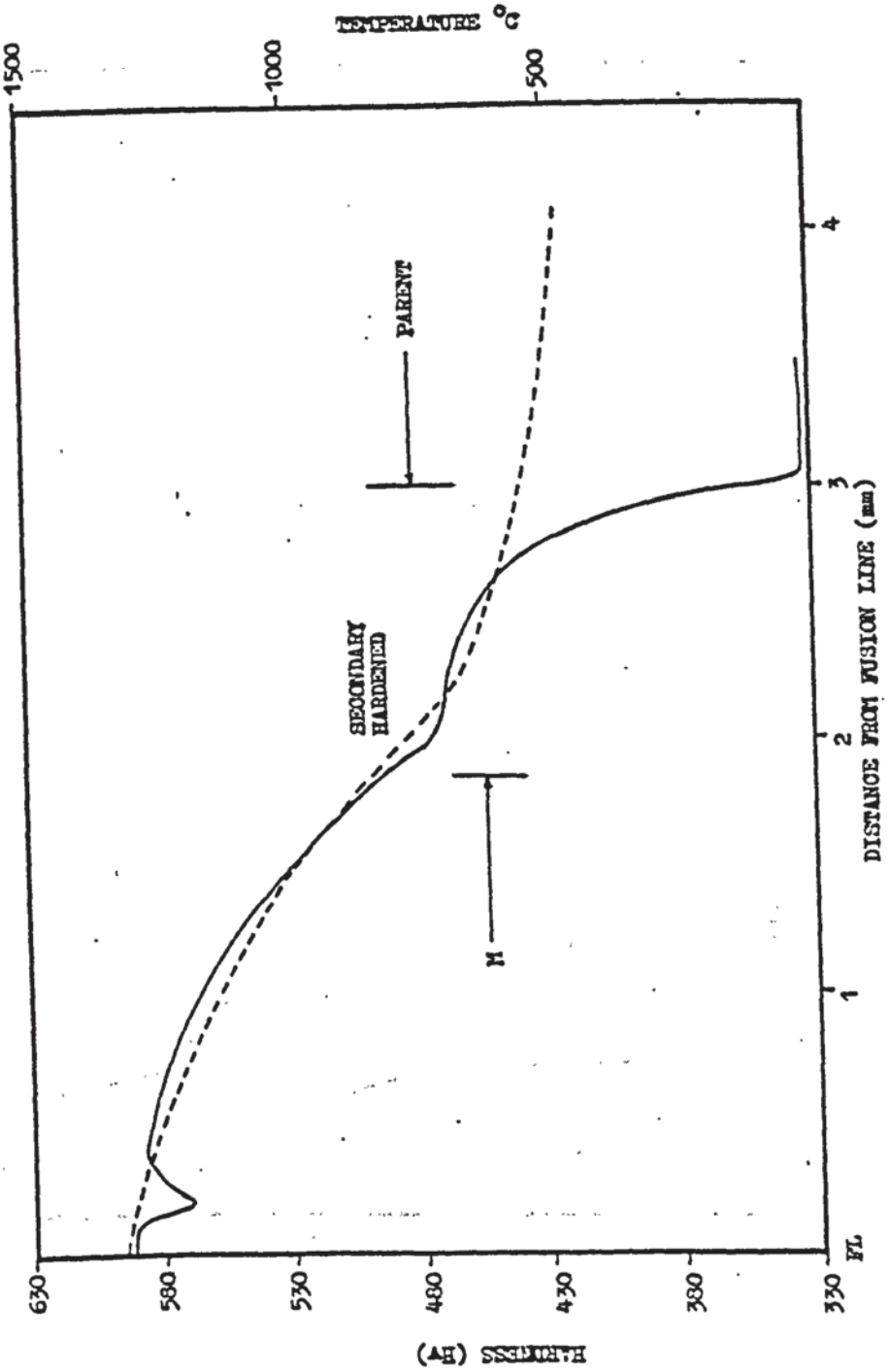


FIGURE 8i PEAK TEMPERATURE DISTRIBUTION FITTED TO HARDNESS AND microstructural findings for weld R1

NB The martensite zone (M) begins at about 900°C whilst δ formation occurs above 1320°C

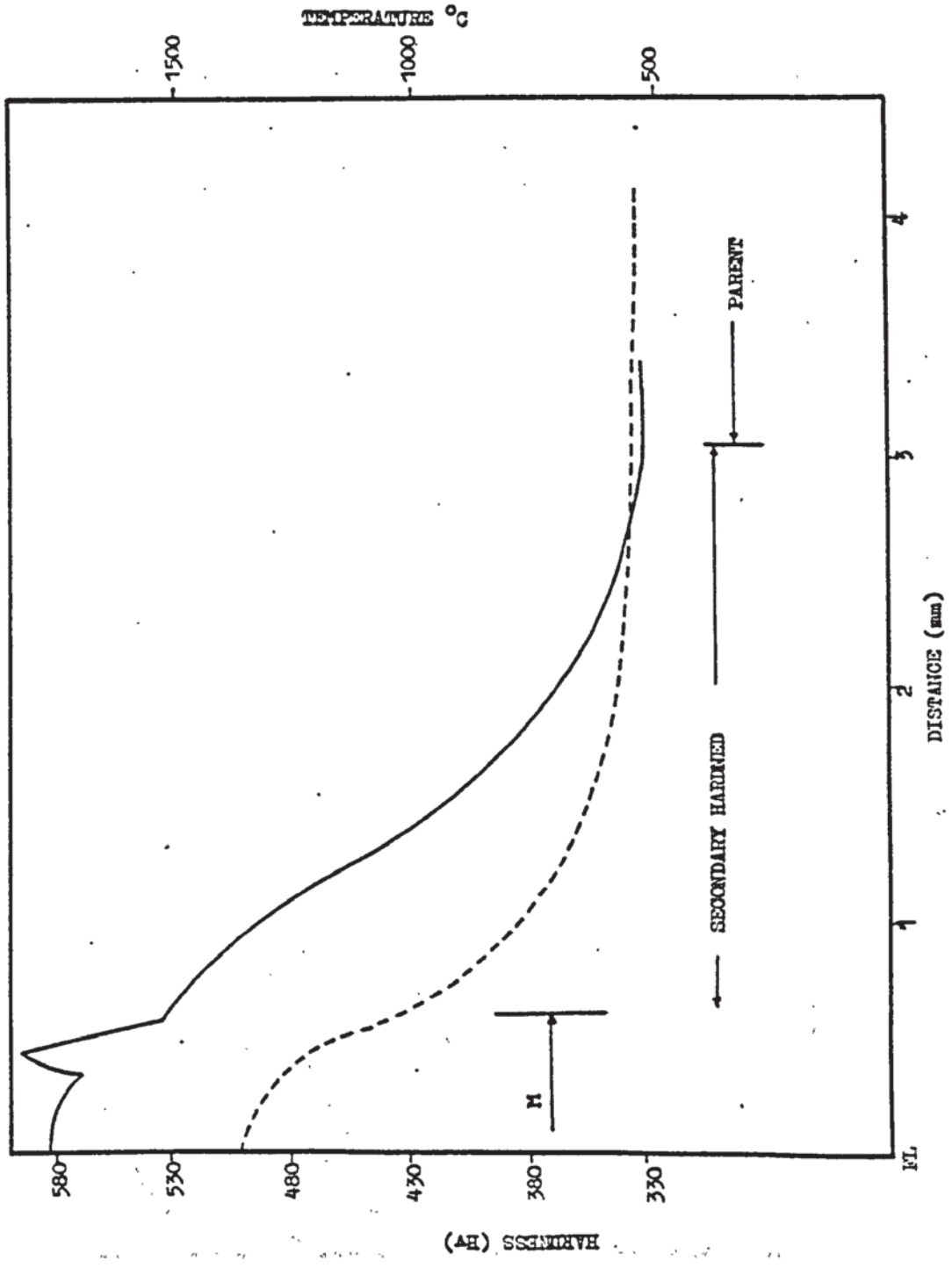


FIGURE 82 PEAK TEMPERATURE DISTRIBUTION FITTED TO HARDNESS AND and microstructural finding for weld S1

NB The martensite zone (M) commences at about 900°C whilst the δ formation region occurs about 1320°C.

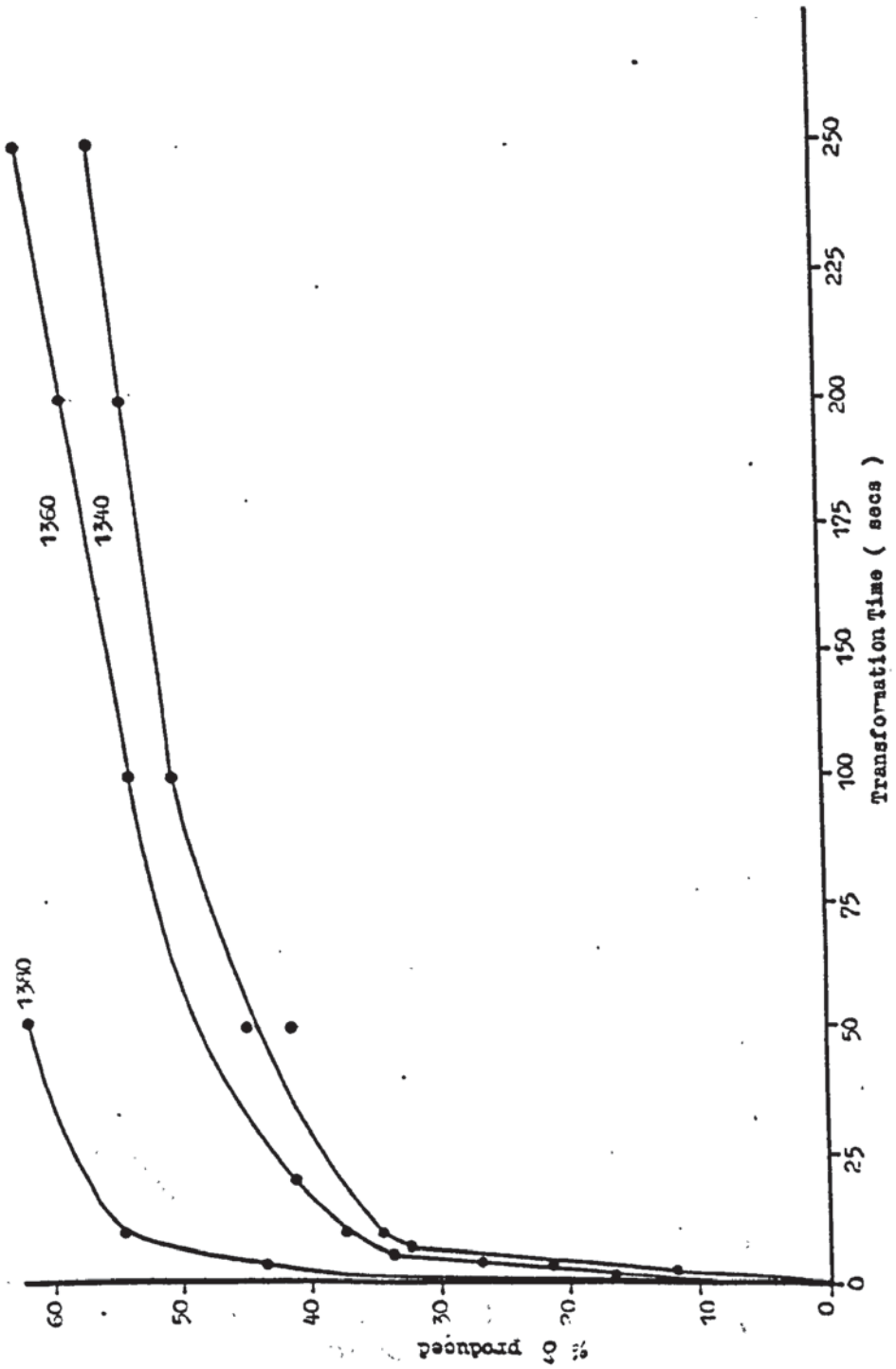


FIGURE 83 Isothermal transformation curves for δ ferrite formation from austenite in Class 2 steel

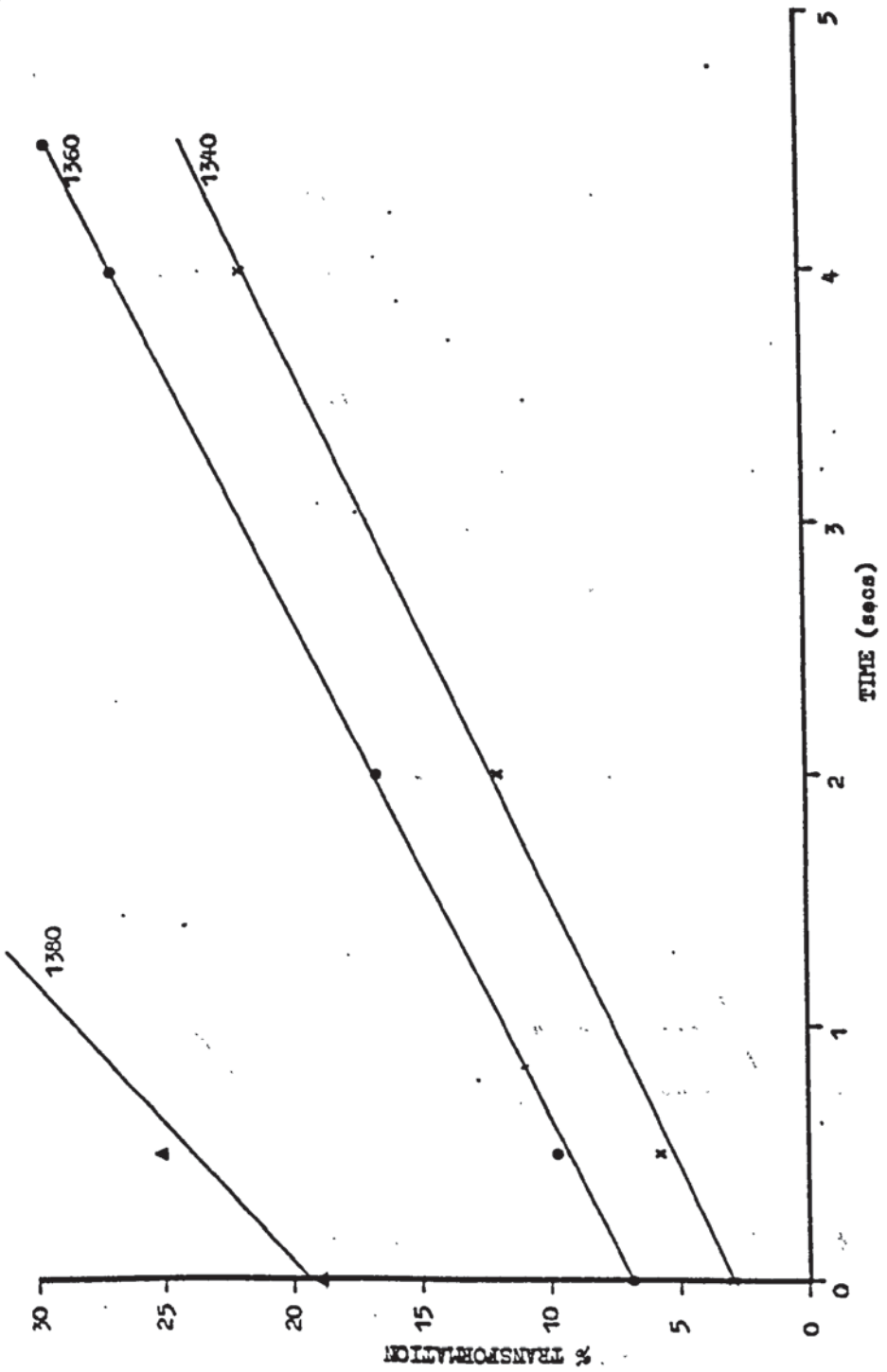


FIGURE 84 Linear regions of the three isothermal transformation curves from figure 83.

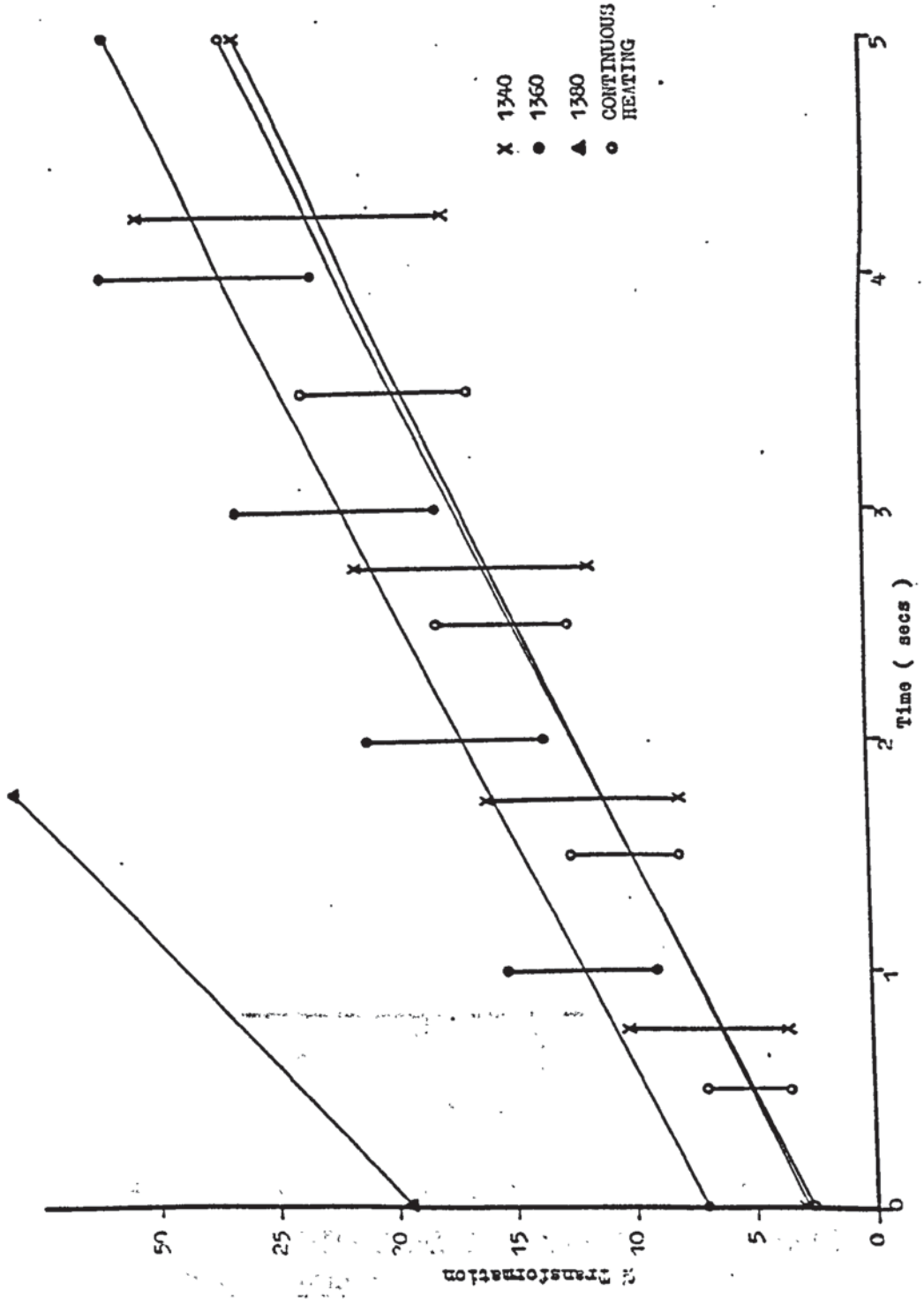


FIGURE 85 The dynamic case (ie time above 1320°C) values plotted with the isothermal transformation information
Vertical bars indicate statistical 95% confidence limits.

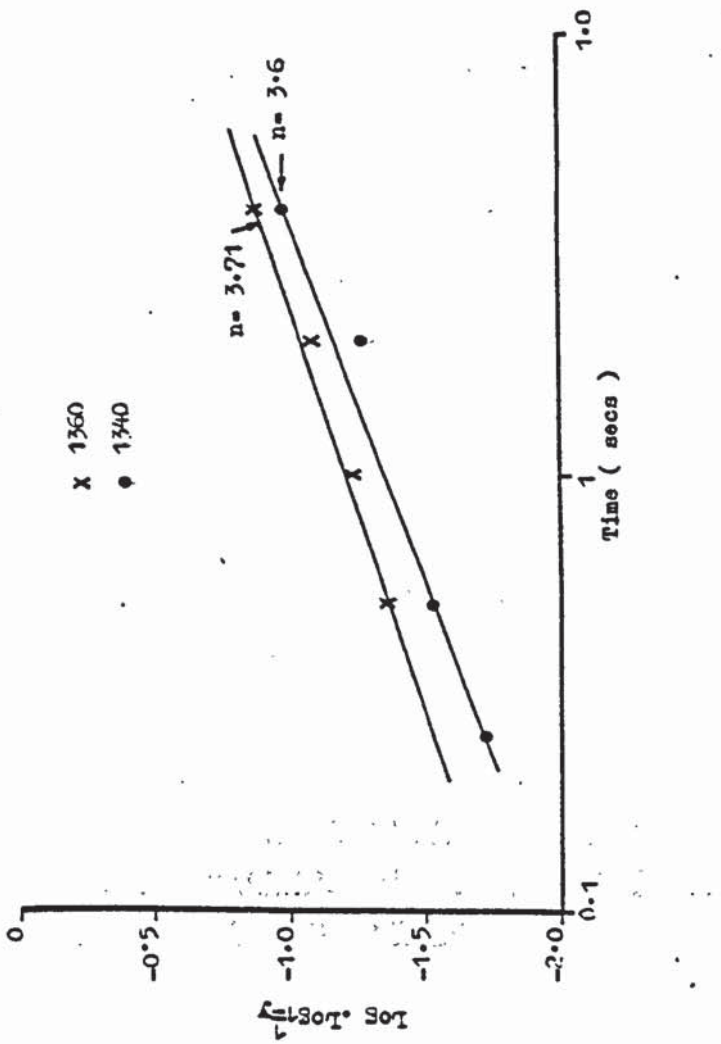


FIGURE 86 Values for 1340°C and 1360°C isothermal transformations plotted in the Johnson-Mehl manner.

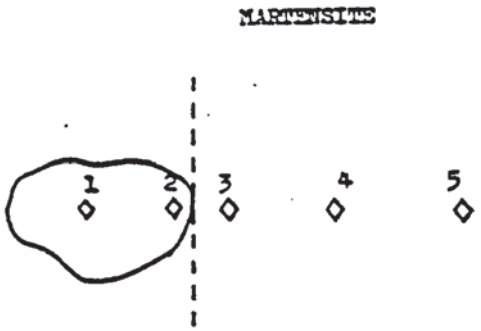


| Test No. | Microhardness (Hv) |
|---|---|
| 1 | 259 |
| 2 | 264 |
| 3 | 348 |
| 4 | 490 |
| 5 | 520 |

FIGURE 88 The position of, and the values found, during hardness traverses across the δ martensite interface

FIGURE 89

Transmission Electron Micrograph showing carbides located within a δ stringer, Taken from a carbon extraction replica.

Note: presence of carbides at martensite/δ interface.


Plate x 40K, Sample etched in Adlers reagent, extracted in perchloric acid.

1.35μ

FIGURE 90

Transmission Electron Micrograph showing carbide at the δ-martensite interface (from carbon extraction replica).
Probe shows carbide particle used for diffraction studies.

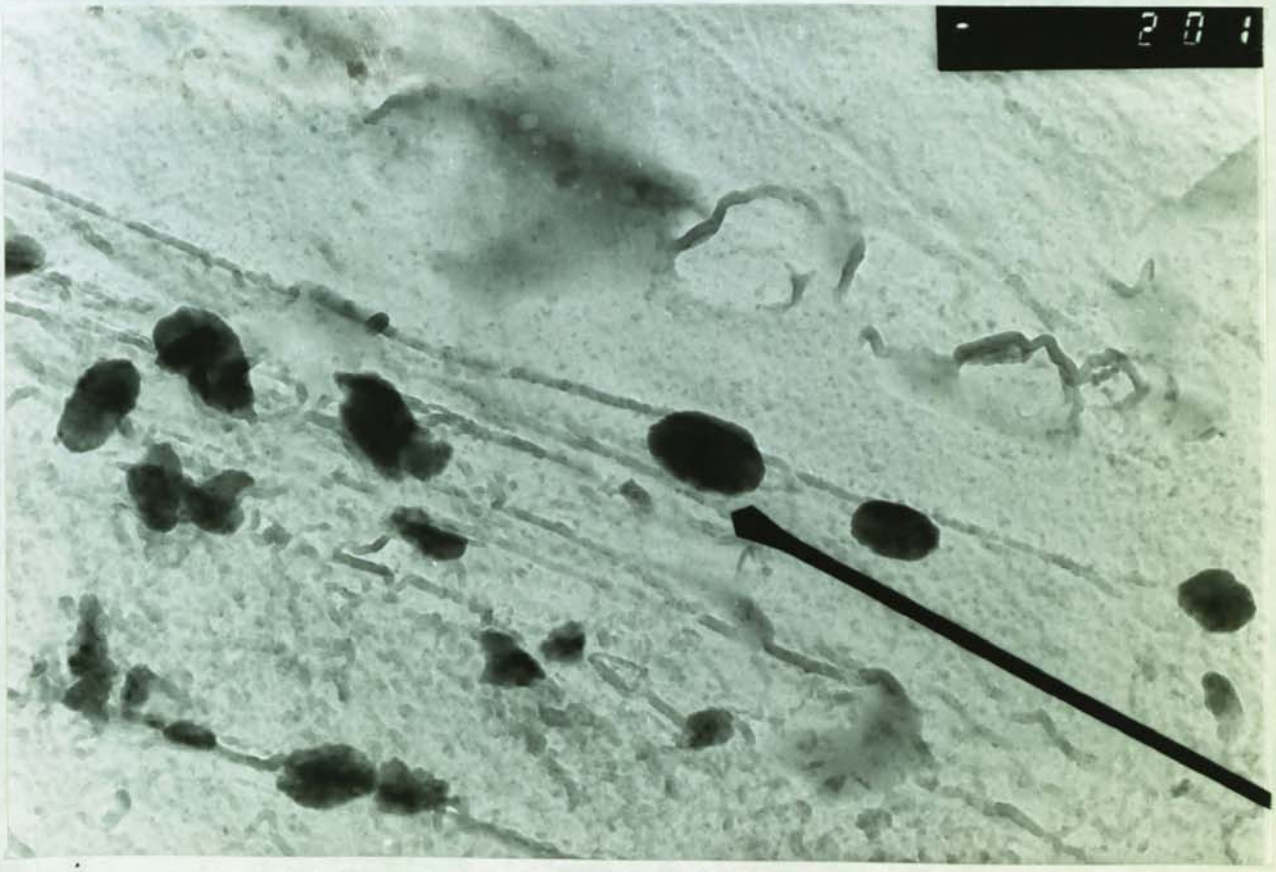


Plate x 97K. Sample etched in Adlers reagent, extracted by perchloric acid.

0.31μ

FIGURE 91

Transmission Electron Micrograph showing carbides as dark layers within the δ region.
Martensite lath is outlined by precipitates at the δ-martensite interfaces.

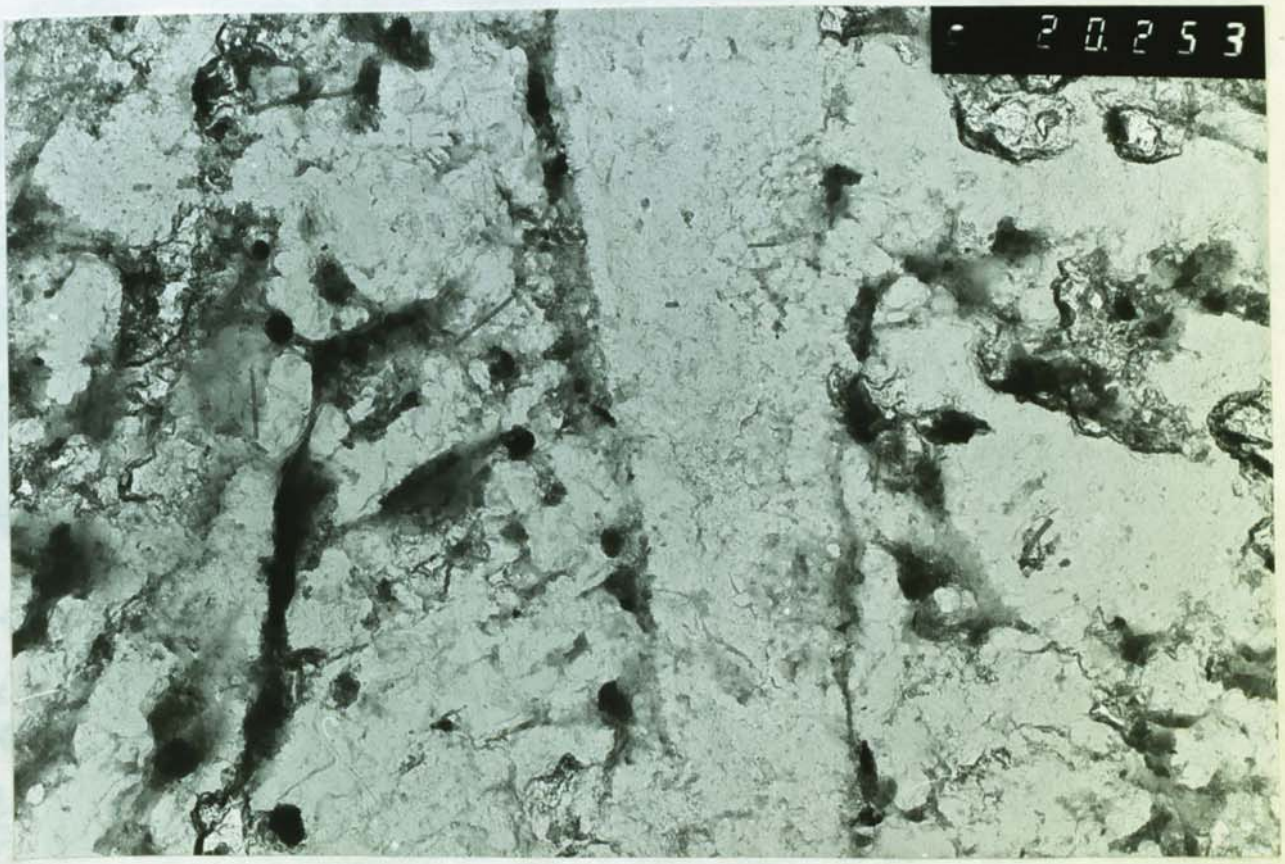


Plate x 36K. Sample etched in Adlers reagent, replica heavily extracted by perchloric acid.

0.834μ

FIGURE 92

Transmission Electron Micrograph showing carbide layering in δ regions (micrograph taken from a heavily extracted replica)

Note:two martensite laths are outlined by interface carbide precipitations.

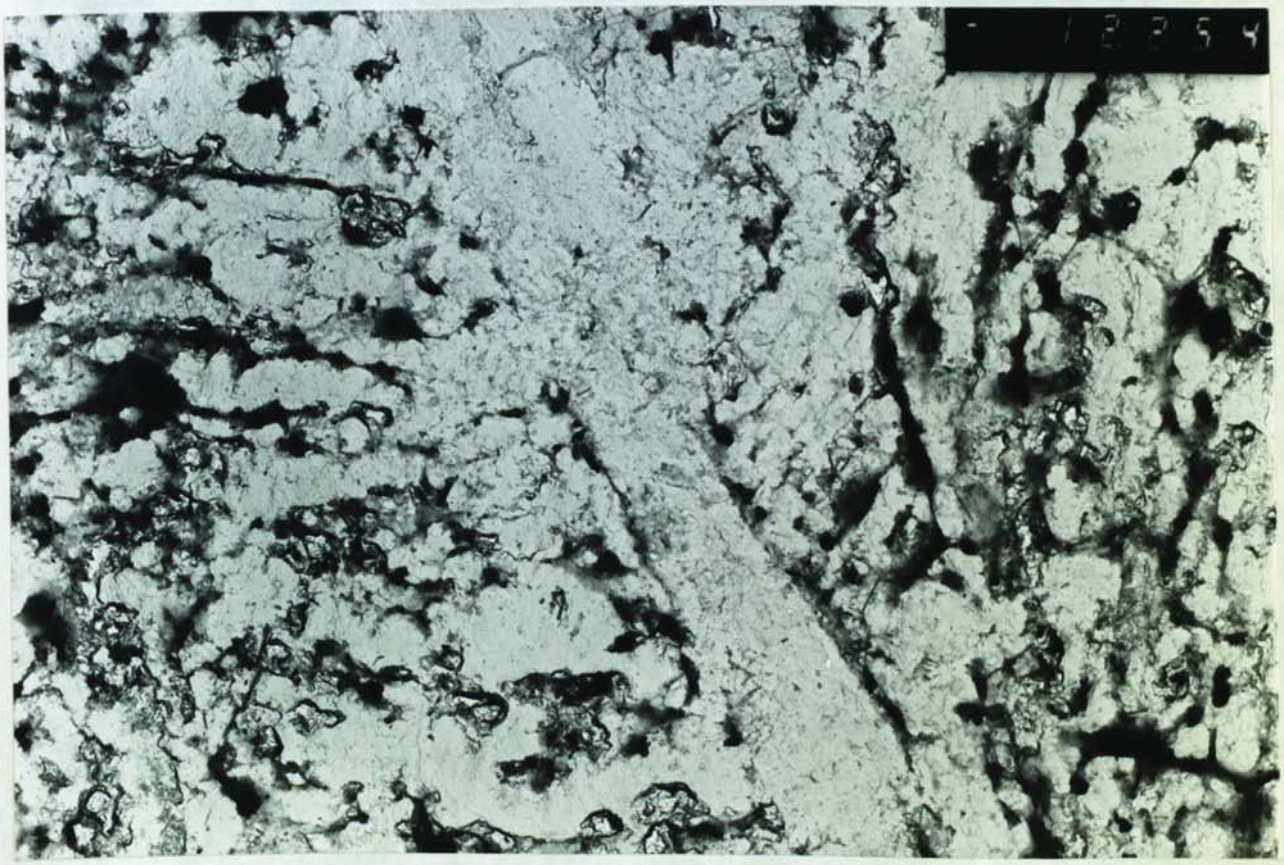

Plate x 21.6K. Sample etched in Adlers reagent, replica extracted in perchloric acid.

0.9μ

FIGURE 93

Transmission Electron Micrograph showing carbide layering (micrograph taken from a heavily extracted replica)

Note: martensite lath outlined by two ferritised regions.

Plate x 15K. Sample etched in Adlers reagent, replica extracted in perchloric acid.

FIGURE 94

Typical mixed diffraction pattern

Two F.C.C. materials

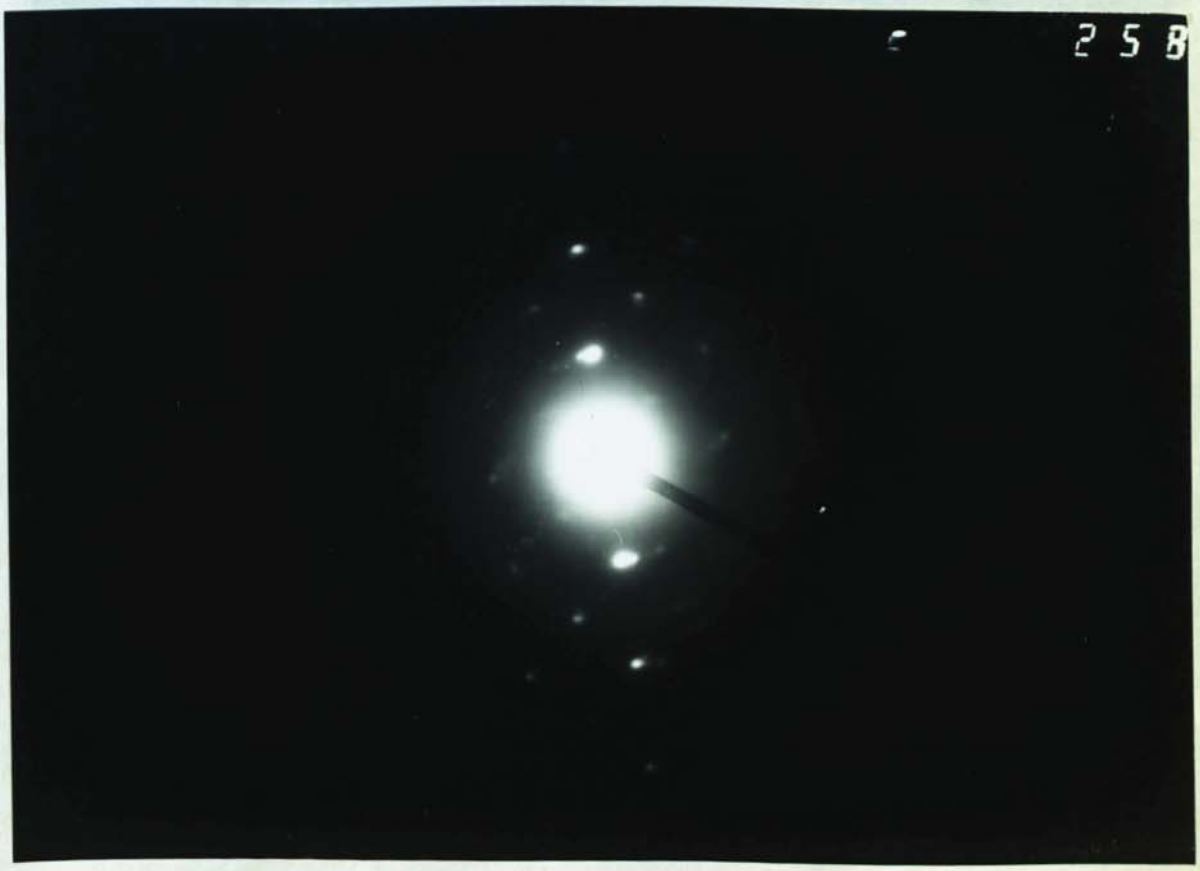

FIGURE 95

Diffraction pattern of single F.C.C. material


Plate x 100 K

FIGURE 96

Carbide from which diffraction pattern in Figure 95 was obtained

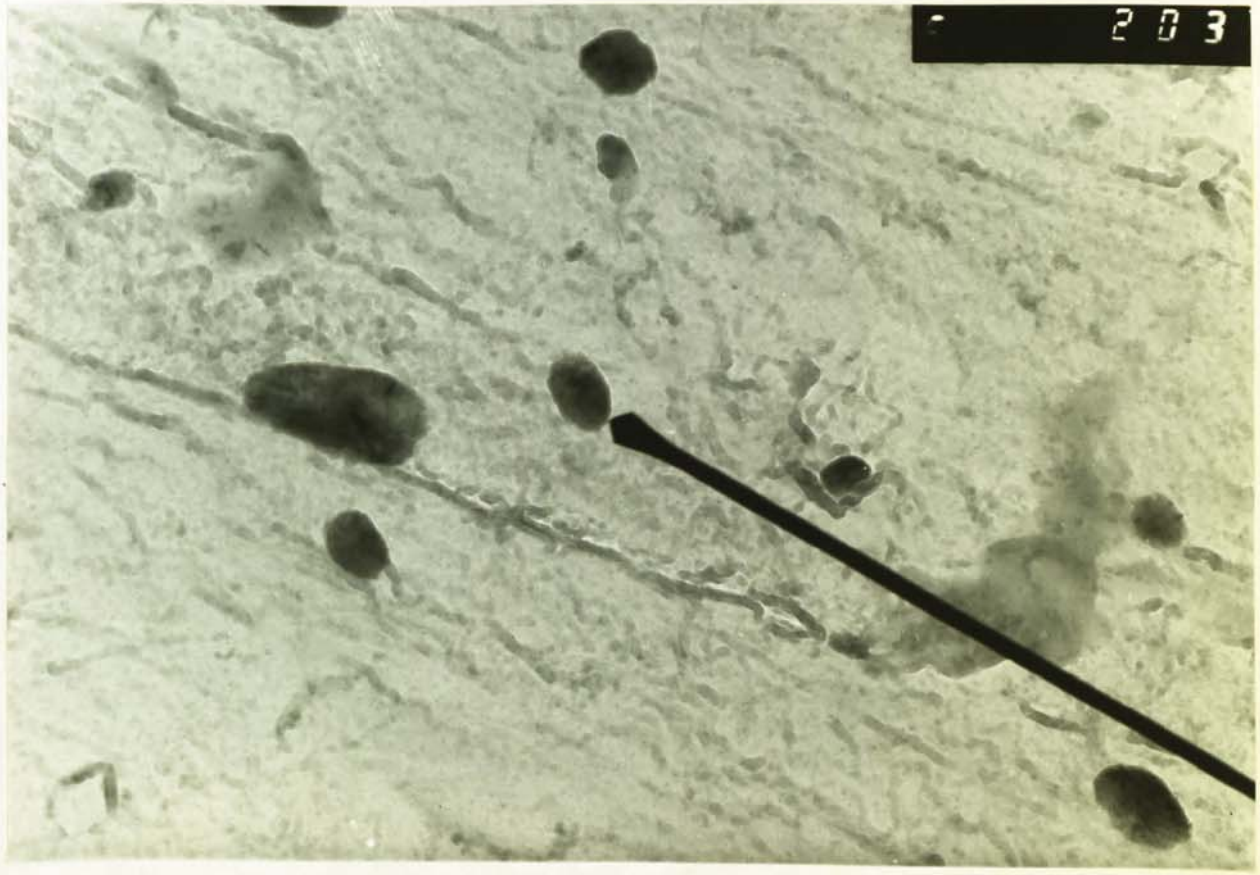


x 100 K, Sample etched in Adlers reagent, replica extracted by perchloric acid.

0.5μ

FIGURE 97 Solution to diffraction pattern no 204

FIGURE 98

Diffraction pattern obtained from a carbide particle

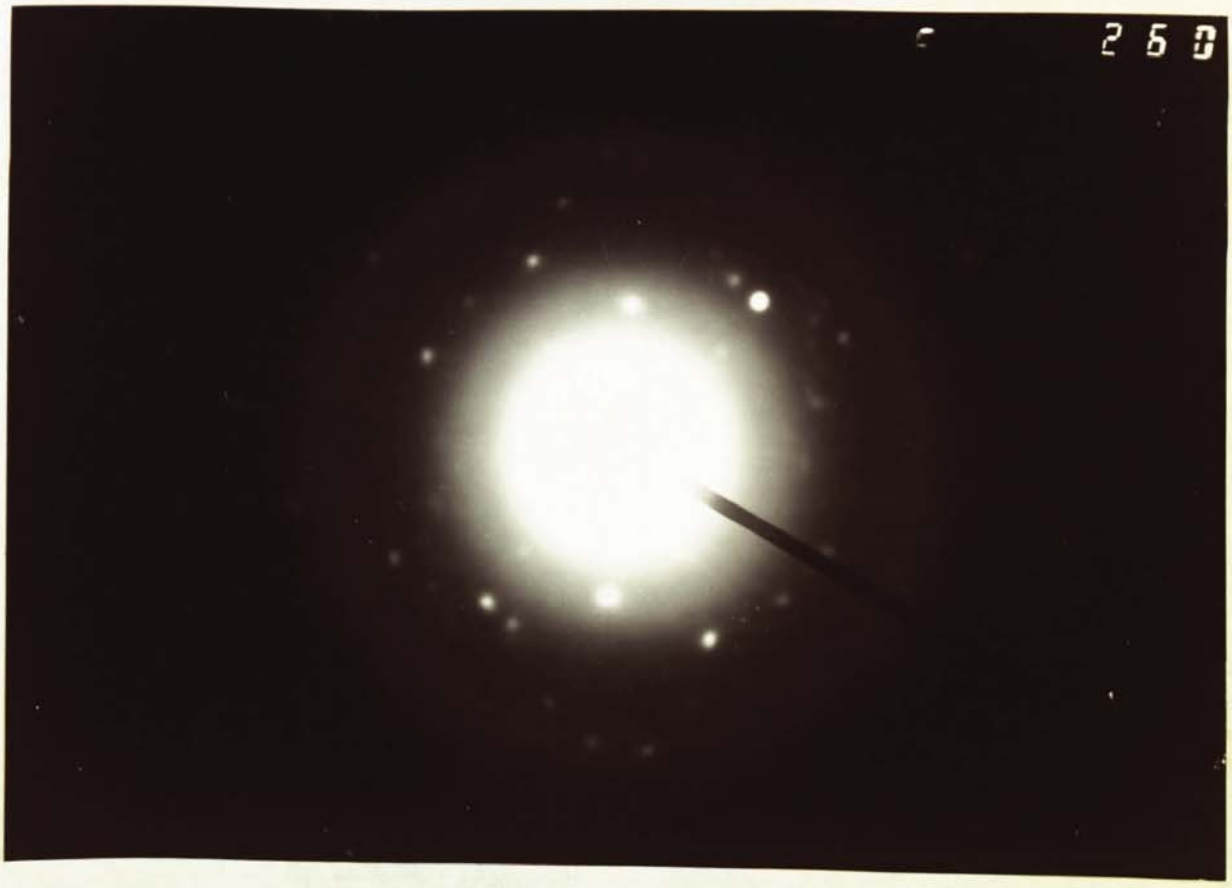


x 100 K

FIGURE 99

Carbide from which diffraction pattern in figure 98 was obtained

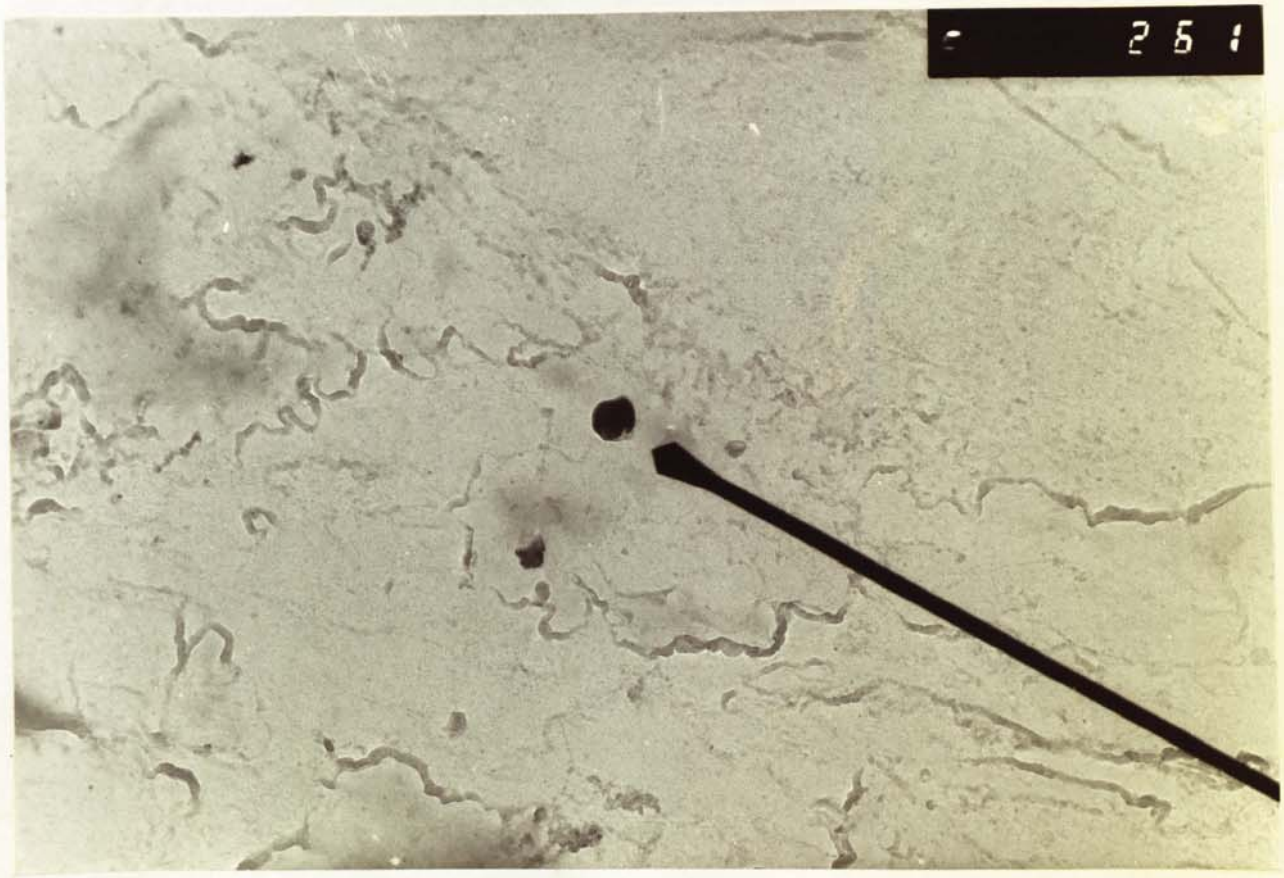


x 100 K, sample etched in Adlers reagent, replica extracted in perchloric acid.

0.5μ

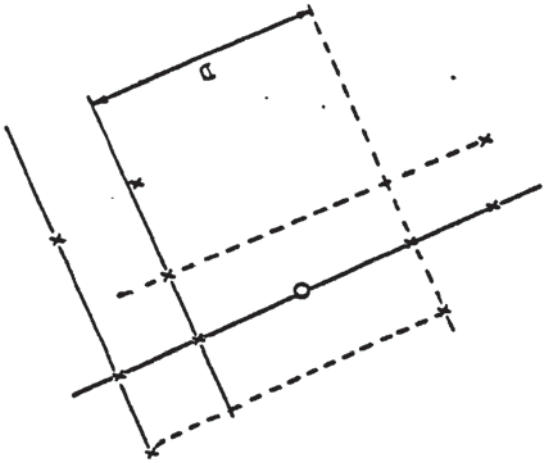


FIGURE 100 Solution to diffraction pattern No 260

FIGURE 101

Schematic representation of carbide formation during ferritising period (from ref.86)

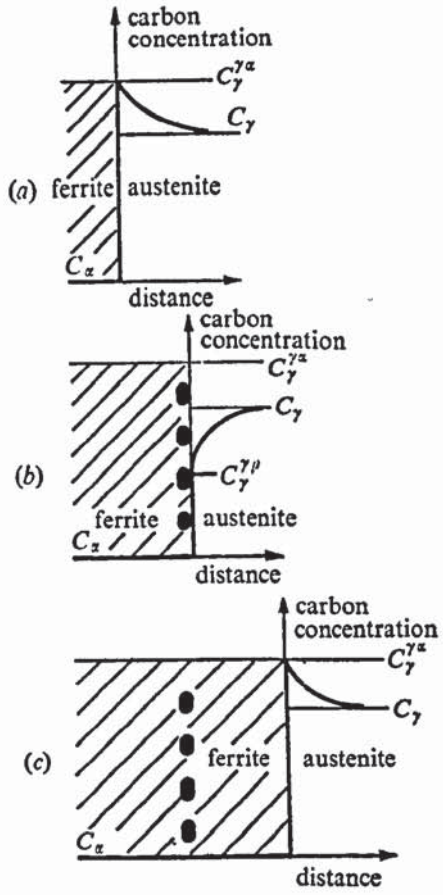


FIGURE 16. Schematic model of the formation of interphase precipitation. In (*a*), partitioning of carbon occurs before precipitation, coupled with a gradual build-up. In (*b*), the concentrations are sufficient for carbide nucleation on the ferrite side of the $\gamma$–$\alpha$ boundary which pins the boundary and depletes the carbon concentration in the adjacent austenite to some level $C_\gamma^{\gamma\rho}$ near the precipitate. Eventually the carbon depletion increases the driving force for ferrite formation sufficiently to drag the $\gamma$–$\alpha$ boundary away, (*c*) and the partitioning process recommences.

a) Carbon concentration ready for carbide formation

b) Carbon partition occurs, carbides form and interface progresses

c) Carbon concentration gradient re-establishes before next partition

FIGURE 102

Effect of re-austenitising steel containing quantities of δ ferrite

Note: some δ no longer austenite grain boundaries

( x 1100 (optical), Adlers etch)

FIGURE 103

Effect of re-austenitising steel containing quantities of δ ferrite

Note: Austenite grain boundary movement has occurred

(x 1100 (optical), Adlers etch)

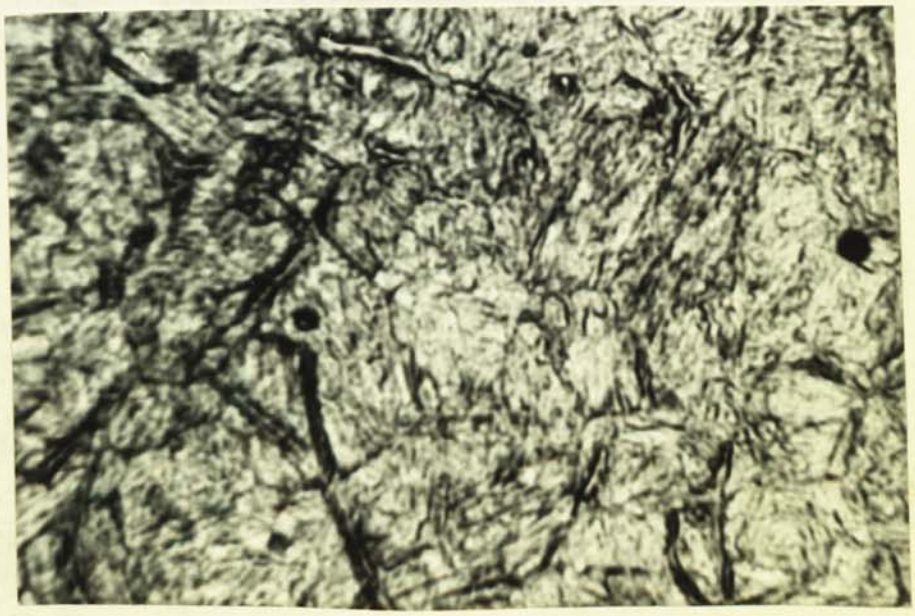

FIGURE 104

Effect of re-austenitising steel containing quantities of δ ferrite

Note: Austenite grain boundary movement has not been impeded, thus some δ is now within prior austenite grains.

( x 1100 (optical), Adlers etch)

# BIBLIOGRAPHY

BIBLIOGRAPHY


1. Z BRIGGS and T D PARKER

   "The Super 12% Cr Steels". Climax Moly. 1965.

2. K J IRVINE, D J CROWE and F B PICKERING

   J.I.S.I. 195 (8) 1960 pp 386 - 405

3. E F NIPPES, W F SAVAGE, L C JANNIELLO and W A OWCZARSKI

   Welding Journal 38 (9) 1959 pp $360_s$ - $366_s$

4. H THIELSCH

   Welding Journal 30 (5) 1951 pp $209_s$ - $250_s$

5. V N MOLYSHENSKAYA and J ANDREEV

   Aut.Weld. 21 (3) 1968 pp 5 - 8

6. N I KAKHOUSKII and A M PONIZOVTSEV

   Aut.Weld. 17 (2) 1964 pp 20 - 26

7. G ARINK, C M MENKEN and C W N VEERLING

   Metal Construction 4 (8) 1972 pp 286 - 290

8. Ya KAUHANSKI and V PONIZOVTSEV

   Weld.Prod. 1969 (7) pp 6 - 9

9. Ya M POTAK etal

   Aut.Weld 25 (10) 1972 pp 5 - 8

10. V PILOUS and J KOUTSKY

    Skoda Review 1968 (4) pp 25 - 33

11. B BANKS

    Welding and Metal Fabrication 37 (2) 1969 pp 46 - 51
    pp 46 - 51

12. S F BOGUSHEVSKII, S N VIVIK and E S LOZOR

    Aut.Weld 17 (4) 1964 pp 24

13. C H KREISCHER, J COTHREN and A E NEAR

    Welding Journal 40 (11) 1961 pp $486_s$ - $496_s$

14. G FABER

Brown-Boveri Review 49 (5) 1961 pp 485 - 489

15. K J IRVINE and F B PICKERING

I.S.I. Special report no 64
"High Strength 12% Chromium steels"

16. J KOUTSKY

Hutnicke Listy 14 (11) 1959 pp 951 - 955

17. R E SMALLMAN

"Modern Physical Metallurgy" 3rd edition
1970 Butterworths

18. A SCHAEFFLER

British Welding Journal 27 (7) 1960 pp

19. V VACK, V FOLDYNA and J KUCERA

Kovove Materiali 4 (1) 1966 pp 3 - 17

20. J KOUTSKY and J JEZEK

J.I.S.I. 200 (11) 1962 pp 938 - 943

21. J D MURPHY and S BRANCH

J.I.S.I. 206 (3) 1968 pp 266 - 274

22. Ya KOUTSKII

Metallovecleniie : Termicheskaya Obrobutka
Metallov No 1. Jan. 1967 pp 15 - 19

23. V PILOUS

S.N.T.L. Technical Digest 10 (s) 1968
pp 283 - 287

24. J PLUHAR, V TUMA, J JEZEK and J POPISIL

Hutnicke Listy 14 (12) 1959 pp 1108 - 1111

25. J KOUTSKY and J JEZEK

J.I.S.I. 203 (7) 1965 pp 707 - 714

26. J BOSANSKY

Zvaranie 16 (5) 1967 pp 133 - 136

27. J JEZEK, F JANDOS and J KOUTSKY

Kovove Materiali 3 (1) 1965 pp 11 - 17

28. F C VER SNYDEN and H J BEATTIE

Trans A.S.M. 47 1955 pp 211 - 230

29. J KOUTSKY

J.I.S.I. 205 (7) 1967 pp 763 - 768

30. W C HAGEL and E F BECHT

Trans A.S.M.E. 78 (10) 1956 pp 1439 - 1446

31. K W ANDREWS and H HUGHES

J.I.S.I. 193 (11) 1959 pp 304 - 311

32. J J HAUSER, J M COPENAS and B R BANERJEE

Trans A.S.M. (53) 1961 pp 514 - 525

33. R L RICKETT, W F WHITE, C S WALTON and J C BUTLER

Trans A.S.M. 44 1952 pp 138 - 168

34. R W K HONEYCOMBE

"Structure and strength of Alloy Steels"
Climax Molybdenum Co.

35. J HENSCHKEL

Welding Journal 39 (11) 1960 pp $502_s$

36. H THIELSCH

Welding Journal 34 (1) 1955 pp $22_s$ - $30_s$

37. Battelle Memorial Institute Report 118

"Welding of high strength steels for aircraft and missile applications" Defence Metal Information Centre, Batelle, Ohio (10.12.59)

38. GEBR. BOHLER GmbH

"Metals for inert gas welding" 1975

39. J A BOARD

Journal of the Institute of Metals 101 1973
pp 241 - 247

40. Private Communication from Clarke-Chapman and International Combustion. March 1976.

41. Private Communication from Bohler and Mannesmann January 1975

42. E KAUHAUSEN, P KAESMACHER and S SADOWSKI

British Welding Journal 7 (12) 1960 pp 693 - 707

43. Ya KOUTSKII

Met.Term.Obrab.Met. 1967 (1) pp 19 - 22

44. R J CASTRO and J J DE CADONET

"Welding metallurgy of Stainless and heat resisting steels" 1st Edition, Cambridge Univ.Press 1975

45. H C CAMPBELL

Welding Journal 54 (5) 1976 pp 867 - 871

46. C D LUNDIN and D F SPOND

Welding Journal 54 (6) 1976 pp $356_s$ - $367_s$

47. A W BREWER and R L MOMENT

Welding Journal 54 (5) 1976 pp $159_s$ - $164_s$

48. J F LANCASTER

"The metallurgy of welding, brazing and soldering" 2nd Edition, Allen and Unwin 1970

49. T BONISZEWSKI and F WATKINSON

Metals and Materials _ (2) 1973 pp 90 - 96

50. T BONISZEWSKI and F WATKINSON

Metals and Materials _ (3) 1973 pp 145 - 151

51. F WATKINSON

"Metallurgical Considerations in the welding of 12 Cr-Mo-V-W steel" Welding Institute 1975

52. R N PARKINS

"An investigation of cracking associated with 12% Cr steel tubes near spacer attachments" Univ. of Newcastle 1975

53. R N PARKINS

"Further work on the cracking of 12% Cr steel in various environmental conditions" Univ. of Newcastle 1975

54. Private Communication from Drs W K C Jones and P J Alberry at C.E.G.B. Marchwood Laboratories February 1977

55. W F SAVAGE

Paper A Welding Research Council Symposium "Methods of high alloy weldability evaluation" 1970

56. A.S.T.M.

Standards parts 31 pp 236 - 240 and 325 - 327 May 1973

57. P F MARTIN and C ROQUES

Paper H Welding Research Council Symposium "Methods of high alloy weldability evaluation" 1970

58. R H PHILLIPS

British Welding Journal 15 (11) 1968 pp 547 - 552

59. Welding Institute Symposium

"Thermal simulators used for problem solving and research" 1973

60. C L M COTTRELL

J.I.S.I. 174 (5) 1953 pp 17 - 24

61. E F NIPPES, W F SAVAGE and O PAEZ

Welding Journal 38 (12) 1959 pp $475_s$ - $481_s$

62. P W HALSBERG and W F SCHREITZ

Paper E Welding Research Council Symposium "Methods of high alloy weldability evaluation" 1970

63. J KOUTSKY, J JEZEK, F JORDAS and L BARACHOVA

Kovove Materiali 11 (3) 1964 pp 257 - 288

64. O WESTBY

Inst. for mekanisk teknologis Norges tekniske Høgskole, Trondhiem 1968

65. Z D PALEY and P D HIBBERT

Welding Journal 54 (11) 1976 pp $385_s$ - $392_s$

66. D ROSENTHAL

Welding Journal 20 (5) 1941 pp $220_s$ - $234_s$

67. N N RYKALIN

Berechnung der warmevorgange beim Schweissen. Berlin 1957

68. A A WELLS

Welding Journal 31 (5) 1952 pp $263_s$ - $267_s$

69. G SMITH, L FUNK and W UDIN

American Welding Society. New York June 1952

70. C M ADAMS

Welding Journal 37 (5) 1958 pp $210_s$ - $215_s$

71. C M ADAMS, W LYNCH and Z D PALEY

Welding Journal 43 (10) 1964 pp $71_s$ - $79_s$

72. R H PHILLIPS

PhD Thesis. Univ of Aston 1973

73. R H PHILLIPS and M F JORDAN

Welding Research International 3 (3) 1973 pp 59 - 68

74. E F NIPPES and C EMERICH

Welding Journal 42 (12) 1963 pp $547_s$ - $556_s$

75. G RATHBONE, H CONNOR and D E GRACE

Metals Engineering Quarterly 5 (1) 1966 pp 7 - 20

76. W F SAVAGE and W A OWCZARSKI

Welding Journal 45 (2) 1966 pp $55_s$ - $65_s$

77. C INOGAKI, I UTA and I WADA

Trans. N.H.M. 6 (6) 1964 pp 386 - 401

78. M M D'ANDERA and C M ADAMS

Welding Journal 42 (11) 1963 pp $503_s$ - $511_s$

79. G A CHADWICK

"Metallurgy of phase transformations"
1st edition Butterworths 1974

80. M WILSON, D J H CORDEROY and H MUIR

Uniciv Report R - 79 Feb. 1972. New South Wales

81. A A WELLS and J ROBERTS

British Welding Journal 1 (11) 1954 pp 553 - 56)

82. N CHRISTENSEN, V DAVIES and K GJERMUNDSEN

British Welding Journal 11 (2) 1965 pp 54 - 75

83. J BOSANSKY and L VEHNER

Compilation of Research 1972
Welding Research Institute, Bratislava

84. K W ANDREWS, D J DYSON and A KEOWN

"Interpretation of electron diffraction patterns"
2nd Edition. Adam Hilger Ltd. 1971

85. W B PEARSON

"Handbook of lattice spacings and structure of metals and alloys" 1st edition
Pergamon 1958

86. A T DAVENPORT and R W K HONEYCOMBE

Proc.Royal Soc. London 322 1971 pp 191 - 205

87. R W K HONEYCOMBE

Met.Trans. of A.I.M.E. 74 (7) 1976 pp 914 - 936

88. K CAMPBELL and R W K HONEYCOMBE

Metal Science 8 (7) 1974 pp 197 - 203

89. A H COTTRELL

"Theoretical Structural Metallurgy"
2nd Edition. Edward Arnold 1965

90. A F SMITH and R HALES

Metals Science 10 (12) 1976 pp 418 - 423

91. S J SANDERSON

Paper 19. Proc. of Conference on ferritic steels for fast reactor steam generators
June 1977

92. R S FIDLER and D J GOOCH

Paper 20 Ibid

93. E A LITTLE, B C EDWARDS and B L EYRE

Paper 22 Ibid

94. W K C JONES and P J ALBERRY

C.E.G.B. report No R/M/R 203

95. W K C JONES and P J ALBERRY

Paper 78 Proc. of conference on ferritic steels for fast reactor steam generators June 1977

96. Question to authors of Paper 78 Ibid

97. J BURKE

"Kinetics of phase transformations in metals" 2nd Edition Pergamon 1965

98. Y S TOULANKIAN and E H BUYCO

"Thermophysical properties of matter" 1970 Edition IFI-Plenum

99. C J SMITHELLS

"Metals Reference Book" 4th Edition 1967 pp 226 - 228

100. W HUME-ROTHERY

"The Structures of Alloys of Iron" 1st Edition Pergamon 1969

101. H R CASTNES

Welding Journal 57 (7) 1977 pp $193_s$ - $200_s$

102. J T BARNBY

Private Communication June 1977

# APPENDIX 1

## APPENDIX 1

### Interpretation of dilatometric data in terms of crystallographic change

Standard condition for both steels used in this work was tempered martensite. In this condition the microstructure consists of α ferrite and carbides, the α being Body Centred Cubic (B.C.C.) crystallographic structure. Transformation to austenite (γ), which occurs over the $Ac_1$ to $Ac_3$ temperature range, is a lattice change from B.C.C. to F.C.C. (Face Centred Cubic). This change can be shown to be an expansion in lattice parameter accompanied by a reduction in unit cell volume.

When δ formation commences, at $Ac_4$, regions of austenite begin to transform to δ thus the F.C.C. structure of γ changes to the B.C.C. structure of δ. This phase (δ) has a reduced lattice parameter and a subsequently increased unit cell volume (see accompanying figures $^{(100)}$).

The volumetric changes involved in each transformation can be calculated thus:-

i) Assume constant number of atoms.

ii) B.C.C. cell has 2 atoms per cell (N = 2)

iii) F.C.C. cell has 4 atoms per cell (N = 4)

a) For $\alpha$ to $\gamma$ transformation

$\alpha$ lattice parameter ($ao_B$) at transformation temperature is 2.90A°

$\gamma$ lattice parameter ($ao_F$) at transformation temperature is 3.64A°

Now:- $\frac{\text{Volume of unit cell}}{\text{No. of atoms in cell}} = \frac{ao^3}{N} = \Omega$

For B.C.C.

$= \frac{24.389}{2} \therefore \Omega = 12.1945$

For F.C.C.

$= \frac{48.228544}{4} \therefore \Omega = 12.057136$

% size change between $\alpha$ and $\gamma$ is:-

$(\frac{12.057136 - 12.1945}{12.1945} \times 100) = -1.1264\%$ (ie contraction of 1.1264%)

b) For $\gamma$ to $\delta$ transformation

$\gamma$ lattice parameter ($ao_F$) at transformation temperature is 3.68A°

$\delta$ lattice parameter ($ao_B$) at transformation temperature is 2.925A°

So $\Omega = \frac{\text{Volume of unit cell}}{\text{No. of atoms in cell}} = \frac{ao^3}{N}$

For $\gamma$

$\Omega = \frac{49.836032}{4} = 12.459008$

For $\delta$

$\frac{25.025203}{2} = 12.5126015$

% size change is $(\frac{12.5126015 - 12.459008}{12.459008} \times 100)$

$= +0.43016\%$ (ie an expansion of this amount)

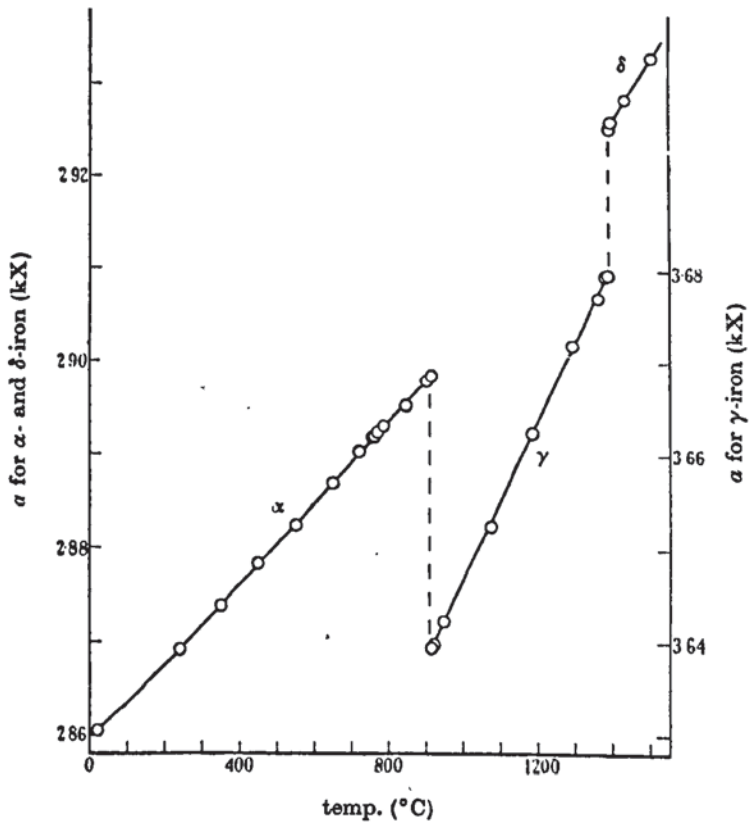


a)

Effect of temperature on lattice spacings of iron.

THE EFFECT OF TEMPERATURE ON a) LATTICE SPACING AND b) MEAN VOLUME PER ATOM OF IRON

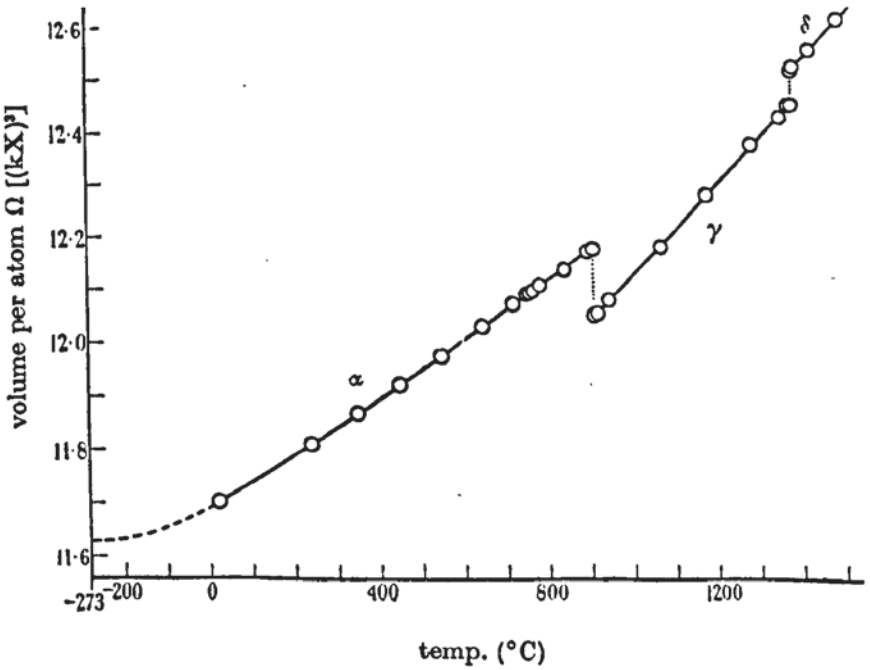


b)

Effect of temperature on mean volume per atom in crystals of iron.

# APPENDIX 2

# APPENDIX 2

## Variab modifications, program listing, input data and subsequent results and mathematic solution for accurate peak temperature location

### A2.1 Modifications to Variab to suit Super 12% Cr Mo steel metallurgy

Variab, as first conceived, only modelled mild steel. To do this a few minor assumptions were made, the two most important being (i) that $\alpha$ to $\gamma$ transformation occurs at one temperature (900°C) and not over a range ($Ac_1$ to $Ac_3$) and (ii) on cooling $\gamma$ to $\alpha$ occurred at the same temperature as $\alpha$ to $\gamma$ on heating, thus no $\gamma$ supercooling occurs [64]. In low carbon, low alloy steels these assumptions are unimportant and modifications are limited to ones resulting from different specific heats and thermal conductivities [64]. The metallurgy of Super 12% Cr Mo steels is somewhat different. Once heated above $Ac_3$ the austenite remains supercooled to Ms temperature and below. This difficulty was overcome by using a three dimensional Boolean matrix set to "FALSE" in each element, which changed to "TRUE" if at any time the element temperature exceeded 900°C. "FALSE" values caused the material cooling rate to be calculated using tempered martensite thermal properties whilst "TRUE" values called supercooled austenite thermal properties into cooling calculations [91]. This step was useful but did not solve the problem, final matrices are martensitic, not austenitic, so allowance was made for Ms. It was assumed that Ms occurred at 250°C, after which the matrix was completely martensitic, so the latent heat of

martensite formation was released at this temperature [92]. This brought the heat content of the matrix equal to untransformed martensite (ie material in "FALSE" conditions) at 250°C. Further cooling was calculated using tempered martensite values.

Thermal properties for 12% Cr steels were used, and were inserted into the program during the Boolean series modification.

## A2.2 Program listing

The program suitable for determining weld thermal history of Super 12% Cr Mo steel exists in both file store and binary versions, permanently stored in the computer. The file store (ie FORTRAN source) version is termed VariabSS whilst the binary version (ie computer language) is termed BNVariabSS. Both versions must be addressed by the correct name otherwise the computer will reject the data.

When called forward the program is listed on 15K "words" in a 32K disc compiler and is compiled (and line printed) within 1 second. (When card listing of program is used before calculations 32K "words" and 5 seconds are required before work starts). The program listing of VariabSS is given below:

```
      PRØGRAM VARIAB (INPUT,ØUTPUT,RESULT ,TAPE5=INPUT,TAPE6=ØUTPUT,
     1TAPE7=RESULT )                                                    VAR  200
C                                                                       VAR  300
C VARIAB                                                                VAR  400
C                                                                       VAR  500
C TEMPERATURE CALCULATIØNS WITH VARIABLE MATERIAL PRØPERTIES            VAR  600
C                                                                       PRØ  700
      DIMENSIØN T( 8,10,40),VJ( 8),VK( 8,40),B(60)                      VAR  800
      DIMENSIØN F(44,40),V4(10),FI(10,40),FY(60)                        VAR  850
      LØGICAL AUSI(8,10,40),AUSTF(22,60)                                VAR  900
      REAL H(13)                                                        VAR  950
      CØMMØN T,B,IMAX2,JMAX2,KM,DL,IMAX1,H,AUST                         VAR 1000
    1 FØRMAT(21H REAL ARCING TIME(S)=,F6,1)                             VAR 1100
    3 FØRMAT(/14F8,2)                                                   VAR 1200
    5 FØRMAT(4F6,1,F6,3,F5,3)                                           VAR 1300
    6 FØRMAT(23H WANTED ARCING TIME(S)=,F6,1)                           VAR 1400
    7 FØRMAT(21H PLATE THICKNESS(CM)=,F6,1)                             VAR 1500
    8 FØRMAT(22H WELDING CURRENT(AMP)=,F6,1)                            VAR 1600
    9 FØRMAT(19H ARC VØLTAGE(VØLT)=,F6,1)                               VAR 1700
   10 FØRMAT(52H SPEED ØF ELECTRØDE ALØNG THE LINE ØF WELDING(CM/S)=,   VAR 1800
     1F6,2)                                                             VAR 1900
   11 FØRMAT(19H EFFICIENCY FACTØR=,F6,2)                               VAR 2000
   12 FØRMAT(35H HEAT SUPPLIED TØ THE PLATE(CAL/S)=,F8,1)               VAR 2030
   13 FØRMAT(14H TIME STEP(S)= ,F7,2)                                   VAR 2060
   14 FØRMAT (F6,2,F5,2,2I2,2I3,3F6,3)                                  VAR 2100
      READ(5,5)TSTART,TYKK,AMP,VØLT,FART,ETA                            VAR 2110
      WRITE (6,5) TSTART,TYKK,AMP,VØLT,FART,ETA                         VAR 2120
      READ(5, 14) DB,DL,IMAX,JMAX,KM,KMAX,        GAMMA,AMBDA,ALFAMX   VAR 2150
      WRITE (6, 14) DB,DL,IMAX,JMAX,KM,KMAX,      GAMMA,AMBDA,ALFAMX   VAR 2200
      WRITE(6,6)TSTART                                                  VAR 2300
      WRITE(6,7)TYKK                                                    VAR 2400
      WRITE(6,8)AMP                                                     VAR 2500
      WRITE(6,9)VØLT                                                    VAR 2600
      WRITE(6,10)FART                                                   VAR 2700
      WRITE(6,11)ETA                                                    VAR 4100
C                                                                       VAR 4200
C INITIALIZATIØN,CALCULATED VALUES
```

```
                      WRITE(6,9)VOLT                                          VAR 2400
                      WRITE(6,10)FART                                         VAR 2500
                      WRITE(6,11)ETA                                          VAR 2600
                C                                                             VAR 2700
                C INITIALIZATION,CALCULATED VALUES                            VAR 4100
                C                                                             VAR 4200
                      A=AMBDA/GAMMA                                           VAR 4300
                      DI=FLOAT(IMAX)                                          VAR 4400
                      DH=TYKK/DI                                              VAR 4500
                      QPRIKK=0.24*ETA*AMP*VOLT                                VAR 4600
                      DH2=DH**2                                               VAR 4700
                      DB2=DB**2                                               VAR 4900
                      DL2=DL**2                                               VAR 5000
                      DU=3.0*DB                                               VAR 5100
                      DV=3.0*DL                                               VAR 5200
                      DU2=DU**2                                               VAR 5300
                      DV2=DV**2                                               VAR 5400
                      N=(JMAX+1)/3+1                                          VAR 5500
                      KMAX2=KMAX+0                                            VAR 5600
                      N=2*KMAX2/3                                             VAR 5700
                      V=DH*DB*DL                                              VAR 5800
                      VINV=1.0/DH**2+1.0/DB**2+1.0/DL**2                      VAR 5900
                      DTG0=DL/FART                                            VAR 6000
                      IMAX1=IMAX+1                                            VAR 6100
                      IMAX2=IMAX+2                                            VAR 6200
                      JMAX1=JMAX+1                                            VAR 6300
                      JMAX2=JMAX+2                                            VAR 6400
                      KMAX1=KMAX2-1                                           VAR 6500
                      WRITE(6,12)QPRIKK                                       VAR 6600
                      RMAX=(FLOAT(JMAX
```

PROGRAM VARIAB  76/76  OPT=1 TRACE  FTN 4.5+433  19/04/77  11.37.1

2

```
      25 BMAX=(FLOAT(JMAX2)-1,5)*DB                                     VAR
         DO 26 J=1,13                                                   VAR
      26 B(J)=(FLOAT(J)-1,5)*DB                                         VAR
         DO 27 I=1,IMAX2                                                VAR
      27 H(I)=(FLOAT(I)-1,5)*DH                                         VAR
C                                                                       VAR
C INITIALIZATION,VALUES AT THE START OF WELDING                         VAR
C                                                                       VAR
         TIDINI=0,0                                                     VAR
         SUMTID=0,0                                                     VAR
      28 VI=0,0                                                         VAR
         V2=0,0                                                         VAR
         V3=0,0                                                         VAR
         DO 29 J=1,JMAX2                                                VAR
         FY(J)=20,0                                                     VAR
         V4(J)=0,0                                                      VAR
         DO 29 K=1,KMAX2                                                VAR
         AUSTF(J,K)=,FALSE,                                             VAR
      29 F(J,K)=2,625                                                   VAR
         DO 30 I=1,IMAX2                                                VAR
         VJ(I)=0,0                                                      VAR
         DO 30 J=1,JMAX2                                                VAR
         VK(I,J)=0,0                                                    VAR
         FI(I,J)=20,0                                                   VAR
         DO 30 K=1,KMAX2                                                VAR
         AUST(I,J,K)=,FALSE,                                            VAR
      30 T(I,J,K)=2,625                                                 VAR
C                                                                       VAR
C RETURN TO THIS LABEL                                                  VAR
C                                                                       VAR
C CALCULATION OF THE MAXIMUM TIME STEP FOR ONE SINGLE LOOP              VAR
C                                                                       VAR
      70 DTID = 0,4/ALFANX/VINV                                         VAR
         IF(DTID,LT,DTGO)GO TO 80                                       VAR
         DTID=DTGO+1,0E-7                                               VAR
         GO TO 90                                                       VAR
      80 DTID=DTGO/FLOAT(IFIX(DTGO/DTID)+1)+1,0E-7                      VAR
      90 WRITE(6,13)DTID                                                VAR
```

```
      DØ 30 I=1,IMAX2                                                  VAR 8300
      VJ(I)=0,0                                                        VAR 8400
      DØ 30 J=1,JMAX2                                                  VAR 8500
      VK(I,J)=0,0                                                      VAR 8600
      FI(I,J)=20,0                                                     VAR 8650
      DØ 30 K=1,KMAX2                                                  VAR 8700
      AUST(I,J,K)=.FALSE.                                              VAR 8750
   30 T(I,J,K)=2,625                                                   VAR 8800
C                                                                      VAR 8900
C RETURN TØ THIS LABEL                                                 VAR 9000
C                                                                      VAR 9100
C CALCULATION ØF THE MAXIMUM TIME STEP FØR ØNE SINGLE LØØP             VAR 9200
C                                                                      VAR 9300
   70 DTID = 0,4/ALFAMX/VINV                                           VAR 9400
      IF(DTID,LT,DTGØ)GØ TØ 80                                         VAR 9420
      DTID=DTGØ+1,0E-7                                                 VAR 9440
      GØ TØ 90                                                         VAR 9460
   80 DTID=DTGØ/FLØAT(IFIX(DTGØ/DTID)+1)+1,0E-7                        VAR 9480
   90 WRITE(6,13)DTID                                                  VAR 9490
C                                                                      VAR 9500
C TIME CHECK CONCERNING SHIFT ØF THE PØSITIØNS ØF THE TEMPERATURE PØINTSVAR 9600
C                                                                      VAR 9700
  100 IF (DTGØ,GT,(TIDINT+DTID)) GØTØ 120                              VAR 9800
  102 IF(TIDINT,GT,DTGØ)GØTØ 104                                       VAR 9900
      GØTØ 120                                                         VAR10100
  104 SUMTID=SUMTID+TIDINT                                             VAR10200
      TIDINT=0,0                                                       VAR10300
C                                                                      VAR10500
C SHIFT ØF THE PØSITIØNS ØF THE TEMPERATURE PØINTS                     VAR10600
C                                                                      VAR10700
      DØ 110 J=2,N                                                     VAR10800
  110 F(J,N)=T(3,3*J-3,2)                                              VAR10900
      DØ 112 K=2,KMAX2                                                 VAR11000
      DØ 112 J=1,JMAX2                                                 VAR11100
```

```
      F(J,K-1)=(2,*F(J,K-1)+F(J,K))/3,                                  VAR11200
      DØ112 I=1,IMAX2                                                   VAR11300
        IF(AUST(I,J,K))AUST(I,J,K-1)=,TRUE,                             VAR11350
  112 T(I,J,K-1)=T(I,J,K)                                               VAR11400
  120 TIDINT=TIDINT+ØTID                                                VAR11500
C                                                                       VAR11600
C HEAT TRANSFER TØ THE PLATE                                            VAR11700
C                                                                       VAR11800
      DTP=ØPRIKK*ØTID/GAMMA/V/2,0                                       VAR11900
      T(2,2,KM)=T(2,2,KM)+DTP                                           VAR12000
C                                                                       VAR12100
C INNER ZØNE                                                            VAR12200
C                                                                       VAR12300
C BØUNDARY CØNDITIØNS BETWEEN ØUTER AND INNER ZØNE PARALLEL TØ THE WELD VAR12400
C                                                                       VAR12500
      KS=KMAX2-N                                                        VAR12600
      DØ 140 K=1,KS,1                                                   VAR12700
      DØ 140 KK=1,3                                                     VAR12800
      KE=KK+3*(K-1)                                                     VAR12900
      DØ 140 I=1,IMAX2                                                  VAR13000
  140 T(I,JMAX2,KE)=(2,0*T(I,JMAX1,KE)+F(M+1,N+K-1))/3,0                VAR13100
C                                                                       VAR13200
C BØUNDARY CØNDITIØNS IN FRØNT ØF THE ARC                               VAR13300
C                                                                       VAR13400
      DØ 141 I=1,IMAX2                                                  VAR13500
      DØ 141 J=1,JMAX2                                                  VAR13600
  141 T(I,J,KMAX2)=2,625                                                VAR13700
C                                                                       VAR13800
C BØUNDARY CØNDITIØNS IN THE VERTICAL PLANE ØF SYMMETRY                 VAR13900
C                                                                       VAR14000
      DØ 142 I=1,IMAX2                                                  VAR14100
      DØ 142 K=1,KMAX2                                                  VAR14200
  142 T(I,1,K)=T(I,2,K)                                                 VAR14300
C                                                                       VAR14400
C BØUNDARY CØNDITIØNS BEHIND THE ARC                                    VAR14500
```

```
      141 T(I,J,KMAX2)=2.025
      C                                                                 VAR13800
      C BOUNDARY CONDITIONS IN THE VERTICAL PLANE OF SYMMETRY           VAR13900
      C                                                                 VAR14000
145         DO 142 I=1,IMAX2                                            VAR14100
            DO 142 K=1,KMAX2                                            VAR14200
      142 T(I,1,K)=T(I,2,K)                                             VAR14300
      C                                                                 VAR14400
      C BOUNDARY CONDITIONS BEHIND THE ARC                              VAR14500
150   C                                                                 VAR14600
            DO 402 J=2,M                                                VAR14700
            JJ=-5                                                       VAR14800
      401 JJ=JJ+1                                                       VAR14825
            JE=3*J+JJ                                                   VAR14850
155         DO 143 I=1,IMAX2                                            VAR15000
      143 T(I,JE,1)=(2.0*T(I,JE,2)+F(J,N-1))/3.0                        VAR15100
          IF (JJ.NE.-2) GOTO 401                                        VAR15120
      402 CONTINUE                                                      VAR15150
      C                                                                 VAR15200
160   C BOUNDARY CONDITIONS FOR THE UPPER AND LOWER SURFACE OF THE PLATE VAR15300
      C                                                                 VAR15400
          DO 145 J=1,JMAX2                                              VAR15500
          DO 145 K=1,KMAX2                                              VAR15600
          T(1,J,K)=T(2,J,K)                                             VAR15700
165   145 T(IMAX2,J,K)=T(IMAX1,J,K)                                     VAR15800
      C                                                                 VAR15900
      C TIME CHECK CONCERNING OUTPUT AND STOP                           VAR16000
      C                                                                 VAR16100
      147 IF(SUMTID.LT.TSTART)GOTO 150                                  VAR16200
170       I = 36                                                        VAR16250
          WRITE(6,1)SUMTID                                              VAR16300
```

```
      148  CALL SKRFIR (I)                                                  VAR16350
           IF (I.EQ.2) STOP                                                 VAR16400
           I = I-1                                                          VAR16450
175        GOTO 148                                                         VAR16500
      C                                                                     VAR16700
      C CALCULATION OF THE TEMPERATURES IN THE INNER ZONE                   VAR16800
      C                                                                     VAR16900
      150 DO 160 K=1,KMAX2                                                  VAR17000
180        DO 160 J=1,JMAX2                                                 VAR17100
           DO 160 I=1,IMAX2                                                 VAR17200
             IF(T(I,J,K).LT.0.0)WRITE  (6,155)T(I,J,K),I,J,K
      155 FORMAT(F10.2,3I6)
           FIK=PHI(T(I,J,K),AUST(I,J,K))                                    VAR17300
185        IF(T(I,J,K).GT.137.529)AUST(I,J,K)=.TRUE.                        VAR19000
           IF(I.EQ.IMAX2.OR.J.EQ.JMAX2.OR.K.EQ.1)GOTO 160                   VAR19100
           FIN=FI(I,J)                                                      VAR19200
           VIU=A*(FIN-FI(I+1,J))/DH2                                        VAR19300
           VJU=A*(FIN-FI(I,J+1))/DB2                                        VAR19400
190        VKU=A*(FIN-FIK)/DL2                                              VAR19500
           T(I,J,K-1) = T(I,J,K-1)+DTID*(VI+VJ(I)+VK(I,J)-VIU-VJU-VKU)      VAR19600
           VI=VIU                                                           VAR19700
           VJ(I)=VJU                                                        VAR19800
           VK(I,J)=VKU                                                      VAR19900
195        FI(I,J)=FIK                                                      VAR20000
      C                                                                     VAR20100
      C OUTER ZONE                                                          VAR20200
      C                                                                     VAR20300
      C BOUNDARY CONDITIONS BEHIND THE ARC                                  VAR20400
200   C                                                                     VAR20500
           DO 176 J=2,M                                                     VAR20600
        176 F(J,N)=T(3,3*J-3,2)                                             VAR20700
      C                                                                     VAR20800
      C BOUNDARY CONDITIONS BETWEEN OUTER AND INNER ZONE PARALLEL TO THE WELD VAR20900
205   C                                                                     VAR21000
           I=KMAX2-M-1                                                      VAR21100
           DO 178 K=1,I                                                     VAR21200
        178 F(M,N+K)=T(3,JMAX1,2+3*K)                                       VAR21300
                                                                            VAR21400
```

```
      C                                                                 VAR21400
 210  C BØUNDARY CØNDITIØNS IN THE VERTICAL PLANE ØF SYMMETRY          VAR21500
      C                                                                 VAR21600
            DØ 180 K=1,N                                               VAR21700
        180 F(1,K)=F(2,K)                                              VAR21800
      C                                                                 VAR21900
 215  C CALCULATIØN ØF THE TEMPERATURES IN THE ØUTER ZØNE               VAR22000
      C                                                                 VAR22100
            DØ 195 K=1,KMAX1                                           VAR22200
            DØ 195 J=1,JMAX2                                           VAR22300
            FYK=PHI(F(J,K),AUSTF(J,K))                                 VAR22400
 220        IF(F(J,K).GT.137.529)AUSTF(J,K)=.TRUE.                     VAR24100
            IF(K.EQ.1.ØR.J.EQ.JMAX2)GØTØ 195                           VAR24200
        192 FYN=FY(J)                                                  VAR24300
            V1=A*(FYN-FY(J+1))/DU2                                     VAR24400
            V2=A*(FYN-FYK)/DV2                                         VAR24500
 225        F(J,K-1) = F(J,K-1)+DTID*(V3+V4(J)-V1-V2)                  VAR24600
            V3=V1                                                      VAR24700
            V4(J)=V2                                                   VAR24800
            FY(J)=FYK                                                  VAR24900
```

```
      PRØGRAM VARIAB     76/76   ØPT=1 TRACE                FTN 4.6+433      19/04/77  11.3
AGE    5
```

```
        195 CØNTINUE                                                   VAR24950
 230  C                                                                 VAR25000
      C BØUNDARY CØNDITIØNS BEHIND AND IN FRØNT ØF THE ARC              VAR25100
      C                                                                 VAR25200
            DØ 196 J=1,JMAX2                                           VAR25300
            F(J,KMAX2)=2.625                                           VAR25400
 235        196 F(J,1)=F(J,2)                                          VAR25500
      C                                                                 VAR25600
      C BØUNDARY CØNDITIØNS ALØNG THE EDGE ØF THE PLATE                 VAR25700
```

```
                DO 188 K=1,KMAX2                                        VAR25900
240             188 F(JMAX2,K)=F(JMAX1,K)                               VAR26000
                GOTO 100                                                VAR26100
                END                                                     VAR26300
```

```
      C                                                                 VAR26400
      C OUTPUT OF CALCULATED TEMPERATURES                               VAR26500
      C                                                                 VAR26600
            SUBROUTINE SKREIR(L  )                                      VAR26700
            DIMENSION T(8,10,40),B(60)                                  VAR26800
            REAL H(13)                                                  VAR26900
            LOGICAL AUST(8,10,40)                                       VAR26950
            COMMON T,B,IMAX2,JMAX2,KM,DL,IMAX1,H,AUST                   VAR26950
          1 FORMAT(//41H TEMPERATURES(DEGR.C) IN A CROSS SECTION ,F6.1,  VAR27000
     1    118H CM BEHIND THE ARC)                                       VAR27100
          2 FORMAT(10H    B(CM)=,14F8.2)                                VAR27200
          3 FORMAT(3H H=,F6.2,2HCM,14F8.1)                              VAR27300
          4 FORMAT(14F8.1)                                              VAR27350
            K=L                                                         VAR27400
            DO 20 I=1,IMAX2                                             VAR27500
            DO 20 J=1,JMAX2                                             VAR27600
            TH=T(I,J,K)                                                 VAR27700
            IF((TH.GT.135.897).OR.(TH.GT.24.541.AND.AUST(I,J,K)))GO TO 11 VAR27800
            TT=-445.646+SQRT(0.1986E06+11626.6*TH)                      VAR27900
            GO TO 19                                                    VAR28100
         11 IF(TH.GT.49.129)GO TO 12                                    VAR28200
            TT=250.0                                                    VAR28300
            GO TO 19                                                    VAR28400
         12 IF(TH.GT.205.529)GO TO 13                                   VAR28500
            TT=-111.24+7.3530*TH                                        VAR28600
            GO TO 19                                                    VAR28700
         13 IF(TH.GT.270.53)GO TO 14                                    VAR28800
            TT=1400.0                                                   VAR28900
            GO TO 19                                                    VAR29000
         14 TT=-137.094+5.6818*TH                                       VAR29100
         19 CONTINUE                                                    VAR29200
         20 T(I,J,K)=TT                                                 VAR30100
            RK=FLOAT(KM-L)                                              VAR30200
            AK=RK*DL                                                    VAR30300
            WRITE(6,1)AK                                                VAR30400
            WRITE(6,2)(B(J),J=2,9)                                      VAR30500
            DO 10 I=2,IMAX1                                             VAR30600
            WRITE(7,4)(T(I,J,L),J=2,9)                                  VAR30650
```

```
            WRITE(7,4)(T(I,J,L),J=2,9)                                      VAR30650
         10 WRITE(6,3)H(I),(T(I,J,L),J=2,9)                                 VAR30700
40          RETURN                                                          VAR30800
            END                                                             VAR30900
```

```
FUNCTION PHI      76/76   OPT=1 TRACE                FTN 4.6+433      19/04/77  11.37.
E   1
```

```
1           C                                                               VAR40000
            C CONVERT HEAT CONTENT TO MODIFIED TEMPERATURE                  VAR40100
            C                                                               VAR40200
            FUNCTION PHI(TH,GAMMA)                                          VAR40300
5           LOGICAL GAMMA                                                   VAR40400
            IF(GAMMA.AND.TH.LT.136)GO TO 100                                VAR40500
            IF(TH.GT.48.867)GO TO 10                                        VAR40600
            PHI=-0.445646E03+SQRT(0.1986E06+11626.6*TH)                     VAR40700
            RETURN                                                          VAR40800
```

```
10          10 IF(TH.GT.135.897)GØ TØ 20                                    VAR40900
               T=-445.646+SQRT(0.1986E06+11626.6*TH)                        VAR41000
               PHI=-23.09+1.1071*T-1.2417E-04*T*T                           VAR41100
               RETURN                                                       VAR41200
            20 IF(TH.GT.152.353)GØ TØ 30                                    VAR41300
15             T=-111.24+7.3530*TH                                          VAR41400
               PHI=-23.09+(1.1071-1.2417E-04*T)*T                           VAR41500
               RETURN                                                       VAR41600
            30 IF(TH.GT.205.529)GØ TØ 40                                    VAR41700
               T=-111.24+7.3530*TH                                          VAR41800
20             PHI=34.313+(0.84848+0.075758E-03*T)*T                        VAR41900
               RETURN                                                       VAR42000
            40 IF(TH.GT.270.529)GØ TØ 50                                    VAR42100
               PHI=1370.67                                                  VAR42200
               RETURN                                                       VAR42300
25          50 PHI=-3287.2+17.21*TH                                         VAR42400
               RETURN                                                       VAR42500
           100 IF(TH.LT.49.129)GØ TØ 110                                    VAR42600
               T=-445.646+SQRT(0.1986E06+11626.6*TH)                        VAR42700
               PHI=-23.09+1.1071*T-1.2417E-04*T**2                          VAR42800
30             RETURN                                                       VAR42900
           110 IF(TH.LT.24.541)GØ TØ 120                                    VAR43000
               PHI=250.0                                                    VAR43100
               RETURN                                                       VAR43200
           120 PHI=-445.646+SQRT(0.1986E06+11626.6*TH)                      VAR43300
35             RETURN                                                       VAR43400
               END                                                          VAR43500
```

## A3.3 Input data

To perform calculations with VariabSS no knowledge of the FORTRAN computer language is required. Apart from the computer system job cards and finish card (****) only three cards are required. The first card is the instruction to load the program and is typed thus:-

UA FORTRAN▽ OWNPD,LOAD▽BNVARIABSS (▽ is space)

After this comes the data card onto which welding parameters are put (spacing in this is absolutely critical). Data is in this order: arcing time required in seconds; plate thickness in centimetres; welding current in Amps; arc voltage in volts; arc travel speed in cms $sec^{-1}$; arc efficiency factor.
A typical data card is given thus:-

▽▽30.0▽▽▽2.5▽1125.0▽30.0▽0.6▽0.99

The parameter card follows this and carries matrix definitions, initialising values etc. Once typed it usually does not require changing unless the matrix is extended or contracted. Information on this card is given in the following order: matrix increment in x direction (width) (cms); matrix increment in y direction (length) (cms); number of through thickness calculation steps; number of width (x) steps to be calculated; position of arc in y direction relative to number of y axis steps; number of y axis steps to be calculated; specific gravity of steel (grammes $cc^{-1}$); thermal conductivity (cal $cm^{-1}sec^{-1}$ degree $C^{-1}$), thermal diffusivity ($cm^2sec^{-1}$). Typical data on the parameter card is given below (spacing is once again critical)

▽▽0.55▽0.65▽3▽8▽15▽18▽7.830▽0.066▽0.074

After this only the end job card (****) is required. Calculation of the thermal history of the weld will be performed in this case for 30 seconds arcing time using the given welding parameters.

## A2.4 Results from computer

Results of the computer calculations appear in matrix form. Temperatures are given at depth/width intersections at each successive length increment. The temperatures calculated are not for the intersect points under which they appear but are in the centre of the rectangular matrix block defined by these co-ordinates. This point is only of importance when undertaking mathematical dealings to accurately locate peak temperature, in graphically determining weld HAZ heating and cooling rates the time base is used.

Results from the computed weld thermal cycle appear overleaf The input data was that given above on both data and parameter cards, computation time on an ICL 1904 S computer was 60 seconds, maximum core usage was 15K words.

Results are shown overleaf.

```
 0.55 0.65  5  8  15  18  7.850  0.066  0.074
WANTED ARCING TIME(S)=   30.0
PLATE THICKNESS(CM)=    2.5
WELDING CURRENT(AMP)=1125.0
ARC VOLTAGE(VOLT)=   30.0
SPEED OF ELECTRODE ALONG THE LINE OF WELDING(CM/S)=  0.60
EFFICIENCY FACTOR=  0.90
HEAT SUPPLIED TO THE PLATE(CAL/S)=  8019.0
TIME STEP(S)=   0.54
REAL ARCING TIME(S)=  30.3


TEMPERATURES(DEGR.C) IN A CROSS SECTION  -1.3 CM BEHIND THE ARC
    R(CM)=     0.28     0.83     1.38     1.93     2.48     3.03     3.58     4.12
H=  0.42CM     33.0     33.0     33.0     33.0     33.0     33.0     33.0     33.0
H=  1.25CM     33.0     33.0     33.0     33.0     33.0     33.0     33.0     33.0
H=  2.08CM     33.0     33.0     33.0     33.0     33.0     33.0     33.0     33.0


TEMPERATURES(DEGR.C) IN A CROSS SECTION  -0.7 CM BEHIND THE ARC
    R(CM)=     0.28     0.83     1.38     1.93     2.48     3.03     3.58     4.12
H=  0.42CM    192.6     49.3     34.6     33.2     33.0     33.0     33.0     33.0
H=  1.25CM     40.5     34.4     33.2     33.0     33.0     33.0     33.0     33.0
H=  2.08CM     33.4     33.1     33.0     33.0     33.0     33.0     33.0     33.0


TEMPERATURES(DEGR.C) IN A CROSS SECTION   0.0 CM BEHIND THE ARC
    R(CM)=     0.28     0.83     1.38     1.93     2.48     3.03     3.58     4.12
H=  0.42CM.  7530.7    376.6     71.4     36.7     33.4     33.1     33.0     33.0
H=  1.25CM    244.9     65.5     37.5     33.6     33.1     33.0     33.0     33.0
H=  2.08CM     41.9     35.2     33.4     33.1     33.0     33.0     33.0     33.0


TEMPERATURES(DEGR.C) IN A CROSS SECTION   0.7 CM BEHIND THE ARC
    R(CM)=     0.28     0.83     1.38     1.93     2.48     3.03     3.58     4.12
H=  0.42CM.  3920.2   3153.9    445.1     81.2     38.1     33.6     33.1     33.0
H=  1.25CM   1481.2    462.7     89.7     40.3     34.0     33.1     33.0     33.0
H=  2.08CM    145.5     61.8     38.7     34.0     33.2     33.0     33.0     33.0
```

TEMPERATURES(DEGR.C) IN A CROSS SECTION 1.3 CM BEHIND THE ARC

| B(CM)= | 0.28 | 0.83 | 1.38 | 1.93 | 2.48 | 3.03 | 3.58 | 4.12 |
|---|---|---|---|---|---|---|---|---|
| H= 0.42CM | 3925.9 | 2391.1 | 1138.2 | 258.2 | 69.5 | 37.8 | 33.6 | 33.1 |
| H= 1.25CM | 1666.1 | 787.6 | 278.1 | 86.1 | 41.6 | 34.5 | 33.2 | 33.0 |
| H= 2.08CM | 298.4 | 162.0 | 71.9 | 41.2 | 34.5 | 33.3 | 33.1 | 33.0 |

TEMPERATURES(DEGR.C) IN A CROSS SECTION 2.0 CM BEHIND THE ARC

| B(CM)= | 0.28 | 0.83 | 1.38 | 1.93 | 2.48 | 3.03 | 3.58 | 4.12 |
|---|---|---|---|---|---|---|---|---|
| H= 0.42CM | 2867.9 | 2061.3 | 1400.0 | 595.1 | 121.2 | 51.9 | 36.3 | 33.5 |
| H= 1.25CM | 1634.1 | 1231.8 | 421.3 | 153.2 | 64.7 | 39.0 | 34.1 | 33.2 |
| H= 2.08CM | 438.8 | 259.3 | 126.2 | 63.7 | 40.8 | 36.6 | 33.3 | 33.1 |

TEMPERATURES(DEGR.C) IN A CROSS SECTION 2.6 CM BEHIND THE ARC

| B(CM)= | 0.28 | 0.83 | 1.38 | 1.93 | 2.48 | 3.03 | 3.58 | 4.12 |
|---|---|---|---|---|---|---|---|---|
| H= 0.42CM | 2377.4 | 1990.0 | 1400.0 | 496.7 | 175.4 | 71.6 | 42.1 | 35.1 |
| H= 1.25CM | 1616.7 | 1337.7 | 555.0 | 224.3 | 94.6 | 50.1 | 37.1 | 33.9 |
| H= 2.08CM | 533.7 | 359.8 | 189.6 | 94.7 | 53.4 | 38.7 | 34.3 | 33.3 |

TEMPERATURES(DEGR.C) IN A CROSS SECTION 3.2 CM BEHIND THE ARC

| B(CM)= | 0.28 | 0.83 | 1.38 | 1.93 | 2.48 | 3.03 | 3.58 | 4.12 |
|---|---|---|---|---|---|---|---|---|
| H= 0.42CM | 2079.1 | 1797.5 | 1400.0 | 566.7 | 223.0 | 94.3 | 50.7 | 38.0 |
| H= 1.25CM | 1554.3 | 1364.7 | 649.9 | 287.5 | 128.3 | 64.5 | 42.1 | 35.5 |
| H= 2.08CM | 607.6 | 441.3 | 251.4 | 131.8 | 71.5 | 45.8 | 36.7 | 34.1 |

TEMPERATURES(DEGR.C) IN A CROSS SECTION 3.9 CM BEHIND THE ARC

| B(CM)= | 0.28 | 0.83 | 1.38 | 1.93 | 2.48 | 3.03 | 3.58 | 4.12 |
|---|---|---|---|---|---|---|---|---|
| H= 0.42CM | 1869.9 | 1668.5 | 1400.0 | 620.4 | 264.8 | 117.4 | 61.1 | 42.4 |
| H= 1.25CM | 1496.7 | 1339.2 | 716.3 | 342.5 | 161.8 | 81.5 | 47.5 | 36.5 |
| H= 2.08CM | 662.7 | 505.2 | 308.3 | 170.2 | 92.9 | 56.0 | 40.8 | 35.6 |

TEMPERATURES(DEGR.C) IN A CROSS SECTION 4.5 CM BEHIND THE ARC

TEMPERATURES(DEGR.C) IN A CROSS SECTION 4.5 CM BEHIND THE ARC

| | R(CM)= 0.28 | 0.83 | 1.38 | 1.93 | 2.48 | 3.03 | 3.58 | 4.12 |
|---|---|---|---|---|---|---|---|---|
| H= 0.42CM | 1719.3 | 1586.1 | 1400.0 | 663.3 | 301.6 | 140.5 | 72.9 | 48.2 |
| H= 1.25CM | 1449.0 | 1287.2 | 762.2 | 389.0 | 193.8 | 99.4 | 58.1 | 42.7 |
| H= 2.08CM | 703.0 | 555.6 | 358.5 | 207.3 | 116.3 | 68.5 | 46.6 | 38.4 |

TEMPERATURES(DEGR.C) IN A CROSS SECTION 5.2 CM BEHIND THE ARC

| | R(CM)= 0.28 | 0.83 | 1.38 | 1.93 | 2.48 | 3.03 | 3.58 | 4.12 |
|---|---|---|---|---|---|---|---|---|
| H= 0.42CM | 1613.1 | 1522.5 | 1400.0 | 699.0 | 354.1 | 162.5 | 85.5 | 55.0 |
| H= 1.25CM | 1410.2 | 1231.9 | 792.9 | 428.2 | 223.8 | 117.9 | 68.1 | 47.6 |
| H= 2.08CM | 732.8 | 595.1 | 402.0 | 243.4 | 140.4 | 82.6 | 54.0 | 42.1 |

TEMPERATURES(DEGR.C) IN A CROSS SECTION 5.9 CM BEHIND THE ARC

| | R(CM)= 0.28 | 0.83 | 1.38 | 1.93 | 2.48 | 3.03 | 3.58 | 4.12 |
|---|---|---|---|---|---|---|---|---|
| H= 0.42CM | 1538.8 | 1475.7 | 1400.0 | 729.3 | 363.1 | 165.5 | 98.4 | 62.6 |
| H= 1.25CM | 1400.0 | 1184.5 | 813.1 | 461.3 | 251.4 | 136.4 | 79.0 | 54.2 |
| H= 2.08CM | 755.7 | 626.2 | 439.5 | 276.5 | 164.5 | 97.8 | 62.6 | 45.9 |

TEMPERATURES(DEGR.C) IN A CROSS SECTION 6.5 CM BEHIND THE ARC

| | R(CM)= 0.28 | 0.83 | 1.38 | 1.93 | 2.48 | 3.03 | 3.58 | 4.12 |
|---|---|---|---|---|---|---|---|---|
| H= 0.42CM | 1467.8 | 1436.3 | 1277.5 | 750.5 | 369.5 | 203.5 | 111.6 | 71.0 |
| H= 1.25CM | 1400.0 | 1156.2 | 825.3 | 489.3 | 276.3 | 154.6 | 93.6 | 61.4 |
| H= 2.08CM | 777.5 | 651.8 | 471.7 | 306.9 | 187.9 | 113.5 | 72.2 | 52.0 |

TEMPERATURES(DEGR.C) IN A CROSS SECTION 7.2 CM BEHIND THE ARC

| | R(CM)= 0.28 | 0.83 | 1.38 | 1.93 | 2.48 | 3.03 | 3.58 | 4.12 |
|---|---|---|---|---|---|---|---|---|
| H= 0.42CM | 1448.5 | 1403.1 | 1189.9 | 753.1 | 411.1 | 222.4 | 124.8 | 79.8 |
| H= 1.25CM | 1400.0 | 1135.5 | 828.4 | 512.3 | 299.9 | 172.2 | 102.4 | 69.1 |
| H= 2.08CM | 798.9 | 674.3 | 499.6 | 354.6 | 219.3 | 129.5 | 82.6 | 59.5 |

TEMPERATURES(DEGR.C) IN A CROSS SECTION 7.8 CM BEHIND THE ARC

R(CM)= 0.28 ...

TEMPERATURES(DEGR.C) IN A CROSS SECTION 7.8 CM BEHIND THE ARC

| R(CM)= | 0,28 | 0,83 | 1,38 | 1,93 | 2,48 | 3,03 | 3,58 | 4,12 |
|---|---|---|---|---|---|---|---|---|
| H= 0,42CM | 1424,7 | 1400,0 | 1129,3 | 748,5 | 428,1 | 259,6 | 137,8 | 88,7 |
| H= 1,25CM | 1400,0 | 1123,0 | 828,1 | 550,3 | 320,7 | 189,1 | 114,4 | 77,3 |
| H= 2,08CM | 817,8 | 694,3 | 523,8 | 359,7 | 231,7 | 145,4 | 93,5 | 66,7 |

TEMPERATURES(DEGR.C) IN A CROSS SECTION 8,5 CM BEHIND THE ARC

| R(CM)= | 0,28 | 0,83 | 1,38 | 1,93 | 2,48 | 3,03 | 3,58 | 4,12 |
|---|---|---|---|---|---|---|---|---|
| H= 0,42CM | 1412,7 | 1400,0 | 1095,0 | 741,6 | 441,1 | 255,6 | 150,1 | 98,1 |
| H= 1,25CM | 1400,0 | 1117,8 | 827,3 | 544,4 | 339,0 | 205,6 | 124,2 | 86,0 |
| H= 2,08CM | 836,2 | 713,0 | 545,8 | 382,1 | 252,0 | 161,7 | 104,6 | 74,9 |

## A1.5 Mathematical solution for accurate peak temperature location

Graph plotting Variab results can be used to construct most of the weld HAZ heating and cooling information. It was found that for accurate metallographic area positioning a more subtle technique to accurately locate the required isotherm was required. This was achieved by differentiating the respective part of the matrix in the following manner (which will be illustrated by using information from weld run T2)

### i) Produce matrix containing required peak temperature (at a constant depth)

| | | | |
|---|---|---|---|
| | 841(a) : | 841(b) | 158(c) (+1) |
| (y axis) | | | |
| | 1400(d) : | 1400(e) | 536(f) (0) |
| $x_2$ | | | |
| | 1043(g) : | 1043(h) | 985(i) (-1) |
| | (-1) | (0) | (+1) |

(x axis) $x_1$ (⋮ defines weld centre line)

### ii) Calculation of curve contour equation

Since the positions at which the temperatures have been calculated are orthogonal, it is simple to fit a 2nd degree equation to the temperature distribution. Formula is:-

$$y = b_o + b_1x_1 + b_2x_2 + b_3x_1^2 + b_4x_2^2 + b_5x_1x_2$$

where $b_0 = (5e + 2b + 2d + 2f + 2h - a - c - g - i) \div 9$

$b_1 = (c + f + i - a - d - g) \div 6$

$$b_2 = (a + b + c - g - h - i) \div 6$$

$$b_3 = (a + d + g + c + f + i - 2b - 2e - 2h) \div 6$$

$$b_4 = (a + b + c + g + h + i - 2d - 2e - 2f) \div 6$$

$$b_5 = (c + g - a - i) \div 4$$

In T2 this became:

$$b_o = 1345.8$$

$$b_1 = -350.8$$

$$b_2 = -121.8$$

$$b_3 = -350.8$$

$$b_4 = -377$$

$$b_5 = -31.25$$

Contour equation for 1360°C isotherm is:

(a) $1360 = 1345.8 - 350.8x_1 - 121.8x_2 - 350.8x_1^2 - 377x_2^2 - 31.25x_1x_2$

or

(b) $0 = -14.2 - 350.8x_1 - 121.8x_2 - 350.8x_1^2 - 377x_2^2 - 31.25x_1x_2$

iii) To locate required temperature position

(ie the distance from the centre line to a point which reaches a maximum temperature of 1360°C)

In the contour equation the 1360°C isotherm is parallel to the x axis (direction of welding arc travel), and occurs when the first differential (ie $\frac{dx_1}{dx_2}$) is zero. Differentiating with respect to $x_2$ the last equation becomes:

(c) $0 = -350.8\frac{dx_1}{dx_2} - 121.8 - 350.8x_1\frac{dx_1}{dx_2} - 754x_2 - 31.2x_2\frac{dx_1}{dx_2}$

When $\frac{dx_1}{dx_2} = 0$

(d) $0 = -121.8 - 754x_2 - 31.2$

(e) $\therefore$ by re-arrangement $x_2 = \frac{121.8}{754} - \frac{31.2}{754}x_1$

(f) $= x_2 = -0.1615 - 0.0414x_1$

Substituting values from (f) into (b) and solving as a quadratic for $x_1$, then

(g) $0 = -14.2 - 350.8x_1 + 19.6 - 5.04x_1 - 350.8x_1^2 - 9.83 - 5.04x_1$
$- 0.646x_1^2 + 5.038x_1 + 1.29168x^2$

(h) $\therefore 0 = -345.88x^2 - 345.762x_1 + 55.7$

Using quadratic solution formula

$$x = \frac{-B \pm \sqrt{B^2 - 4AC}}{2A}$$

where A is -345.88, B is -345.762 and C is 55.7 thus :

$$x_1 = \frac{-(345.88 \pm 278.23)}{691.6}$$

$\therefore x_1 = -0.902$ or $+0.097$

By inspection it may be seen that one value (-0.902) falls, quite correctly within the mirror image high temperature zone but is not the desired solution, so the real value is

+ 0.097 units. This, then, is the deviation of peak temperature around the $x_2$ axis, the $x_1$ unit is 0.6 cms (incremental step in variab). ∴Outer limit of the 1360°C isotherm is $x_2 + 0.097 \times (0.6)$ cms.

When thermal gradients in the $x_1$ direction (x axis) are required this computational process can be repeated to locate various isotherms. In this case the differentiator is $\frac{dx_2}{dx_1}$ and the orthoganol equation is thus differentiated with respect to $x_1$.

# ACKNOWLEDGEMENTS

ACKNOWLEDGEMENTS

The author wishes to thank Professor R H Thornley, Head of the Department of Production Engineering, for the use of facilities throughout this work. I would like to extend my gratitude to the Central Electricity Generating Board who financed the work throughout and to Mannesmann Rohrwerke A.G. for their generous donation of 224 Kg of tubular material, used for experimental purposes.

I would also like to take this opportunity to thank Dr M F Jordan, who initiated and supervised the project throughout; Dr J Aston, for his aid with the computer program modifications and Dr S Murphy for many helpful discussions.

In conclusion I would like to thank my wife, for providing both moral and financial support and innumerable cups of coffee; my mother-in-law, for a) proof reading the script and b) providing my wife; the technicians of the departments of Production Engineering and Metallurgy and Materials and the people at Aston Services. Finally, my thanks are also due to the typist, Miss Mavis Fletcher, for typing, and correcting the spelling of, this thesis.